Medium modifications of antikaons in dense matter

Vom Fachbereich Physik
der Technischen Universität Darmstadt

zur Erlangung des Grades
eines Doktors der Naturwissenschaften
(Dr. rer. nat)

genehmigte Dissertation von
Dipl.-Phys Thomas Roth
aus Hanau

Darmstadt 2004
D17

Referent:	Prof. Dr. Jochen Wambach
Korreferent:	Prof. Dr. Robert Roth

Tag der Einreichung:	27.5.2004
Tag der Prüfung:	7.7.2004

Zusammenfassung:

In dieser Arbeit werden die Eigenschaften von Antikaonen in dichter hadronischer Materie untersucht. Ziel ist eine Beschreibung des Kaonpropagators im Medium, die seine volle Energie– und Impulsabhängigkeit über einen weiten Energie–Impuls–Bereich beinhaltet/einschließt.
Als Grundlage für die Darstellung der Wechselwirkung des Antikaons mit den anderen Hadronen dient die Lagrangedichte der chiralen Störungstheorie für den $SU(3)$–Sektor.

In einem erstem Schritt berechnen wir die Vakuumstreuung von Mesonen und Baryon aus dem $SU(3)$–Sektor der chiralen Störungstheorie. Dazu wird die Bethe–Salpeter–Streugleichung für ein System gekoppelter Kanäle von Mesonen und Baryonen gelöst. Das Resultat ist die T–Matrix dieser Streuprozesse. Neben den Kaon–Nukleon–Kanälen werden Kombinationen aus Pionen, Eta–Mesonen sowie den Lambda – und Sigma – Baryonen berücksichtigt, die die Quantenzahl *Strangeness* $= -1$ aufweisen. Dabei ist der $\pi\Sigma$–Kanal von besonderer Bedeutung, da er in der Kopplung mit $\bar{K}N$ in der Streuamplitude zu Isospin $I = 0$ eine Resonanz erzeugt, die als $\Lambda(1405)$ bezeichnet wird. Das Auftreten dieser Resonanz etwas unterhalb der $\bar{K}N$–Schwelle ist der Grund dafür, daß die Berechnung der Streuung nicht auf störungsstheoretische Weise erfolgen kann, sondern vielmehr durch Aufsummieren aller Ordnungen in der Bethe–Salpeter–Gleichung bestimmt werden muß.
Diese Rechnung wird dann für den Fall der Streuung in einem Medium endlicher Baryonendichte wiederholt. Es ergeben sich entsprechende Änderungen der T–Matrix durch die Existenz des „Fermi–Sees“ bereits besetzter Nukleonzustände.
Da auch die Pionen einer starken Mediummodifikation unterliegen, muß ihre Selbstenergie ebenfalls berechnet und in den Propagatoren der Pion–Streukanäle berücksichtigt werden.

Das T–Matrixelement der KN–Streuung im Medium wird nun benutzt, um die Selbstenergie des Antikaons in diesem Medium zu berechnen.
Der solcherart modifizierte Propagator des Kaons wird erneut in die Streugleichung eingesetzt. Es ergibt sich ein Iterationsschema, das zur Selbstkonsistenz in Streuamplitude und Kaonpropagator geführt werden kann.

Das Verfahren wird auf die Fälle symmetrischer und asymmetrischer Kernmaterie angewendet. Letztere Umgebung liegt typischerweise in Neutronensternen vor. Mit Hilfe des vollen Propagators der Antikaonen kann damit die Frage der Kaonkondensation in Neutronensternen untersucht werden. Dabei handelt es sich um die Möglichkeit einer Umwandlung von Elektronen in negative Kaonen bei genügend hoher Dichte, falls die durch die Wechselwirkungen mit dem Medium verringerte Masse des K^- unter das elektrochemische Potential der Elektronen sinkt. Die Kaonen liegen dann in Form eines Bose–Kondensats vor, die verminderte Anzahl an Elektronen führt zu einem verringerten Elektronentartungsdruck.
Dabei ist von einem ladungsneutralen System im β–Gleichgewicht auszugehen. Realistische Beschreibungen unter Einbeziehung einer nuklearen Zustandgleichung können der Literatur entnommen werden. Die errechnete Masse der Antikaonen liegt jedoch bei den untersuchten Dichten bis zu fünffacher Kernmateriedichte über dem angegebenen elektrochemischen Potential, so daß keine Kaonkondensation möglich ist.
Schließlich werden die Möglichkeiten einer erweiterten Beschreibung des $\bar{K}N$–Problems mit Hinblick auf thermodynamische Selbstkonsistenz diskutiert.

Contents

List of Figures

Chapter 1

Introduction

Understanding the properties of the low–energy phase of the hadronic physics is a most intriguing task. Here the effective degrees of freedom are hadrons rather than quarks and gluons. The latter however are the constituents of the basic theory of hadronic interactions, quantum chromodynamics. The mechanism that confines the quarks and gluons into hadrons remains an open question.
Besides confinement, hadronic matter exhibits another prominent feature that has been attracting intense attention over many years. This is triggered by the observation that of the six elementary particles, the quarks, two are almost massless: the *up* and *down* quarks. Therefore QCD shows an invariance under $SU(2)_L \times SU(2)_R$ transformations of left– and right–handed quarks. This is the celebrated chiral symmetry. Yet particles composed of the *up*– and *down* quarks are all rather heavy particles: a nucleon is made up of three (u, d) quarks, but its mass is $m_N = 939$ MeV. Obviously the three constituents have a mass of roughly 300 MeV. The accepted explanation is that chiral symmetry is spontaneously broken in the vacuum, hence a $\overline{q}q$ condensate with a finite vacuum expectation value is formed which gives the compound particles their masses. The possible restoration of this symmetry at very high temperatures or densities is called the chiral phase transition of hadronic matter.
The theoretical investigation of strong interactions is pursued in a number of ways. Perturbative treatment of QCD fails at low and medium energies due to the strength of the strong coupling constant. One approach is the evaluation of QCD properties on a finite lattice of space–time points. Thus, ëxact solutions"are possible for some (mainly static) quantities like ground state energies. This approach, called lattice–QCD, involves an enormous numerical effort. The lattices used are relatively small, and the masses of the $((u, d))$ quarks that are put onto the lattice points are un–physically large. Nevertheless the method has been applied successfully to a number of questions. A prediction that is widely thought reliable is the critical temperature for the chiral phase transition at about 170 MeV. Lattice QCD however has very basic problems when going to finite baryon density, although progress has been made on this topic in the recent years [1].

The other extreme of approaching QCD problems at low energy is employed by the development of a large variety of effective models. Constructing such a model one usually tries to mimic QCD to some extent, keeping the QCD–features one believes important for the respective problem while forfeiting the complications of the fundamental theory. One example would be the Nambu–Jona–Lasinio model. It is a chirally symmetric model of quark–quark interactions that has been used to describe the breaking of chiral symmetry at low temperatures, the arise of constituent quark masses and a variety of other topics. However, it does not contain a confinement mechanism.
Another class of models are the purely hadronic ones, where mesons and baryons are the elementary degrees of freedom.

Another not–model–dependent approach is called chiral perturbation theory (χPT). Here the parameters used for the perturbative expansion are the small explicit breaking of chiral symmetry (that one leads to the finite current masses of *up* and *down* quarks) and the momenta of the particles (see sec. 3.1). This method has been applied with great success especially in the $SU(2)$ $(u, d\,-)$ sector of QCD, describing the properties of pions at low energies, the pion–nucleon interaction or the behavior of the quark condensate that forms the order parameter for chiral symmetry breaking [2]. Perturbative expansions always fail when non–perturbative phenomena show up. The basic form of χPT will thus cease to be reliable somewhere below the mass of the ρ meson at 770 MeV. Including baryons into χPT also poses a problem (see subsec. 3.2.1).
In this work the Lagrangian of chiral perturbation theory will actually be used as an effective hadronic model. That is, we take χPT formulated in terms of mesons and baryons as the given interaction. However, the problem we want to tackle proves to be of a nonperturbative nature. The methods of χPT cannot be applied. Instead, the calculation is restricted to the simplest diagram which is summed up to all orders. Nevertheless, the procedure involves a number of constants and parameters which are ingredients from χPT, so it is worthwhile to understand where they come from.

The generalization of the successful chiral $SU(2)$ scheme to the $SU(3)$ flavor group is straightforward. Although the mass of the strange quark is much larger, $m_s \approx 20\, m_{u,d}$, perturbation theory is expected to work still quite well, since the relevant chiral scale is of the order 1 GeV [3]. The octet of Goldstone bosons connected with the spontaneous breaking of chiral symmetry in this sectors is found in the π, K and η mesons. Thus $SU(3)$ χPT should give insight also into the dynamics of kaons and etas. Nevertheless it is kaon–nucleon scattering that immediately provides an example where the perturbative (χPT) predictions fail.
The kaon–nucleon scattering Lagrangian as derived from $SU(3)$ chiral perturbation theory contains at the lowest (mean field) level two s–wave interaction terms for the kaons: (i) a constant scalar term due to explicit chiral symmetry breaking, which is attractive for both K^+ and K^-, and which involves the kaon–nucleon–sigma term. (ii) a momentum–dependent vector term which is called Weinberg–Tomozawa term [4, 5]. This term is attractive for the K^- and repulsive for the K^+. For the K^+ these two terms essentially cancel each other leading to a small repulsive potential for the K^+. For the K^-, on the other hand, the terms add up to a large attractive mean field potential. The problem is that the empirical value of the s–wave K^- nucleon scattering length is repulsive at threshold ($\Re e a_{K^-p} = -0.78$ fm).
This discrepancy between experiment and (too simple) theory is caused by the existence of a resonance slightly below the kaon–nucleon threshold: the $\Lambda(1405)$ lies just 30 MeV below $m_K + m_N = 1.435$ GeV, and some 70 MeV above the pion–Σ threshold at 1.33 GeV. Scattering through this resonance gives rise to a repulsive contribution to the scattering amplitude at threshold. The $\Lambda(1405)$ is nowadays understood as a $\bar{K}N$ bound state and can as such not arise from tree–level perturbation theory. The construction of this resonance out of the χPT contributions in a coupled–channel scheme where the mentioned $\pi\Sigma$ channel is most prominent will be an important part of this work.

Originally, χPT was developed as a theory for the sector of hadron physics governed by the Goldstone bosons created in spontaneous chiral symmetry breaking – just pions in $SU(2)$ or the full octet in $SU(3)$ [6]. Applying it to topics as kaon–nucleon scattering requires the inclusion of baryons into the theory. A formalism to do that was developed by Jenkins and Manohar (Heavy Baryon χPT, [7], see subsec. 3.2.1). But whereas it gave good agreement with experiment at lowest order (e.g. for the baryon masses, see sec. 3.3), the leading loop corrections are so large that they seem to invalidate the whole concept of baryon chiral perturbation theory ([8, 9]). Only in recent years a satisfactory solution has been found by Meißner et al. [10]. While these problems do not directly concern this work, they give an example of how the $SU(3)$ sector leads to new insight into an otherwise quite well established theory.

Particular interest in the application of chiral perturbation theory to the strange sector of hadron physics was spawned by the suggestions of Kaplan and Nelson [11, 12] that attractive s–wave interactions between kaons and nucleons could lower the effective mass of kaons to the extent that kaons could form a Bose condensate in dense nuclear matter. Experimentally accessible samples might be found in collisions of heavy nuclei, in cores of collapsing stars or in the interior of neutron stars.

The formation of a condensate depends crucially on the nature of the kaon–nucleon interaction. In particular the size of the scalar interaction terms mentioned above proves to be of great importance [2]. In the χPT Lagrangian these "σ–terms' appear as the coefficients of the matrix elements $m_q\,\overline{q}q$ in the baryons. That means they are generated by the explicit breaking of chiral symmetry. Since the values of these coefficients cannot be derived but have to be fitted to data, the mentioned problems with higher order corrections in the chiral expansion play a role at this point [13].

The basic considerations are simple however [14]: Due to the scalar interaction term the nucleons behave as an effective scalar field $\mathcal{S} \sim \frac{1}{f_\pi^2}\overline{N}N$. The coupling strength is given by the so–called kaon–nucleon sigma term Σ^{KN}. Thus the $\bar{K}N$ Lagrangian will contain the kaon mass term

$$\frac{1}{2}(m_K^2 - \mathcal{S}\Sigma^{KN})\bar{K}K\ .$$

This effective kaon mass can be written as

$$m_K^* = m_K(1 - \frac{\rho}{\rho_c})^{1/2},$$

so the critical density would be

$$\rho_c = \frac{f_\pi^2 m_K^2}{\Sigma^{KN}}.$$

However, the value of the sigma term Σ^{KN} is not known very well. It is a measure of the strangeness content of the nucleon,

$$\Sigma^{KN} = \frac{1}{2}(m_u + m_s)\langle N|\overline{u}u + \overline{s}s|N\rangle.$$

Yet the strangeness content of the nucleon is uncertain [15, 16]. Varying it between zero and one (i.e. equal to the non–strange quark–content) gives the estimate $2.5\rho_0 < \rho_c < 5\rho_0$. Here ρ_0 stands for the nuclear saturation density of 0.16 nucleons$/fm^3$. Often the density is given in terms ρ_0: $\rho = u\,\rho_0$.

Actually, it is the vector term in the χPT Lagrangian that contributes more strongly to the $\bar{K}N$ interaction. Judging from the tree–level estimate that contribution seems to be attractive, lowering the antikaon mass further. The negative experimental scattering turns that argument around. This situation requires the treatment in terms of coupled channels of mesons and baryons, leading to the $\Lambda(1405)$ resonance and connected effects. Of course, this substantially increases the sophistication of the problem. The question of kaon condensation can no longer be pinned down to a single value as that of the amount of strangeness in the nucleon.

Also in the $SU(2)$ sector the question of Bose condensation was investigated [17]. It is somewhat easier to address s–wave pion condensation and to find that it is more unlikely to happen: The corresponding pion–nucleon sigma term $\Sigma_{\pi N} \approx 45$ MeV is well known and considerably smaller than the KN σ–terms. In addition the pion–proton vector meson exchange potential is only half as attractive as that for kaons, while the corresponding pion–neutron potential is repulsive and of the same magnitude as for kaons. The vector–mediated pion–nucleon interaction is thus repulsive in neutron rich matter.

In the case of antikaons, however, there are both experimental and theoretical indications that once the K^- propagates through dense nuclear matter, it really feels an attractive potential. Nuclear matter of densities between zero and ρ_0 can be probed by studying the energy shifts and the widths of the lowest levels in kaonic atoms. A collection of data over a wide range of atoms was analyzed by Friedman [18]. These results certainly require an attractive potential for the antikaons. Since the negative sign of the K^-p scattering length is caused by the $\Lambda(1405)$, the dynamics of that resonance in nuclear matter surroundings have to be investigated. Performing the coupled channels calculation at finite density results in a $\Lambda(1405)$ that is shifted upwards in energy [19, 20, 21]. At lower energies around the original (vacuum) threshold the optical potential for the K^- becomes attractive, explaining the data from kaonic atoms.

Antikaons were also proposed as a probe of heavy–ion collisions by Kaplan and Nelson [12]. In a nucleon–nucleon collision there is a significant difference in the yields of K^+ and K^- simply due to the different production reactions and thresholds. The K^+ with its $u\bar{s}$ – quark content can be created in $NN \to K^+YN$, $(Y = \Lambda, \Sigma)$ at energies above 1.6 GeV, while the K^- $(\widehat{=}\ \overline{u}s)$ cannot appear alone as there are no (non–exotic, see [22]) baryons with positive strangeness. Thus the K^- is only produced at energies beyond 2.5 GeV in the reaction $NN \to K^+K^-NN$. Since the interaction with a dense medium is different for K^+ and K^-, the ratio of the K^-/K^+ multiplicities in nucleus–nucleus collisions will change. Indeed, the FOPI and KaoS collaborations report different in–medium behavior of K^+ and K^- [23, 24]. Repulsion (in the case of K^+) from the regions of increased baryonic density and attraction (in the case of K^-) are seen in the azimuthal emission pattern of the kaons. In addition the K^- yield is enhanced because secondary production mechanisms become more important. Thus $\pi Y \to K^-N$ becomes possible once there are hyperons around, e.g. due to prior K^+ production. It is exactly this coupling of πY to $\bar{K}N$ that turns out to be the key to the interaction of the $\bar{K}$ with matter, giving rise to the $\Lambda(1405)$ resonance. This will be extensively discussed in this work.
Evaluation of the selfenergy of the $\bar{K}$ in these surroundings leads to a reduced antikaon mass. This of course lowers the production threshold and thus increases the K^- yield [25, 26, 27].

However, there are some caveats in this analysis. In the first works that went beyond a mean field description to include the $\Lambda(1405)$ (e.g. [28, 19, 20]), the repercussion of the dynamics of the $\Lambda(1405)$ on the antikaons where not included selfconsistently. This proves to be of great importance. The selfconsistent $\Lambda(1405)$ does not move very much [29, 30]. Thus the argument explaining the kaonic atoms becomes questionable.

In heavy–ion collisions the optical potential of the antikaon is probed at finite momentum. At a moderate temperature of $T = 80$ MeV [23] the kaon has a momentum of more than 300 MeV with respect to the matter rest frame. Momenta above ~ 300 MeV are typical in the experimental data on heavy ion collisions. Nevertheless, calculations have often assumed that the attractive potential for the kaons, i.e. their change in the mass is independent of momentum [31, 19]. This is not justified. To the contrary, a considerable momentum dependence of all in–medium properties is found ([21], see also chapters 4, 7 ,8).

This work starts with a more detailed introduction of chiral perturbation theory and its conse-

quences for the description of the antikaon–nucleon scattering process in chapter 3. The actual calculation with all its technical sophistications will be explained in chapter 4. Given the indicated importance of the πY channels, an important aspect of the whole problem is the behavior of the pion in the dense medium. This is the topic of chapter 5. The remaining chapters deal with the results for antikaons in isospin symmetric matter as well as asymmetric matter with different densities of protons and neutrons, as found in realistic systems. The implications of these results for the question of kaon condensation in neutron stars are discussed in the final chapter 9.
Just as the program for this work is of iterative nature, in order to achieve a selfconsistent result, the presentation of the calculation also involves some iterations and repetitions. Therefore the purpose of the following chapter, chap. 2, is to provide a kind of guideline. It will present the two major steps of calculation, the scattering amplitude and the selfenergy, in its most basic form. Keeping in mind these basic forms and results will be helpful when these steps recur in enhanced form subsequently.

For ease of reading (and writing) quite often the label ‘kaon’ will be used while actually an antikaon is meant. There can be however no confusion because this work is only concerned with the modifications of the antikaons. Where K^+ and K^0 appear, the differentiation will be made clear.

Chapter 2

Overview

The purpose of this chapter is to give an outline of the key topics that will be discussed in this work. There are basically two main themes: kaon–nucleon scattering and the kaon selfenergy, which will here be represented in the most simple way.

Antikaon–nucleon scattering

We start with the description of the scattering process. The interaction is provided by the lowest order chiral Lagrangian [32, 33, 34, 35, 30]. We just pick the so called Weinberg–Tomozawa term

$$\mathcal{L}_{WT} = i\, tr(\overline{B}\,[\mathcal{V}^0, B])\ , \tag{2.1}$$

where B is the octet of spin 1/2 baryons (nucleons, Λ, Σ, Ξ), and $\mathcal{V}^0$ contains derivatives with respect to time of the octet Φ of pseudoscalar mesons (π, η, K). Putting the time derivatives to their on–shell values, we arrive at point–vertices of the form

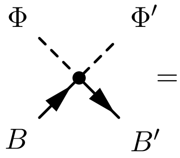

$$= \quad C\,\frac{m+m'}{f_\pi^2}, \qquad C = const.$$

Figure 2.1: *Weinberg–Tomozawa vertex*

The incoming and outgoing mesons are denoted by m and m'.
In the first step we drop η and Ξ. The scattering of the remaining three channels $\overline{K}N$, $\pi\Sigma$ and $\pi\Lambda$ can be described by a Bethe–Salpeter scattering equation [36]:

$$T = V + V\,J\,T \tag{2.2}$$

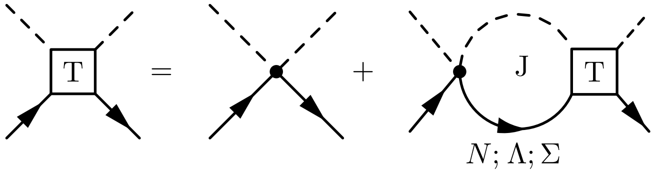

Figure 2.2: *Bethe–Salpeter scattering equation*

Since the interaction vertices are local, this integral equation reduces to a matrix equation and can easily be solved for T.

Grouping the particle channels into isospin zero and isospin one channels [33], the most prominent result is the emergence of a resonance in the isospin zero $\overline{K}N$ scattering amplitude $f^0_{\overline{K}N}$ below the $\overline{K}N$ threshold:

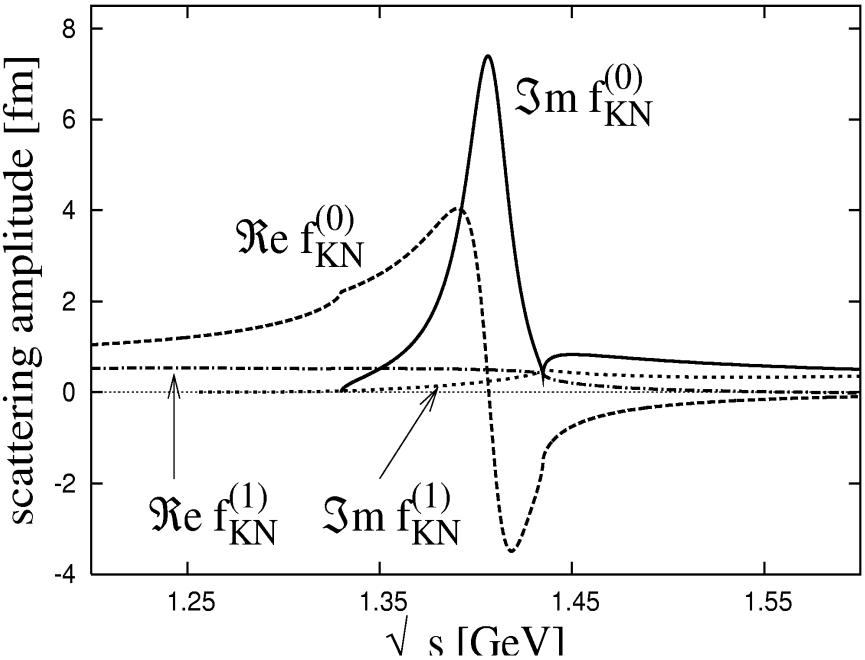

Figure 2.3: *$\bar{K}N$ scattering amplitudes for isospin 0 and isospin 1*

This resonance is identified as the $\Lambda(1405)$. Experimentally it is seen in the invariant mass spectrum of $\pi\Sigma$ scattering [37, 38].

The isospin one channel ($f^{(1)}_{KN}$ in fig. 2.3) does not exhibit a similar resonant behavior [38]. There are free parameters of the model which can be fixed by fitting this result to the isospin zero and isospin one scattering lengths [39, 40],

$$\begin{aligned} a^{(I=0)}_{\bar{K}N} &= (-1.7 + i\,0.68)\text{fm} \\ a^{(I=1)}_{\bar{K}N} &= (0.37 + i\,0.60)\text{fm}\;. \end{aligned} \tag{2.3}$$

Kaon selfenergy

Once the T–matrix is known, the in–medium selfenergy of the antikaon can be constructed in the following way [29, 30, 33]:

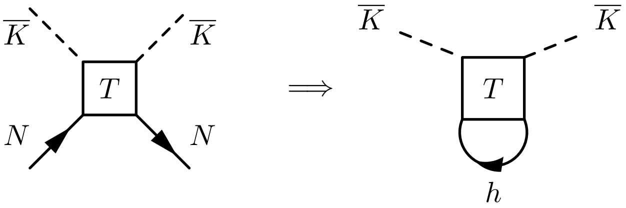

Figure 2.4: *From T–matrix to $\bar{K}$ selfenergy*

Here the scattering matrix T is evaluated in the medium, i.e. at finite baryon chemical potential (but vanishing temperature). The $T_{\overline{K}N}$–matrix element is to be integrated with the nucleon (–hole) propagator over the nucleon Fermi sea. To achieve a selfconsistency, the kaon propagator is fed into a repeated calculation of the T–matrix. Iteration of this procedure leads to selfconsistency after 4–5 cycles.

The result is best seen in the kaons spectral function ($= -\frac{\pi}{2} \times$ imaginary part of the kaon propagator) that becomes broad and whose most prominent peek is shifted to lower energies as compared to the vacuum. Fig. 2.5 shows that for Fermi momenta of $p_f = 150$ MeV and $p_f = 300$ MeV ($\rho \approx 0.2\rho_0$ and $\rho \approx 1.5\rho_0$).

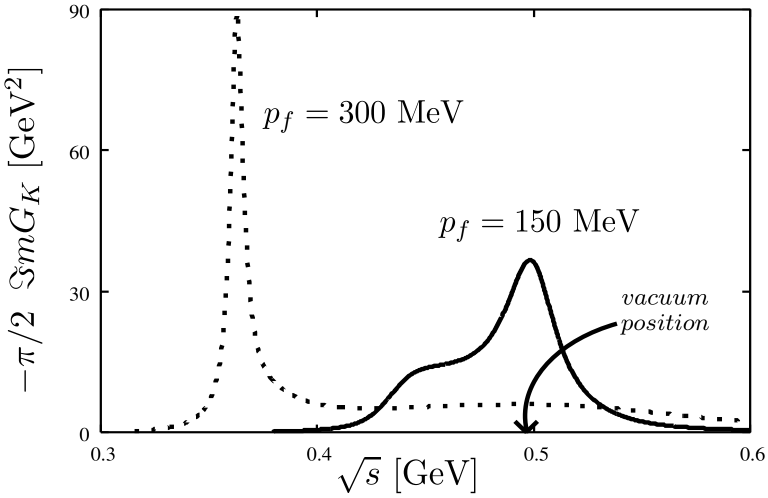

Figure 2.5: *Kaon spectral function at different densities*

Chapter 3

Chiral perturbation theory and $\bar{\mathrm{K}}$N scattering

3.1 Chiral Symmetry

Strong interactions at low energies are an extremely involved problem, since the established theory for these interactions cannot be used to straightforwardly calculate objects like masses, propagators or cross sections. QCD is asymptotically free, but in the very non–asymptotic energy regime of up to 1–2 GeV we are forced to use some kind of effective theory instead.
An effective theory tries to simulate the manifestations of the true underlying dynamics, in other words the effective outcome of, in our case, QCD. An effective theory tries to do so by a finite analytical and numerical effort, in other words in an effective way [41, 42, 43]. Generally this is possible if the physical situation provides two scales, one heavy and one light. Working at energies small compared with the heavy scale, one can describe the interactions in terms of the light degrees of freedom, expanding the theory in powers of the characteristic energy scale. At a given order in the expansion, the interactions of the light particles are specified by a finite number of low–energy coupling constants. The values of the low–energy constants represent the effect of the original heavy (high–energy) scale.
To write down an effective theory, one tries to find the most general Lagrangian compliant with the symmetries of the fundamental theory, written in terms of the light degrees of freedom.

In the case of the low–energy regime of the strong interactions, one does indeed find light and heavy scales. The octet of pseudoscalar mesons, π, K, η, are considerably much lighter than all other hadrons. This observation suggests the possibility of developing an effective field theory in this sector. In this theory the complicated interactions of quarks and gluons of QCD will be replaced by a simpler form in terms of mesons (and baryons), while the relevant symmetries of the underlying QCD Lagrangian have to be incorporated. For the low–energy sector of hadrons, the crucial symmetry principle that tells us how to construct the Lagrangian for the effective theory is chiral symmetry (and its spontaneous breaking).

Chiral symmetry is manifest in QCD, where the Lagrangian as written in terms of the quark fields q and the gluon field strength tensor $G^{\mu\nu}$ reads:

$$\mathcal{L}_{QCD} = \overline{q}(i\mathcal{D} - \mathcal{M})q - \frac{1}{2} tr G_{\mu\nu} G^{\mu\nu} \ .$$

The current quark masses are contained in the quark mass matrix $\mathcal{M}$.

For massless u, d and s quarks, $\mathcal{L}_{QCD}$ is invariant under chiral transformations [43, 44, 45, 35]

$$q_L \to \exp\,(i \sum_j \lambda_j \alpha_j)\, q_L, \qquad q_R \to \exp\,(i \sum_j \lambda_j \beta_j)\, q_R,$$

where $q_{L/R}$ are the left/righthanded quark fields and λ_j the SU(3) Gell–Mann matrices.
Of course the non–zero mass terms in $\mathcal{M}$ break this invariance. But since the masses of the u, d, and (to some extent) s quarks are very small, chiral symmetry should be a rather well obeyed. However, observations show that the opposite is true. One striking example is provided by the hadronic spectrum: if chiral symmetry was conserved for the QCD ground state, for every hadron there should exist a partner of equal mass but opposite parity, generated by the axial charges of the would–be–conserved axial currents. No such parity partners have been found, however. Consequently, chiral symmetry must be broken in the QCD ground state, while it was an invariance of the QCD Lagrangian. This is called spontaneous symmetry breaking. According to Goldstone's theorem, the appearance of a massless bosons is associated with spontaneous symmetry breaking, one such Goldstone boson for each broken generator of the original symmetry transformation. Hence there should be eight massless pseudoscalar bosons for the eight broken axial charges. Again, this is not exactly the situation in nature. There is an octet of pseudoscalar mesons – $\pi^0, \pi^\pm, K^0, \bar{K}^0, K^\pm, \eta$ – which are not massless, but much lighter than any other hadron. The masses of these "pseudo"–Goldstone bosons are due to the explicit symmetry breaking caused by the finite current quark masses already at the QCD–Lagrangian level. The Goldstone bosons decay via the axial currents into the QCD vacuum, introducing another important scale, f_π, to the theory: The decay matrix element reads $\langle 0|\mathcal{A}^a_\mu|\pi^b\rangle = ip_\mu \delta^{ab} f_\pi$, where f_π is the pion decay constant in the chiral limit.

Chiral perturbation theory is the effective field theory for QCD at low energies. It is based on two features: (i) The masses of the light quarks are small compared with the typical hadronic scale Λ_{QCD}, so they can be treated as perturbations. (ii) In the chiral limit, chiral symmetry remains broken spontaneously, generating the pseudoscalar Goldstone bosons.
Chiral perturbation theory is constructed as a systematic low–energy expansion around the chiral limit, using the two small parameters at hand, the momenta of the Goldstone bosons (q) and the quark masses ($\mathcal{M}$). The successive orders of this expansion are denoted by their chiral power (or chiral dimension) which counts the powers of meson momenta q and meson masses. The quark mass matrix $\mathcal{M}$ that appears in $\mathcal{L}_{QCD}$ is of chiral power 2 by virtue of the Gell–Mann – Oakes – Renner relation ($\mathcal{M} \sim m_\pi^2 \sim q^2$). From what is explained above, QCD at low energies is the domain of Goldstone–boson interactions. Consequently, the Goldstone fields form the effective degrees of freedom in the theory. (Thus the use of q and m_π as expansion parameters comes about naturally.)

As the building block one chooses a nonlinear representation of the Goldstone fields of the form of a unitary 3×3 matrix U in flavor space [41, 42, 43, 35],

$$U = \exp\,(i\lambda^a \phi_a(x)/f_\pi)\ . \tag{3.1}$$

More explicitly, the field matrix takes the form

$$\frac{1}{\sqrt{2}}\lambda_j \phi_j =: \Phi = \frac{1}{\sqrt{2}} \begin{pmatrix} \frac{\eta}{\sqrt{6}} + \frac{\pi^0}{\sqrt{2}} & \pi^+ & K^+ \\ \pi^- & \frac{\eta}{\sqrt{6}} - \frac{\pi^0}{\sqrt{2}} & K^0 \\ K^- & \overline{K^0} & -\frac{2\eta}{\sqrt{6}} \end{pmatrix}\ . \tag{3.2}$$

In the literature, the following abbreviations are also used frequently:

$$u = U^{1/2} = \exp\left(i/f_\pi \Phi\right) , \qquad\qquad u_\mu = i\, u^\dagger\, \partial_\mu U\, u^\dagger \; . \tag{3.3}$$

One now looks for combinations of U with constants or derivatives that respect the necessary symmetries, in particular chiral symmetry [42].
Thus, under a chiral transformation $U \;\rightarrow\; L\,U\,R^\dagger \quad (L, R\,\epsilon\, SU(3)_{L,R})$, a term of the form

$$tr\,\partial^\mu U\,\partial_\mu U^\dagger \;\rightarrow\; tr\,L\partial^\mu U R^\dagger\,R\partial_\mu U^\dagger L^\dagger = tr\,\partial^\mu U\,\partial_\mu U^\dagger$$

is invariant, so one should expect it to be part of the Lagrangian.
Since the Goldstone fields are known to be massive, one also wants to construct a term containing the mass. It is usually written as

$$\frac{f_\pi^2}{4}\,tr\,2B_0\mathcal{M}(U + U^\dagger). \tag{3.4}$$

Along with the pion decay constant f_π, here appears another constant, B_0, that is related to the explicit breaking of chiral symmetry.

With these terms, the lowest order χPT Lagrangian is given by

$$\mathcal{L}_{(2)} = \frac{1}{4}\,f_\pi^2\,\left(tr[\partial^\mu U\,\partial_\mu U^\dagger + \chi^\dagger U + \chi U^\dagger]\right). \tag{3.5}$$

The chiral object χ stands for $\chi = 2B_0(s{+}ip) \rightsquigarrow 2B_0\mathcal{M}$ (s, p being external scalar and pseudoscalar sources, i.e. physical values are given by $p = 0, s = \mathcal{M}$) [32].
The subscript (2) indicates the chiral dimension of this term: there are two derivatives and one quark mass terms in $\mathcal{L}_{(2)}$.

One can show that $\mathcal{L}_{(2)}$ is already the most general form of the Lagrangian of order 2 that is consistent with Lorentz invariance chiral symmetry, parity, G–Parity and charge conjugation invariance [3, 46].

Already from this term a relation of the masses of the Goldstone bosons can be read off.
Expanding the mass term (eq. (3.4)) in powers of the meson fields gives

$$\begin{aligned}\frac{1}{2}f_\pi^2\,B_0 tr[\mathcal{M}(U+U^\dagger)] \approx{}& f_\pi^2\,B\,tr\mathcal{M} - \frac{1}{2}B_0(m_u+m_d)\pi^+\pi^- - \frac{1}{4}B_0(m_u+m_d)\pi^0\pi^0\\ &- \frac{1}{2}B_0(m_u+m_s)K^+K^- - \frac{1}{2}B_0(m_u+m_s)K^0\bar{K}^0\\ &- \frac{1}{2}B_0(\frac{4}{3}m_s + \frac{1}{3}(m_u+m_d))\eta\eta\;.\end{aligned} \tag{3.6}$$

The first term on the r.h.s. of eq. (3.6) is related to the vacuum energy. Since $\partial\mathcal{H}_{QCD}/\partial m_q = \bar{q}\,q$, the coefficient B_0 can be associated with the quark condensate,

$$<\bar{q}\,q> = -f_\pi^2 B_0 + \ldots$$

Setting $m_u = m_d = \hat{m}$, we can read off the masses

$$\begin{aligned} m_\pi^2 &= 2B_0\hat{m}\\ m_K^2 &= B_0(\hat{m}+m_s)\\ m_\eta^2 &= \frac{2}{3}B_0(\hat{m}+2m_s).\end{aligned} \tag{3.7}$$

This leads to the Gell–Mann – Okubo mass relation

$$3m_\eta^2 + m_\pi^2 - 4m_K^2 = 0,$$

which predicts an η mass just 3% larger than the measured value.
Eq. (3.7) nicely shows that the masses of the Goldstone bosons are generated by the explicit symmetry–breaking mass term of QCD. If we identify $B_0 = -<\bar{q}\,q>/f_\pi^2$, eq. (3.6) can be used to obtain the Gell–Mann – Oakes – Renner relations

$$\begin{aligned}
f_\pi^2\, m_\pi^2 &= -2\,\hat{m}\ <\bar{q}\,q> \\
f_\pi^2\, m_K^2 &= -(\hat{m}\, + m_s)\ <\bar{q}\,q> \\
f_\pi^2\, m_\eta^2 &= -\frac{2}{3}\,(\hat{m}\, + m_s)\ <\bar{q}\,q>\ \ .
\end{aligned}$$

The theory as a whole is not renormalizable because at each new order of the expansion new interactions of higher order in the fields will appear. The form of the divergences will thus change from order to order, in contrast to e.g. QED. For example, assume that one calculates some amplitude using the Lagrangian $\mathcal{L}_{(2)}$ above. The result will be of order $\mathcal{O}(p^2/f_\pi^2)$: The characteristic momentum p appears to the second power, hence the label (2) on the Lagrangian. A loop correction to this result will carry a factor $\frac{1}{f_\pi^4}$, so to keep the dimension of the amplitude the same, a factor p^4 must appear in the numerator. Therefore the counterterm needed to cancel the corresponding divergence must also contain four derivatives. However, successive loop corrections from higher orders in the chiral expansion or higher loops at a fixed chiral order are always suppressed by additional orders $\mathcal{O}(E^2/\Lambda_\chi^2)$, with $\Lambda_\chi \sim 4\pi f_\pi \sim 1$ GeV.
Accordingly one can truncate the perturbation series at the given order, provided that the typical energy E is small compared with the chiral scale.

3.2 χPT with baryons

Along the lines of the preceding section, one can also construct an interaction of mesons and baryons [47].
In addition to the meson matrix Φ (eq.(3.2)) we need another $SU(3)$ matrix that collects the baryons we want to include:

$$B = \begin{pmatrix} \frac{1}{\sqrt{6}}\Lambda + \frac{1}{\sqrt{2}}\Sigma^0 & \Sigma^+ & p \\ \Sigma^- & \frac{1}{\sqrt{6}}\Lambda - \frac{1}{\sqrt{2}}\Sigma^0 & n \\ \Xi^- & \Xi^0 & -\sqrt{\frac{2}{3}}\Lambda \end{pmatrix} \tag{3.8}$$

The covariant derivative reads

$$\begin{aligned}
\mathcal{D}_\mu B &= \partial_\mu B + [\Gamma_\mu, B], \\
\Gamma_\mu &= \frac{1}{2}(u^\dagger \partial_\mu u + u \partial_\mu u^\dagger),
\end{aligned} \tag{3.9}$$

with u from eq. (3.3) containing the meson fields.

Again one seeks possible combinations of the building blocks that yield a proper Lagrangian. Here Γ_μ and u_μ (c.f. eq. (3.3)), combined with the vector and axial vector currents, give the lowest order [35]:

$$\mathcal{L}_{MB}^{(1)} \quad = \quad tr(i\overline{B}\gamma^{\mu}\mathcal{D}_{\mu}B - \overset{\circ}{m}\overline{B}B + \frac{1}{2}D\overline{B}\gamma^{\mu}\gamma_5\{u_{\mu}, B\} + \frac{1}{2}F\overline{B}\gamma^{\mu}\gamma_5[u_{\mu}, B]) \tag{3.10}$$

The trace runs over flavor indices. $\overset{\circ}{m}$ denotes for the octet mass in the chiral limit. The two coupling constants F and D add up to the axial coupling constant $F + D = g_A = 1.26$.

The first term in $\mathcal{L}_{MB}^{(1)}$ (eq.(3.10)) – called the Weinberg–Tomozawa term – will be the main interaction term used in the description of the $\bar{K}N$ scattering (see sec. 3.4).

3.2.1 Heavy Baryon Formalism

The attempt to include baryons [48] in the theory leads to a new problem: While the suppression factor in the meson sector is of the order $\mathcal{O}(m_{meson}^2/\Lambda_{\chi}^2)$, in the baryon sector it would be of the order $\mathcal{O}(m_{baryon}/\Lambda_{\chi}) \sim \mathcal{O}(1)$ – that means no suppression at all. A way out was shown by Jenkins and Manohar [7]. They treated the baryon fields as heavy static fermions. In an expansion in powers of $1/m_B$ the baryon mass term then disappears to leading order, leading to a one–to–one correspondence between the expansion in small momenta/derivatives and quark masses and the expansion in Goldstone boson loops, i.e. the power counting becomes consistent again [7, 49, 50].

The essential observation is that in the chiral limit the baryon mass does not vanish, but the momentum transferred between baryons by pion exchange is small compared with the baryon mass. Hence the baryon velocity is conserved.
The baryon momentum is written as

$$p^{\mu} = \overset{\circ}{m}v^{\mu} + l^{\mu} \ ,$$

where $\overset{\circ}{m}$ is the baryon mass, v^{μ} is the 4–velocity of the baryon field ($v^2 = 1$) and l^{μ} is some small off–shell momentum.
The baryon fields are now rewritten as

$$B'(x) = e^{i\overset{\circ}{m}v_{\mu}x^{\mu}}\, B(x) \ .$$

This field has simultaneously a definite position and a definite velocity: $[v^{\mu}, x^{\nu}] = i\hbar g^{\mu\nu}/\overset{\circ}{m} \rightarrow 0$ in the heavy fermion limit.
The Dirac equation of the transformed fields reads:

$$\partial\!\!\!/ B' = 0,$$

and the Lagrangian eq. (3.10) takes the form

$$\mathcal{L}^{(1)} = i\, tr(\overline{B}v\cdot\mathcal{D}B) \ + \ F\, tr(\overline{B}\, S_{\mu}[u^{\mu}, B]) \ + \ D\, tr(\overline{B}\, S_{\mu}\{u^{\mu}, B\}) \ . \tag{3.11}$$

S_{μ} is the Pauli–Lubanski spin operator $\frac{i}{2}\gamma_5\sigma_{\mu\nu}v^{\nu}$
The Lagrangian $\mathcal{L}^{(1)}$ does no longer contain a term $\sim \overset{\circ}{m}\,\overline{B}B$. Derivatives acting on the B field will lead to powers of l^{μ} instead of p^{μ}. Instead of a factor $\mathcal{O}(1) \sim \mathcal{O}(m_{baryon}/\Lambda_{\chi})$, real suppression factors $\mathcal{O}(l/\Lambda_{\chi})$ will arise and the χPT expansion is consistent again.

3.3 Σ terms

As already mentioned, the first term in $\mathcal{L}_{(1)}$ (eq.(3.11)) will be the main interaction term. Nevertheless one should not leave out couplings of comparable strengths at amplitude level. Indeed, at second order there are three terms that are of strength comparable to the Weinberg–Tomozawa contribution when evaluated at the meson–baryon thresholds. These are the "Sigma–terms"representing the explicit symmetry breaking at chiral dimension 2 [44, 13, 32].

$$\mathcal{L}^{(2,br)} = b_D\, tr(\overline{B}\{\chi_+, B\}) \;+\; b_F\, tr(\overline{B}[\chi_+, B]) \;+\; b_o\, tr(\overline{B}B)\, tr(\chi_+) \tag{3.12}$$

The chiral object χ_+ is built from $\chi = 2B_0\mathcal{M}$ (c.f. eq. (3.5)) and the meson matrix u (eq. (3.3))

$$\chi_+ = u^\dagger\, \chi\, u^\dagger \;+\; u\, \chi\, u\ ,$$

where $\mathcal{M} = diag(m_u, m_d, m_s)$ is again the quark mass matrix.

The constants b_D, b_F and b_0 are examples of the so called low–energy–constants (LECs). These parameters are not restrained by symmetries and have to be fixed from phenomenology. Here, one can use the predictions of the theory for the baryon masses to pin down the values of at least b_D and b_F.

To that end, we expand χ_+,

$$\chi_+ \approx 4B_0M - 4B_0\, \frac{1}{2f_\pi^2}\, (2\, \Phi M \Phi + \Phi^2 M + M\Phi^2)\ ,$$

and insert the constant part $4B_0M$ into $\mathcal{L}^{(2,br)}$. This should give just $-m_B\, \overline{B}\, B$. Comparing coefficients one derives expressions for the baryon masses in terms of quark masses, sigma terms and the constant B_0. The quark masses can be replaced using the Gell–Mann – Oakes – Renner relation. Again we identify $B_0 = -<\overline{q}\, q>/f_\pi^2$ (as below eq. (3.6)) and obtain

$$\begin{aligned}
m_N &= m_8\ + 4b_F\, (m_K^2 - m_\pi^2) - 4\, b_D\, m_K^2 \\
m_\Lambda &= m_8\ - \frac{4}{3}\, b_D\, (4\, m_K^2 - m_\pi^2) \\
m_\Sigma &= m_8\ - 4\, b_D\, m_\pi^2 \\
m_\Xi &= m_8\ - 4b_F\, (m_K^2 - m_\pi^2) - 4\, b_D\, m_K^2\ ,
\end{aligned}$$

where m_8 is the common mass of the baryon octet. In the SU(3) chiral limit

$$m_8 = m_{heavybaryon}(m_u = m_d = m_s\ = 0) = 0\ ,$$

since we are using the heavy baryon formalism: No explicit mass term should remain in the Lagrangian.

Starting instead with $\mathcal{L}^{(1)}_{MB}$ from eq.(3.10) and $\mathcal{L}^{(2,br)}$ from eq.(3.12) and writing down just the same derivation, there would be the explicit $\overset{\circ}{m}\, B\, \overline{B}$–term in addition. We would then have a baryon mass $\overset{\circ}{m}$ (through spontaneous symmetry breaking), a mass term due to b_0 as shown above that shifts the common octet mass by some amount, and then the b_F and b_D terms that generate the splitting within the octet. Within the heavy baryon formalism, the first term ($\overset{\circ}{m}$) has been transformed away, while the others remain.

Of course, $\overset{\circ}{m}$ is part of the physical baryon mass, the common contribution to the octet masses is given by $\overset{\circ}{m} + m_8$; so when trying to fit the parameters, only b_D and b_F can be fixed easily, while it is hard to disentangle $\overset{\circ}{m}$ and the b_0 term.

For b_D and b_F, we express the relations among the baryon masses using the mesons masses:

$$\begin{aligned} m_\Sigma - m_N &= 4\,(b_D - b_F)\,(m_K^2 - m_\pi^2) \\ m_\Sigma - m_\Lambda &= \frac{16}{3}\,b_D\,(m_K^2 - m_\pi^2) \\ m_\Xi - m_N &= -8\,b_F\,(m_K^2 - m_\pi^2) \end{aligned}$$

The four masses are given by only three parameters, therefore there is a sum rule (Gell–Mann – Okubo):

$$m_\Sigma - m_N = \frac{1}{2}\,(m_\Xi - m_N) + \frac{3}{4}\,(m_\Sigma - m_\Lambda)$$

The values from the particle data booklet are 251 MeV for the left side, 245 MeV for the right side, so this is fulfilled quite well. Nevertheless, there are considerable difficulties incorporating corrections from loops or terms of higher chiral order [8, 51, 32]. Loop calculations are inevitable, since tree level diagrams are real and, left alone, would violate unitarity. To improve chiral convergence, an elaborate counting scheme was developed by Meißner et al. [10].
The values used for the calculations in this work are taken from [30], eq.(145):

$$b_D = 0.061 \text{ GeV}^{-1}, \qquad b_F = 0.195 \text{ GeV}^{-1}, \qquad b_0 = -0.346 \text{ GeV}^{-1}$$

3.4 Full interaction

3.4.1 Weinberg–Tomozawa term

Having found out about the parameters of the Lagrangian, we can have a look at the particular interaction terms. The Weinberg–Tomozawa term (first term in eq. (3.11)) reads

$$\begin{aligned} \mathcal{L}^{WT} &= i\, tr(\overline{B} v_\mu \left[\Gamma^\mu, B\right]) \\ \Gamma^\mu &= \frac{1}{2}\left(u^\dagger \partial_\mu u + u \partial_\mu u^\dagger\right) . \end{aligned} \tag{3.13}$$

The difficult point in solving the Bethe–Salpeter equation (fig. 2.2) is any 3–momentum dependence in the interaction vertices. The Weinberg–Tomozawa term will lead to such terms via the derivatives ∂_μ. The approximation commonly used to avoid this difficulty is to evaluate $\mathcal{L}^{WT}$ in the baryon rest frame [30, 33]. This amounts to setting $v_\mu = (1,0,0,0)$ or

$$\mathcal{L}^{WT} = i\, tr(\overline{B}\left[\Gamma^0, B\right]) ,$$

whence the vertices will only depend on the energies of the meson fields.
The object Γ^0 is given by

$$\Gamma^0 = \frac{1}{2}\left(u \partial^0 u^\dagger + u^\dagger \partial^0 u\right) .$$

Upon expansion of the meson matrix

$$u = e^{i/f_\pi \, \Phi} \quad \approx 1 + \frac{i}{f_\pi}\Phi - \frac{1}{2 f_\pi^2}\Phi^2 ,$$

it takes the form

$$\begin{aligned} \Gamma^0 &= -\frac{1}{2}\frac{1}{2 f_\pi^2}\, 2\left((\partial^0\Phi)\Phi - \Phi(\partial^0\Phi)\right) \\ &= \frac{1}{2 f_\pi^2}\left(\Phi(\partial^0\Phi) - (\partial^0\Phi)\Phi\right) . \end{aligned}$$

Keeping only kaons and nucleons in B (eq.(3.8)) and Φ (eq.(3.2)), the Lagrangian reads (c.f. [15])

$$\begin{aligned} \mathcal{L}^{KN}_{WT} = \frac{i}{4 f_\pi^2} & \left((\partial^0 K^- K^+ - \partial^0 K^+ K^-) n\overline{n} + \partial^0 K^- K^0 \overline{n} p - \partial^0 K^+ \overline{K^0} n\overline{p} \right. \\ & + (2\partial^0 K^- K^+ - 2\partial^0 K^+ K^-) p\overline{p} + (2\partial^0 \overline{K^0} K^0 - 2\overline{K^0}\partial^0 K^0) n\overline{n} \\ & \left. - K^- \partial^0 K^0 \overline{n} p + \partial^0 \overline{K^0} K^+ n\overline{p} + (\partial^0 \overline{K^0} K^0 - \overline{K^0}\partial^0 K^0) p\overline{p} \right) . \end{aligned} \tag{3.14}$$

However, the calculation becomes realistic only once we couple the $\bar{K}N$ system to the other channels. The only particle we do not include is the Ξ. Since it has strangeness $+2$, it would couple to the $\bar{K}N$ channels only in loops with K^+ or K^0 (strangeness -1). The threshold for these loops is at $m_K + M_\Xi \approx 1816$ GeV. Thus its main influence would be via its real part. As will be shown in chap. 4, the real part of the loops serves mainly as a tool to regularize the integrals, the ΞK channel would thus only lead to a renormalization of the results.

Nevertheless, the remaining channels lead to a very large expression for $\mathcal{L}_{WT}$. Instead of writing it down here, we give the result in the form of the couplings or bare vertex factors V_{ij} between the channels obtained from that expansion.

$V_{ij} =$

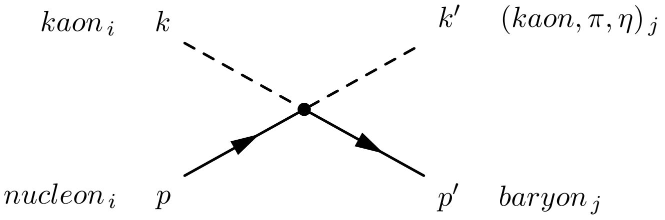

We use the following notation: The incoming and outgoing mesons at this vertex have the momenta k_K, k_π and k_η, respectively.
The Lagrangian (c.f. eq.(3.14)) explicitly names K^+, K^0 along with the antikaons. To describe $\bar{K}N$ scattering, however, the incoming kaon fields are to be interpreted as outgoing antikaons. To distinguish between incoming and outgoing particle pairs, we use a dagger for the outgoing ones, as in $\pi^{0\,\dagger}$ or $\overline{\Sigma^+}$.
Then the resulting vertex factors can be collected in tables. Table (3.1) gives the Weinberg–Tomozawa vertices for the channels with vanishing total charge.

V_{ij}	$K^{-\,\dagger}\overline{p}$	$\overline{K^0}^\dagger\overline{n}$	$\pi^{0\,\dagger}\overline{\Lambda}$	$\pi^{0\,\dagger}\overline{\Sigma^0}$	$\pi^{+\,\dagger}\overline{\Sigma^-}$	$\pi^{-\,\dagger}\overline{\Sigma^+}$	$\eta^\dagger\overline{\Lambda}$	$\eta^\dagger\overline{\Sigma^0}$
K^-p	$4\,c$	$2\,c$	$\sqrt{3}\,a$	a	0	$2\,a$	$3\,b$	$\sqrt{3}\,b$
$\overline{K^0}n$	$2\,c$	$4\,c$	$-\sqrt{3}\,a$	a	$2\,a$	0	$3\,b$	$-\sqrt{3}\,b$
$\pi^0\Lambda$	$\sqrt{3}\,a'$	$-\sqrt{3}\,a'$	0	0	0	0	0	0
$\pi^0\Sigma^0$	a'	a'	0	0	$4\,d$	$4\,d$	0	0
$\pi^+\Sigma^-$	0	$2\,a'$	0	$4\,d$	$4\,d$	0	0	0
$\pi^-\Sigma^+$	$2\,a'$	0	0	$4\,d$	0	$4\,d$	0	0
$\eta\Lambda$	$3\,b'$	$3\,b'$	0	0	0	0	0	0
$\eta\Sigma^0$	$\sqrt{3}\,b'$	$-\sqrt{3}\,b'$	0	0	0	0	0	0

(3.15)

Table 3.1: Weinberg-Tomozawa vertices for the uncharged channels.
The abbreviations read: $c = (k_K^0 + k_K'^0),\ d = (k_\pi^0 + k_\pi'^0),$
$a = (k_K^0 + k_\pi'^0),\ b = (k_K^0 + k_\eta'^0),$
$a' = (k_K'^0 + k_\pi^0),\ b' = (k_K'^0 + k_\eta^0).$
Each entry is to be multiplied by $\frac{1}{8f_\pi^2}$.

There are also meson–baryon combinations of non–zero electrical charge. The Weinberg–Tomozawa term here leads to the entries in table 3.2. The charged channels differ only in the sign of the couplings $\bar{K}N \leftrightsquigarrow \pi\Sigma$.

V_{ij}	$K^- n$	$\pi^-\overline{\Lambda}$	$\pi^-\Sigma^0$	$\pi^0\overline{\Sigma^-}$	$\eta\Sigma^-$
$K^- n$	$2\,c$	$\sqrt{6}\,a$	$-\sqrt{2}\,a$	$\sqrt{2}\,a$	$\sqrt{6}\,b$
$\pi^-\Lambda$	$\sqrt{6}\,a$	0	0	0	0
$\pi^-\Sigma^0$	$-\sqrt{2}\,a'$	0	0	$-4\,d$	0
$\pi^0\Sigma^-$	$\sqrt{2}\,a'$	0	$-4\,d$	0	0
$\eta\Sigma^-$	$\sqrt{6}\,b'$	0	0	0	0

V_{ij}	$\overline{K^0}p$	$\pi^+\overline{\Lambda}$	$\pi^+\Sigma^0$	$\pi^0\overline{\Sigma^+}$	$\eta\Sigma^+$
$\overline{K^0}p$	$2\,c$	$\sqrt{6}\,a$	$\sqrt{2}\,a$	$-\sqrt{2}\,a$	$\sqrt{6}\,b$
$\pi^+\Lambda$	$\sqrt{6}\,a$	0	0	0	0
$\pi^+\Sigma^0$	$\sqrt{2}\,a'$	0	0	$-4\,d$	0
$\pi^0\Sigma^+$	$-\sqrt{2}\,a'$	0	$-4\,d$	0	0
$\eta\Sigma^+$	$\sqrt{6}\,b'$	0	0	0	0

(3.16)

Table 3.2: Weinberg-Tomozawa vertices for the charged channels.
The abbreviations read: $c = (k_K^0 + k_K'^0)$, $d = (k_\pi^0 + k_\pi'^0)$,
$a = (k_K^0 + k_\pi'^0)$, $b = (k_K^0 + k_\eta'^0)$,
$a' = (k_K'^0 + k_\pi^0)$, $b' = (k_K'^0 + k_\eta^0)$.
Each entry is to be multiplied by $\frac{1}{8f_\pi^2}$.

3.4.2 Σ terms

In addition to the Weinberg–Tomozawa term, there are the explicit symmetry–breaking Σ terms, c.f. eq. (3.12):

$$\mathcal{L}^{(2,br)} = b_D\, tr(\overline{B}\{\chi_+, B\}) \; + \; b_F\, tr(\overline{B}[\chi_+, B]) \; + \; b_o\, tr(\overline{B}B)\, tr(\chi_+)$$

To get the vertices, we expand in the meson matrix Φ. First take the b_D term:

$$\begin{aligned} \mathcal{L}_{b_D} &= b_D\, tr(\overline{B}\{\chi_+, B\}) \\ &\approx -\frac{B_0}{2f_\pi^2}\, b_D\, tr(\overline{B}\{2\,\Phi M\Phi + \Phi^2 M + M\Phi^2, B\}) \end{aligned}$$

The quark masses ($\mathcal{M}$) are replaced by their meson counterparts from the GOR–relation:

$$
\begin{aligned}
m_u &= \frac{1}{4B_0}\,(4m_K^2 + m_\pi^2 - 3m_\eta^2) \\
m_d &= \frac{1}{4B_0}\,(-4m_K^2 + 3m_\pi^2 + 3m_\eta^2) \\
m_s &= \frac{1}{4B_0}\,(3m_\eta^2 - m_\pi^2) \\
\\
m_\eta^2 &= \frac{1}{3}\,(4m_K^2 - m_\pi^2)
\end{aligned}
$$

The same is done for the b_F term,

$$
\begin{aligned}
\mathcal{L}_{b_F} &= b_F\, tr(\overline{B}[\chi_+, B]) \\
&\approx -\frac{B_0}{2f_\pi^2}\, b_F\, tr(\overline{B}[2\,\Phi M \Phi + \Phi^2 M + M\Phi^2, B]) \;.
\end{aligned}
$$

and the b_0 term,

$$
\mathcal{L}_{b_0} = b_0\, tr(\overline{B}B)\, tr(\chi_+)
$$

The vertex factors extracted from these contributions are collected in tables (3.3 – 3.5) for the uncharged channels and in tables (3.17 – 3.6) for the charged ones.

V_{ij}	K^-p	$\overline{K^0}n$	$\pi^0\Lambda$	$\pi^0\Sigma^0$	$\pi^+\Sigma^-$	$\pi^-\Sigma^+$	$\eta\Lambda$	$\eta\Sigma^0$
K^-p	$24\,m_K^2$	$12\,m_K^2$	$-\sqrt{3}a$	$3\,a$	0	$6\,a$	b	$-\sqrt{3}\,b$
$\overline{K^0}n$	$12\,m_K^2$	$24\,m_K^2$	$\sqrt{3}\,a$	$3\,a$	$6\,a$	0	b	$\sqrt{3}\,b$
$\pi^0\Lambda$	$-\sqrt{3}\,a$	$\sqrt{3}\,a$	$8\,m_\pi^2$	0	0	0	0	$8\,m_\pi^2$
$\pi^0\Sigma^0$	$3\,a$	$3\,a$	0	$24\,m_\pi^2$	0	0	$8\,m_\pi^2$	0
$\pi^+\Sigma^-$	0	$6\,a$	0	0	$24\,m_\pi^2 0$	0	$8\,m_\pi^2$	0
$\pi^-\Sigma^+$	$6\,a$	0	0	0	0	$24\,m_\pi^2$	$8\,m_\pi^2$	0
$\eta\Lambda$	b	b	0	$8\,m_\pi^2$	$8\,m_\pi^2$	$8\,m_\pi^2$	$\frac{8}{3}(16\,m_K^2 - 7\,m_\pi^2)$	0
$\eta\Sigma^0$	$-\sqrt{3}\,b$	$\sqrt{3}\,b$	$8\,m_\pi^2$	0	0	0	0	$8\,m_\pi^2$

Table 3.3: Vertex factors from the b_D–term, charged channels. *The abbreviations read:* $a = m_K^2 + m_\pi^2$, $b = 5m_K^2 - 3m_\pi^2$, *Each entry is to be multiplied by* $-b_D/6f_\pi^2$.

V_{ij}	K^-p	$\overline{K^0}n$	$\pi^0\Lambda$	$\pi^0\Sigma^0$	$\pi^+\Sigma^-$	$\pi^-\Sigma^+$	$\eta\Lambda$	$\eta\Sigma^0$
K^-p	0	$12\,m_K^2$	$-3\sqrt{3}\,a$	$-3\,a$	0	$-6\,a$	$3\,b$	$\sqrt{3}\,b$
$\overline{K^0}n$	$12\,m_K^2$	0	$3\sqrt{3}\,a$	$-3\,a$	$-6\,a$	0	$3\,b$	$-\sqrt{3}\,b$
$\pi^0\Lambda$	$-3\sqrt{3}\,a$	$-3\,a$	0	0	0	0	0	0
$\pi^0\Sigma^0$	$-3\,a$	$-3\,a$	0	0	0	0	0	0
$\pi^+\Sigma^-$	0	$-6\,a$	0	0	0	0	0	$8\sqrt{3}\,m_\pi^2$
$\pi^-\Sigma^+$	$-6\,a$	0	0	0	0	0	0	$-8\sqrt{3}\,m_\pi^2$
$\eta\Lambda$	$3\,b$	$3\,b$	0	0	0	0	0	0
$\eta\Sigma^0$	$\sqrt{3}\,b$	$-\sqrt{3}\,b$	0	0	$8\sqrt{3}\,m_\pi^2$	$-8\sqrt{3}\,m_\pi^2$	0	0

Table 3.4: Vertex factors from the b_F–term, uncharged channels.
The abbreviations read: $a = m_K^2 + m_\pi^2$, $b = 5m_K^2 - 3m_\pi^2$,
Each entry is to be multiplied by $-\,b_F/6f_\pi^2$.

V_{ij}	K^-p	$\overline{K^0}n$	$\pi^0\Lambda$	$\pi^0\Sigma^0$	$\pi^+\Sigma^-$	$\pi^-\Sigma^+$	$\eta\Lambda$	$\eta\Sigma^0$
K^-p	$24\,m_K^2$	0	0	0	0	0	0	0
$\overline{K^0}n$	0	$24\,m_K^2$	0	0	0	0	0	0
$\pi^0\Lambda$	0	0	$24\,m_\pi^2$	0	0	0	0	0
$\pi^0\Sigma^0$	0	0	0	$24\,m_\pi^2$	0	0	0	0
$\pi^+\Sigma^-$	0	0	0	0	$24\,m_\pi^2$	0	0	0
$\pi^-\Sigma^+$	0	0	0	0	0	$24\,m_\pi^2$	0	0
$\eta\Lambda$	0	0	0	0	0	0	$8\,c$	0
$\eta\Sigma^0$	0	0	0	0	0	0	0	$8\,c$

Table 3.5: Vertex factors from the b_0–term, charged channels.
$c = 4m_K^2 - m_\pi^2$. *Each entry is to be multiplied by* $-\,b_0/6f_\pi^2$.

b_D : (3.17)

V_{ij}	K^-n	$\pi^-\overline{\Lambda}$	$\pi^-\Sigma^0$	$\pi^0\overline{\Sigma^-}$	$\eta\Sigma^-$
K^-n	$12\,m_K$	$-\sqrt{6}\,a$	$-3\sqrt{2}\,a$	$3\sqrt{2}\,a$	$-\sqrt{6}\,b$
$\pi^-\Lambda$	$-\sqrt{6}\,a$	$8\,m_\pi^2$	0	0	$8\,m_\pi^2$
$\pi^-\Sigma^0$	$-3\sqrt{2}\,a$	0	$24\,m_\pi^2$	0	0
$\pi^0\Sigma^-$	$3\sqrt{2}\,a$	0	0	$12\,m_\pi^2$	0
$\eta\Sigma^-$	$-\sqrt{6}\,b$	$8\,m_\pi^2$	0	0	$4\,m_\pi^2$

b_F : (3.18)

V_{ij}	K^-n	$\pi^-\overline{\Lambda}$	$\pi^-\Sigma^0$	$\pi^0\overline{\Sigma^-}$	$\eta\Sigma^-$
K^-n	$-12\,m_K$	$-3\sqrt{6}\,a$	$3\sqrt{2}\,a$	$-3\sqrt{2}\,a$	$\sqrt{6}\,b$
$\pi^-\Lambda$	$-3\sqrt{6}\,a$	0	0	0	0
$\pi^-\Sigma^0$	$3\sqrt{2}\,a$	0	0	0	$8\sqrt{3}\,m_\pi^2$
$\pi^0\Sigma^-$	$-3\sqrt{2}\,a$	0	0	0	$-4\sqrt{3}\,m_\pi^2$
$\eta\Sigma^-$	$\sqrt{6}\,b$	0	$8\sqrt{3}\,m_\pi^2$	$-4\sqrt{3}\,m_\pi^2$	0

b_0 : (3.19)

V_{ij}	K^-n	$\pi^-\overline{\Lambda}$	$\pi^-\Sigma^0$	$\pi^0\overline{\Sigma^-}$	$\eta\Sigma^-$
K^-n	$24\,m_K^2$	0	0	0	0
$\pi^-\Lambda$	0	$24\,m_\pi^2$	0	0	0
$\pi^-\Sigma^0$	0	0	$24\,m_\pi^2$	0	0
$\pi^0\Sigma^-$	0	0	0	$24\,m_\pi^2$	0
$\eta\Sigma^-$	0	0	0	0	$48(4\,m_K^2 - m_\pi^2)$

Table 3.6: Vertex factors from the Σ–terms, charged channels.
The abbreviations read: $a = m_K^2 + m_\pi^2$, $b = 5m_K^2 - 3m_\pi^2$,
Each entry is to be multiplied by the corresponding LEC and by $-1/6f_\pi^2$.

The couplings for the $\overline{K^0}p$ and connected channels are obtained from the $K^-n\ldots$ above by flipping the sign of the elements $V_{13}, V_{14}, V_{35}, V_{45}$.

We have now extracted the χPT–ingredients that we need in our model. The vertex factors of tables (3.1)–(3.6) will now be used to calculate the T–matrix elements for $\bar{K}N$ scattering in chapter 4.

3.4.3 F and D terms

The first order Lagrangian (eq. (3.10)/(3.11)) contains two terms hitherto not taken into account. They couple the baryons to the axial object $u_\mu = iu^\dagger \partial_\mu U u^\dagger$:

$$\mathcal{L}^{(1)}_{FD} := \frac{1}{2} D \overline{B} \gamma^\mu \gamma_5 \{u_\mu, B\} + \frac{1}{2} F \overline{B} \gamma^\mu \gamma_5 [u_\mu, B])$$

Expanding $u_\mu = iu^\dagger \partial_\mu U u^\dagger \approx -\frac{2}{f_\pi} \partial_\mu \Phi$ this gives

$$\mathcal{L}^{(1)}_{FD} \approx -\frac{1}{f_\pi} \left[(F+D)\, tr(\overline{B}\, \gamma^\mu\, \gamma_5\, \partial_\mu \Phi\, B) - (F-D)\, tr(\overline{B}\, \gamma^\mu\, \gamma_5\, B\, \partial_\mu \Phi) \right].$$

Restricting the fields B and Φ to $\bar{K}$, nucleon, Λ and Σ, we obtain

$$\begin{aligned} \mathcal{L}^{(1)}_{FD} \quad \rightarrow \quad & -\frac{1}{2f_\pi} \left[-\frac{1}{\sqrt{3}} (3F+D) \overline{\Lambda}\, \gamma_\mu\, \gamma_5\, p \;+\; (D-F)(\overline{\Sigma^0}\, \gamma_\mu\, \gamma_5\, p + \sqrt{2} \overline{\Sigma^-}\, \gamma_\mu\, \gamma_5\, n) \right] \partial^\mu K^- \\ & -\frac{1}{2f_\pi} \left[-\frac{1}{\sqrt{3}} (3F+D) \overline{\Lambda}\, \gamma_\mu\, \gamma_5\, n \;+\; (D-F)(-\overline{\Sigma^0}\, \gamma_\mu\, \gamma_5\, n + \sqrt{2} \overline{\Sigma^+}\, \gamma_\mu\, \gamma_5\, p) \right] \partial^\mu \overline{K^0}\ . \end{aligned}$$

Going to the nonrelativistic limit ($\not{k}\, \gamma_5 = \,-\, \gamma_5 \not{k} \;\rightarrow -\vec{k} \vec{\sigma}$) leads to the following vertices:

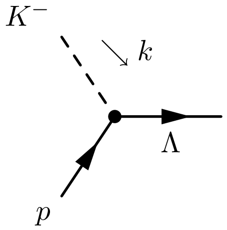

$$= \frac{1}{2f_\pi}\, \vec{k} \cdot \vec{\sigma}\, \frac{3F+D}{\sqrt{3}}$$

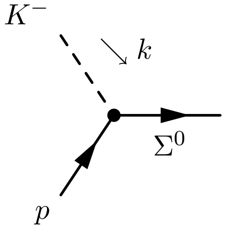

$$= \frac{1}{2f_\pi}\, \vec{k} \cdot \vec{\sigma}\, (D-F) \tag{3.20}$$

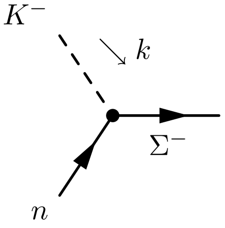

$$= -\frac{1}{2f_\pi}\, \vec{k} \cdot \vec{\sigma}\, \sqrt{2} (D-F)$$

Obviously, these are p–wave vertices, depending on the kaon 3–momentum $\vec{k}$. The difference is of course the appearance of γ_5: the nonrelativistic form of the Weinberg–Tomozawa vertices depends on k^0 instead.

For two reasons this interaction is not included in the general calculation but as an add–on on top of it: As will be shown in section 6.3, the selfenergy contributions constructed with these p–wave vertices are negligibly small compared with the main s–wave contributions. The second reason is that inclusion of these vertices in the scheme of eq. (2.2) prohibits a direct solution of the Bethe–Salpeter equation. Instead a partial wave analysis would be needed. Subsection 4.1.1 will sketch a way to do so, if a certain approximation – the K–matrix approach – can be used. However, it will become clear that this simplification cannot be applied here.

Chapter 4

Detailed treatment of $\bar{\mathrm{K}}$N scattering

4.1 Bethe–Salpeter equation

In this section the formalism of two–particle scattering is introduced [30]. We want to calculate the amplitude of a scattering process like $\overline{K}N \to \overline{K}N$,

$$\langle \overline{K}^i(k')\, N(p')|\, T\, |\overline{K}^j(k)\, N(p)\rangle \;=\; (2\pi)^4\, \delta^4(0)\, \overline{u}(p') T^{ij}_{KN\to KN}(k',p';k,p)\, u(p)\;. \tag{4.1}$$

The scattering matrix element $T_{KN\to KN}$ is given by the Bethe–Salpeter [36] equation[1]

$$T_{fi}(k,k',s) \;=\; V_{fi}(k,k',s) \;+\; \int d^4l\, V_{fc}(k,l,s)\, \mathcal{G}^{BS}_c(k',k,l,s)\, T_{cf}(l,k',s). \tag{4.2}$$

The indices f,i mark the incoming and outgoing channels of mesons and baryons, i.e. kaon and nucleon in the present example. The index c indicates the particular channel of the intermediate state, that is the baryon–meson pair that forms the loop. We will refer to this equation also as the T–matrix equation. It can be displayed graphically in the following way:

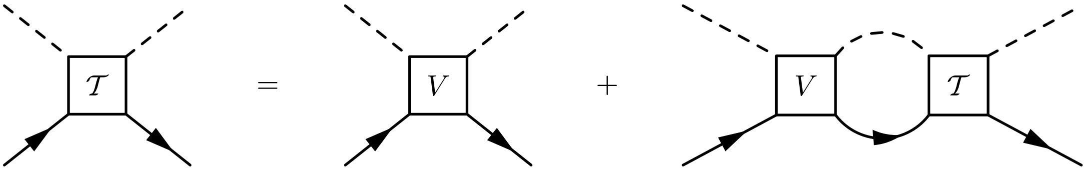

Figure 4.1: *Graphical form of the T–matrix equation*

The T–Matrix equation is constructed from the interaction kernel V and the two–particle propagator $\mathcal{G}^{BS}$. For V we will use the vertices derived in the previous chapter.

---

[1] In the following we drop the nucleon momenta p, p' from the notation and just keep the total energy s: As we have seen in section 3.4, the vertices eqs. (3.1)–(3.6) do not depend on the nucleon momenta. Thus these momenta do not enter the discussion of the T–matrix equation.

For a given loop, the two–particle propagator $\mathcal{G}_c^{BS}$ is written as the product of the baryon and meson propagators

$$\mathcal{G}_c^{BS}(k', k, l, s) = i\, S_{B_c}(k', k, l, s)\, G_{M_c}(k', k, l, s)\;.$$

The integral equation eq. (4.2) is of course rather difficult to solve in the general case. Here, the use of the chiral Lagrangian already simplifies the task significantly. At a given chiral order, the chiral interaction contains only a finite number of derivatives. The typical vertex we derived from $\mathcal{L}_{\chi PT}$ (chap. 3) is shown again in fig. 4.2. It is is point–like and depends only on the momenta k, k' of the in– and outgoing mesons.

$V \;=$

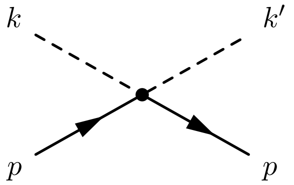

$$\approx \;\frac{i}{2f_\pi^2}\,(k^0 + k'^0)$$

Figure 4.2: *Weinberg–Tomozawa vertex*

In the T–matrix equation, only diagrams of this (fig. 4.2) structure appear.
This can be seen treating the Bethe–Salpeter equation in a perturbative way, i.e. expanding fig. 4.1 into a chain of loop graphs that are summed up:

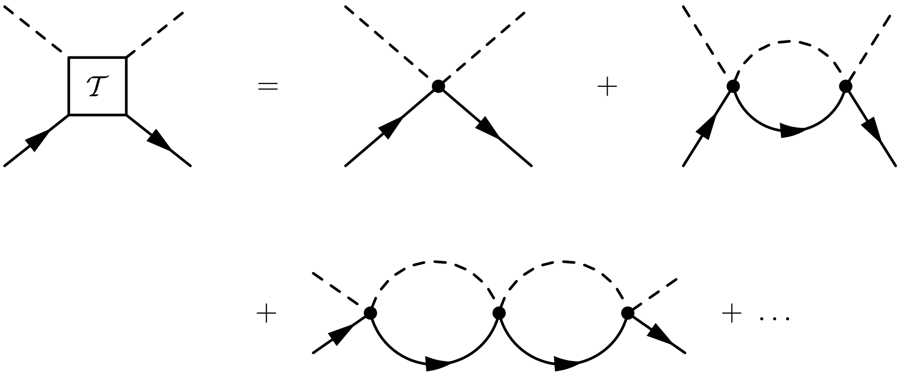

Figure 4.3: *"Perturbative"expansion of the BS equation*

It becomes clear that the energy–momentum dependence of T is just the one of V. If we were to stop with the second graph on the right ($T \sim V + \int V\mathcal{G}_{BS}V$), the nature of T with respect to the energy–momentum dependence would be equal to that of V. This is the case order by order and thus also for the full T–matrix.
However, the integral equation eq. (4.2) is not solved by this observation alone, as the vertices of type eq. (4.2) do not form a separable potential. We would like to find a simplification that makes it possible to treat the Bethe–Salpeter equation as an equation of matrix products. Looking back to the introduction of the vertex in chapter 2, fig. 2.1, we see that setting the incoming and outgoing mesons on their mass shells would fulfill the objective: Eq. (4.2) would be reduced to a sum of

meson masses, both V and T would drop out of the integral in eq. (4.2) and the calculation would be facilitated immensely. While this approximation becomes exact at the thresholds of the meson–baryon pairs, it will be rather crude in different kinematical regions. But we can improve on it by keeping the exact expression of eq. (4.2) at every vertex. This introduces an energy–dependence into the vertices, but since they still do not depend on the internal loop momenta, the factorization of the Bethe-Salpeter equation still can be done.

This approximation is in fact not as severe as it seems at first sight. It is important to realize that only the amplitude as given in (4.1) provides direct physical information – connecting the two asymptotic on–shell states. The Bethe–Salpeter equation provides the *off–shell continuation* of the physical amplitude. Amplitudes obtained off–meson–mass–shell (or off–baryon–mass–shell) are subject to the choice of the meson and baryon fields in the underlying Lagrangian and are thus giving model dependent results [30, 52, 53, 54]. To keep the physical amplitude independent of this choice the interaction kernel V can be divided into an on–shell part V_{on} and an off–shell part V_{off} – see also the extensive discussion in [30]. The off–shell part is to vanish if evaluated with on–shell kinematics, $V_{off}\, u(p)\,|_{on-shell} = 0$. Accordingly, the $\tilde{T}$–matrix constructed from V_{on} alone is on–shell equivalent to the general T–matrix:

$$\overline{u}\, T\, u(p)\,|_{on-shell} \equiv \overline{u}\, \tilde{T}\, u(p)\,|_{on-shell}$$

One can also argue that the off–shell part has been incorporated into the renormalization of the constants of the chiral Lagrangian such that the physical coupling constants emerge.

Consequently, the interaction kernel we keep in the Bethe–Salpeter equation is given by the factor $V_{on} \sim \frac{1}{2f_\pi^2}\,(k^0 + k'^0)$ — also inside the integral. Thus the interaction can be factored out of the integral. Since T can be treated just like V, it can also be factored out [30, 55, 56]). Hence the remaining integral extends just over the propagators of meson and baryon and the entire Bethe–Salpeter equation reduces to an equation of matrix multiplication. It can then be solved for T:[2]

$$T = (1 - V\, J)^{-1}\, V \;, \tag{4.3}$$

where J is the loop integral

$$J(k, k', s) = i \int \frac{d^4 l}{(2\pi)^4}\, S_B(k, k', l, s)\, G_M(k, k', l, s) \;. \tag{4.4}$$

The task for the next sections will be to see how the loop integral J can be solved. Before that, we would like to mention another approach to the Bethe–Salpeter equation.

4.1.1 K–matrix approximation

There is another way (not used in this work) to simplify the Bethe–Salpeter equation and thus obtain a solution. The Bethe–Salpeter equation reads

$$T = V + V\, G_{BS}\, T$$

$$T(k, k', s) = V(k, k', s) + \int \frac{d^4 l}{(2\pi)^4}\, V(k, l, s)\, G_{BS}(k, k', l, s)\, T(l, k', s) \;. \tag{4.5}$$

---

[2] The distinction in notation made above is dropped from here on: $V_{on} \to V$, $\tilde{T} \to T$

K–matrix

The K–matrix is the solution to the Bethe–Salpeter equation if only the real part of G_{BS} is used:

$$K(k,k',s) = V(k,k',s) + \int \frac{d^4l}{(2\pi)^4}\, V(k,l,s)\, \Re e(G_{BS}(k,k',l,s))\; K(l,k',s)\ . \tag{4.6}$$

Once the K–matrix is known, the T–matrix can be calculated as

$$T(k,k',s) = K(k,k',s) + \int \frac{d^4l}{(2\pi)^4}\, K(k,l,s)\, i\Im m(G_{BS}(k,k',l,s))\; T(l,k',s)\ . \tag{4.7}$$

K–matrix approximation

The approximation to the Bethe–Salpeter equation that is commonly called K–matrix approach actually consists in setting $K = V$ in (4.6). This simplified K–matrix is inserted in (4.7), which is then solved for T.
Of course, this amounts to a replacement of G_{BS} by $i\Im m(G_{BS})$ in (4.5).

$$T(k,k',s) \approx V(k,k',s) + \int \frac{d^4l}{(2\pi)^4}\, V(k,l,s)\, i\Im m(G_{BS})(k,k',l,s)\; T(l,k',s) \tag{4.8}$$

This kind of simplification of the Bethe–Salpeter equation is justified if there are certain properties or symmetries to be conserved while others can be discarded. An instructive example for the K–matrix approach can be found in [57]. There it is applied to pion–nucleon scattering. Care is used to ensure the unitarity of the S–matrix. On the other hand, causality is not guaranteed, since the intermediate particles (represented by G_{BS}) are put on their mass–shell by the substitution $G_{BS} \rightarrow i\Im m(G_{BS})$.

4.2 Loop integral

As the loop integral in our approximation does no longer contain the V and T matrices, we introduce the sum q of baryon and meson momentum and write

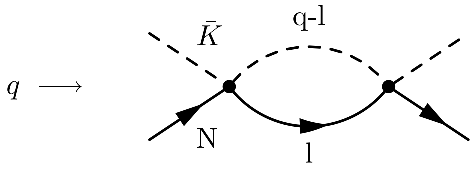

$$J_{\bar{K}N}(q) = -i \int \frac{d^4l}{(2\pi)^4}\, G_N(l)\; G_{\bar{K}}(q-l)\ . \tag{4.9}$$

The nucleon propagator at temperature $T = 0$ but finite density in general reads [58]

$$G_N(p) \quad = \quad \frac{\not{p} + m_N}{2\omega_N(\vec{p})} \left(\frac{\Theta(|\vec{p}| - p_f)}{p^0 - \omega_N(\vec{p}) + i\varepsilon} + \frac{\Theta(p_f - |\vec{p}|)}{p^0 - \omega_N(\vec{p}) - i\varepsilon} - \frac{1}{p^0 + \omega_N(\vec{p}) - i\varepsilon} \right) .$$

Here p_f is the Fermi momentum of the nucleon. The third term is the contributions of antinucleons. The second term represents a hole in the Fermi sea and has thus a momentum below p_f. For $p_f \to 0$ it vanishes and the vacuum propagator is recovered. This propagator also has the correct dispersive behavior as marked by the sign of the $i\varepsilon$ term. However, both the hole and antinucleon terms will eventually be found to give no contribution to the scattering amplitude of interest.

In the nonrelativistic approximation, that means neglecting the small components of the Dirac spinor of the nucleon, the nucleon propagator reads

$$G_N(p) = \frac{m_N}{\omega_N(\vec{p})} \left(\frac{\Theta(|\vec{p}| - p_f)}{p^0 - \omega_N(\vec{p}) + i\varepsilon} + \frac{\Theta(p_f - |\vec{p}|)}{p^0 - \omega_N(\vec{p}) - i\varepsilon} - \frac{1}{p^0 + \omega_N(\vec{p}) - i\varepsilon} \right) . \tag{4.10}$$

An important technique which is of special use for in–medium calculations is the use of dispersion representations (Lehmann representations) of the propagators [58]. In this form, the nucleon propagator reads

$$-\frac{1}{\pi} \int_0^\infty d\omega \, \frac{\Im m G_N^{(p)}(\omega, \vec{p})}{p^0 - \omega + i\varepsilon} + \frac{1}{\pi} \int_0^\infty d\omega \, \frac{\Im m G_N^{(h)}(\omega, \vec{p})}{p^0 - \omega - i\varepsilon} + \frac{1}{\pi} \int_0^\infty d\omega \, \frac{\Im m G_N^{a}(-\omega, \vec{p})}{p^0 + \omega - i\varepsilon} \tag{4.11}$$

with

$$\begin{aligned}
\Im m G_N^{(p)}(\omega, \vec{p}) = & \quad \frac{m_N}{\omega_N(\vec{p})} \, \Theta(|\vec{p}| - p_f) \; \Im m\left(\frac{1}{\omega - \omega_N(\vec{p}) + i\epsilon}\right) \\
= & -\pi \, \frac{m_N}{\omega_N(\vec{p})} \, \Theta(|\vec{p}| - p_f) \; \delta(\omega - \omega_N(\vec{p})) \\
\Im m G_N^{(h)}(\omega, \vec{p}) = & \quad \frac{m_N}{\omega_N(\vec{p})} \, \Theta(p_f - |\vec{p}|) \, \Im m\left(\frac{1}{\omega - \omega_N(\vec{p}) - i\epsilon}\right) \\
= & \quad \pi \, \frac{m_N}{\omega_N(\vec{p})} \, \Theta(p_f - |\vec{p}|) \, \delta(\omega - \omega_N(\vec{p})) \\
\Im m G_N^{a}(-\omega, \vec{p}) = & \quad -\frac{m_N}{\omega_N(\vec{p})} \; \Im m\left(\frac{1}{-\omega + \omega_N(\vec{p}) - i\epsilon}\right) \\
= & -\pi \, \frac{m_N}{\omega_N(\vec{p})} \; \delta(-\omega + \omega_N(\vec{p})) \, .
\end{aligned}$$

The kaon propagator is given by

$$\begin{aligned}
G_{\bar{K}}(k) &= \frac{1}{k^{0\,2} - \omega_K(\vec{k})^2 - \Sigma(k) + i\varepsilon} \\
&= -\frac{1}{\pi} \int_0^\infty d\omega \, \frac{\Im m G_{\bar{K}}(\omega, \vec{k})}{k^0 - \omega + i\varepsilon} + \frac{1}{\pi} \int_0^\infty d\omega \, \frac{\Im m G_{\bar{K}}(-\omega, \vec{k})}{k^0 + \omega - i\varepsilon} \, .
\end{aligned} \tag{4.12}$$

This form of the kaon propagator already contains the selfenergy Σ which we will calculate later on.

The other meson–baryon channels are constructed the same way. The propagators of the pion and the eta are given by the form of the kaon propagator above, substituting the respective masses of the mesons. There are no strange baryons present in the nuclear medium, so the propagators of the Λ and Σ are just

$$G_{\Lambda,\Sigma}(p) = \frac{m_{\Lambda,\Sigma}}{\omega_{\Lambda,\Sigma}(\vec{p})} \left(\frac{1}{p^0 - \omega_{\Lambda,\Sigma}(\vec{p}) + i\varepsilon} - \frac{1}{p^0 + \omega_{\Lambda,\Sigma}(\vec{p}) - i\varepsilon} \right) . \tag{4.13}$$

4.2.1 Vacuum

The next step is to evaluate the loop integral in the vacuum. Setting $p_f = 0$, the expression is

$$J_{\bar{K}N}(q) = -i \int \frac{d^4 l}{(2\pi)^4} \frac{m_N}{\omega_N(\vec{l})} \left(\frac{1}{l^0 - \omega_N(\vec{l}) + i\varepsilon} - \frac{1}{l^0 + \omega_N(\vec{l}) - i\varepsilon} \right) \tag{4.14}$$

$$\frac{1}{2\omega_K(\vec{q} - \vec{l})} \left(\frac{1}{q^0 - l^0 - \omega_K(\vec{q} - \vec{l}) + i\epsilon} - \frac{1}{q^0 - l^0 + \omega_K(\vec{q} - \vec{l}) - i\epsilon} \right) .$$

The l^0 integration can be done by closing contours in the complex plane, e.g.:

$$\frac{-i}{2\pi} \int dl^0 \frac{1}{l^0 - \omega_N(\vec{l}) + i\varepsilon} \; \frac{1}{q^0 - l^0 - \omega_K(\vec{q} - \vec{l}) + i\varepsilon}$$

$$= \frac{(-2\pi i)(-i)}{2\pi} \frac{1}{q^0 - \omega_N(\vec{l}) - \omega_K(\vec{q} - \vec{l}) + i\varepsilon}$$

$$= -\frac{1}{q^0 - \omega_N(\vec{l}) - \omega_K(\vec{q} - \vec{l}) + i\varepsilon}$$

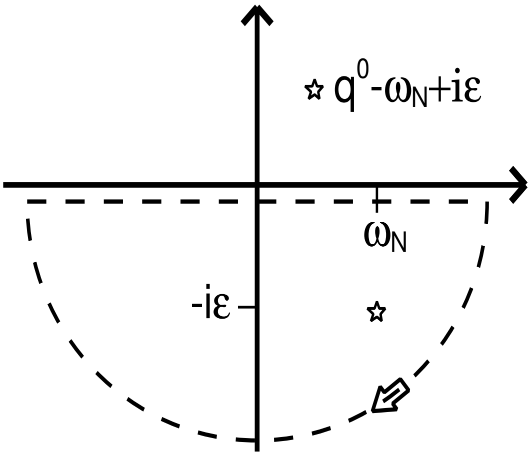

We get two terms for positive and negative energy (q^0):

$$\begin{aligned} J_{\bar{K}N}(q) = &- \int \frac{d^3 l}{(2\pi)^3} \frac{m_N}{\omega_N(\vec{l})} \frac{1}{2\omega_K(\vec{q} - \vec{l})} \frac{1}{q^0 - \omega_N(\vec{l}) - \omega_K(\vec{q} - \vec{l}) + i\epsilon} \\ &+ \int \frac{d^3 l}{(2\pi)^3} \frac{m_N}{\omega_N(\vec{l})} \frac{1}{2\omega_K(\vec{q} - \vec{l})} \frac{1}{q^0 + \omega_N(\vec{l}) + \omega_K(\vec{q} - \vec{l}) - i\epsilon} \end{aligned} \tag{4.15}$$

Substituting $z = \omega_K(\vec{q} - \vec{l}), \quad \omega_\pm = \sqrt{\vec{q}^2 + \vec{l}^2 \pm 2|\vec{q}||\vec{l}|}$, this can be written as:

$$\begin{aligned} J_{\bar{K}N}(q) \;\; = \;\; &- \frac{m_N}{8\pi^2 |\vec{q}|} \int_0^\infty d|\vec{l}| \, \frac{|\vec{l}|}{\omega_N(\vec{l})} \int_{\omega_-}^{\omega_+} dz \frac{1}{q^0 - \omega_N(\vec{l}) - z + i\epsilon} \\ &+ \frac{m_N}{8\pi^2 |\vec{q}|} \int_0^\infty d|\vec{l}| \, \frac{|\vec{l}|}{\omega_N(\vec{l})} \int_{\omega_-}^{\omega_+} dz \frac{1}{q^0 + \omega_N(\vec{l}) + z - i\epsilon} \end{aligned} \tag{4.16}$$

Taking the imaginary part leads to

$$\begin{aligned} \Im m J_{\bar{K}N}(q) = \frac{m_N}{8\pi |\vec{q}|} \int_0^\infty d|\vec{l}| \, \frac{|\vec{l}|}{\omega_N(\vec{l})} \Big(&\Theta(\omega_+ - q^0 + \omega_N(\vec{l})) \;\; \Theta(q^0 - \omega_N(\vec{l}) - \omega_-) \\ &+ \Theta(\omega_+ + q^0 + \omega_N(\vec{l})) \;\; \Theta(-q^0 - \omega_N(\vec{l}) - \omega_-) \; \Big) \; . \end{aligned}$$

Obviously the Θ–functions in the second term are the same as in the first term after replacing q^0 by $-q^0$. Therefore we have two axially symmetric branches for positive and negative energies q^0, each of which has the form

$$\begin{aligned} \Im m J_{\bar{K}N}(q) &= \frac{m_N}{8\pi|\vec{q}|} \int_{l_{min}}^{l_{max}} d|\vec{l}|\, \frac{|\vec{l}|}{\omega_N(\vec{l})} \\ &= \frac{m_N}{8\pi|\vec{q}|} \left(\sqrt{l_{max}^2 + m_N^2} - \sqrt{l_{min}^2 + m_N^2} \right) , \end{aligned} \tag{4.17}$$

where $\quad (q^2 = {q^0}^2 - \vec{q}^{\,2})$

$$l_{max/min} = \frac{1}{2q^2} \left(\pm|\vec{q}|(q^2 + m_N^2 - m_K^2) + \sqrt{{q^0}^2 \left((q^2 + m_N^2 - m_K^2)^2 - 4\, q^2 m_N^2\right)} \right) .$$

4.2.2 Vacuum loop in back–to–back kinematics

To gain insight into the properties of the loop function, the calculation can be done in 'back–to–back' kinematics, which amounts to setting $|\vec{q}| \to 0$. Eq. (4.15) then takes the form

$$J_{\bar{K}N}(q^0, 0) = -\frac{m_N}{4\pi} \int_0^\infty dl \frac{\vec{l}^{\,2}}{\omega_N(\vec{l})} \frac{1}{\omega_K(\vec{l})} \frac{1}{q^0 - \omega_N(\vec{l}) - \omega_K(\vec{l}) + i\epsilon} \tag{4.18}$$

$$+\frac{m_N}{4\pi} \int_0^\infty dl \frac{\vec{l}^{\,2}}{\omega_N(\vec{l})} \frac{1}{2\omega_K(\vec{l})} \frac{1}{q^0 + \omega_N(\vec{l}) + \omega_K(\vec{l}) - i\epsilon} . \tag{4.19}$$

The result for the imaginary part is very compact:

$$\Im m J_{\bar{K}N}(q^0, 0) = \frac{m_N}{8{q^0}^2} \sqrt{({q^0}^2 + m_N^2 - m_K^2)^2 - 4{q^0}^2 m_N^2} \tag{4.20}$$

This result is symmetric in q^0. Negative q^0 stem from the anti–nucleon part of the nucleon propagator and can be neglected for this discussion since we are only interested in the nucleon–contribution at positive energies.

The expression obviously approaches a constant value for large energies, see fig. 4.4. This feature is important for the next step, the calculation of the real part of $J_{\bar{K}N}$.

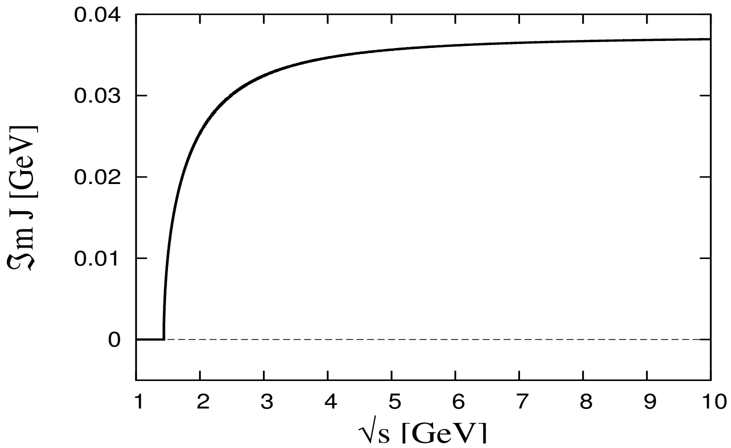

Figure 4.4: Imaginary part of the loop function $\Im m J_{\bar{K}N}$ in back–to–back kinematics, approaching a constant value at high energies

4.2.3 Real part of the vacuum loop function

So far the calculation has rendered not the full complex function $J_{\bar{K}N}$ but rather its imaginary part, eq.(4.17). The real part of $J_{\bar{K}N}$ has to be calculated by an dispersion integral:

$$\Re e J_{\bar{K}N}(\omega) \quad = \quad -\frac{1}{\pi} \int_{\infty}^{\infty} d\tilde{\omega}\, \frac{\Im m J_{\bar{K}N}(\tilde{\omega})}{\omega - \tilde{\omega}}$$

Since the imaginary part approaches a constant, this integral diverges $\sim \ln \omega$.
The typical way to regularize the integral as found in the literature [20, 19, 55, 31, 33, 29] is by introducing a cut–off λ in the imaginary part, i.e. restricting the loop momentum to values below the cut–off:

$$J_{\bar{K}N}(q) \quad = \quad -i \int\limits_{|\vec{\boldsymbol{l}}| \leq \boldsymbol{\lambda}} \frac{d^4 l}{(2\pi)^4}\, G_N(l)\, G_{\bar{K}}(q-l)$$

The dispersion integral will then only range from its lower bound given by the $\bar{K}N$–threshold up to the upper bound given by the cut–off λ.

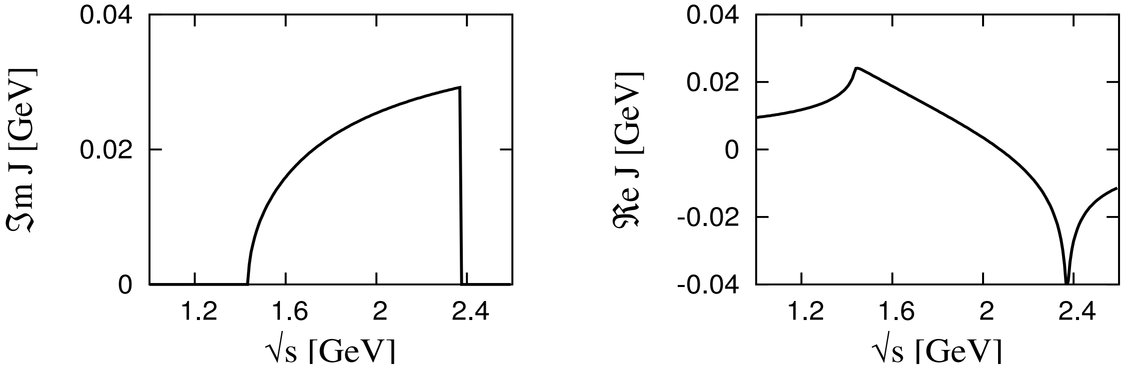

Figure 4.5: *$\Im m J$ and $\Re e J$ with a cut–off*

Fig. 4.5 shows the resulting form of the imaginary and real parts of $J_{\bar{K}N}$ for a value of $\lambda = 0.7$ GeV.

Of course, the parameter λ has to be adjusted to reproduce a scattering amplitude as in fig. 2.3, i.e. it is to be fitted to the $\bar{K}N$–scattering lengths. This can easily be achieved. However, two problems arise: The Lorentz–invariance of the vacuum amplitude is destroyed and the cut–off leads to peaks and kinks in the T–Matrix that should not be there.

The first problem is obvious: a three–dimensional cut–off will make the result to depend on the frame of reference it is calculated in. Fig. 4.6 shows the typical form taken by the proton–K^- scattering amplitude f_{K^-p}. It is connected to the T–matrix by

$$f = \hbar c \frac{m_N}{4\pi\sqrt{s}} T_{K^-p} \, .$$

The scattering amplitude is plotted in fig. 4.6 for two momenta ($|\vec{q}| = 100$ MeV and $|\vec{q}| = 400$ MeV) as a function of $\sqrt{s}$: If the calculation had obeyed Lorentz invariance, the two curves would fall on top of each other. However, we see that they are separated quite clearly.

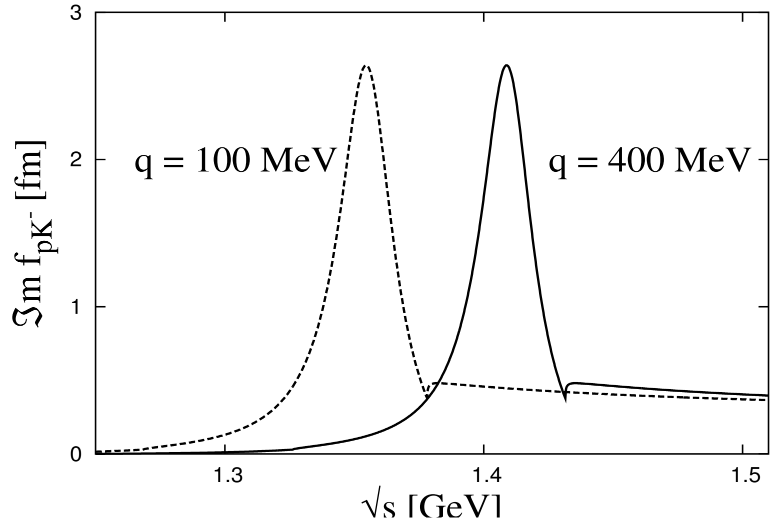

Figure 4.6: *The "cut–off" $\bar{K}N$ scattering amplitude in vacuum at two different momenta, plotted against $\sqrt{s}$: The amplitude is not covariant*

There is an additional ambiguity introduced by the cut–off: In the Feynman diagram above eq.(4.9), the internal lines are assigned the momenta l and $q - l$. This is of course an entirely arbitrary choice of labels. Consequently the result must not depend on this choice. Yet the use of a cut–off will do exactly that – make the loop integral depend on the choice of momentum labels. This is clearly not desirable.

Even more serious is the second consequence of the use of a cut–off. Fig. 4.7 shows the matrix element T_{pK^-} $|\vec{q}| = 400$ MeV for a larger energy interval. A second peak develops at the far end of this interval.

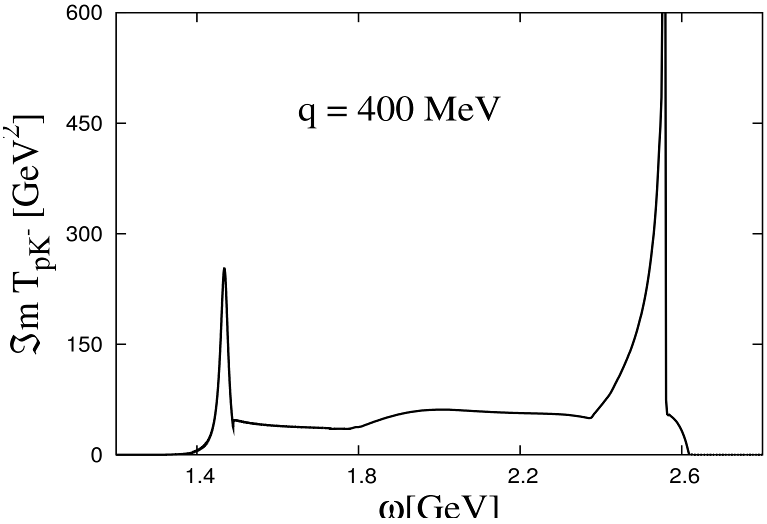

Figure 4.7: $\Im m T_{pK^-}$ *at* $|\vec{q}| = 400$ *MeV, with cut–off*

The form, position and height of that second peak at higher energies depends strongly on the value of the cut–off and has no physical meaning. It also depends on the momentum $\vec{q}$ and distorts the T–matrix elements heavily, "filling up"the range between the two peaks. Fig.4.8 shows this for a momentum of $|\vec{q}| = 1.2$ GeV.

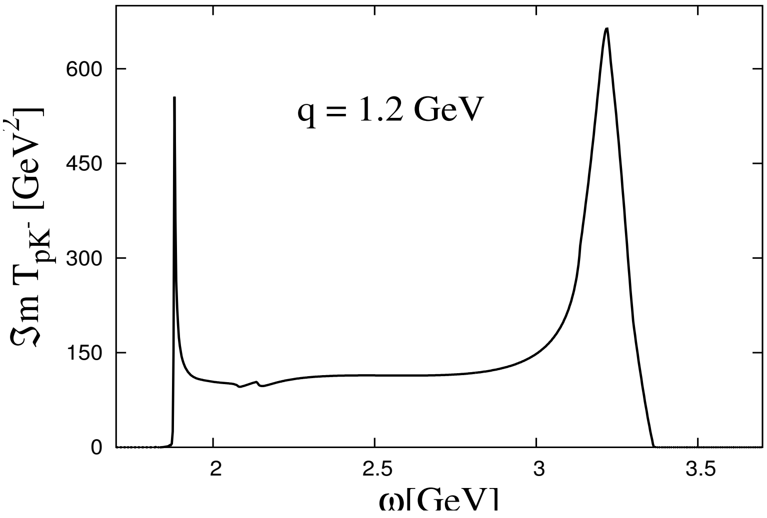

Figure 4.8: $\Im m T_{pK^-}$ *at* $|\vec{q}| = 1.2$ *GeV, with cut–off*

The question is now how to cope with these features. Is a properly Lorentz–invariant amplitude needed? That is, do we need to have a momentum dependence in the loop function and consequently in the T–matrix, or is a calculation in back–to–back kinematics sufficient? Is it necessary to pursue the amplitude to high energies, or can one simply stop at about 1.8 GeV?

First of all obtaining covariant vacuum quantities is not a matter of mere esthetics. The aim of this work is the calculation of the kaon propagator in nuclear matter. Now, the medium itself 'breaks Lorentz invariance', i.e. its own rest frame forms a distinct frame of reference. The calculation of in–medium properties is based on the vacuum result. That means we will fix the parameters of our model in the vacuum and leave them unchanged in the in–medium calculation. In addition, both the real and the imaginary part of the loop functions will be re–used in the in–medium ones. Proceeding in this manner with a vacuum quantity calculated in back–to–back kinematics will then lead to an uncontrolled mixing of frames of reference in the medium calculation. For example, a way to facilitate the calculation might be to evaluate the loop integral in the center of mass frame but evaluate the Fermi occupation numbers in the laboratory frame (c.f. [31]). Lacking proper momentum dependence, the required boosts cannot be done correctly.

Concerning the peculiar peaks in figs. 4.6 and 4.7 one might suggest restricting the T–matrix elements to energies below, say, 1.8 GeV. However, this is impossible. To understand the reason we have to examine a central, albeit technical problem of this work, the question of how to arrange the calculation to achieve our goal of selfconsistency for the scattering amplitude and the kaon selfenergy. We have to consider the following two integrals:

The first one is the imaginary part of the loop function after performing the l^0 integration, as in eq.(4.16), but for a general form of the kaon propagator $G_{\bar{K}}$:

$$\Im m J_{\bar{K}N}(q) = -\int \frac{d^3l}{(2\pi)^3}\,\frac{m_N}{\omega_N(\vec{l})}\,\Im m G_{\bar{K}}(q^0-\omega_N(\vec{l}),|\vec{q}-\vec{l}|)\;\Theta(q^0-\omega_N(\vec{l}))\Theta(|\vec{l}|-p_f) \tag{4.21}$$

The second is the expression for the imaginary part of the kaon selfenergy. This is just the explicit form[3] of fig. 2.4 in the guideline–chapter 2:

$$\Im m\Sigma_{\bar{K}}(k) = \int \frac{d^3p}{(2\pi)^3}\,\frac{m_N}{\omega_N(\vec{p})}\,\Im m T_{\bar{K}N}(k^0+\omega_N(\vec{p}),|\vec{p}+\vec{k}|)\;\Theta(p_f-|\vec{p}|) \tag{4.22}$$

The real parts of both functions, $J_{\bar{K}N}$ and $\Sigma_{\bar{K}}$, will be obtained from dispersion relations. The T–matrix element will then be constructed from $J_{\bar{K}N}$ using the matrices of couplings of chap. 3, and the kaon propagator will be obtained by inserting the selfenergy into $G_{\bar{K}}$. By virtue of this procedure the two integrals eq. (4.21) and (4.22) respectively represent the input to each other. Both integrations are over three–momenta, so the momentum dependence of these functions is crucial. Moreover, it is necessary to know both functions in a large (actually infinite) momentum range:

If $T_{\bar{K}N}$ is needed at some maximum momentum q_{max}, the loop $\Im m J_{\bar{K}N}$ is to be calculated at the same maximum momentum. According to eq.(4.21), the propagator in the integral then has to be known at momenta up to

$$|\vec{q}-\vec{l}|_{max} = q_{max} + l_{max} = q_{max} + \sqrt{q^{0\,2} - m_N^2},$$

$l_{max} = \sqrt{q^{0\,2} - m_N^2}$ being given by the Θ–functions.

In turn, the corresponding $\Sigma_{\bar{K}}$–integral needs its integrand $\Im m T_{\bar{K}N}$ at maximum momentum

$$|\vec{p}+\vec{k}|_{max} = |\vec{p}|_{max} + |\vec{k}|_{max} = p_f + q_{max} + \sqrt{q^{0\,2} - m_N^2} > q_{max}.$$

The required input is sought at values higher than the starting value – as such, the self–consistency procedure is a runaway process, it cannot be restricted to a finite interval of energy and momentum.

---

[3] The calculation of the kaon selfenergy in this form will be explained in detail in chap. 6.

In the case of the kaon propagator, this problem can be solved by a quite intuitive approximation. The in–medium kaon propagator is replaced by the free one at momenta greater than some maximum value: at very large momenta the interaction between kaon and surrounding medium will become very weak, the kaon will just pass through without taking notice of the medium. As it turns out, $k_{max} = 3$ GeV is a very safe value for this limit (cf. fig. 7.1). This works because the Lorentz–invariant vacuum kaon propagator is available at arbitrary energies and momenta and because the imaginary part of the vacuum propagator gives a δ–function, rendering the integral analytically solvable.
In the case of the T–matrix this problem can only be solved if the imaginary part of the T–matrix element $\Im m T_{\bar{K}N}$ vanishes above some maximum energy. The curves in figs. 4.6 and 4.7 do that, but only *beyond* those peaks at high energy we have found to be artificial. Yet the intent of the present considerations is to get rid of them in some way. Cutting the T–matrix (thus introducing yet another cut–off parameter) is no option because it is not clear where to do that. It would be hard to decide in e.g. fig. 4.8 which part of the curve is to be trusted and which is not.

Furthermore one has to realize that the integrals above (eqs. (4.21), (4.22)) run over three–momentum. But it is even less feasible to deduce a range of validity by examining the T–matrix elements as a function of momentum instead of energy: there is no guiding idea how such a curve should look like, which kinks are to be ignored or which peaks might be thrown away. Actually it is rather difficult to get a picture of how the two imaginary parts discussed above look like as integrands. Each integrand is a function of the respective loop momentum, but both arguments of the two functions, energy and momentum, depend on the loop momentum. The integration thus takes the two functions on a bent curve through the ω–$\vec{q}$ plane.

If cutting off the imaginary part of $J_{\bar{K}N}$ is no option, one might try to use a form factor instead [19]. However, this only rounds off the sharp edges of the cut imaginary part yet leads to similar problems in the T–matrix. On the other hand, a form factor that is smooth and slow enough as to not cause artificial structures in the T–matrix elements is basically no form factor at all. Then the convergence of the real part of $J_{\bar{K}N}$ is again questionable.

In any case the behavior of $\Im m T_{\bar{K}N}$ calculated by tampering with cut–offs or form factors is badly controlled when entering the selfconsistency calculation due to the peculiar way through the ω–$\vec{q}$ plane as prescribed by the integrals eqs. (4.21) and (4.22). Here might also be the reason why the use of cut–offs and form factors did not present such a serious problem in other works [19, 20, 21, 31]: Often the momentum dependence was neglected all together. In back–to–back kinematics most integrals can be done analytically anyhow. Or the aim was not a selfconsistent result — a one–step – only calculation greatly simplifies the task because one does not have to care about the high–momentum behavior. However, we shall see in the following chapters that both scattering amplitude as well as kaon selfenergy are strongly momentum dependent and that the selfconsistency procedure has influence even on the qualitative behavior of the result.

4.2.4 Subtracted dispersion relations

Physically relevant quantities are of course finite. If divergences occur, they are due to shortcomings of the model that was used or due to a general lack of understanding of the underlying physics. The task of a renormalization scheme is then to separate the divergent parts and put them elsewhere – like assigning the divergence in the QED vacuum polarization to the physical electric charge and interpreting only the finite part as physics

Along these lines of reasoning a much simpler procedure can help to address the calculation of the real part of $J_{\bar{K}N}$. The idea is to use a once or (as it turns out to be necessary) twice subtracted dispersion relation.

Single subtraction is performed by taking the difference of dispersion integrals at two different energies, ω and ω_0:

$$\begin{aligned}\Re e J(\omega) &= \frac{1}{\pi}\int_0^\infty d\tilde{\omega}\,\frac{\Im m J(\tilde{\omega})}{\tilde{\omega}-\omega}\\ \Re e J(\omega_0) &= \frac{1}{\pi}\int_0^\infty d\tilde{\omega}\,\frac{\Im m J(\tilde{\omega})}{\tilde{\omega}-\omega_0}\end{aligned}$$

The difference of these two expressions reads

$$\Re e J(\omega) = \Re e J(\omega_0) + \frac{1}{\pi}\int_0^\infty d\tilde{\omega}\,\Im m J(\tilde{\omega})\,\left(\frac{1}{\tilde{\omega}-\omega} - \frac{1}{\tilde{\omega}-\omega_0}\right)\,. \tag{4.23}$$

The subtraction point ω_0 is held fixed and the expression is evaluated as a function of ω. The trick is to interpret $\Re e J(\omega_0)$ as an unknown, free parameter. Its value can be fixed by fitting the resulting T–matrix to the experimental scattering lengths.

However, single subtraction turns out to be insufficient. This can be seen by examining the high–energy behavior of the T–matrix elements. As the discussion of eq. (4.22) showed, $\Im m T_{\bar{K}N}$ is input to the kaon selfenergy. We denote the cosine of the angle θ between the kaon momentum $\vec{k}$ and the nucleon momentum $\vec{p}$ by $\cos\theta = x_p$ and rewrite eq. (4.22) as

$$\Im m \Sigma_{\bar{K}}(k) = \frac{m_N}{4\pi^2}\int_0^{p_f} d|\vec{p}|\,\frac{\vec{p}^{\,2}}{\omega_N(\vec{p})}\int_{-1}^{1} dx_p\,\Im m T_{\bar{K}N}(k^0+\omega_N(\vec{p}),\vec{p}+\vec{k})$$

At kaon momenta large compared with the Fermi momentum, we can approximate this expression as

$$\begin{aligned}\Im m \Sigma_{\bar{K}}(k) &\approx \frac{m_N}{4\pi^2}\;2\,\Im m T_{\bar{K}N}(k^0+E_f,\vec{k})\;\int_0^{p_f} d|\vec{p}|\,\frac{\vec{p}^{\,2}}{\omega_N(\vec{p})}\\ &= \frac{m_N}{4\pi^2}\,\Im m T_{\bar{K}N}(k^0+E_f,\vec{k})\;\left(p_f E_f - m_N^2 \ln\frac{p_f+E_f}{m_N}\right)\,.\end{aligned}$$

E_f is the Fermi energy, $E_f = \sqrt{p_f^2 + m_N^2}$.

At momenta $|\vec{k}|$ of several hundred MeV the difference between the exact integral and the approximation given is negligible above $\omega \approx 3-5$ GeV. Hence the high energy behavior of $\Im m\Sigma_{\bar{K}}$ is given directly by $\Im m T_{\bar{K}N}$.

It is this high energy behavior that comes into focus here. The real part of the kaon selfenergy will be calculated by a dispersion relation as well:

$$\Re e \Sigma_{\bar{K}}(k^0,\vec{k}) = \frac{1}{\pi}\int_{-\infty}^{\infty} d\tilde{\omega}\,\frac{\Im m \Sigma_{\bar{K}}(\tilde{\omega},\vec{k})}{\tilde{\omega}-k^0}\,. \tag{4.24}$$

To carry out this integration one has to know $\Im m\Sigma_{\bar{K}}$ in principle for all energies. It is thus the high energy behavior of $\Im m T_{\bar{K}N}$ that decides about the convergence of the selfenergy.

The dispersion relation for the real part of the loop function can be simplified by making use of the fact that the imaginary part of the loop function approaches a constant at sufficiently large (3–5 GeV) energies, c.f. fig. 4.4. For energies larger than this energy, ω_{max}, we put $\Im m J(\omega > \omega_{max}) = const$. The expression for the real part eq. (4.23) becomes

$$\begin{aligned}
\Re e J(\omega) &= \Re e J(\omega_0) + \frac{1}{\pi} \int_0^{\omega_{max}} d\tilde{\omega}\ \Im m J(\tilde{\omega})\ (\frac{1}{\tilde{\omega}-\omega} - \frac{1}{\tilde{\omega}-\omega_0}) \\
&\quad + \frac{1}{\pi}\ \Im m J(\infty) \int_{\omega_{max}}^{\infty} d\tilde{\omega}\ (\frac{1}{\tilde{\omega}-\omega} - \frac{1}{\tilde{\omega}-\omega_0}) \\
&= \Re e J(\omega_0) + \frac{1}{\pi} \int_0^{\omega_{max}} d\tilde{\omega}\ \Im m J(\tilde{\omega})\ (\frac{1}{\tilde{\omega}-\omega} - \frac{1}{\tilde{\omega}-\omega_0}) \\
&\quad + \frac{1}{\pi}\ const.\ \ln \frac{|\omega_{max}-\omega_0|}{|\omega_{max}-\omega|} ,
\end{aligned}$$

where the integral is now finite.

We can now derive an analytical estimate of $\Re e J$ by replacing the imaginary part of the loop function in the integral with a step function. Fig. 4.4 shows that this is a quite good approximation to the overall energy dependence of $\Im m J$:

$$\Im m J_{\bar{K}N}(\omega) \approx \frac{m_N}{8\pi}\, \Theta(\omega-\omega_s)\ + \frac{m_N}{8\pi}\, \Theta(\omega+\omega_s)\ ,$$

where $\omega_s = \sqrt{m_N + m_K}$ is the threshold energy.

The real part then reads

$$\begin{aligned}
\Re e J(\omega) &= \Re e J(\omega_0) + \frac{m_N}{8\pi^2} \int_{\omega_s}^{\infty} d\tilde{\omega}\ (\frac{1}{\tilde{\omega}-\omega} - \frac{1}{\tilde{\omega}-\omega_0}) \\
&= \Re e J(\omega_0) - \frac{m_N}{8\pi^2}\ \ln \frac{|\omega_s-\omega|}{|\omega_s-\omega_0|} - \frac{m_N}{8\pi^2}\ \ln \frac{|\omega_s+\omega|}{|\omega_s+\omega_0|} .
\end{aligned}$$

Setting the subtraction point to 0:

$$\omega_0 \to 0: \qquad \Re e J(\omega) = \Re e J(0) - \frac{m_N}{8\pi^2}\ \ln \frac{|\omega_s-\omega||\omega_s+\omega|}{\omega_s^2} . \tag{4.25}$$

Thus we can write the approximative form of the loop function as

$$J_{\bar{K}N}(\omega) \approx \Re e J_{\bar{K}N}(0) + \mathcal{C}\ \ln\omega\ + i\, \Im m J_{\bar{K}N} . \tag{4.26}$$

This form is now inserted into the T–matrix element. To keep the expression as clear as possible, we use the simplest model for the interaction (sec. 2), with the channels $\bar{K}N, \pi\Sigma$ and $\pi\Lambda$ in the isospin[4] basis. The energy–independent threshold values (fig. 2.1) for the couplings are here renamed as (g_{11},g_{12}, g_{22}). The $(1,1)$–element of the (isospin=0) T–matrix then reads:

$$T_{11}^{(0)} = \frac{g_{11} + (g_{12}^2 - g_{11}g_{22})J_{\pi\Sigma}}{1 - g_{11}J_{\bar{K}N} - g_{22}J_{\pi\Sigma} - (g_{12}^2 - g_{11}g_{22})J_{\pi\Sigma}J_{\bar{K}N}}$$

---

[4] For details of the isospin decomposition, see sec. 4.3

Obviously, we need expressions corresponding to eq. (4.26) for the other two channels also. Putting in the loop integrals in the approximated form of eq. (4.26), the imaginary part of $T_{11}^{(0)}$ takes the form

$$\Im m T_{11}^{(0)} = \frac{\alpha + \beta \ln \omega + \gamma (\ln \omega)^2}{\delta (\ln \omega)^4 + \lambda (\ln \omega)^3 + \kappa (\ln \omega)^2 + \theta \ln \omega + \xi} \, .$$

The leading term turns out to be proportional to $(1/\ln \omega)^2$. The isospin–1 T–matrix element behaves much in the same manner, just containing many more terms.[5] The energy–independent terms are collected in the constants $\alpha, \beta \ldots$. That means that the dispersion integral for $\Re e \Sigma_{\bar{K}}$ eq. (4.24) is of the form $\int dx \frac{1}{x (\ln x)^2}$. Looking up the integral tables one finds that this is among the slowest converging integrals, $\int dx \frac{1}{x \ln x}$ is already divergent. Consequently, the integration for $\Re e \Sigma_{\bar{K}}$ would have to be extended over a vast energy interval ($\sim$ 1 J), way beyond the limits of applicability of this calculation. And of course the value of this integral, the strength of $\Re e \Sigma_{\bar{K}}$, would be highly questionable. On the other hand, in the case of $\Re e \Sigma_{\bar{K}}$, subtraction is no option: it would mean to introduce density–dependent subtraction parameters, something one surely wants to avoid.

The solution is to make $\Im m T$ fall off more rapidly. This can be achieved by using a twice subtracted dispersion relation for $\Re e J$.

Twice subtracted dispersion relation

To see how this works, we write down the first and second terms of the Taylor expansion of some function $f(x)$

$$f(x) = f(x_0) + (x - x_0) f'(x_0) + \big(f(x) - f(x_0) - (x - x_0) f'(x_0) \big) \, .$$

The dispersion representation for the various terms are put in:

$$f(x) = \frac{1}{\pi} \int d\tilde{x} \frac{\Im m f(\tilde{x})}{\tilde{x} - x} \qquad \Rightarrow f'(x_0) = \frac{1}{\pi} \int d\tilde{x} \frac{\Im m f(\tilde{x})}{(\tilde{x} - x_0)^2}$$

In case of the loop function, this reads

$$\Rightarrow \Re e J'(\omega) = \frac{1}{\pi} \int_0^\infty d\tilde{\omega} \, \frac{\Im m J(\tilde{\omega})}{(\tilde{\omega} - \omega)^2}$$

$$\begin{aligned} \Rightarrow \Re e J(\omega) = & \Re e J(\omega_0) + (\omega - \omega_0) \, \Re e J'(\omega_0) \\ & + \frac{1}{\pi} \int_0^\infty d\tilde{\omega} \, \Im m J(\tilde{\omega}) \left(\frac{1}{\tilde{\omega} - \omega} - \frac{1}{\tilde{\omega} - \omega_0} - \frac{\omega - \omega_0}{(\tilde{\omega} - \omega_0)^2} \right) \end{aligned}$$

Again we set $\Im m J$ to a constant for energies above ω_0:

$$\begin{aligned} \Re e J(\omega) = & \Re e J(\omega_0) + (\omega - \omega_0) \, \Re e J'(\omega_0) \\ & + \frac{1}{\pi} \int_0^{\omega_{max}} d\tilde{\omega} \, \Im m J(\tilde{\omega}) \left(\frac{1}{\tilde{\omega} - \omega} - \frac{1}{\tilde{\omega} - \omega_0} - \frac{\omega - \omega_0}{(\tilde{\omega} - \omega_0)^2} \right) \\ & - \frac{1}{\pi} \Im m J(\omega_{max}) \left(\ln \frac{|\omega_{max} - \omega|}{|\omega_{max} - \omega_0|} + \frac{\omega - \omega_0}{\omega_{max} - \omega_0} \right) \, . \end{aligned}$$

---

[5] However, even at extremely large energies the contributions of the various powers of $\ln \omega$ still contribute substantially. It is thus not possible to approximate the asymptotic behavior of $\Im m T_{\bar{K}N}$ simply by $1/(\ln \omega)^2$.

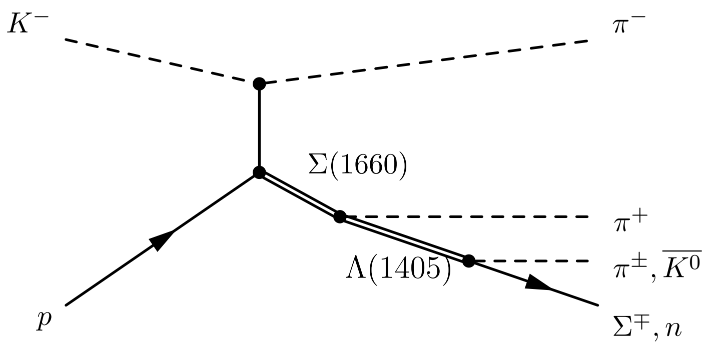

Figure 4.9: *Production process of* $\Lambda(1405)$ *in experiment*

The subtraction point is set to zero, $\omega_0 = 0$.

$$\begin{aligned}\Re e J(\omega) &= \Re e J(0) + \omega\, \Re e J'(0) \\ &+ \frac{1}{\pi} \int_0^{\omega_{max}} d\tilde{\omega}\; \Im m J(\tilde{\omega}) \left(\frac{1}{\tilde{\omega} - \omega} - \frac{1}{\tilde{\omega}} - \frac{\omega}{\tilde{\omega}^2} \right) \\ &- \frac{1}{\pi} \Im m J(\omega_{max}) \left(\ln \frac{|\omega_{max} - \omega|}{|\omega_{max}|} + \frac{\omega}{\omega_{max}} \right)\end{aligned}$$

In this form the real part of the loop function and the resulting T–matrix are behaving well enough to be used in the selfconsistency scheme.

Subtraction parameters

The method of twice subtracted dispersion relations introduces parameters to the model. Model parameters are usually fixed by fitting the calculated results to measured ones. Of course, in the case of the $\bar{K}N$–scattering, the interesting part lies just below the $\bar{K}N$ threshold at 1.435 GeV. That is where the $\Lambda(1405)$ (fig.2.3) shows up in the scattering amplitude.

Experimentally, the $\Lambda(1405)$ is seen in the $\pi\Sigma$ mass spectrum [37]. The reaction investigated is the scattering of K^- on protons that proceeds via the $\Sigma(1660)$ to $\pi\Lambda(1405)$, see fig. 4.9.
From measurements of this process, the $\pi\Sigma$ mass spectrum can be extracted. It is defined as [33, 59]

$$\frac{d\sigma}{dm} = C |T_{\pi\Sigma\to\pi\Sigma}|^2 p_{cm},$$

where p_{cm} is the pion momentum in the $\pi\Sigma$ rest frame. The experimental data are given in arbitrary units. In fig. 4.10 they are scaled up by a factor 80 to match the calculated mass distribution.

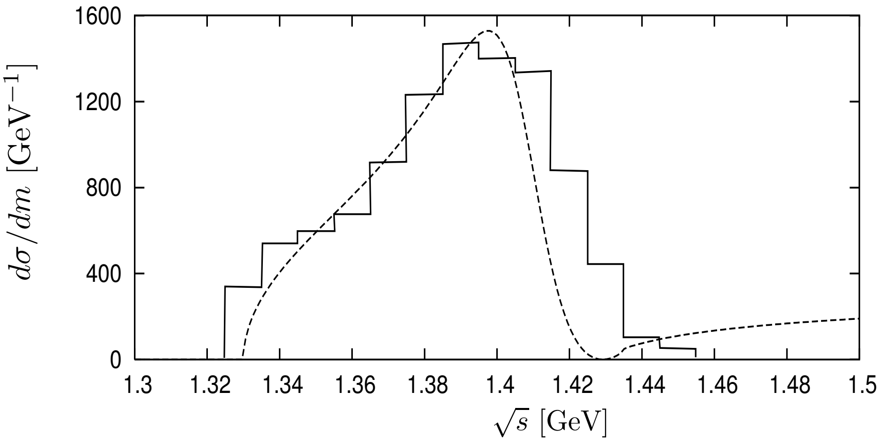

Figure 4.10: $\Lambda(1405)$ *in* $\pi\Sigma$ *mass spectrum, data (bar chart) from [37]*

Since this quantity does not allow for a very precise fit, the most important experimental input is indeed given by the scattering lengths at the $\bar{K}N$–threshold (eq.(2.3)). The question arises whether another restriction in another kinematic regime can be found. To get a constraint at large energies, one might be tempted to try the procedure discussed in the following.

To illustrate the argument, we write down the T–matrix equation for one channel only

$$T = g + g\,J\,T \;\Rightarrow\; T = \frac{g}{1 - g\,J}\,.$$

Now we imagine the vertex g not to be point like but rather being generated by the following process:

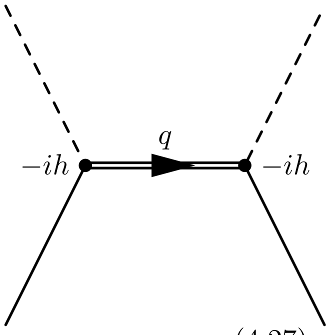

The diagram gives:

$$\begin{aligned} iT &= (ih)^2\,\frac{i}{q^2 - M^2} \\ T^{-1} &= \frac{1}{h^2}(M^2 - q^2) \overset{!}{=} \frac{1}{g} - J \end{aligned} \qquad (4.27)$$

If this relation were to be correct, J should asymptotically follow q^2, going to $+\infty$. But once we fit the scattering amplitude to the experimental scattering lengths it turns out we cannot obtain this behavior of the real part of the loop functions simultaneously.

This issue is closely connected to the degree of sophistication the formalism is bearing. For one thing, more than one meson–baryon channel has to be included. This is vital for the existence of the $\Lambda(1405)$, as we have seen in fig. 2.3. The simple picture drawn above will probably not hold. Nevertheless, the net effect of coupled channels could still lead to the desired behavior. However, if we increase the sophistication of the couplings used, from the simplest version introduced in chap. 2 to the full couplings of eqs.(3.1)–(3.6), the fit to the experimental scattering lengths the various real parts cannot be brought into agreement with the high–energy constraint derived above. This development will be discussed in detail in the next section.

In any case, the final version of a typical $\Re eJ$ does look as in fig. 4.11.

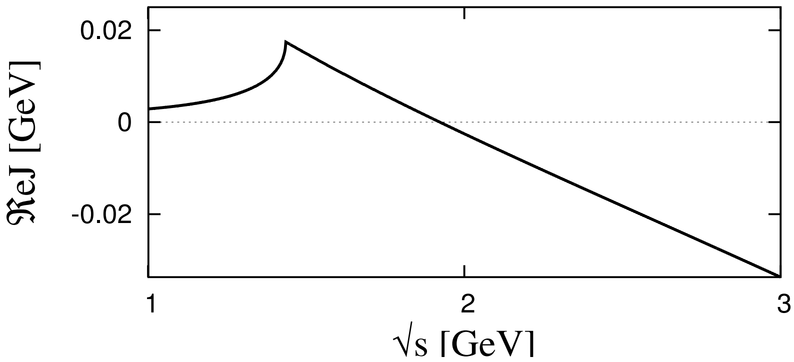

Figure 4.11: *Typical* $\Re eJ$

This function is clearly not following $q^2 \rightarrow +\infty$. But then, this behavior was not mandatory.

What can be said in general about the choice of parameters? The guideline is to concentrate on the physics in the 1–3 GeV range. That means there should be no influence from outside this interval other than e.g. the tails of the real parts $\Re eJ$. No additional peaks in the imaginary part of the T–matrix nor any poles or resonances in its real part that stem from the choice of parameters instead of physical effects are acceptable.
Finally, a comparison with the literature is always useful. In this case, a comparison with the $\Im mT$–amplitudes of M. Lutz [30, 60] was possible and a good match could be achieved.

4.3 Dependence of the loops and T–matrix elements on the form of the couplings

In this section we will inspect the consequences of the considerations presented in the previous sections in greater detail. As it turns out, the form of the couplings that was presented in chapter 3 together with the choice of the subtraction parameters has significant influence on the result of the calculation. To illustrate this behavior, we will start with a basic form and then add more ingredients, inspecting the differences this will cause in our curves. All plots are at vanishing 3–momentum $|\vec{q}| = 0$.

In the first, basic step we can follow Lutz [29] and Oset [33]. The problem is here formulated in an isospin basis for just three channels, $\bar{K}N, \pi\Sigma$ and $\pi\Lambda$.

The states of good isospin $I = 0, 1$ are

$$\begin{aligned}
|\bar{K}N, I=0\rangle =& \frac{1}{\sqrt{2}}(|\bar{K^0}n\rangle + |K^- p\rangle) \\
|\bar{K}N, I=1\rangle =& \frac{1}{\sqrt{2}}(|\bar{K^0}n\rangle - |K^- p\rangle) \\
|\pi\Sigma, I=0\rangle =& -\frac{1}{\sqrt{3}}(|\pi^+\Sigma^-\rangle + |\pi^0\Sigma^0\rangle + |\pi^-\Sigma^+\rangle) \\
|\pi\Sigma, I=1\rangle =& \frac{1}{\sqrt{2}}(|\pi^-\Sigma^+\rangle - |\pi^+\Sigma^-\rangle) \\
|\pi\Lambda, I=1\rangle =& \frac{1}{\sqrt{3}}(|\pi^-\Lambda\rangle + |\pi^+\Lambda\rangle + |\pi^0\Lambda\rangle)\ .
\end{aligned} \tag{4.28}$$

The lowest–order coupling constants (cf. fig.2.1) read:

$I{=}0$	$\bar{K}N$	$\pi\Sigma$
$\bar{K}N$	$\frac{3}{2}\frac{m_K}{f_\pi^2}$	$\frac{\sqrt{6}}{8}\frac{m_\pi+m_K}{f_\pi^2}$
$\pi\Sigma$	$\frac{\sqrt{6}}{8}\frac{m_\pi+m_K}{f_\pi^2}$	$2\frac{m_\pi}{f_\pi^2}$

$I{=}1$	$\bar{K}N$	$\pi\Sigma$	$\pi\Lambda$
$\bar{K}N$	$\frac{m_K}{2\,f_\pi^2}$	$\frac{m_\pi+m_K}{4\,f_\pi^2}$	$\frac{\sqrt{6}}{8}\frac{m_\pi+m_K}{f_\pi^2}$
$\pi\Sigma$	$\frac{m_\pi+m_K}{4\,f_\pi^2}$	$\frac{m_\pi}{f_\pi^2}$	0
$\pi\Lambda$	$\frac{\sqrt{6}}{8}\frac{m_\pi+m_K}{f_\pi^2}$	0	0

Table 4.1: *Threshold coupling constants in the isospin basis. Left: isospin–0, right: isospin–1*

We now proceed as described in subsection 4.2.1 to calculate the imaginary part of the loop functions and then their real parts using twice subtracted dispersion relations (subsec. 4.2.4).
The scattering amplitudes are given directly by the resulting T–matrix,

$$f_{\bar{K}N} = \hbar c \frac{m_N}{4\pi\sqrt{s}} T_{\bar{K}N}\ .$$

The experimental scattering lengths are taken from [40]:

$$\begin{aligned}
f^{(I=0)}_{\bar{K}N}(\omega = m_N + m_K, \vec{q} = 0) =& a^{(I=0)}_{\bar{K}N} = (-1.7 + i\,0.68)\text{fm} \\
f^{(I=1)}_{\bar{K}N}(\omega = m_N + m_K, \vec{q} = 0) =& a^{(I=1)}_{\bar{K}N} = (0.37 + i\,0.6)\text{fm}
\end{aligned}$$

The parameters of the subtracted dispersion relations for each channel are adjusted such that these values are reproduced in our scattering amplitudes at threshold. This leads to the curves in fig. 4.12, where the left panel shows the real and imaginary parts of $f_{\bar{K}N}$ for isospin–0, the right panel for isospin–1.

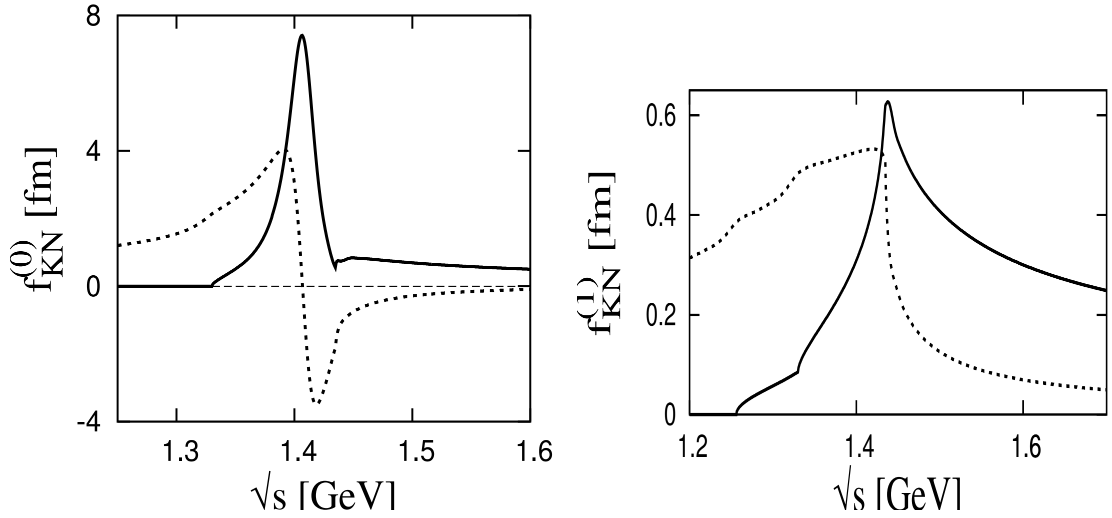

Figure 4.12: $f_{\bar{K}N}$, *isospin 0 (left) and isospin 1 (right), solid lines: imaginary parts, dotted lines: real parts*

The real parts of the loop functions contained herein, $\Re e J_{\bar{K}N}, \Re e J_{\pi\Sigma}$ and $\Re e J_{\pi\Lambda}$, can indeed be made to turn towards $+\infty$, just as demanded at the end of the last section (eq. (4.27)). But this will change in the following.

An obvious extension of the scheme is the inclusion of the η meson (see eq.(3.2)) and the corresponding $\eta\Lambda$ and $\eta\Sigma$ channels. The thresholds for these channels lie at 1.683 GeV and 1.757 GeV, respectively. This is right in the middle of the energy range of interest. Furthermore, the coupling to $\bar{K}N$ is not small,

$$g_{\bar{K}N\eta\Sigma} = \sqrt{\frac{3}{2}}\frac{m_\eta + m_K}{4\,f_\pi^2}, \qquad g_{\bar{K}N\eta\Lambda} = -\frac{3}{\sqrt{2}}\frac{m_\eta + m_K}{4\,f_\pi^2},$$

so there is no good reason to exclude them. Adding more channels (or coupling the channels together with changed functions or constants) will always force a change in the loop functions themselves, since coupled together they are to reproduce the scattering lengths and the shape or at least the mass of the $\Lambda(1405)$. The latter properties, of course, do not change.

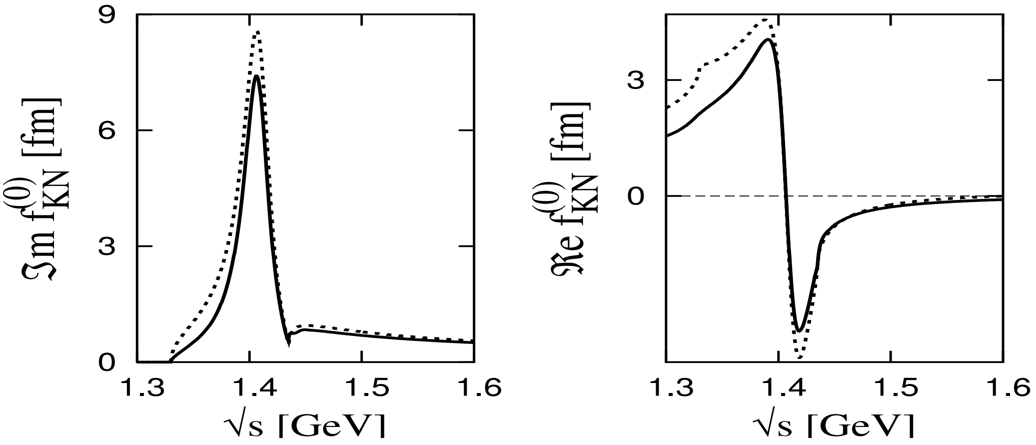

Figure 4.13: $f_{\bar{K}N}$, *isospin 0 (solid line: without η channels, dotted line: η channels included)*

The resulting isospin–0 and isospin–1 scattering amplitudes are shown in figs. 4.13 and 4.14. It turns out to be more difficult to find subtraction parameters that lead to the correct scattering lengths (fig. 4.13, left) and the correct mass of the $\Lambda(1405)$ (fig. 4.13, right) – this is obvious since the number of parameters has increased. But the result is also differing from the previous one. This is, of course, a desired consequence, the inclusion of additional channels should have some effect on the result.

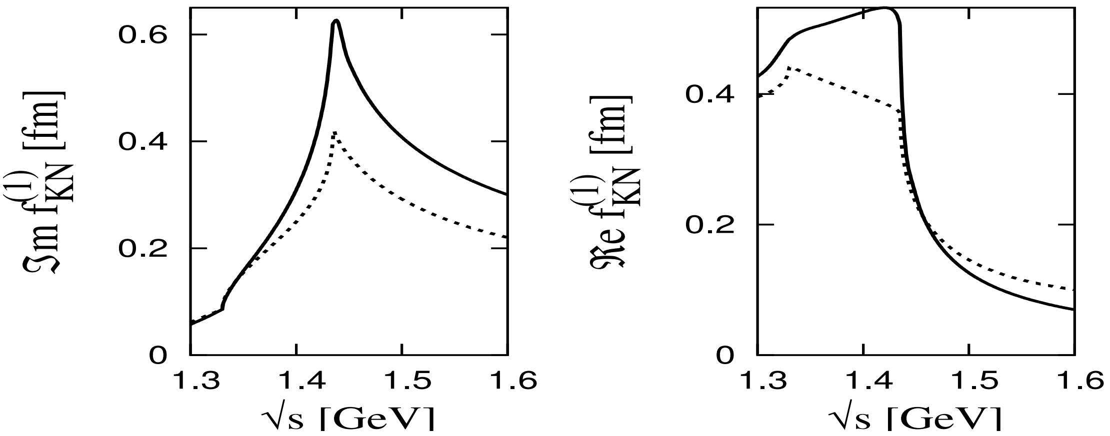

Figure 4.14: $f_{\bar{K}N}$, *isospin 1 (solid line: without* η *channels, dotted line:* η *channels included)*

In the isospin–1 case (fig. 4.14) where the differences are bigger, the imaginary part gives a scattering length that is closer to the experimental value of $\Im m a_{\bar{K}N}^{(I=1)} = 0.6$ fm without the η, while for the real part ($\Re e a_{\bar{K}N}^{(I=1)} = 0.37$ fm) it is just the other way around. In any case there is only little knowledge about the form of the $I = 1$ amplitude. It does not show resonant behavior (note the different scales on the $I = 0$ and $I = 1$ figures), hence also gives only a smaller contribution to the total $T_{\bar{K}N}$ and the kaon selfenergy.

The next step is to use the full couplings eqs.(3.1)–(3.6).
First we inspect again the isospin–0 scattering amplitude in the vacuum, shown in fig. 4.15. The differences are not huge, as it is to be expected: the $\Lambda(1405)$ is situated right at the thresholds, so the coupling strengths will be very close to their threshold values.

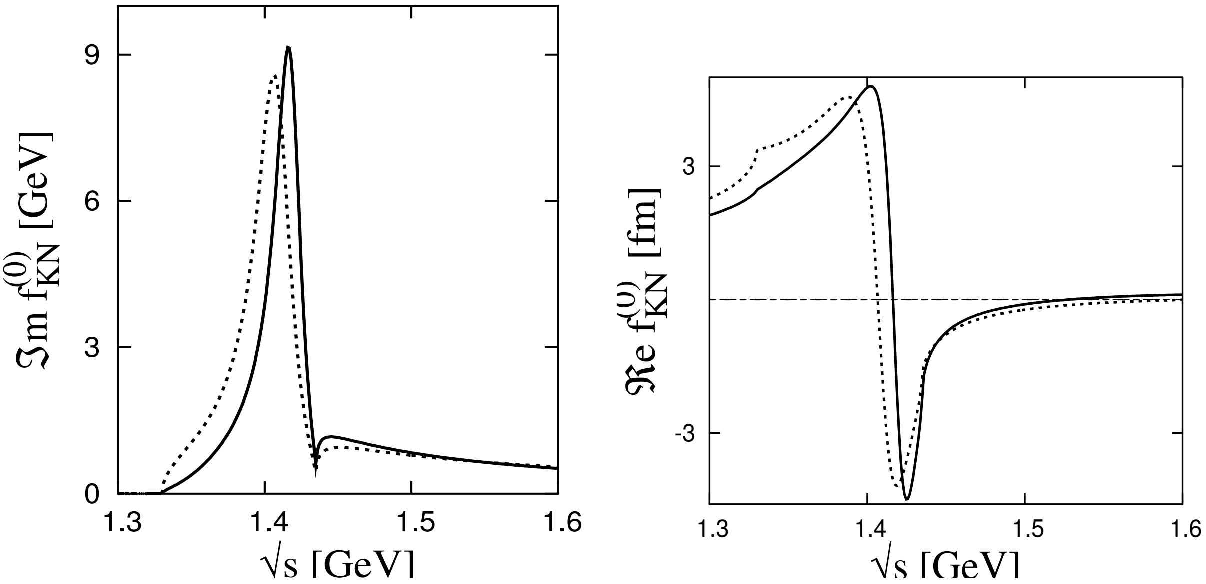

Figure 4.15: *$\bar{K}N$ scattering amplitude (isospin 0) with constant (dotted line) and full couplings (solid line). Left panel: imaginary part, right panel: real part*

Again, the variation in the isospin–1 amplitude (fig. 4.16) is larger:

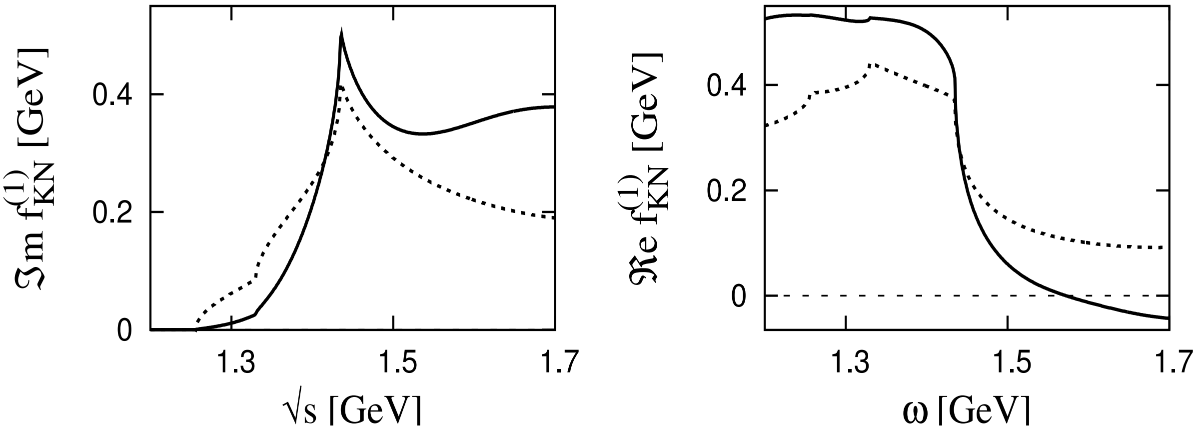

Figure 4.16: *$\bar{K}N$ scattering amplitude (isospin 1) with constant (solid line) and full couplings (dotted line). Left panel: imaginary part, right panel: real part*

So far, we have presented the result of the parameter fixing in the form of the amplitudes $f_{\bar{K}N}$. These have to coincide at threshold with the experimental data. Yet, the curves that are directly influenced by the changes in the subtraction parameters are the real parts of the loop functions. We inspect some of these curves in the following figures (figs. 4.17, 4.18).

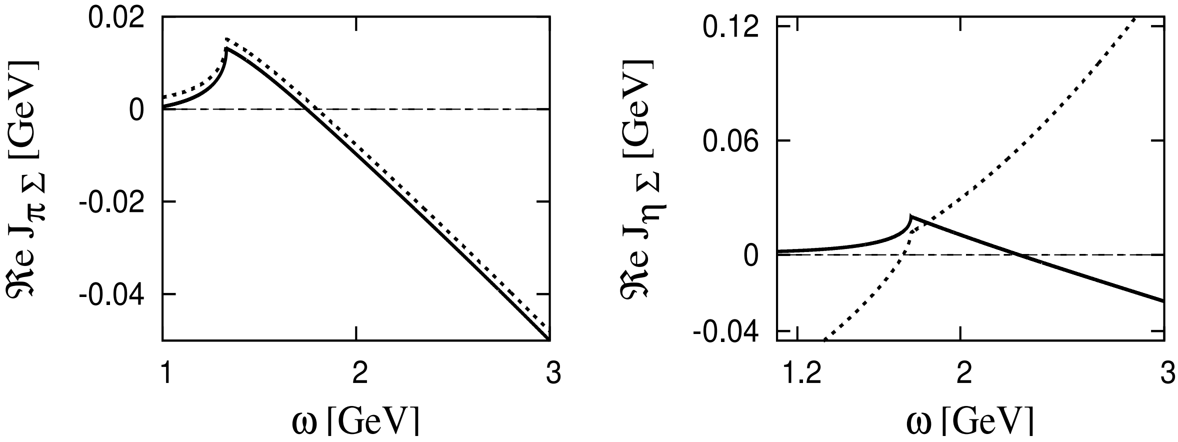

Figure 4.17: *Real parts of the $\pi\Sigma$ loop (left) and $\eta\Sigma$ (right), again for constant (solid line) and full couplings (dotted line)*

The $\pi\Sigma$ loop on the left of fig. 4.17 is the main contribution to the isospin–0 case (alongside the $\bar{K}N$ loop). It does not change much with the couplings. The $\eta\Sigma$ loop on the right of fig. 4.17 is pure isospin 1, and differs significantly.
During the calculation it became clear that the large energy constraint proposed in eq. (4.27) cannot be applied to these real parts: There is no possibility of bending e.g. $\Re e J_{\pi\Sigma}$ toward positive values at large energies while simultaneously obtaining the correct scattering lengths in $f_{\bar{K}N}$.

Similar conclusions apply to the $\pi\Lambda$ loop, which behaves all differently depending on which couplings are used (fig. 4.18).

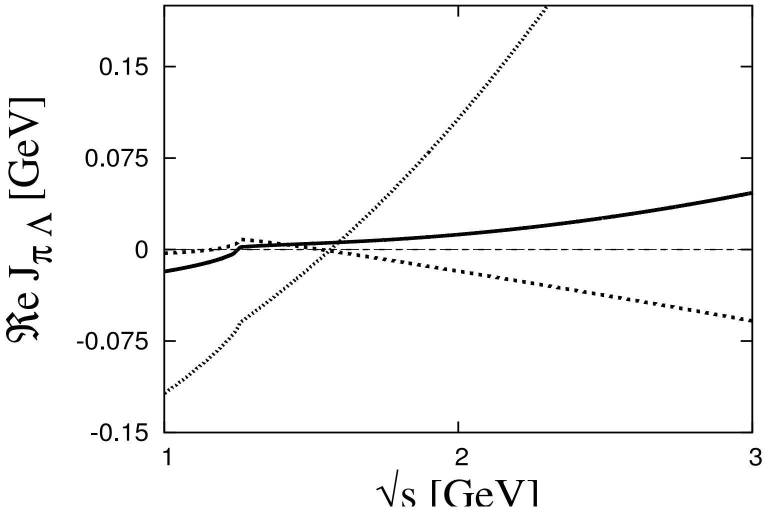

Figure 4.18: *Real part of the $\pi\Lambda$ loop: constant couplings (solid line), constant couplings +η (dashed) and full couplings (dotted line)*

It is a rather general realization that effects observed within the coupled channels calculation cannot be pinned down on the influence of one particular channel or coupling. Here we ‘observe’ that the calculated scattering amplitude is (or is not) in agreement with the scattering lengths. Switching off the couplings of the channels or investigating the behavior of one channel only cannot give any clue how this result comes about, since the latter is entirely a coupled–channels effect. Tracing back an effect through the full T–matrix element is entirely impossible due to the complexity of the analytic expressions.

There is also another difficulty that can easily be overlooked. To inspect the result of the calculation one usually plots the imaginary part of the $\bar{K}N$–T–Matrix as a function of energy (e.g. figs. 4.12–4.16). Its real part is only needed to fit the corresponding scattering lengths, for the calculation of the kaon selfenergy it plays no role. But the manipulation of the parameters in the subtracted dispersion relation for $\Re e J$ can easily introduce poles in this real part of T [61]. Depending on the actual values of the parameters chosen, such a pole might lie closely below or even above threshold. Clearly, this is an unacceptable feature, since no bound states or resonances besides the $\Lambda(1405)$ have been found.

This difficulty also prohibits the use of the $\bar{K}N$ scattering amplitude to obtain an expression for KN scattering via crossing symmetry [30]. For this the $T_{\bar{K}N}$–matrix elements would be probed below threshold – the threshold for kaon–nucleon scattering is at $\sqrt{s} \simeq m_N - m_K$. The unphysical poles in the real part of T that usually arise below $\sqrt{s} \sim 500$ MeV clearly show that this approach is not valid. However, in our case we are not interested in this energy region in $\Re e T$. Only the imaginary part is reused in the calculation, so the aim must be to avoid effects of possible unphysical pole structures in the real part.

The important question is now: How severe is the variability apparent in figs. 4.13–4.16 ? The objective of this work is the calculation of the kaon propagator. The corresponding formalism will be developed in chap.6,7. Here we just want to inspect the result, with emphasis on the repercussions of the different couplings:

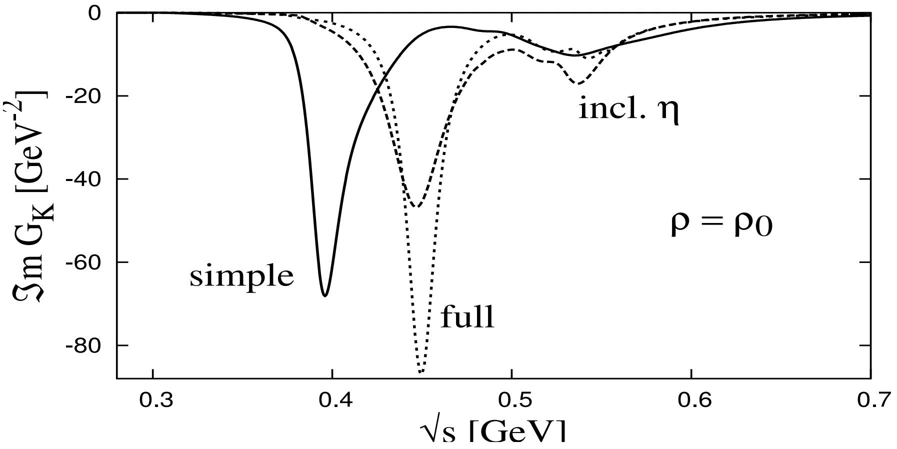

Figure 4.19: *Imaginary part of $G_{\bar{K}}$, constant couplings (solid line), constant couplings $+\eta$ (dashed) and full couplings (dotted line), density $\rho = \rho_0$*

In fig. 4.19, $G_{\bar{K}}$ is taken after one interactive step in the selfconsistency procedure to have the maximum effect of the vacuum parameters visible.
At twice nuclear matter density (fig. 4.20) the picture is quite similar.

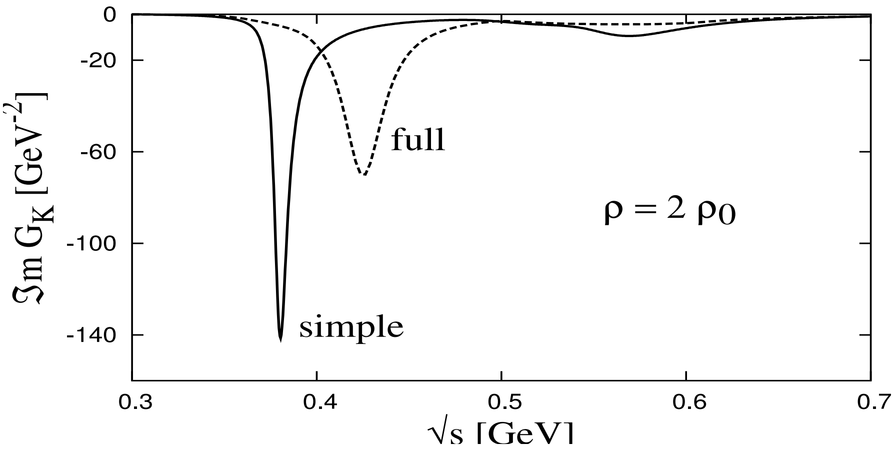

Figure 4.20: *Imaginary part of* $G_{\bar{K}}$*, constant couplings (solid line) and full couplings (dotted line)*

Obviously there is a significant influence of the choice of the couplings and the corresponding subtraction parameters. Leaving out some channels or neglecting the Σ terms will lead to a kaon with an exaggerated broadening and a shift towards lower energies that is too strong. Since the inclusion of all possible couplings of comparable strengths and of the energy–dependence is surely an improvement over constant threshold couplings, the differences becoming apparent in the figures above certainly constitute an improvement of the model.

4.4 Medium

The loop function $J_{\bar{K}N}$,

$$J_{\bar{K}N}(q) = -i \int \frac{d^4l}{(2\pi)^4}\, G_N(l)\, G_{\bar{K}}(q-l)$$

can now be calculated in a medium of finite density (vanishing temperature).

Using the nucleon propagator as in eq.(4.10), the medium is characterized by the value of the Fermi momentum p_f. The saturation density $\rho_0 = 0.16$ fm^3 of normal nuclear matter is reached at a Fermi momentum of $p_f = 263$ MeV. This is approximately the density in the center of a large nucleus, e.g. lead. Nuclear densities therefore range from zero at the surface of the nucleus up to this value. Similarly, density and pressure vanish at the surface of a neutron star, but the density will increase towards the core of the star to reach up to $10\,\rho_0$. A simple estimate shows that at such densities one leaves the known hadronic world: The rms radius of the nucleon is $\sqrt{<r^2>} \approx 0.8$ fm. The mean distance between two nucleons will be $d \sim \frac{1}{\rho^{1/3}}$. While this indicates a rather dilute system at ρ_0 ($d \approx 1.8$fm), at $10\rho_0$ the nucleons start to overlap. We shall want to stay clear of the troublesome region of the deconfinement phase transition at finite density, studying effects that take place in a neutron star where it still consists of normal matter. Therefore the maximum density used here is $\rho = 5\rho_0$ (although some models find a phase transition even at these 'moderate' densities [62]).

The in–medium calculation is initialized by a finite value for the Fermi momentum p_f in eq.(4.10), the expression for the nucleon propagator. Using the Lehmann representation of the propagators, the loop integral can be written as

$$\begin{aligned} J_{\bar{K}N}(q) = \int \frac{d^3l}{(2\pi)^3} (\frac{-i}{2\pi^3}) \int_0^\infty d\omega_1 \int_0^\infty d\omega_2 \int_{-\infty}^\infty dl^0 \left(\frac{\Im m G_{\bar{K}}(\omega_2, \vec{q}-\vec{l})}{q^0 - l^0 - \omega_2 + i\varepsilon} - \frac{\Im m G_{\bar{K}}(-\omega_2, \vec{q}-\vec{l})}{q^0 - l^0 + \omega_2 - i\varepsilon} \right) \\ \cdot \left(\frac{\Im m G_N^{(p)}(\omega_1, \vec{l})}{l^0 - \omega_1 + i\varepsilon} - \frac{\Im m G_N^{(h)}(\omega_1, \vec{l})}{l^0 - \omega_1 - i\varepsilon} - \frac{\Im m G_N^{a}(-\omega_1, \vec{l})}{l^0 + \omega_1 - i\varepsilon} \right) . \end{aligned} \tag{4.29}$$

In appendix A it is shown how to reduce this expression further. The result for the imaginary part is

$$\Im m J_{\bar{K}N}(q^0, \vec{q}) = -\frac{m_N}{4\pi^2} \int_{p_f}^{\sqrt{q^{0\,2} - m_N^2}} d|\vec{l}|\, \frac{\vec{l}^2}{\omega_N(\vec{l})} \int_{-1}^{1} dx_l\, \Im m G_{\bar{K}}(q^0 - \omega_N(\vec{l}), \vec{q} - \vec{l})\, \Theta(q^0 - E_f)\ . \tag{4.30}$$

Evaluation of this expression results in the so–called Pauli–blocking: The integral has a new lower limit of p_f. Nucleon states with momenta below p_f are not accessible for the scattering, they are blocked due to the Pauli principle. This is the difference to the vacuum result, and it shows clearly in the following figure.

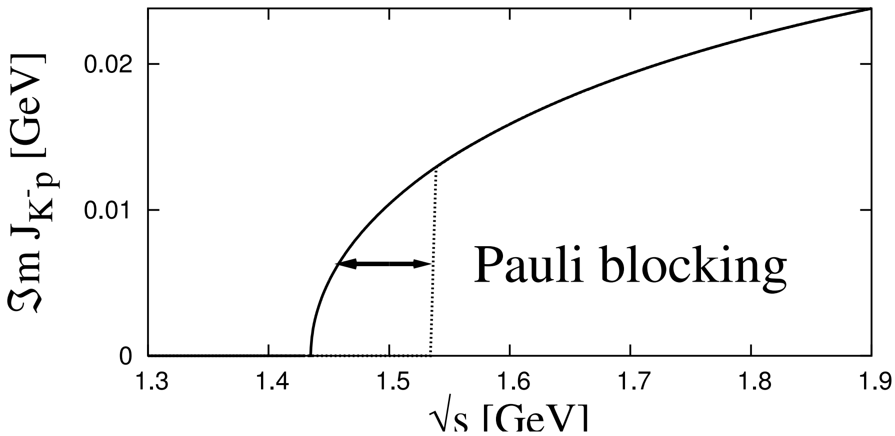

Figure 4.21: *Pauli–blocking manifest in* $\Im m J_{K^-p}$. *Solid line: vacuum result, dotted line:* $\Im m J_{K^-p}$ *at density* $\rho = \rho_0$

Pauli–blocking has considerable influence on the $\Lambda(1405)$. This becomes evident in the following figure (fig. 4.22):

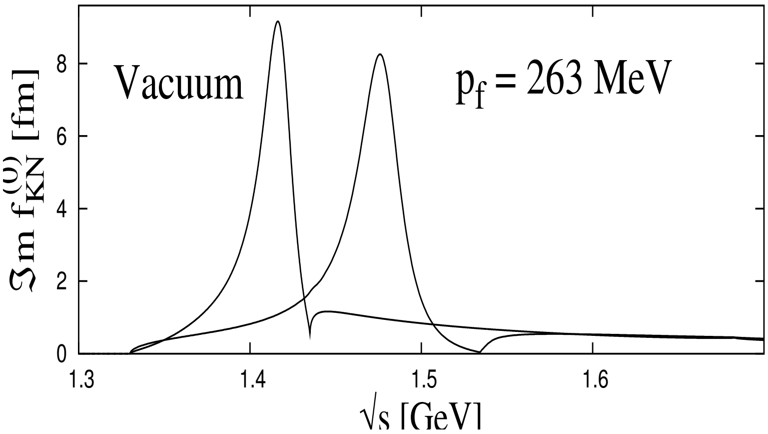

Figure 4.22: *Pauli–blocking effect on* $\Im m f_{\bar{K}N}$. *The left curve again shows the vacuum result (*$\Lambda(1405)$*), the curve that is shifted to the right displays* $\Im m f_{\bar{K}N}$ *at density* $\rho = \rho_0$

The form of $\Im m f_{\bar{K}N}$ in fig. 4.22 is not effected strongly by Pauli–blocking – the in–medium curve (to the right) is still recognizable as the $\Lambda(1405)$ resonance. But its position is shifted upwards in energy by an considerable amount ($\sim$ 80 MeV at normal nuclear matter density ρ_0 in fig. 4.22).

It is also instructive to have a look on the momentum dependence of the T–matrix. The vacuum amplitude is of course Lorentz–invariant. This has been assured by our way of regularizing the loop integral, using subtracted dispersion relations instead of a cut–off. But the in–medium amplitude is covariant. What we look at is actually the T–matrix in the rest frame of the medium – corresponding to the laboratory system in an experiment with the target at rest.

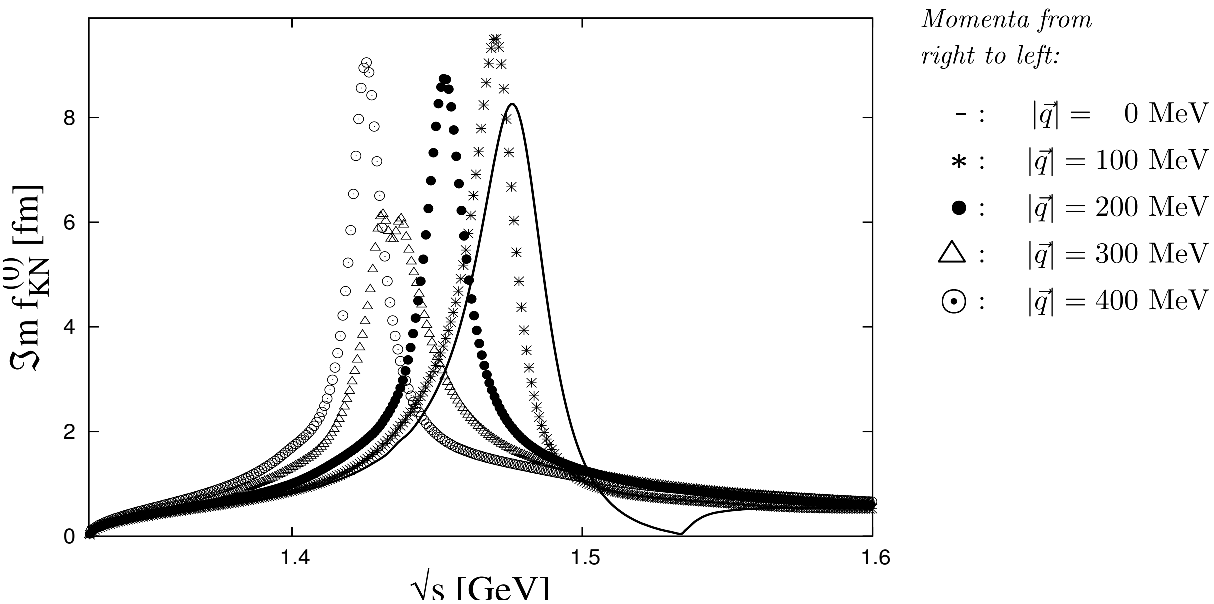

Figure 4.23: $\Im m f_{\bar{K}N}$, $\rho = \rho_0$ *for different momenta* $|\vec{q}|$

Fig. 4.23 shows the in–medium scattering amplitude for different momenta. The amplitude gets pushed downwards with increasing momentum. It is also broadened, but at 400 MeV it already starts narrowing again. This means that the influence of the medium becomes less important with increasing momentum. The expression eq. (4.30) approaches the vacuum result in that limit. This is also illustrated by fig. 4.24:

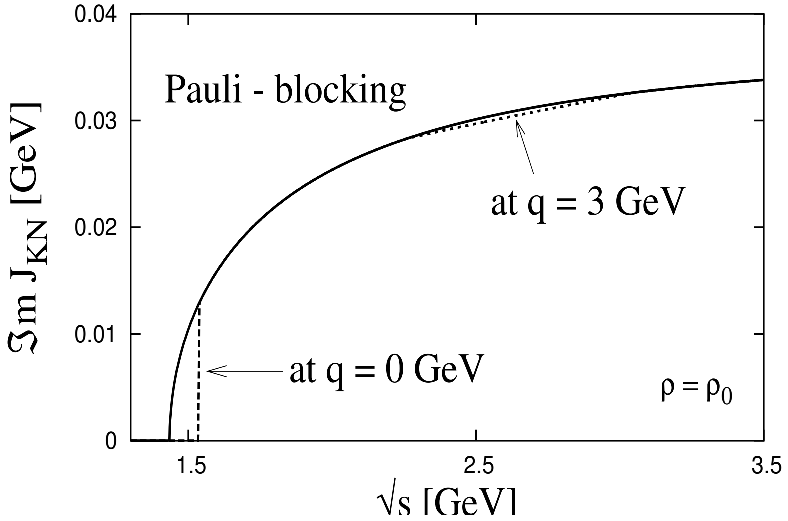

Figure 4.24: *Effect of Pauli–blocking on* $\Im m J_{\bar{K}N}$ *at momenta* $|\vec{q}| = 0 GeV$ *and* $|\vec{q}| = 3\ GeV$ *(density* $\rho = \rho_0$*)*

At very large momenta, the effect of Pauli–blocking is reduced to cutting off only a tiny ‘strip’ of $\Im m J_{\bar{K}N}$.

Consequently, in this limit the vacuum behavior of the scattering amplitude is regained to some extent: The following figure (fig. 4.25) shows the amplitude at $q = 800$ MeV, $q = 1.6$ GeV and $q = 3$ GeV, in addition at $q = 0$ MeV for reference.

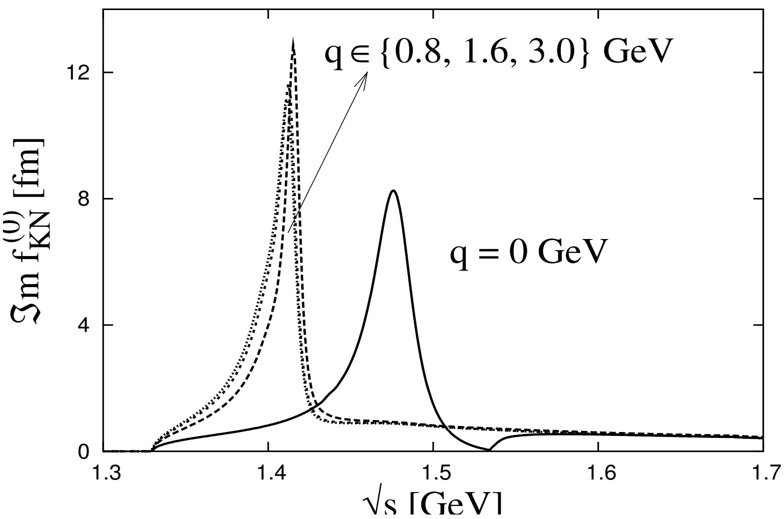

Figure 4.25: $\Im m f_{\bar{K}N}$, *at high momenta* $|\vec{q}|$ *(density* $\rho = \rho_0$*)*

The high momenta curves lie basically on top of each other, at the position where the vacuum amplitude is situated ($\Lambda(1405)$). Their shapes also closely follow the vacuum result, just the dip at the $\bar{K}N$ threshold gets washed out by the finite momentum.

Chapter 5

Pions in matter

5.1 Isospin symmetric matter

In the previous chapter, the formalism of calculating the $\bar{K}N$ scattering in dense matter was introduced and some results for the scattering amplitude were shown.
These calculations take into account the effect of finite density only via the Pauli–blocking of the nucleons involved. However, it has become clear that one of the key ingredients of our model is the coupling of $\bar{K}N$ to the channels involving a pion. Yet a pion will undergo considerable modifications when placed in dense matter. One should therefore include such modifications in the model. We will follow the description of the pion as given in [58].
The main sources of the pion selfenergy are particle–hole and delta ($\Delta(1232)$)–hole excitations. To calculate these contributions the interaction of the pion with nucleons and deltas [63] are needed. Just as in the $SU(3)$ case of sec.(3.2), the πN Lagrangian can be constructed from the chiral building blocks, $\mathcal{D}_\mu$ (eq.(3.9)), $u_\mu = iu^\dagger \partial_\mu U u^\dagger$ and $\mathcal{L}_{\Phi\Phi}$ as in eq.(3.5) (see [35]):

$$\begin{aligned} \mathcal{L}_{(\pi,N)} &= \mathcal{L}_{\Phi\Phi} \;-\; \bar{B}\,\mathcal{D}\,B \\ &= \frac{1}{4}\, f_\pi^2 \,\left(tr[\partial_\mu U\, \partial_\mu U^\dagger + \chi^\dagger U + \chi U^\dagger] \right) \;+\; \bar{B}\,(i\gamma^\mu \mathcal{D}_\mu - \mathring{m} + \frac{g_A}{2}\gamma^\mu \gamma_5 u_\mu)\,B \end{aligned}$$

The dominant interaction is given by the last term, the axial part. We keep only pions and nucleons in the field matrices B and Φ (eq.(3.8), eq.(3.2)). Then B reduces to a two–component iso–spinor, while Φ can be substituted by

$$\Phi \rightarrow \vec{\tau}\cdot\vec{\phi}, \qquad \vec{\phi} = (\pi_1, \pi_2, \pi_3),$$

Applying the Goldberger–Treiman relation, $g_A \mathring{m} = g_{\pi N} f_\pi$, and expanding (cf. subsec. (3.4.3)) $u_\mu = iu^\dagger \partial_\mu U u^\dagger \approx -\frac{2}{f_\pi}\partial_\mu \Phi$ leads to

$$\mathcal{L}_{\pi N} \;=\; -\,\frac{g_{\pi N}}{2\mathring{m}}\;\bar{\psi}\,\gamma^\mu\,\gamma_5\,\vec{\tau}\cdot\partial_\mu\,\vec{\phi}\;\psi \;\;=\;\; \frac{f_N}{m_\pi}\;\bar{\psi}\,\gamma^5\,\gamma^\mu\;\vec{\tau}\,\psi\;\cdot\;\partial_\mu\,\vec{\phi}, \tag{5.1}$$

using $g_{\pi N}/m_N = f_N/m_\pi$ with the usual pseudovector πN coupling constant $f_N = 1.01$.

The coupling to the Δ looks quite similar:

$$\mathcal{L}_{\pi N\Delta} = -\frac{f_\Delta}{m_\pi}\bar{\psi}\vec{T}^\dagger\psi_\mu\cdot\partial^\mu\vec{\phi} \quad + \quad \text{h. c.}, \tag{5.2}$$

with the spinor ψ_μ for the (spin–3/2) Δ and the isospin transition operator $\vec{T}$ (see eq. (5.3) below).

The following nonrelativistic vertices can be derived from these interactions ([58], appendices A, B therein):

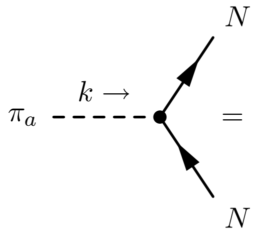

$$= \frac{f_N}{m_\pi}\,\vec{k}\cdot\vec{\sigma}\tau_a.$$

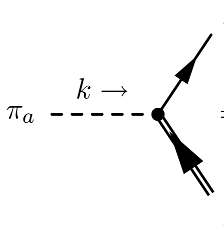

$$= \frac{f_\Delta}{m_\pi}\,\vec{k}\cdot\vec{S}^\dagger\,T_a^\dagger.$$

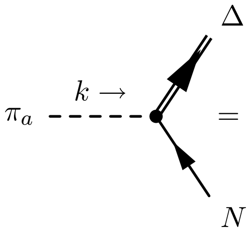

$$= \frac{f_\Delta}{m_\pi}\,\vec{k}\cdot\vec{S}\,T_a.$$

The latter two vertices contain the spin and isospin transition operators $\vec{S}$ and $\vec{T}$, since the Δ, being a spin/isospin–3/2 particle, here couples to the spin/isospin–1/2 nucleons. This coupling gives the definition of the transition operator:

$$\vec{S} = \sum_{m_j,m_l,m_s} \left(1, m_l; \frac{1}{2}, m_s \middle| \frac{3}{2}, m_j\right) \chi^{(\frac{3}{2})}(m_j)\chi^\dagger(m_s)\vec{e}^{\,*}(m_l) \tag{5.3}$$

Here $\chi(m_s)$ is the two–component spinor of the nucleon, $\chi^{(\frac{3}{2})}(m_j)$ the four–component spinor of the Δ. The basis vectors $\vec{e}(m_l)$ read

$$\vec{e}(+1) = \frac{1}{\sqrt{2}}\begin{pmatrix} -1 \\ -i \\ 0 \end{pmatrix}, \quad \vec{e}(-1) = \frac{1}{\sqrt{2}}\begin{pmatrix} 1 \\ -i \\ 0 \end{pmatrix}, \quad \vec{e}(0) = \begin{pmatrix} 0 \\ 0 \\ 1 \end{pmatrix}. \tag{5.4}$$

They are also useful to describe an isospin–1 field as the pion.
The nucleon propagator was given in eq.(4.10) (with the antinucleon part dropped).

The Δ is not stable but decays into nucleon and pion with a width of $\Gamma_\Delta \approx 120$ MeV. Here this fact is taken into account by adding a constant imaginary part to the Δ propagator:

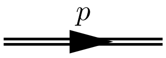

$$= iG_\Delta(p) = i\,\frac{1}{p^0 - \omega_\Delta(\vec{p}) + \frac{i}{2}\Gamma_\Delta}. \tag{5.5}$$

Using these building blocks, the following selfenergy contributions to the pion can be constructed.

Nucleon–hole:

$$-i(\Sigma_{Nh})_{ab}(k) =$$

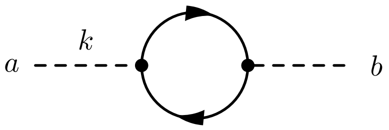

$$\begin{aligned} &= \int \frac{d^4p}{(2\pi)^4}\,(-)\mathrm{tr}\Big(\Big(\frac{f_N}{m_\pi}\,\vec{k}\cdot\vec{\sigma}\tau_a\Big) iG_N(p) \Big(\frac{f_N}{m_\pi}\,(-\vec{k})\cdot\vec{\sigma}\tau_b\Big) iG_N(p+k)\Big) \\ &= -i\vec{k}^2\delta_{ab}\Pi_{Nh}(k), \end{aligned}$$

with the Lindhard function

$$\Pi_{Nh}(k) = -i\,4\Big(\frac{f_N}{m_\pi}\Big)^2 \int \frac{d^4p}{(2\pi)^4}\, G_N(p)G_N(p+k). \tag{5.6}$$

Δ–hole:

$-i(\Sigma_{\Delta h})_{ab}(k) =$

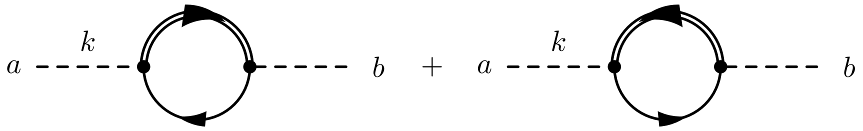

$$\begin{aligned}
&= \int \frac{d^4p}{(2\pi)^4}\,(-)\mathrm{Sp}\Big(\Big(\frac{f_\Delta}{m_\pi}\vec{k}\cdot\vec{S}T_a\Big)iG_N(p)\Big(\frac{f_\Delta}{m_\pi}(-\vec{k})\cdot\vec{S}^\dagger T_b^\dagger\Big)iG_\Delta(p+k)\Big)\\
&+\Big(k, a \longleftrightarrow -k, b\Big)\\
&= -i\vec{k}^2\delta_{ab}\Pi_{\Delta h}(k),
\end{aligned}$$

with

$$\Pi_{\Delta h}(k) = -i\,\frac{16}{9}\Big(\frac{f_\Delta}{m_\pi}\Big)^2 \int \frac{d^4p}{(2\pi)^4}\, G_N(p)\Big(G_\Delta(p+k) + G_\Delta(p-k)\Big). \tag{5.7}$$

If particle–hole and Δ–hole contributions are just added to get the pion selfenergy, results can become unphysical [64]. Among other undesirable features, pion condensation can occur at moderate densities around ρ_0 which is not seen in experiment. The reason is that so far we have neglected of any nucleon–nucleon interaction (except for pion exchange). Yet this interaction has a strong repulsive short–range part. This feature can be accommodated by the following graphs:

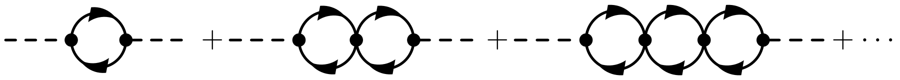

The 4–point vertices are parameterized by the renowned Migdal parameters,
g'_{11} for the nucleon case :

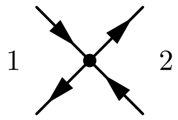

$$= -ig'_{11}\Big(\frac{f_N}{m_\pi}\Big)^2 \vec{\sigma}_1\cdot\vec{\sigma}_2\vec{\tau}_1\cdot\vec{\tau}_2,$$

and similar vertices for the $N\Delta$ and $\Delta\Delta$ interaction with Migdal parameters g'_{12} and g'_{22}. Summing up all diagrams one finally gets the polarization function of the pion

$$\Pi = \frac{\Pi_{Nh} + \Pi_{\Delta h} - (g'_{11} - 2g'_{12} + g'_{22})\Pi_{Nh}\Pi_{\Delta h}}{1 - g'_{11}\Pi_{Nh} - g'_{22}\Pi_{\Delta h} + (g'_{11}g'_{22} - g'^2_{12})\Pi_{Nh}\Pi_{\Delta h}}. \tag{5.8}$$

There is yet another effect to be taken into account. Pion, nucleon and Δ are not elementary particles. They have a finite size, reducing the strength of their interaction at high momenta. To allow for this feature, a form factor at the πNN and $\pi N\Delta$ vertices is introduced. The form chosen by Urban et.al. [58, 65, 66]) is

$$\Gamma_\pi(\vec{k}) = \frac{\Lambda^2}{\Lambda^2 + \vec{k}^2} \qquad \Lambda = 550\text{MeV}\ . \tag{5.9}$$

The pion selfenergy then reads

$$\Sigma'_{ab}(k) = \vec{k}^2\delta_{ab}\Pi'(k) = \vec{k}^2\delta_{ab}\Gamma_\pi^2(\vec{k})\Pi(k). \tag{5.10}$$

The influence of the particle–hole and Δ–hole excitation on the pion are strongest around a 3–momentum of $|\vec{k}| \sim 300$ MeV. The respective contributions are shown in fig. 5.1 below.

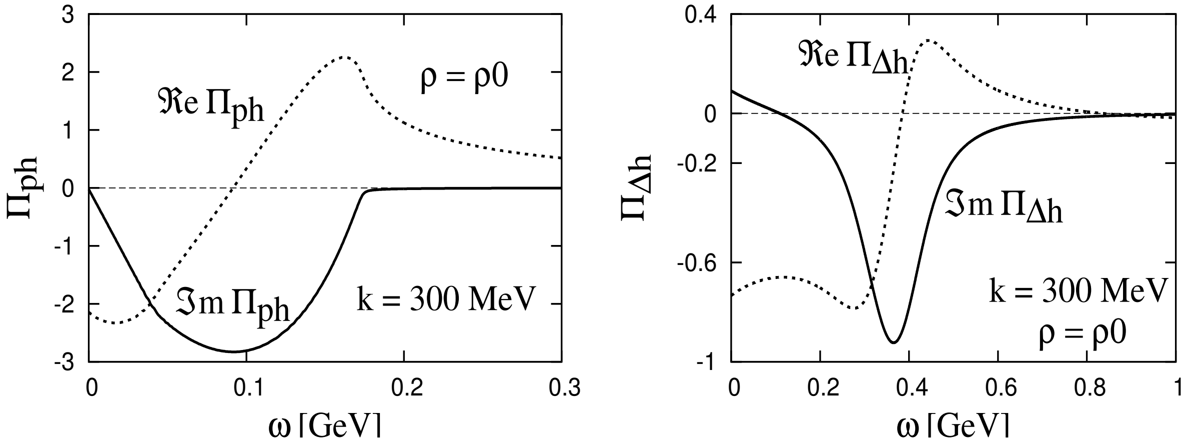

Figure 5.1: *Pion polarization functions. Left panel: particle–hole excitation, right panel: Δ–hole excitation, at $\rho = \rho_0$ and $|\vec{k}| = 300 MeV$*

The pion propagator is seen to split into several branches, as is displayed in the following figure (fig 5.2):

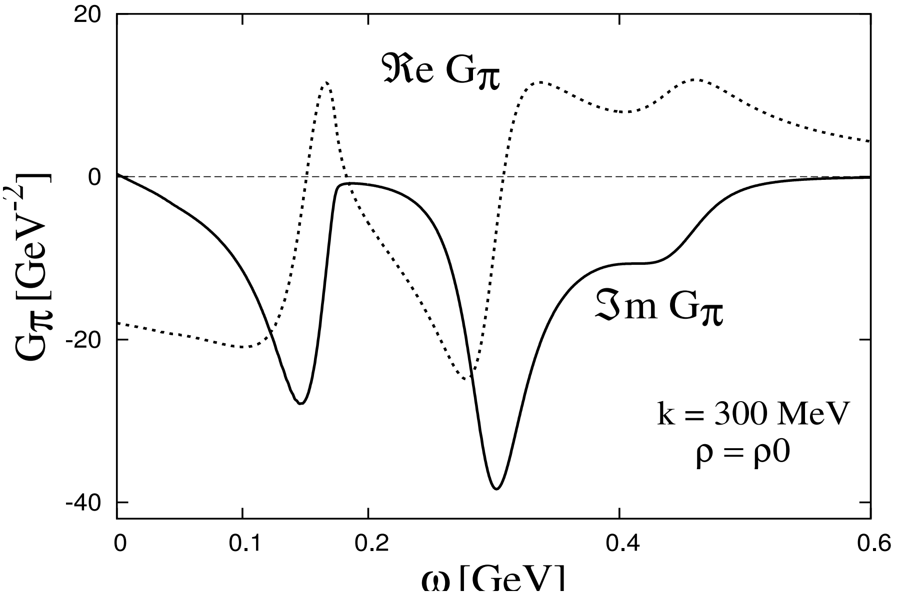

Figure 5.2: *Pion propagator at $\rho = \rho_0$ and $|\vec{k}| = 300 MeV$*

The three maxima at $\omega \approx 100$ MeV, $\omega \approx 250$ MeV and $\omega \approx 420$ MeV can be understood as quasiparticle excitations: The dispersion relation for the excitation stemming from *nucleon*–hole is proportional to $|\vec{k}|$ at low momenta, hence the branch peaking at $\omega \approx 100$ MeV starts at zero. The two upper branches consist of the pion itself that has now a dispersion relation different from the vacuum one, and the Δ–hole excitation whose dispersion starts at finite energy due to the mass gap between Δ and nucleon.

5.2 Loop function with dressed pions

Having developed a description of the pion in dense matter, this pion propagator is now to be put into the loops with the Λ and Σ baryons. These loops are then coupled to the other meson–baryon channels to obtain the T–matrix element. This also means that we do not further modify the pion: we do not aim for selfconsistency in the case of the pion. Of course the model as employed by Urban et.al. [58, 67] is already designed to give a realistic result as it stands, without further iteration.

There is another point to observe here. In the model of [67], the actual calculation is carried out using the finite temperature Matsubara formalism. To obtain results for vanishing temperature, the limit $T \to 0$ is taken in the end. This procedure greatly facilitates the numerical handling of the model. An example will be presented in the section on pions in isospin–asymmetric matter, sec. 8.2, and in appendix D. However, the Matsubara formalism uses retarded propagators whereas the formalism developed in chap. 4 relies on time–ordered functions. This issue will be examined in further detail in appendix D.1. It is found that although in general the two procedures lead to different results (for the loop function), the interesting part at positive energies is the same, so this apparent inconsistency does not pose a problem for our calculation.

Typically, the effect of the broadening of the pion in dense matter will show up in the loop function as a bump around threshold. As an example, fig. 5.3 displays the imaginary part of the $\pi\Sigma$ channel at normal nuclear matter density and vanishing 3–momentum.

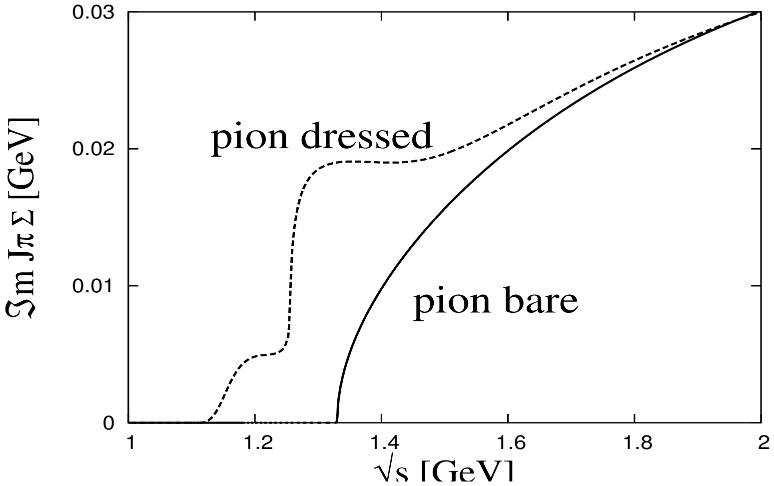

Figure 5.3: $\Im m J_{\pi\Sigma}$ *with dressed (dashed line) and bare (solid line) pion propagators*

The effect is considerable and as it shows up right in the interesting energy range around threshold, the inclusion of the pion broadening is certainly necessary.

On the other hand, considerable numerical effort is required. As for all loop functions, the entire energy–momentum plane has to be mapped out. While the figures in section 5.1 suggest a considerable broadening of the pion in the medium, the pion propagator at energies and momenta away from the Δ–hole excitation is a very narrow object. Hence the integrations involved prove to be very time–consuming.

5.3 Kaon propagators under the influence of dressed pions

At this stage, we can compare various combinations of couplings and pion selfenergies. Fig. 5.4 shows them all together.

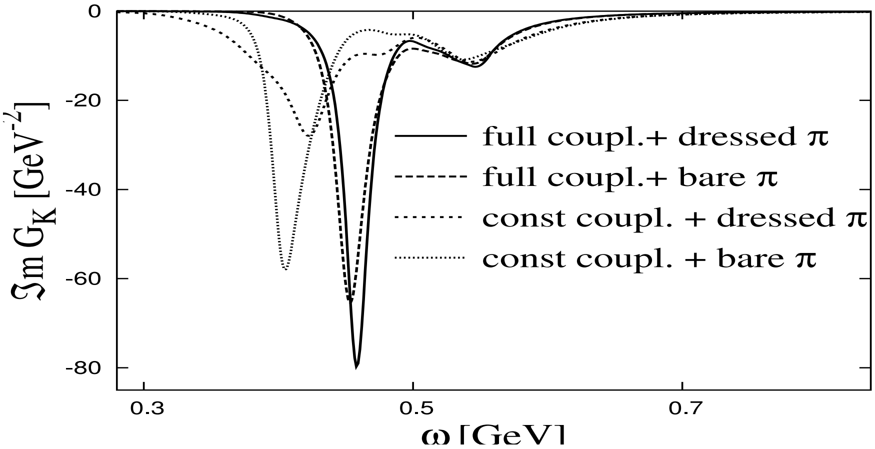

Figure 5.4: $\Im m G_{\bar{K}}$, *with dressed/bare* G_π *and constant/full couplings*

These four curves all represent the kaon propagator at normal nuclear matter density and a 3–momentum of $|\vec{k}| = 100$ MeV, after one iteration. The differences among them are quite large. One effect is caused by the form of the couplings used to tie the channels together. The full, energy dependent form that includes the Σ–terms (eqs. (3.1)–(3.5)) leads to a significantly smaller downward shift of the kaon peak. But the choice of the full form also softens the impact of the broadened pion propagator. This becomes evident if the curves of the previous figure are shown separately. Thus fig. 5.5 displays the effect the dressing of the pion has on $\Im m G_{\bar{K}}$ if the constant couplings of eq. (2.1) are used. This effect is quite pronounced.

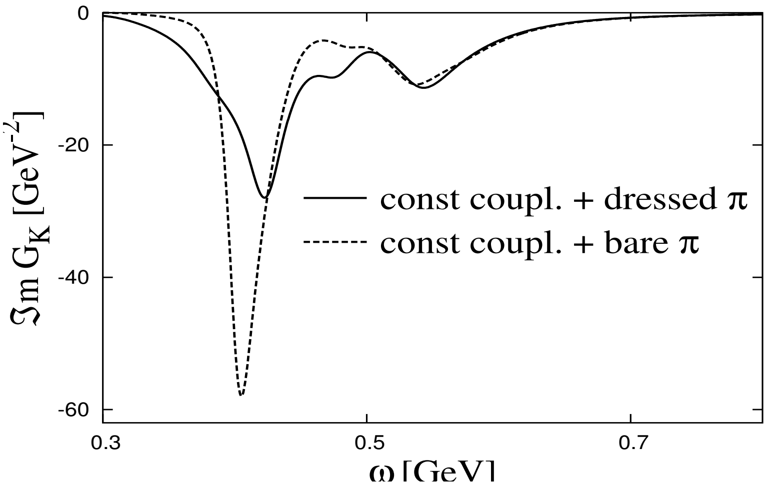

Figure 5.5: $\Im m G_{\bar{K}}$, *with dressed/bare* G_π *and constant/full couplings*

On the other hand, fig. 5.6 indicates the difference in $\Im m G_{\bar{K}}$ that results from using the bare or the dressed pion propagator as input, if the channels are coupled by the vertices of eqs. (3.1)–(3.5). The impact of pion dressing is then reduced considerably.

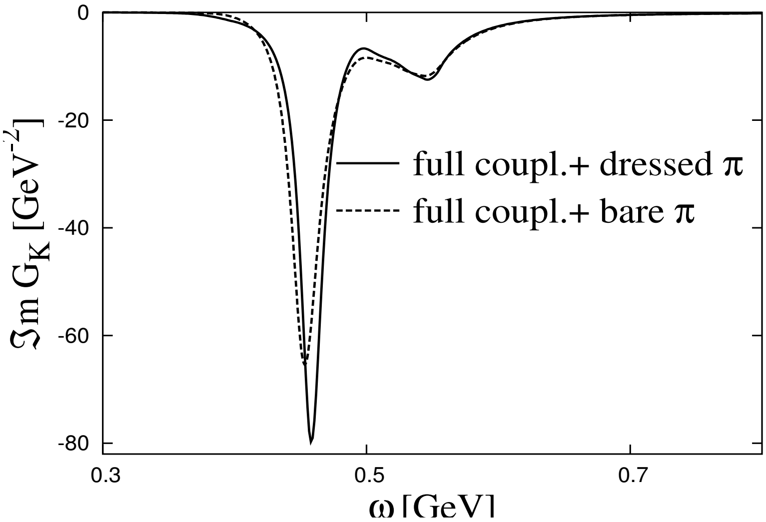

Figure 5.6: $\Im m G_{\bar{K}}$, *with dressed/bare* G_π *and constant/full couplings*

Chapter 6

Kaon selfenergy

6.1 $\Im m\Sigma_{\bar{K}}$

The step from the $\bar{K}N$ T–matrix to the kaon selfenergy has been mentioned several times already. It can be graphically represented as follows:

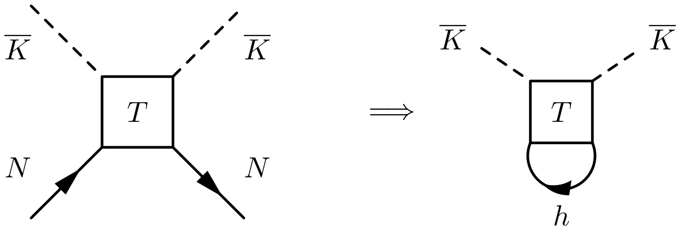

Figure 6.1: *Calculate* $\Sigma_{\bar{K}}$ *from* $T_{\bar{K}N}$

Closing the nucleon leg of the scattering diagram (left of fig.6.1) to arrive at the selfenergy diagram (right of fig.6.1) means integrating the T–matrix element with the nucleon (hole) propagator:

$$\Sigma_{\bar{K}}(k) = -i \int \frac{d^4p}{(2\pi)^4}\, G_N(p)\, T(p+k)$$

Appendix B explains in detail how to proceed with this integral. The result reads

$$\Im m\Sigma_{\bar{K}}(k) = \frac{m_N}{4\pi^2} \int_0^{p_f} d|\vec{p}|\, \frac{\vec{p}^2}{\omega_N(\vec{p})} \int_{-1}^{1} dx_l\, \Im m T_{\bar{K}N}(k^0 + \omega_N(\vec{p}), \vec{p} + \vec{k})\ . \tag{6.1}$$

In the literature (e.g. [29], eq.(15) or [30], eq.(5.13); [33]) at this stage one often finds an isospin–summed T–matrix put into the diagrams above: $4\overline{T} = T^{(0)} + 3T^{(1)}$. Adding isospin m–quantum numbers, this can be rewritten as

$$4\overline{T} = T^{(0,0)} + 3T^{(1,0)} = T^{(0,0)} + T^{(1,0)} + T^{(1,1)} + T^{(1,-1)}\ .$$

Using the particle basis, these terms read

$$\begin{aligned}
T^{(0,0)} &= \frac{1}{2}T(pK^- \to pK^-) + \frac{1}{2}T(n\bar{K}^0 \to n\bar{K}^0) + T(pK^- \to n\bar{K}^0) \\
T^{(1,0)} &= \frac{1}{2}T(pK^- \to pK^-) + \frac{1}{2}T(n\bar{K}^0 \to n\bar{K}^0) - T(pK^- \to n\bar{K}^0) \\
T^{(1,1)} &= T(p\bar{K}^0 \to p\bar{K}^0) \\
T^{(1,-1)} &= T(nK^- \to nK^-)
\end{aligned}$$

$$\Rightarrow 4\overline{T} = T(pK^- \to pK^-) + T(n\bar{K}^0 \to n\bar{K}^0) + T(p\bar{K}^0 \to p\bar{K}^0) + T(nK^- \to nK^-)\ .$$

Now the question arises, what is meant by $\bar{K}$ in the diagram above ? Usually the symbol is used to label the antikaon isospin doublet as a whole or a generic member of that doublet. Here the interactions are not formulated in terms of isospin doublets but single particles, hence the $\bar{K}$–symbol means either a K^- or a $\bar{K}^0$.

However, if a K^- enters the medium, causing T–matrix–hole excitations, of the sum above only the two terms with the K^- should play a role[1]. If we refer to a calculation of isospin–symmetric matter, the propagators for proton–hole and neutron–hole are identical. In addition we have

$$\begin{aligned}
& T(pK^- \to pK^-) = T(n\bar{K}^0 \to n\bar{K}^0) \qquad T(p\bar{K}^0 \to p\bar{K}^0) = T(nK^- \to nK^-) \\
\Longrightarrow \quad & 4\overline{T} \ = \ 2T(pK^- \to pK^-) + 2T(nK^- \to nK^-)
\end{aligned} \tag{6.2}$$

The K^-–selfenergy has the form

$$\begin{aligned}
\Sigma_{K^-} &= -i \int G_N \ \left[T(pK^- \to pK^-) \,+\, T(nK^- \to nK^-)\right] \\
&\neq -i \int G_N \, \frac{1}{4} \ \left[\,4\overline{T}\,\right]
\end{aligned}$$

While in the case of isospin–symmetric matter one has merely to insert an appropriate factor 2, in the case of isospin–asymmetric nuclear matter it is simply wrong to add $T(pK^- \to pK^-)$ and $T(n\bar{K}^0 \to n\bar{K}^0)$ like that. The label h in the selfenergy diagram can be a proton – or a neutron hole, but in the latter case these have different Fermi momenta. Then the selfenergy integrals differ in their upper integration limit, making it impossible to do the incorrect summing to $4\overline{T}$.

Our result eq. (6.1) is derived with $\Im m T_{\bar{K}N}$ containing only the proper two channels for each antikaon. $\Im m \Sigma_{\bar{K}}$ will typically look as in fig. 6.2, which was evaluated at normal nuclear matter density for a kaon with 3–momentum $|\vec{k}| = 100$ MeV.

---

[1] There is an influence of the $\bar{K}^0$ also in the K^- selfenergy, but only due to the loops hidden inside $T(pK^- \to pK^-)$ and $T(nK^- \to nK^-)$.

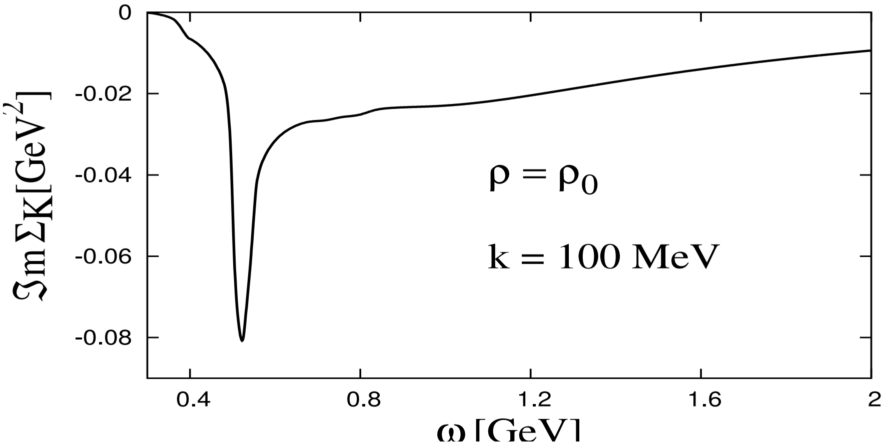

Figure 6.2: $\Im m\Sigma(\omega, \vec{k} = 100 MeV)$ *at* $\rho = \rho_0$

As we have seen in the discussion of the real part of $J_{\bar{K}N}$ in subsec. 4.2.3, $\Im m\Sigma_{\bar{K}}$ as well as $\Im m T_{\bar{K}}$ have to be known over a quite large range of energy and momentum. The connection between the two quantities suggests a trick for high energies: instead of calculating $\Im m\Sigma_{\bar{K}}$ for extremely large energies, evaluate eq. (6.1) assuming that $\Im m T_{\bar{K}}$ does not depend on the integration variables:

$$\begin{aligned}\Im m\Sigma_{\bar{K}}(k^0, \vec{k}) &\approx \frac{m_N}{4\pi^2}\,\Im m T(\hat{\omega}, \vec{k}) \int_0^{p_f} d|\vec{p}|\,\frac{\vec{p}^2}{\omega_N(\vec{p})}\int_{-1}^{1} dx_l \\ &= \frac{m_N}{4\pi^2}\left(p_f\,\omega_N(p_f) - m_N^2\,\ln\frac{p_f + \omega_N(p_F)}{m_N}\right)\Im m T_{\bar{K}N}(\hat{\omega}, \vec{k}) \qquad (6.3)\end{aligned}$$

The value of $\hat{\omega}$ can be chosen such that the curves in fig. 6.3 overlap nicely. That is the case for $\hat{\omega} = k^0 + (m_N + E_f)/2$ ($E_f = \omega_N(p_f) = \sqrt{p_f^2 + m_N^2}$).

Fig. 6.3 shows how well this works: the difference between the two curves becomes visible only below 1 GeV.

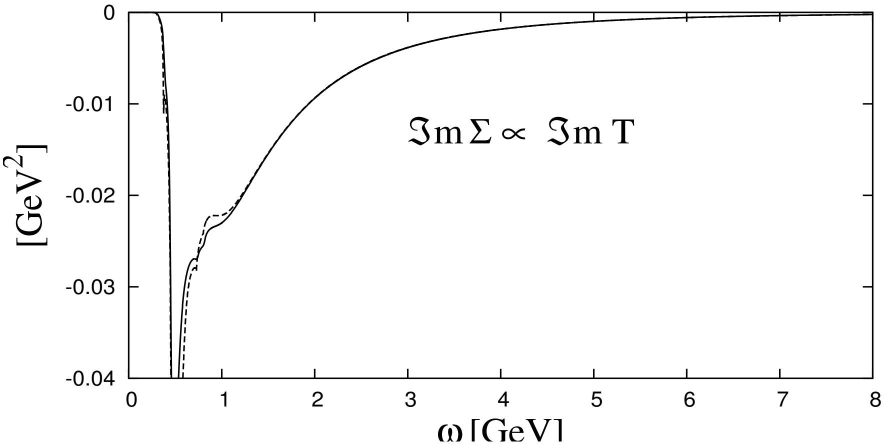

Figure 6.3: $\Im m\Sigma$ *(dashed line) can be replaced by* $\Im m T$ *(solid line) for large energies* ($\rho = \rho_0$, $|\vec{k}| = 100\ MeV$)

One has to make sure that this trick works for different 3–momenta. But as it does, it saves a lot of computing time.

6.2 $\Re e \Sigma_{\bar{K}}$

The real part of the kaon selfenergy does not pose a problem any more after all the preparations of the prior chapters. There is one more point to check: The kaon selfenergy is not a symmetric function in energy. Instead the relation $\Sigma_K(-k^0) = \Sigma_{\bar{K}}(k^0)$ holds. The dispersion relations we have employed in chapter 4 are written for symmetric functions (although there we neglected the part for negative energies). Appendix C shows how to apply dispersion relations to asymmetric functions as well.

The expression is then simply

$$\Re e \Sigma_K(k^0, \vec{k}) = \frac{1}{\pi} \int_0^\infty d\tilde{\omega} \, \frac{\Im m \Sigma_K(\tilde{\omega}, \vec{k})}{\tilde{\omega} - k^0} \, .$$

The typical $\Re e \Sigma_{\bar{K}}$ will look as in fig. 6.4.

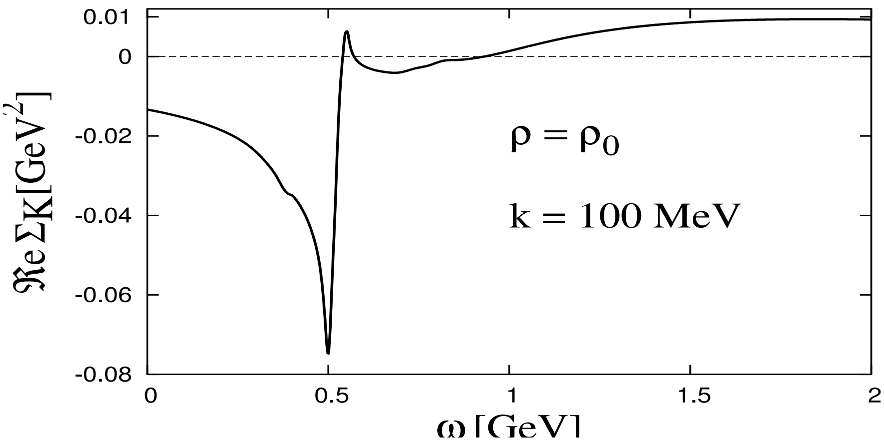

Figure 6.4: $\Re e \Sigma(\omega, \vec{k} = 100 MeV)$ *at* $\rho = \rho_0$

Kaon propagator

Putting the ingredients together, the kaon propagator as shown in fig. 6.5 is obtained. The figure displays the typical properties of the kaon when it is modified by the scattering processes described in this work. The peak of the spectral function (the imaginary part of $G_{\bar{K}}$) is shifted to lower energies compared with its vacuum position at $m_K = 495$ MeV. But this mass shift is not dramatic. A much stronger effect is the broadening. Taking the full width at half maximum in fig. 6.5, the kaon is “spread”over roughly ~ 130 MeV.

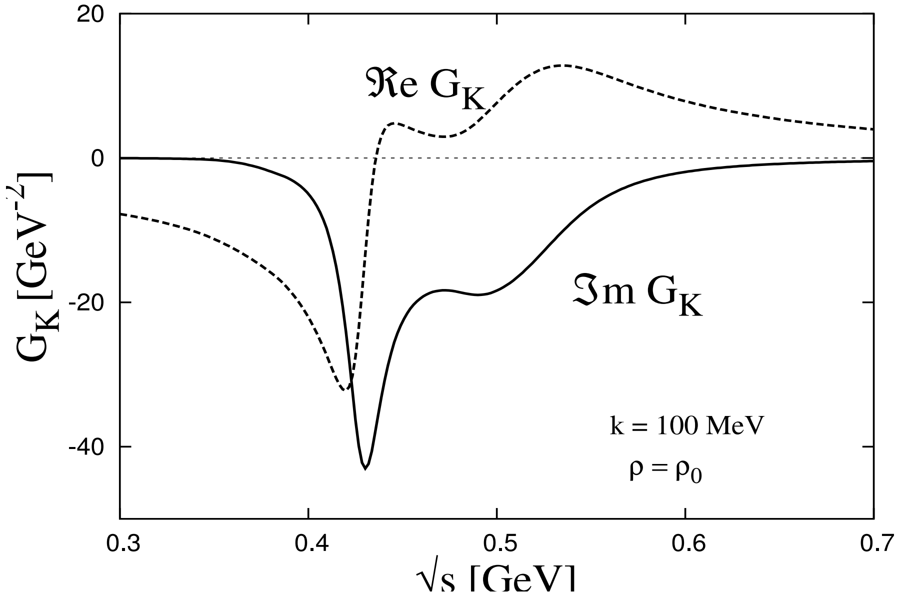

Figure 6.5: *Kaon propagator at* $|\vec{k}| = 100MeV, \rho = \rho_0$. *Solid line: imaginary part, dashed line: real part*

6.3 p–wave kaon selfenergy

In subsection (3.4.3) an additional class of interactions was introduced that has been neglected so far. The p–wave vertices of eqs. (3.20) will lead to K^- selfenergy contributions $-i\,\Sigma_{K^-}$ from Λ and Σ of the form

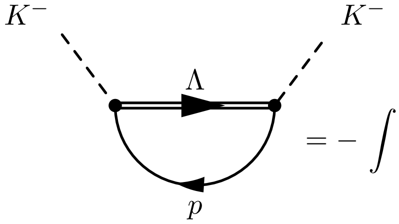

$$= -\int \frac{d^4p}{(2\pi)^4}\, tr\left\{\frac{1}{2f_\pi}\,\vec{k}\vec{\sigma}\,\frac{3F+D}{\sqrt{3}}\,iG_\Lambda(p+k)\,\frac{1}{2f_\pi}\,(-\vec{k}\vec{\sigma})\,\frac{3F+D}{\sqrt{3}}\,iG_p(p)\right\}$$

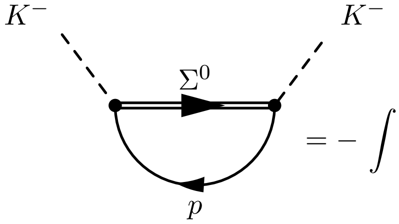

$$= -\int \frac{d^4p}{(2\pi)^4}\, tr\left\{\frac{1}{2f_\pi}\,\vec{k}\vec{\sigma}\,(D-F)\,iG_\Sigma(p+k)\,\frac{1}{2f_\pi}\,(-\vec{k}\vec{\sigma})\,(D-F)\,iG_p(p)\right\}$$

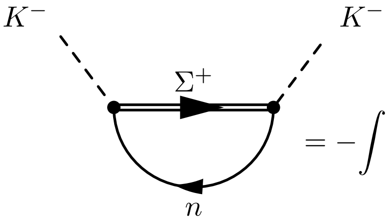

$$= -\int \frac{d^4p}{(2\pi)^4}\, tr\left\{\frac{1}{2f_\pi}\,\vec{k}\vec{\sigma}\,\sqrt{2}(D-F)\,iG_\Sigma(p+k)\,\frac{1}{2f_\pi}\,(-\vec{k}\vec{\sigma})\,\sqrt{2}(D-F)\,iG_n(p)\right\}\ .$$

Writing $-i\,\Sigma^{\Lambda}_{K^-} = -i\,\vec{k}^{\,2}\,\Pi^{\Lambda}_{K^-}$, the polarization functions for the K^- read

$$\begin{aligned}\Pi_{K^-} &= -\frac{i}{2f_\pi^2}\left[\frac{(3F+D)^2}{3}\int\frac{d^4p}{(2\pi)^4}\,G_\Lambda(p+k)\,G_N(p) \;+\; 3\,(D-F)^2\int\frac{d^4p}{(2\pi)^4}\,G_\Sigma(p+k)\,G_N(p)\right]\\ &= -\frac{1}{2f_\pi^2}\left[\frac{(3F+D)^2}{3}\,I_\Lambda(k) \;+\; 3\,(D-F)^2\,I_\Sigma(k)\right]\;.\end{aligned}$$

Analogously the expression for the $\overline{K^0}$ is:

$$\begin{aligned}\Pi_{\overline{K^0}} &= -\frac{i}{2f_\pi^2}\left[\frac{(3F+D)^2}{3}\int\frac{d^4p}{(2\pi)^4}\,G_\Lambda(p+k)\,G_N(p) \;+\; 3\,(D-F)^2\int\frac{d^4p}{(2\pi)^4}\,G_\Sigma(p+k)\,G_N(p)\right]\\ &= -\frac{1}{2f_\pi^2}\left[\frac{(3F+D)^2}{3}\,I_\Lambda(-k) \;+\; 3\,(D-F)^2\,I_\Sigma(-k)\right]\;.\end{aligned}$$

The integral $I_{\Lambda,\Sigma}$ reads

$$I_x = i\int\frac{d^4p}{(2\pi)^4}\,G_x(p+k)\,G_N(p) = -\int\frac{d^3p}{(2\pi)^3}\frac{\Theta(p_f-|\vec{p}|)}{k^0+\omega_N(\vec{p})-\omega_x(\vec{p}+\vec{k})+i\varepsilon}\;.$$

We take its imaginary part

$$\begin{aligned}\mathrm{Im}(I_x) &= \frac{1}{4\pi|\vec{k}|}\int_0^{p_f}dp\,|\vec{p}|\int_{\omega_-}^{\omega_+}dz\,z\,\delta(k^0+\omega_N(\vec{p})-z) \qquad\qquad (z=\omega_x(\vec{p}+\vec{k}))\\ &= \frac{1}{4\pi|\vec{k}|}\int_0^{p_f}dp\,|\vec{p}|\,(\omega_N(\vec{p})-k0)\,\Theta(\omega_+-\omega_N(\vec{p})-k0)\,\Theta(\omega_N(\vec{p})+k0-\omega_-)\;,\end{aligned}$$

where

$$\omega_\pm = \sqrt{\vec{p}^{\,2}+\vec{k}^{\,2}+m_N^2+2\,|\vec{p}||\vec{k}|}\;.$$

The arguments of the Θ–functions have zeros at

$$\begin{aligned}p1 &= \frac{1}{2(k^{02}-\vec{k}^{\,2})}\Big[-|\vec{k}|(k^{02}-\vec{k}^{\,2}+m_N^2-m_x^2)\\ &\qquad -k^0\sqrt{(k^{02}-\vec{k}^{\,2}+m_N^2-m_x^2)^2-4(k^{02}-\vec{k}^{\,2})m_N^2}\;\Big]\\ p2 &= \frac{1}{2(k^{02}-\vec{k}^{\,2})}\Big[|\vec{k}|(k^{02}-\vec{k}^{\,2}+m_N^2-m_x^2)\\ &\qquad +k^0\sqrt{(k^{02}-\vec{k}^{\,2}+m_N^2-m_x^2)^2-4(k^{02}-\vec{k}^{\,2})m_N^2}\;\Big]\;.\end{aligned}$$

The values $p1, p2$ will restrict the range of integration to $p_{min} \twoheadrightarrow p_{max}$, depending on k^0 and $|\vec{k}|$.

$$\Im m(I_x) = \begin{cases} 0 \qquad \text{if } \; p_f < p_{min} \quad \text{or} \; \begin{cases} k^{02} > \vec{k}^{\,2} + (m_N - m_x)^2 \wedge k^{02} < \vec{k}^{\,2} + (m_N + m_x)^2 \\ k^{02} < \vec{k}^{\,2} + (m_N - m_x)^2 \wedge k^{02} > \vec{k}^{\,2} + (m_N + m_x)^2 \end{cases} \\ \frac{1}{4\pi|\vec{k}|}\,(\frac{k^0}{2}(p_{max}^2 - p_{min}^2) + \frac{1}{3}[\sqrt{p_{max}^2 + m_N^2}^{\,3} - \sqrt{p_{min}^2 + m_N^2}^{\,3}]) \end{cases}$$

The real part reads

$$\begin{aligned} \Re e(I_x) &= -\int_{|\vec{p}|<p_f} \frac{d^3p}{(2\pi)^3} \frac{1}{k^0 + \omega_N(\vec{p}) - \omega_x(\vec{p} - \vec{k})} \\ &= \frac{1}{4\pi^2|\vec{k}|} \int_0^{p_f} d|\vec{p}|\, \vec{p}^{\,2} \left((\omega_+ - \omega_-) - (k^0 - \omega_N(\vec{p}))\, \ln \left| \frac{k^0 - \omega_N(\vec{p}) + \omega_+}{k^0 - \omega_N(\vec{p}) + \omega_-} \right| \right) \,. \end{aligned}$$

The momenta $p1, p2$ determine the position of the poles of the integrand.

As in the case of the pion selfenergy (chap.(5), eq. (5.10)), a form factor at the KBN vertices is introduced, $\Gamma = \frac{\Lambda^2}{\Lambda^2 + \vec{k}^2}$, where Λ is again put to a value of 550 MeV.

The resulting selfenergy for the K^- is shown in fig. 6.6, for normal nuclear matter density and a kaon momentum of $k = 400$ MeV. The two contributions from Λ–hole and Σ–hole are clearly visible.

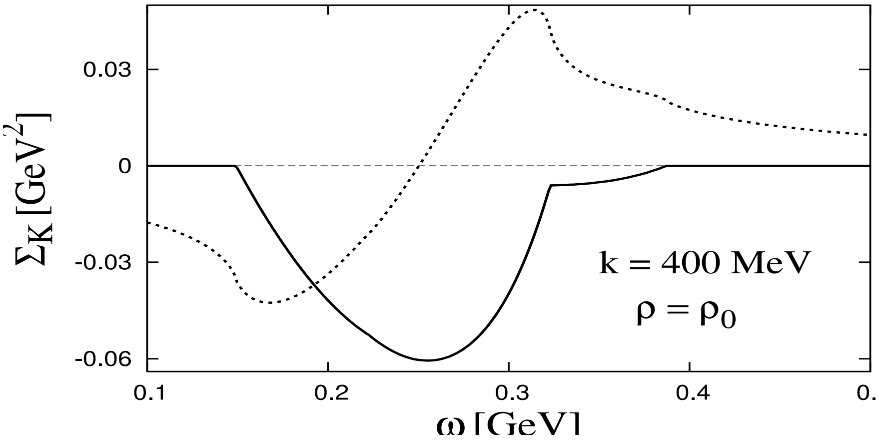

Figure 6.6: *K^- p–wave selfenergy, imaginary (solid line) and real part (dashed line) at $\rho = \rho_0$ and $|\vec{k}| = 400$ MeV*

The p–wave selfenergy is by its very nature growing quadratically with the kaon momentum. At some stage, this effect is damped by the form factor. The value of $|\vec{k}| = 400$ MeV was chosen here because for the given form factor, the p–wave selfenergy is maximal there.
The strength of this contribution seems to be sizeable. Yet the importance for the kaon becomes only clear when a comparison is made in terms of the kaon propagator. Fig. 6.7 shows that the influence of the p–wave selfenergy is extremely small.

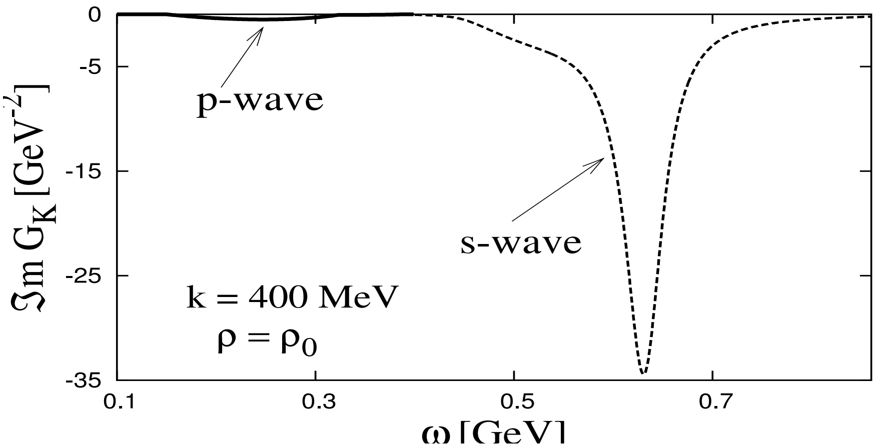

Figure 6.7: *Imaginary part of the K^- propagator, s–wave and p–wave contributions*

This behavior is due to the position of the p–wave selfenergy at very low energies. In fact, it entirely lies in the space–like region. Thus the kaon with its bare pole at $\sim$ 500 MeV does not feel much of the p–wave selfenergy.

Chapter 7

Kaons in symmetric nuclear matter

7.1 Medium: selfconsistency program

7.1.1 Iteration procedure

A summary of the problems encountered with the selfconsistency requirement is now in order. There are three key integrations whose interplay is to be considered. The imaginary part of the loop function,

$$\Im m J_{\bar{K}N}(q) = -\int \frac{d^3l}{(2\pi)^3}\,\frac{m_N}{\omega_N(\vec{l})}\,\Im m G_{\bar{K}}(q^0-\omega_N(\vec{l}),|\vec{q}-\vec{l}|)\;\Theta(q^0-\omega_N(\vec{l}))\Theta(|\vec{l}|-p_f),$$

the imaginary part of the kaon selfenergy,

$$\Im m\Sigma_{\bar{K}}(k) = \int \frac{d^3p}{(2\pi)^3}\,\frac{m_N}{\omega_N(\vec{p})}\,\Im m T_{\bar{K}N}(k^0+\omega_N(\vec{p}),|\vec{p}+\vec{k}|)\;\Theta(p_f-|\vec{p}|)$$

and the real part of $\Sigma_{\bar{K}}$,

$$\Re e\Sigma_{\bar{K}}(k^0,\vec{k}) = \frac{1}{\pi}\int_{-\infty}^{\infty} d\tilde{\omega}\;\frac{\Im m\Sigma_{\bar{K}}(\tilde{\omega},\vec{k})}{\tilde{\omega}-k^0}\;.$$

As discussed in subsec. 4.2.3 in connection with the question of cut–offs and dispersion relations for the real part of the loop function, the coupling of the two imaginary parts requires the knowledge of both functions in an increasing momentum range.
To calculate $\Im m J_{\bar{K}N}(q_{max})$, $\Im m G_{\bar{K}}$ is needed up to

$$|\vec{q}-\vec{l}|_{max} = q_{max} + l_{max} = q_{max} + \sqrt{{q^0}^2 - m_N^2}\;.$$

To get the kaon propagator at that momentum, $\Im m T_{\bar{K}N}$ as an integrand is needed at a maximum momentum of

$$|\vec{p}+\vec{k}|_{max} = |\vec{p}|_{max} + |\vec{k}|_{max} = p_f + q_{max} + \sqrt{{q^0}^2 - m_N^2} > q_{max}.$$

This escalation in the $\vec{q}$ direction can only be avoided by cutting the procedure at some maximum momentum. The kaon propagator lends itself to a corresponding approximation scheme.

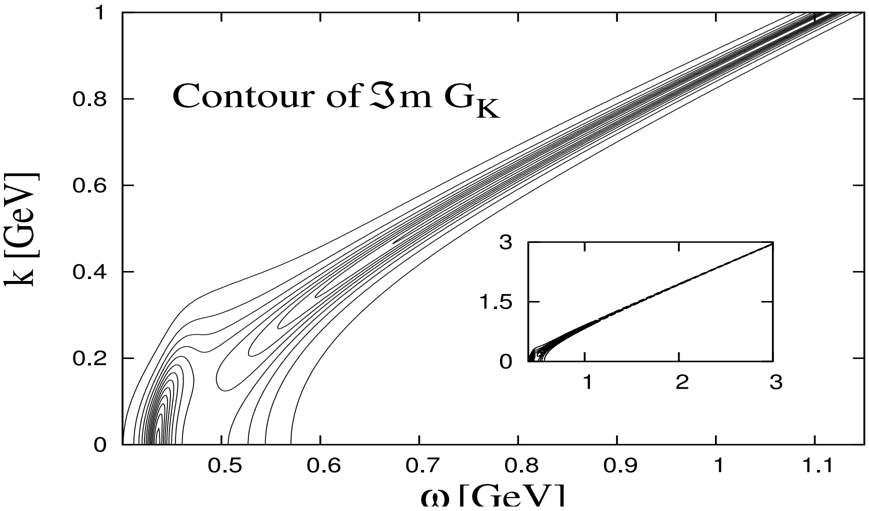

Figure 7.1: *Contour of* $\Im m G_{\bar{K}}$ *in the energy–momentum plane* ($\rho = \rho_0$)

Fig. 7.1 shows the kaon propagator at normal nuclear matter density after the first iteration step, i.e. only Pauli–blocking in the input–T-matrix. Obviously, the free dispersion relation of the kaon is regained already around $\omega = 900$ MeV, $|\vec{k}| = 800$ MeV. The insert shows that this trend definitely continues at larger energies and momenta. We find that the use of the free kaon is justified beyond $\omega = 1.5$ GeV, $|\vec{k}| = 1.2$ GeV.

Dispersion relations need the imaginary parts as input in principle for all energies from $-\infty$ to $+\infty$. The solution to this problem was already discussed in chap.(5). To accomplish the task of repeatedly evaluating the two integrals given above while the integrand is known only numerically, the functions have to be saved in each step as a grid of spline coefficients on the energy–momentum plane. When the function is then needed in an integration, its values are obtained by interpolation.

The iteration to selfconsistency is actually working very well. Fig. 7.2 shows an example of the imaginary part of the $\bar{K}^0$ selfenergy after several iterations. No difference is visible anymore between the third and fourth iteration.

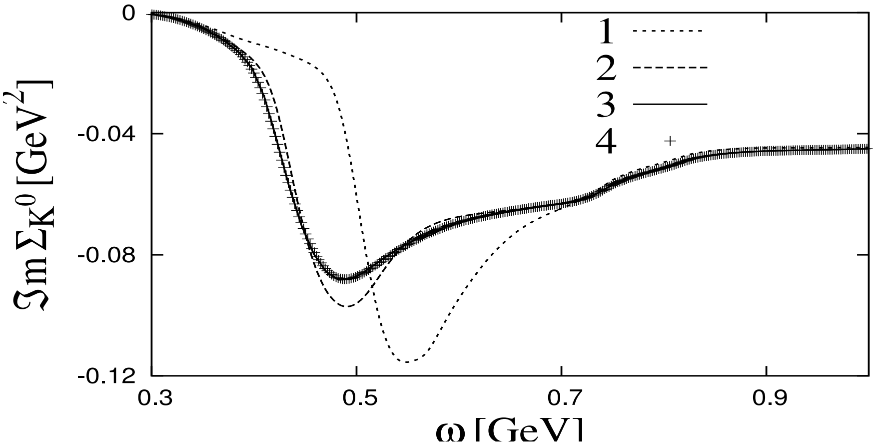

Figure 7.2: $\Im m\Sigma_{\overline{K^0}}$ *after* $1, \ldots 4$ *iterations (density* $\rho = 2\rho_0$, *proton:neutron ratio* $= 30:70$)

7.1.2 $\bar{K}N$ loop in cylindric coordinates

It is now clear that special care has to be taken to ensure that $\Im m T_{\bar{K}N}$ and $\Im m G_{\bar{K}}$ fit together perfectly. The selfconsistency procedure requires that $\Im m T_{\bar{K}N}$ and $\Im m G_{\bar{K}}$ repeatedly become integrands of each other. While $\Im m T$ as integrand does not pose a big problem, $\Im m G_{\bar{K}}$ has to be substituted by the free kaon propagator at sufficiently high momenta. There is a limiting momentum k_{lim} that introduces an additional vector. Thus the calculation of the loop function has a somewhat more complicated geometry.
k_{lim} can be as large as 3 GeV, but beyond that, the bare kaon propagator has to be used.
The starting expression was (eq.(4.9))

$$J_{\bar{K}N}(q) = -i \int \frac{d^4 l}{(2\pi)^4}\, G_N(l)\, G_{\bar{K}}(q-l)\ .$$

The imaginary part of $J_{\bar{K}N}$ reads (eq. (4.30))

$$\Im m J_{\bar{K}N}(q^0,\vec{q}) = -\int \frac{d^3 l}{(2\pi)^3}\, \frac{m_N}{\omega_N(\vec{l})}\, \Im m G_{\bar{K}}(q^0-\omega_N(\vec{l}),\vec{q}-\vec{l})\ \Theta(q^0-\omega_N(\vec{l}))\ \Theta(|\vec{l}|-p_f)\ .$$

The restriction $|\vec{l}| \geq p_f$ is imposed by the presence of the nuclear medium. Now the argument of the kaon propagator is also restricted to remain below the limiting momentum.

$$|\vec{l}-\vec{q}| \ \leq\ k_{lim}$$

Figure 7.3 illustrates the problem for one particular distribution of the momenta.
The incoming momentum $\vec{q}$ defines the axis. If there were no limit on $|\vec{l}-\vec{q}|$, i.e. $k_{lim}=\infty$, $|\vec{l}|$ would be allowed to vary between the inner circle, given by the Fermi momentum p_f, and the outer circle, given by the kinematic constraint $W=\sqrt{q^{0\,2}-m_N^2}$. For finite k_{lim} $|\vec{l}|$ is restricted to the area of overlap of the W–circle and the k_{lim}–circle.

To incorporate this in the loop function, it is advisable to chose cylindrical coordinates for the integration: $l_{||}$ is the component of $\vec{l}$ parallel to $\vec{q}$, $l_\perp$ comprises the perpendicular components.

$$\begin{aligned}\Im m J_{\bar{K}N}(q^0,\vec{q}) &= -\frac{m_N}{4\pi^2}\int dl_{||}\int dl_\perp \frac{l_\perp}{\omega_N(\vec{l})}\,\Im m G_{\bar{K}}(q^0-\omega_N(\vec{l}),\vec{q}-\vec{l})\Theta(q^0-\omega_N(\vec{l}))\ \Theta(|\vec{l}|-p_f)\\ &= -\frac{m_N}{4\pi^2}\int_{-W}^{+W} dl_{||}\int_{l_{\perp_{min}}}^{l_{\perp_{max}}} dl_\perp \frac{l_\perp}{\omega_N(\vec{l})}\,\Im m G_{\bar{K}}(q^0-\omega_N(\vec{l}),\vec{q}-\vec{l})\ . \qquad (7.1)\end{aligned}$$

The following quantities can be read off of fig. 7.3:

$$\begin{aligned} W &= \sqrt{q^{0\,2}-m_N^2}\\ l_{\perp_{max}} &= \sqrt{q^{0\,2}-m_N^2-l_{||}^2}\\ l_{\perp_{min}} &= \begin{cases}\sqrt{p_f^2-l_{||}^2} & for \quad l_{||}<p_f\\ 0 & for \quad l_{||}>p_f\end{cases}\end{aligned}$$

Now the condition $|\vec{l}-\vec{q}| \leq k_{lim}$ can be imposed.

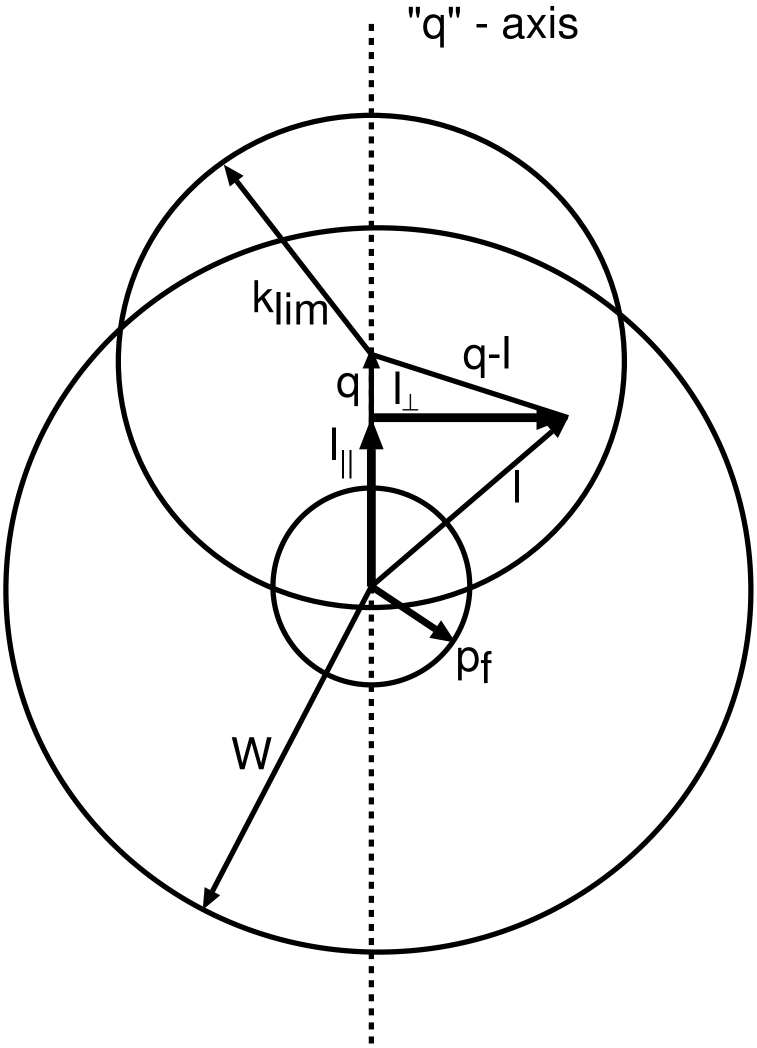

Figure 7.3: *Shifted momentum spheres*

$$
\begin{aligned}
|\vec{l} - \vec{q}| &= \sqrt{(l_{\|} - |\vec{q}|)^2 + l_{\perp}^2} \;\leq\; k_{lim} \\
l_{\perp}^2 &\leq k_{lim}^2 - (l_{\|} - |\vec{q}|)^2 \\
\Rightarrow\; l_{\perp_{max}} &= \min\left(\sqrt{W^2 - l_{\|}^2}\,,\; \sqrt{k_{lim}^2 - (l_{\|} - |\vec{q}|)^2}\right)
\end{aligned}
$$

Of course, the three circles of fig. 7.3 will vary in size. Many configurations are possible, and one has to verify that the found condition is sufficient for all. Then the integral of eq.(7.1) will be evaluated numerically, using the kaon propagator obtained in the prior step as input.
The really sophisticated part is actually the calculation of the analytic part. It corresponds to the integral in eq.(7.1) for the inverse condition $|\vec{l} - \vec{q}| > k_{lim}$. The imaginary part of the kaon propagator will then be replaced by a δ–function. But this only generates several Θ functions with

a number of subdivisions that have to be carefully investigated. This lengthy elaboration is not discussed here.

7.2 $\bar{K}N$ scattering amplitude after iteration

Fig. 7.2 showed that the selfconsistency procedure is converging rapidly. Here, the effect of this iteration shall be inspected more closely.

The following figures (figs. 7.4–7.6) show the T–matrix element for three densities: normal nuclear matter density ρ_0, $\rho = 2\rho_0$ and $\rho = 5\rho_0$.

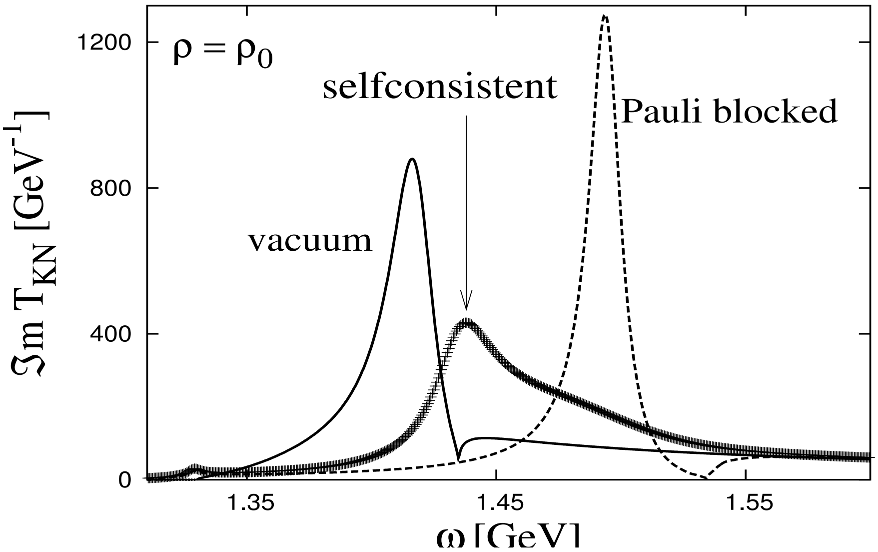

Figure 7.4: $\Im m T_{\bar{K}N}$ *($\rho = \rho_0$, $|\vec{k}| = 0$ MeV), solid line: vacuum result, dotted line: in–medium result, only Pauli–blocking, crosses: result after selfconsistency is reached*

Starting at normal nuclear matter density ρ_0 in fig. 7.4, the T–matrix element for in–medium $\bar{K}N$ scattering becomes quite broad and deformed. The effects are similar and just enhanced with increasing density, fig. 7.5 and fig. 7.6.

The first step of the in–medium calculation presented in these figures was already described in section (4.4). The amplitude is calculated employing only Pauli–blocking according to eq.(4.30) (cf. figs. 4.21,4.22). This causes the $\Lambda(1405)$ to be pushed upwards: the $\bar{K}N$ scattered states at the lower energies are blocked by the Pauli principle. The subsequent iterations to selfconsistency pull the resonance down again. The Pauli principle is still obeyed of course, but the change in the kaon mass and especially the broadening of the spectral function re–enables scattering into lower lying states.

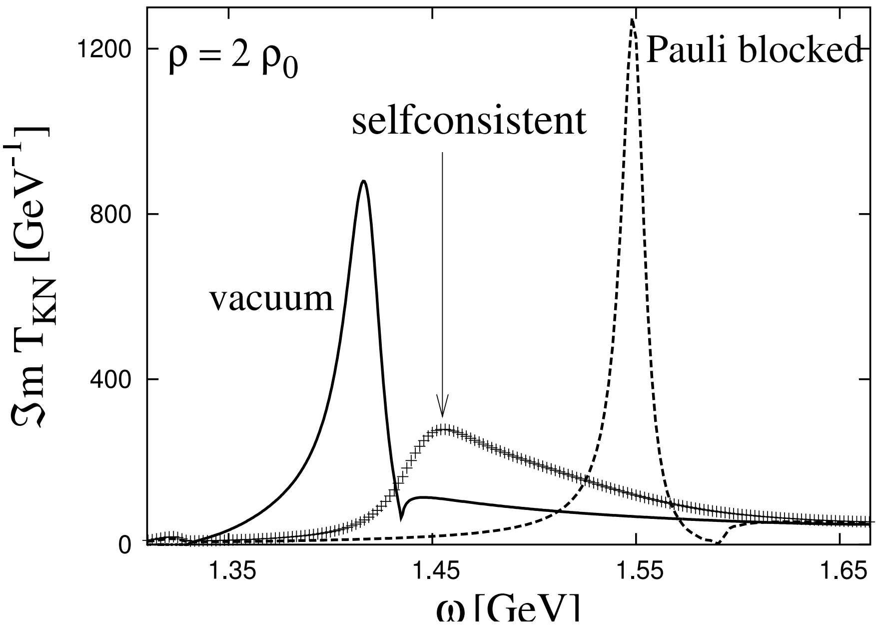

Figure 7.5: $\Im m T_{\bar{K}N}$ *($\rho = 2\rho_0$, $|\vec{k}| = 0$ MeV), solid line: vacuum result, dotted line: in–medium result, only Pauli–blocking, crosses: result after selfconsistency is reached*

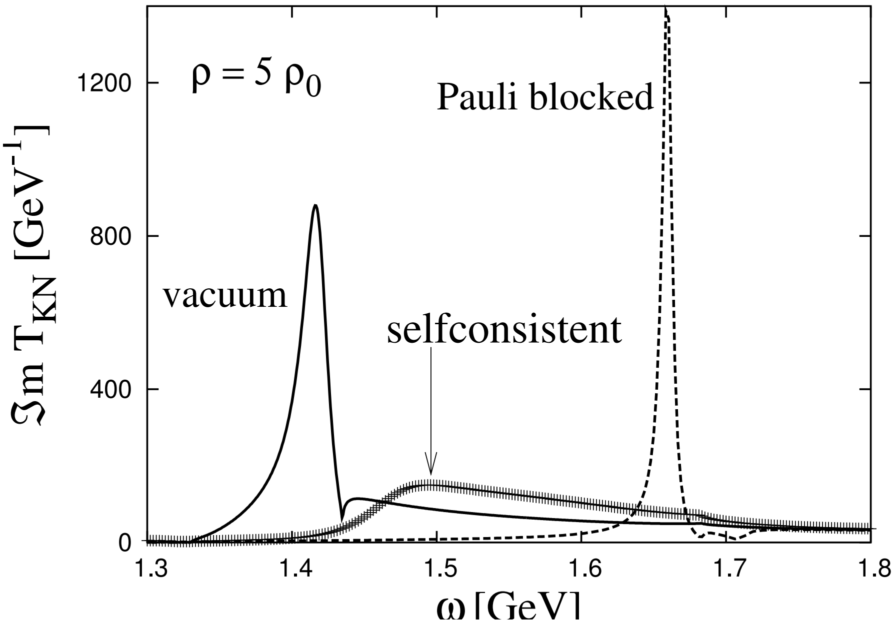

Figure 7.6: $\Im m T_{\bar{K}N}$ *($\rho = 5\rho_0$, $|\vec{k}| = 0$ MeV), solid line: vacuum result, dotted line: in–medium result, only Pauli–blocking, crosses: result after selfconsistency is reached*

This downward movement of the amplitude is important since the Pauli–blocking shift is used to give an explanation for the data obtained in kaonic atoms [18] and the kaon yields in heavy ion collisions [23, 24]. This was brought up already in the introduction (chap. 1) and can now be checked with our results.

From the Lagrangian eq. (3.11) one obtains in lowest order the $\bar{K}N$ scattering length

$$a_{K^\pm p} = \mp(1 + \frac{m_K}{m})^{-1}\frac{m_K}{4f_\pi^2} \approx \mp 0.6 fm\,.$$

The antikaon proton scattering length is thus positive, meaning an attractive potential close to threshold. The experimental value is repulsive, however: $\Re e a_{K^-p} = -0.78$ fm [40]. The reason is the existence of the $\Lambda(1405)$. Being a $\bar{K}N$ bound state just below threshold, it causes a repulsive contribution to the scattering amplitude at threshold.

Secondly, there are the data from kaonic atoms and the kaon yields in HIC. From the measurements of the strong–interaction shifts and widths of the lowest energy levels in kaonic atoms [18], an attractive kaon potential can be extracted.

To leading order in the density, the in–medium properties of the kaon are related to the kaon nucleon scattering amplitude via a low–density expansion (low–density theorem) [68]. The antikaon potential is given as [28, 21, 68]

$$U_{\bar{K}} \sim \; -4\pi\, a_{\bar{K}N}\,\rho \quad \sim -T_{\bar{K}N}\,\rho\,.$$

The antikaon potential can also be defined more generally as [69] $U_{\bar{K}} = \Sigma_{\bar{K}}/2\,m_K$. We see that the low–density approximation is actually quite similar to the trick employed in section 6.1 (eq.(6.3)) that helped express $\Sigma_{\bar{K}}$ by the amplitude $T_{\bar{K}N}$ for energies/momenta much larger than the Fermi momentum.

Since the free scattering amplitude leads to a repulsive potential ($\Re e f_{\bar{K}N} < 0$), the in–medium amplitude must reverse its sign. This behavior is found in the scattering amplitudes of our calculation, displayed in fig. 7.7:

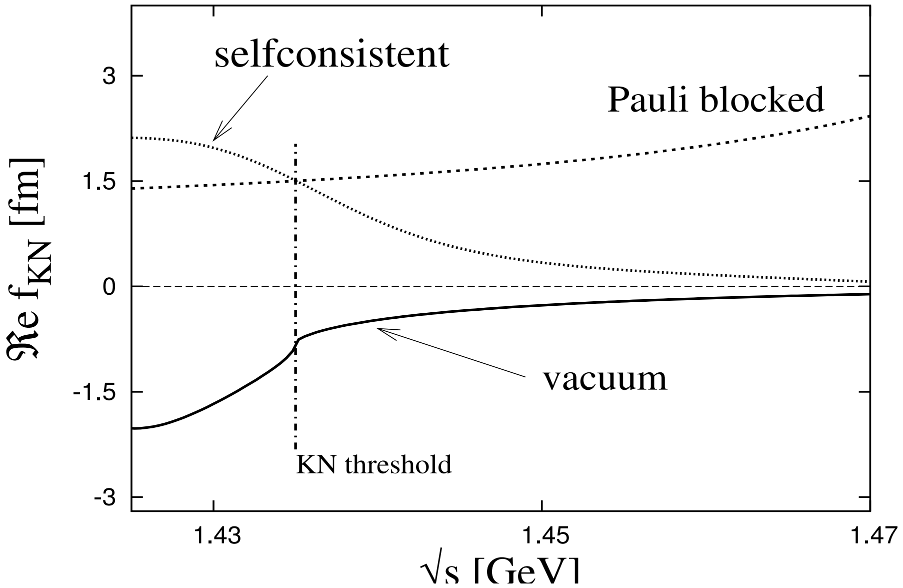

Figure 7.7: *$\Re e f_{\bar{K}N}$ near $\bar{K}N$ threshold (1.435 GeV). Vacuum curve (solid line), amplitude including Pauli–blocking (dashed line) and fully selfconsistent result (dotted line), both at $\rho = \rho_0$, sc. $|\vec{q}| = 0$*

The vacuum curve runs below zero, while the two in-medium curves in fig. 7.7 have positive values around threshold.If we concentrate first on the Pauli–blocked amplitude we see that it appears strongly positive directly above threshold in fig. 7.7, thus suggesting an attractive in–medium potential [28].

There are still repulsive contributions contained in the Pauli–blocked amplitude, but these are found only at a higher energy. This becomes clear from fig. 7.8 which also displays the energy range above threshold:

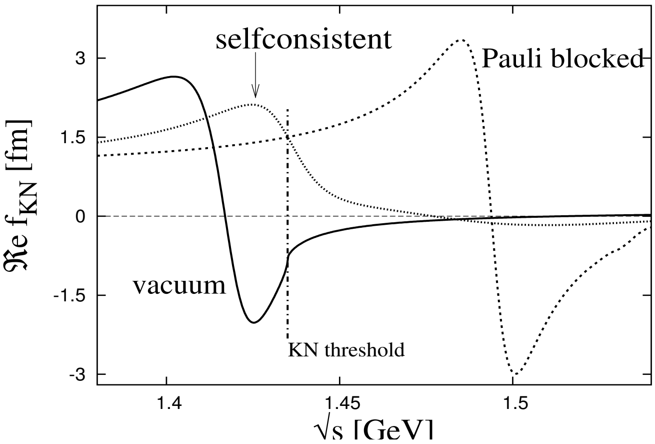

Figure 7.8: $\Re e f_{\bar{K}N}$ *around* $\bar{K}N$ *threshold* ($\rho = \rho_0$, $|\vec{q}| = 0$)

Yet both figures 7.7 and 7.8 indicate the fully selfconsistent result is much smaller above threshold than the Pauli–blocked one. Thus the explanation of the level shifts in kaonic atoms by an attractive potential that is generated by the moving $\Lambda(1405)$ seems to become a moot point.

The other experimental observation explained by the Pauli–blocking of the $\bar{K}N$ amplitude is the enhanced yield of K^- in heavy ion collisions at GSI [23]. In this case it is essential to take into account the momentum dependence of the $\bar{K}N$ amplitude. In a typical SIS–heavy ion collision where the temperature is estimated to be around $T \sim 80$ MeV [23], the kaons will move with a momentum larger than 300 MeV with respect to the matter rest frame [21]. Since we have the full information about energy and momentum dependence available, we should inspect the result for some finite momentum. Fig. 7.9 shows the same three curves as in the plots above, but now at a momentum of 500 MeV.

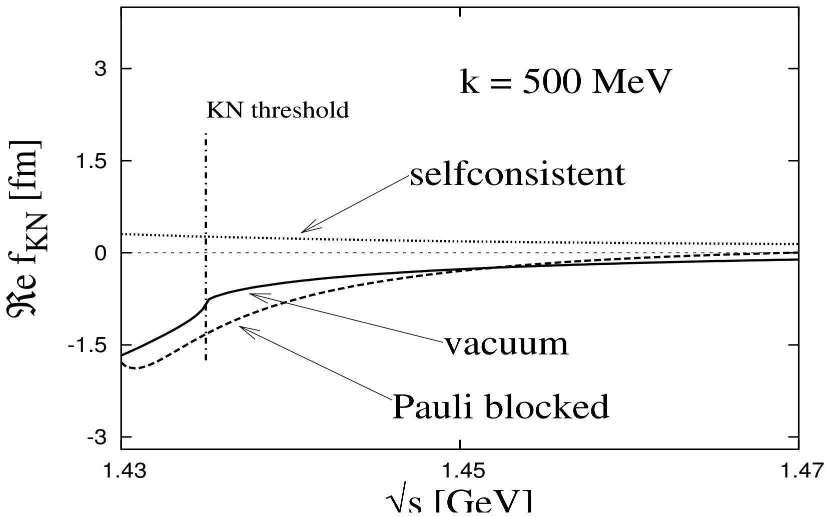

Figure 7.9: $\Re e f_{\bar{K}N}$ *around* $\bar{K}N$ *threshold*

Plotted against $\sqrt{s}$ to compare at the vacuum threshold at 1.435 GeV, the Pauli–blocked curve has moved down a lot and would lead back to a repulsive potential. The selfconsistent amplitude, however, remains positive, albeit small. This is also true for other densities. In addition it does not change sign even at higher momenta $>$ 500 MeV. This is in contrast to the work by Schaffner–Bielich et. al. [21], who found the optical potential to become repulsive for high momenta. The reason is probably the interaction used: in [21], only the constant form of the Weinberg–Tomozawa vertex (cf. fig. 2.1) was employed. Using this simplification, we can reproduce the sign change at higher momenta. Especially the σ–terms we included in the full calculation seem to be important here, which is not surprising since they always give an attractive contribution.

Momentum dependence

The momentum dependence of the $\bar{K}N$ amplitude can also be studied for its imaginary part. $\Im m T^{(0)}_{\bar{K}N}$ at several 3–momenta is displayed in fig. 7.10 for the three densities discussed before. The effect noted in figs. 7.7 and 7.9 is here visible over a larger energy interval. With increasing momentum, the peak of the T–matrix moves down on the $\sqrt{s}$–axis, but the vacuum resonance is nearly melted, especially at higher density. This causes attraction everywhere, but that attractive potential is very small.
We can also infer that even at the highest momenta the interaction is still effective for the T–matrix. The form and position of the vacuum T–matrix are not regained. This is in contrast to the kaon propagator (see also section (7.3) below). As expected, however, the Lorentz–invariance breaking effect of the surrounding nuclear matter system vanishes at high momentum. That is why the three high–momentum curves always coincide.

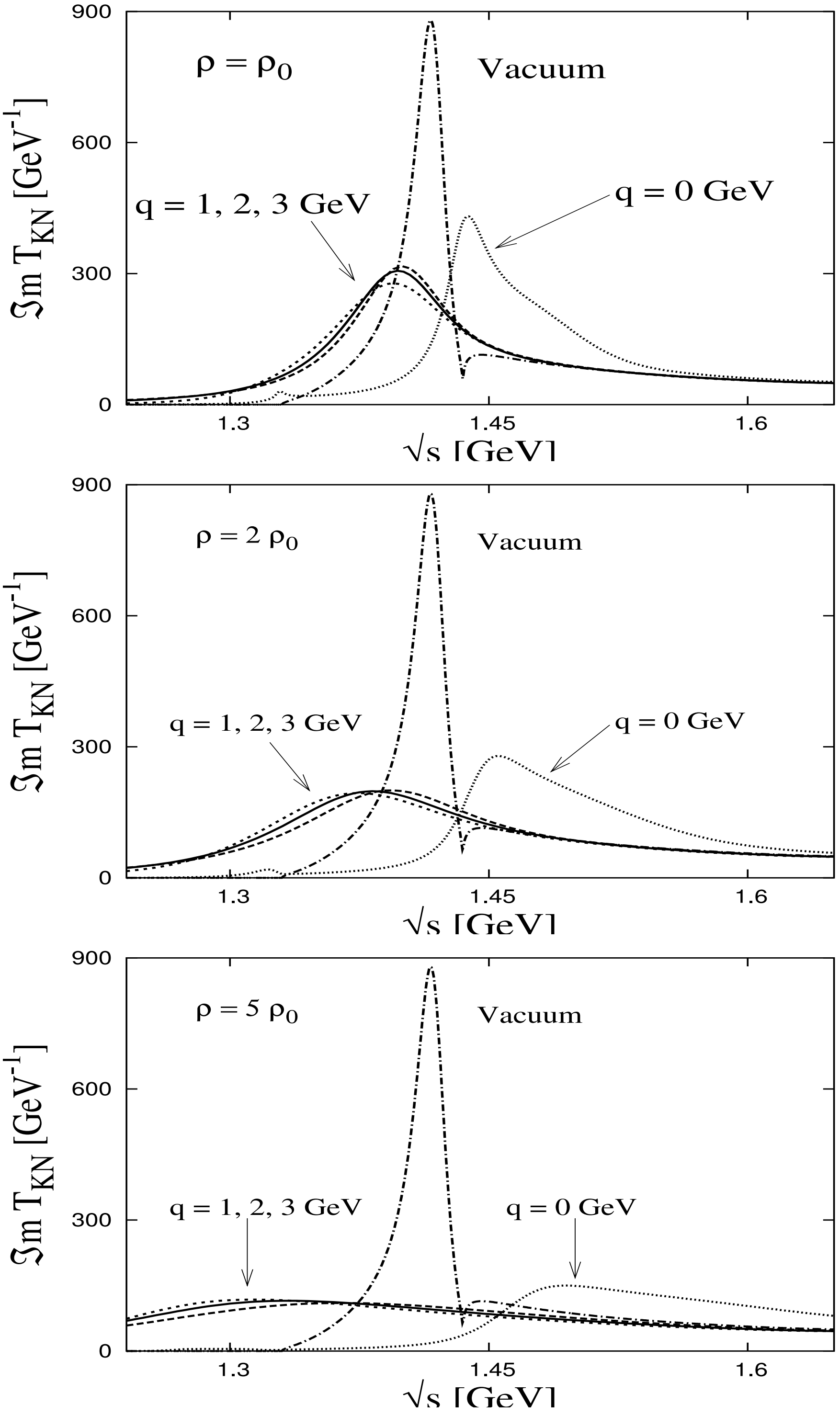

Figure 7.10: $\Im m T_{\bar{K}N}$ *in vacuum and at* $\rho = \rho_0$ *(top panel),* $\rho = 2\rho_0$ *(middle panel) and* $\rho = 5\rho_0$ *(lower panel),* $|\vec{q}| = 0$ *MeV (rightmost curve),* $|\vec{q}| = \{1, 2, 3\}$ *GeV (curves to the left)*

7.3 Kaon propagator after iteration

The following plots show the effect of the selfconsistency iteration on the kaon propagator (imaginary part).

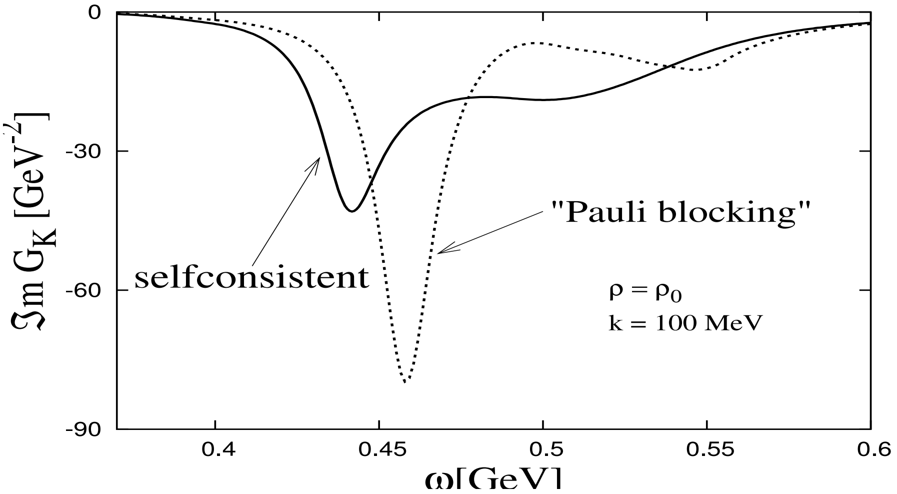

Figure 7.11: $\Im m G_K$ *($\rho = \rho_0$, $|\vec{k}| = 100$ MeV), dotted line: after one iteration, solid line: after selfconsistency is reached*

The label "Pauli–blocking"in fig. 7.11 and subsequent figures refers here to the input used to calculate these curves. These curves show the result after the first step of iteration when only the Pauli–blocked T–matrix elements as mentioned in the previous section where used in the selfenergy integrals. The selfconsistency iterations (cf. solid line in fig. 7.11) broaden the kaon and shift it down, compared with the result that incorporates just the effect of Pauli–blocking (dotted line). One striking feature of the "Pauli–blocking"– in–medium kaon is the splitting of $\Im m G_{\bar{K}}$ into two maxima. This feature is largely washed out by the selfconsistency iterations. At higher momentum this is even more obvious. There the upper level is more pronounced at first. The iteration then smoothes out the difference between the levels. At $|\vec{k}| = 200$ MeV and 300 MeV (figs. 7.12, 7.13), the selfconsistent kaon is very broadly distributed among the former two maxima:

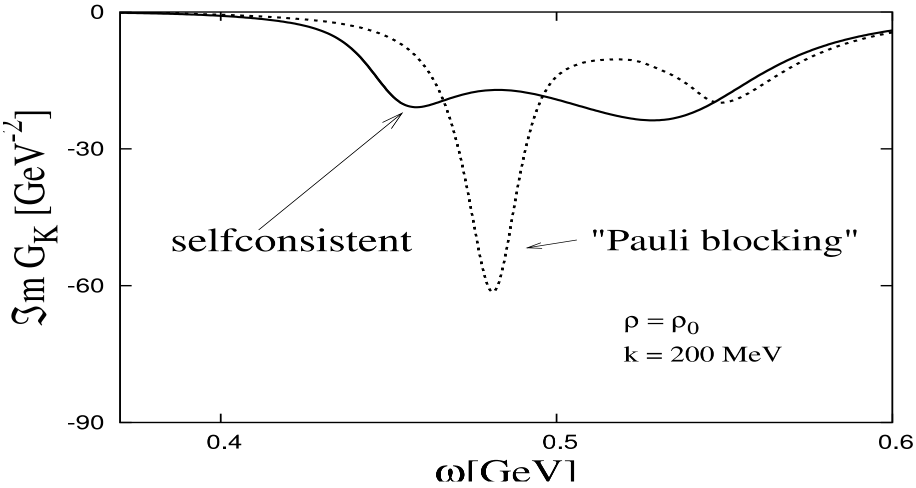

Figure 7.12: $\Im m G_K$ *($\rho = \rho_0$, $|\vec{k}| = 200$ MeV), dotted line: after one iteration, solid line: after selfconsistency is reached*

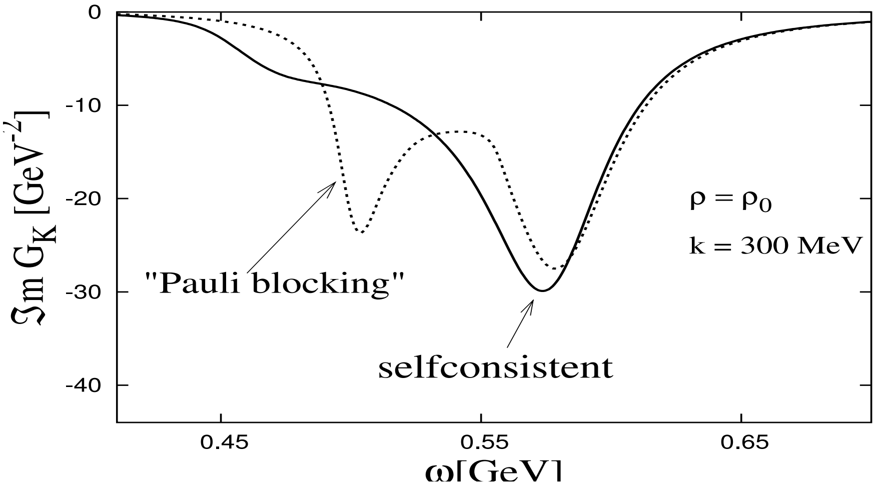

Figure 7.13: $\Im m G_{\bar{K}}$ *($\rho = \rho_0$, $|\vec{k}| = 300$ MeV), dotted line: after one iteration, solid line: after selfconsistency is reached*

At $|\vec{k}| = 500$ MeV (fig. 7.14) the effect of the iteration is almost gone:

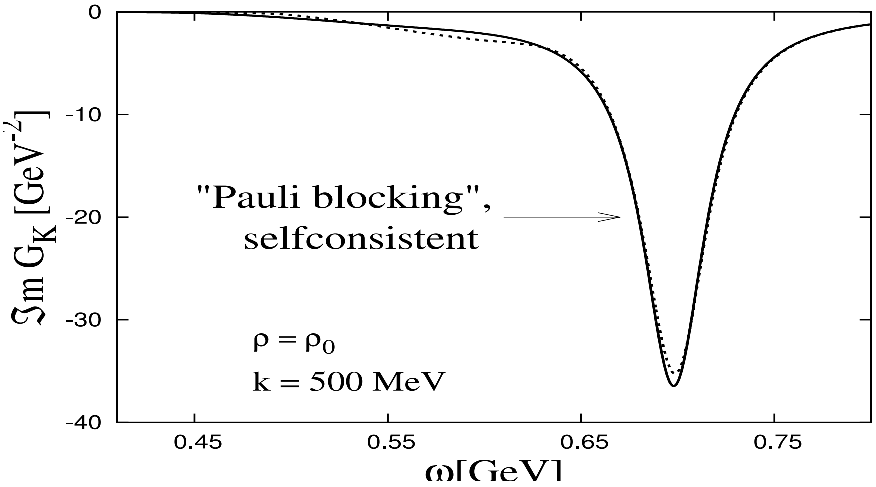

Figure 7.14: $\Im m G_{\bar{K}}$ *($\rho = \rho_0$, $|\vec{k}| = 500$ MeV), dotted line: before, solid line: after selfconsistency*

A similar behavior is found for the densities $\rho = 2\rho_0$ and $\rho = 5\rho_0$.

We can now concentrate on the selfconsistent result and have a closer look at the interesting momentum range where the imaginary part of the kaon propagator exhibits two maxima.

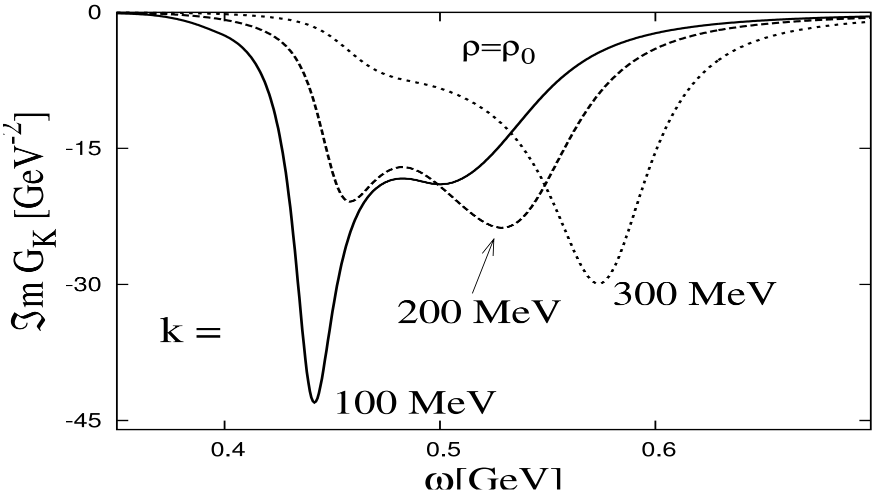

Figure 7.15: $\Im m G_{\bar{K}}$ *($\rho = \rho_0$, $|\vec{k}| = 100, 200, 300$ MeV)*

Fig. 7.15 shows the kaon propagator at 3–momenta $|\vec{k}| = 100$ MeV, 200 MeV and 300 MeV. With increasing 3–momentum the main peak sitting at low energies for small or vanishing 3–momenta loses strength and gets shifted towards higher energies.

In accordance with the well–known rule of level repulsion, the two maxima are separate and lie below and above the mass of the bare kaon at 495 MeV. The stronger one at lower energies is basically given by the 'T–matrix–hole excitation'. In contrast to the pion case (section 5.1, cf. [58]), we cannot resolve these peaks into particular quasiparticle states. This is again a consequence of using a model of coupled channels.

The upper maximum could be interpreted as the kaon itself with a modified in–medium dispersion relation, in analogy with the pion branch of fig. 5.2. At least at higher momenta this becomes clear, as can be seen in fig. 7.16 below. It shows the contour of $\Im m G_{\bar{K}}$ in the ω–$\vec{k}$ plane:

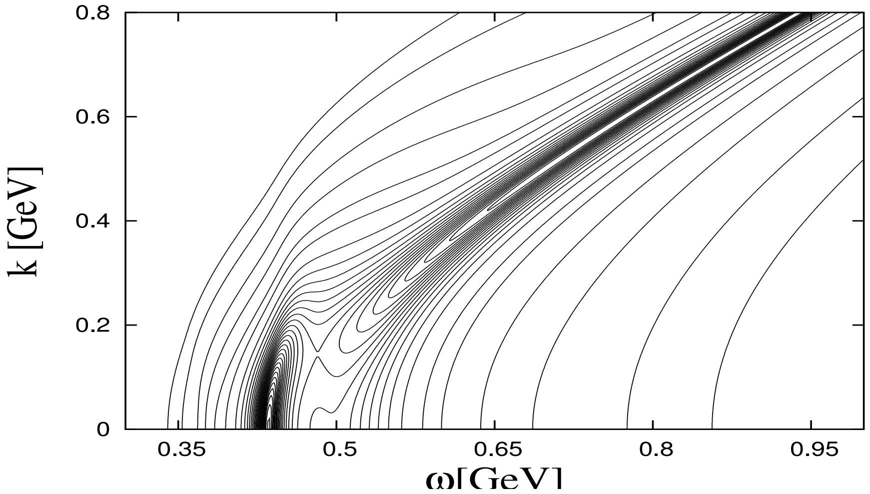

Figure 7.16: *Contour of $\Im m G_{\bar{K}}$ in the energy–momentum plane (density = ρ_0)*

While strength is concentrated around 400 − 450 MeV at low momentum, at momenta above $|\vec{k}| = 400$ MeV the kaon, though still broadened, follows the free dispersion relation, as indicated by the 'valley' in the contour bending to the right.

This feature of the kaon propagator is present at all densities. For comparison fig. 7.17 displays the same curves as fig. 7.15 but at $\rho = 2\rho_0$.

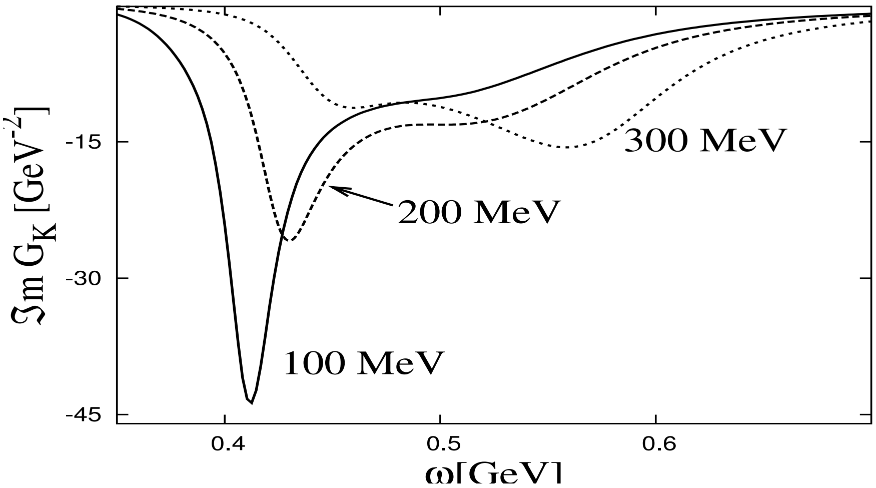

Figure 7.17: $\Im m G_{\bar{K}}$ $(\rho = 2\rho_0,\ |\vec{k}| = 100, 200, 300\ MeV)$

Yet another comparison can be made between different densities. Fig. 7.18 shows the density dependence of the kaon propagator at the three densities discussed respectively at $|\vec{k}| = 300$ MeV.

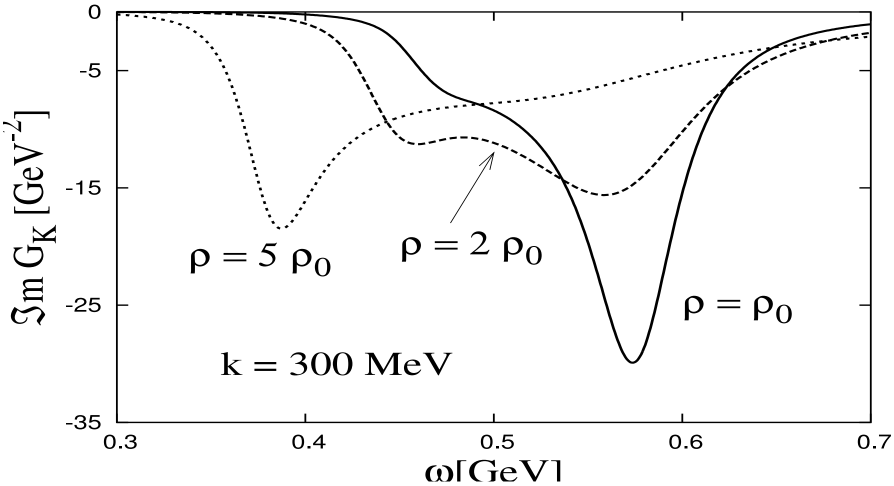

Figure 7.18: $\Im m G_{\bar{K}}$ $(|\vec{k}| = 300\ MeV,\ \rho = \rho_0, 2\rho_0, 5\rho_0)$

The fact that the peak value of the kaon becomes smaller with increasing 3–momentum (cf. fig. 7.17) is due to the inherent momentum dependence of the kaon selfenergy. The peak shrinks and the broadening becomes stronger with increasing 3–momentum, since the (input elements) ingredients to the selfenergy loop depend on the momentum via their energy (cf. eqs. (4.21) and (4.22)). At momenta above 600 MeV this effect is again diminished, the impact of the selfenergy on the propagator quickly becoming unimportant. This can be seen in the following figure that shows the kaon pole for a number of 3–momenta in the momentum range taken into account.

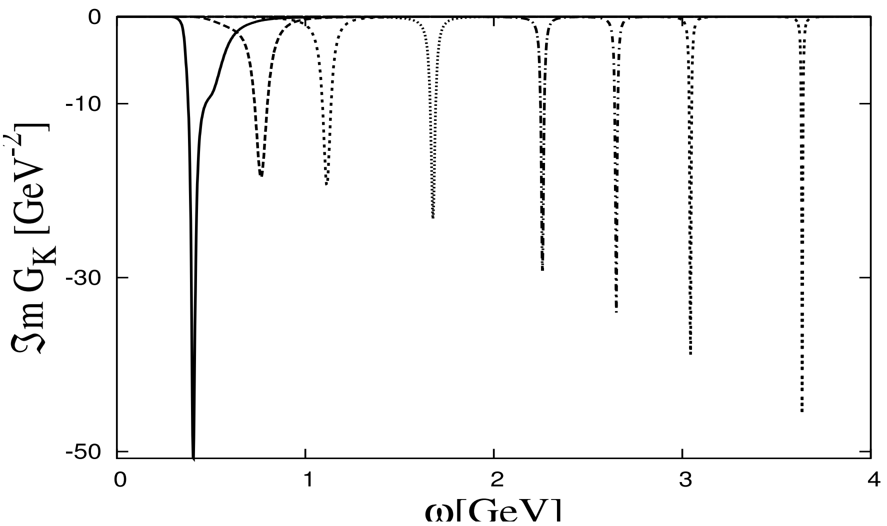

Figure 7.19: $\Im m G_{\bar{K}}$ *at* $\rho = 2\rho_0$, $|\vec{k}| = \{0, 0.6, 1.0, 1.6, 2.2, 2.6, 3.0, 3.6\}$ *GeV (from left to right)*

Chapter 8

Asymmetric nuclear matter

8.1 Asymmetric nuclear matter

So far the discussion in this work has concentrated on modifications that pions and kaons experience in isospin symmetric nuclear matter. However this is a state of matter never found in nature. Already the concept of an infinitely extending system of nuclear matter is quite questionable. Still, large nuclei such as the lead nucleus seem to provide quite a good approximation to nuclear matter. Even better will be the high–density regions of heavy–ion collisions and the interior of compact astrophysical objects such as neutron stars.
Successful modern approaches to nuclear theory build the nuclei out of the basic nucleon–nucleon interaction rather than trying to extrapolate from the nuclear matter result down to finite nuclei. On the other hand, investigations of the in–medium behavior of certain particles as the kaons and pions here are usually done in a nuclear matter system. This is mainly a question of feasibility.
But in any case realistic systems usually contain different numbers of protons and neutrons. The objects that comes closest to nuclear matter are neutron stars, where the name alone suggest a huge surplus of neutrons over protons.

Investigating the kaon selfenergy in isospin–asymmetric high–density nuclear matter is of course done with neutron stars in mind. Chapter 9 will elaborate on the details of neutron stars relevant for our model. Here it suffices to observe that densities inside these stars are expected to range up to 10 times nuclear matter density. Of course the nature of the system at very high density is not clear: The charge radius of the proton is currently measured to be $0.81 \ldots 0.87$ fm. At a density of $\rho = 10\,\rho_0 = 1.6\,\mathrm{fm}^{-3}$, the distance between the protons can be estimated to be ≈ 0.85 fm – the protons would be overlapping completely [70]. Here we are clearly touching a transition region to another (quark–gluon) phase. Since we do not have suitable tools to handle this density region, we should stay away from it. We will concentrate on ρ_0 and $2\,\rho_0$, and a calculation at $\rho = 5\,\rho_0$ is then meant to explore the behavior of the model in the direction of increasing density.

The discussion of asymmetric nuclear matter requires a somewhat more precise terminology. The density ρ referred to is always the total baryon number density. Since we consider the temperature $T = 0$ situation, the only baryons occurring in sizeable number are the nucleons. A density of $\rho = \rho_0 = 0.16\,\mathrm{fm}^{-3}$ then means to have 0.16 nucleons per fm^{-3}. Of these, a fraction x_p consists of protons. Thus the symmetric case is characterized by $x_p = 0.5$, which means 0.08 protons per cubic Fermi.

8.2 Pions in asymmetric nuclear matter

While we do not subject the η–channels (cf. eq. (3.1)) to any medium modifications, the channels involving a pion are changed according to chap. (5), which was based on the work of Urban et al. [58]. However, the case of isospin asymmetric matter was not covered there, so it needs to be developed here.
First we have to revisit the Lagrangian eq. (5.1) and extract the vertices in the particle basis. This is straightforward and gives the following relativistic and non–relativistic ('n.r.') contributions:

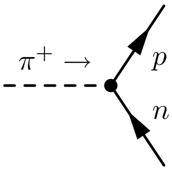

$$= \; -\sqrt{2}\,\frac{f_N}{m_\pi}\,\gamma_5\gamma^\mu\,k_\mu \overset{\text{n.r.}}{=} -\sqrt{2}\,\frac{f_N}{m_\pi}\,\vec{k}\cdot\vec{\sigma}$$

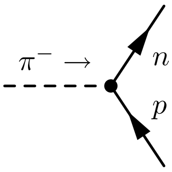

$$= \; \sqrt{2}\,\frac{f_N}{m_\pi}\,\gamma_5\gamma^\mu\,k_\mu \overset{\text{n.r.}}{=} \sqrt{2}\,\frac{f_N}{m_\pi}\,\vec{k}\cdot\vec{\sigma}\;.$$

The neutral pion is blind to isospin variations, the $\pi^0 pp$ or $\pi^0 nn$ vertex just reads $\pm\frac{f_N}{m_\pi}\,\vec{k}\cdot\vec{\sigma}$.

For the Δ, we have more possible combinations. Thus the procedure leads to a large number of vertices which are given in detail in appendix D.3. They are all of the form

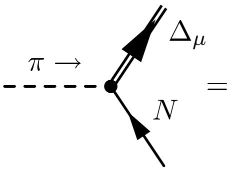

$$= \; -\,\mathrm{C}\,\frac{f_\Delta}{m_\pi}\,k_\mu \;\rightarrow\; \mathrm{C}\,\frac{f_\Delta}{m_\pi}\,\vec{k}\cdot\vec{S}\;,$$

where the nucleon and Δ legs can also appear interchanged. The factor C is equal to 1 or $\frac{1}{\sqrt{3}}$, depending on the particular particle combination, see appendix D.3.

8.2.1 Example: π^+ selfenergy

As an example for the medium modifications of the pion in asymmetric matter we write down the π^+ selfenergy. The procedure goes along the lines of [58] and [67]. Again we point out that the pion selfenergy is calculated using the finite–temperature Matsubara formalism, taking the limit $T \rightarrow 0$ in the end, in order to facilitate the numerical treatment of the model. The Matsubara formalism enables a diagrammatic representation of thermal expectation values quite similar to the usual Feynman diagrams. The Feynman rules differ somewhat, however.

There are five diagrams contributing to the selfenergy of the π^+. The first one (fig. 8.1) consists of a particle-hole excitation.

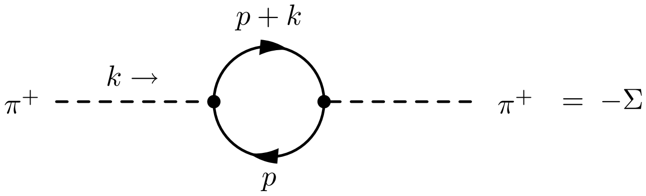

Figure 8.1: *Particle–hole contribution to* Σ_{π^+}

$$-\Sigma = -T\sum_l \int \frac{d^3p}{(2\pi)^3}\, tr[(-i\sqrt{2}\,\frac{f_N}{m_\pi}\,\vec{k}\vec{\sigma})(-G_p(i(\omega_l+\omega_k),\vec{k}+\vec{p}))\,(i\sqrt{2}\,\frac{f_N}{m_\pi}\,\vec{k}\vec{\sigma})(-G_{nh}(i\omega_l,\vec{p}))]$$

Evaluating the trace leads to

$$\Sigma = 4\,\vec{k}^2\left(\frac{f_N}{m_\pi}\right)^2 T\sum_l \int \frac{d^3p}{(2\pi)^3}\, G_p(i(\omega_l+\omega_k),\vec{k}+\vec{p})\, G_{nh}(i\omega_l,\vec{p})\ . \tag{8.1}$$

It becomes obvious how the vertices and propagators differ from the temperature $T = 0$ case. Further details can be taken from [71].

The other four diagrams are similarly constructed from the $\pi N\Delta$ vertices. Again we leave the details of working out the selfenergies to appendix D.4 and skip to the result.

The selfenergy contribution from particle–hole reads

$$\begin{aligned}\Sigma(\omega_k,\vec{k}) = -4\,\vec{k}^2\left(\frac{f_N}{m_\pi}\right)^2 \frac{1}{4\pi^2 k}\Bigg(&\int_0^\infty dp\,p\,n_n(\vec{p})\ (\omega_{p,+}-\omega_{p,-}\\ &+(\omega_n(\vec{p})+k^0+\mu_p-\mu_n+i\varepsilon)\ln\frac{\omega_{p,+}-\omega_n(\vec{p})-k^0-\mu_p+\mu_n-i\varepsilon}{\omega_{p,-}-\omega_n(\vec{p})-k^0-\mu_p+\mu_n-i\varepsilon}\Bigg)\\ &+\int_0^\infty dp\,p\,n_p(\vec{p})\ (\omega_{n,+}-\omega_{n,-}\\ &+(\omega_p(\vec{p})-k^0-\mu_p+\mu_n-i\varepsilon)\ln\frac{\omega_{n,+}-\omega_p(\vec{p})+k^0+\mu_p-\mu_n+i\varepsilon}{\omega_{n,-}-\omega_p(\vec{p})+k^0+\mu_p-\mu_n+i\varepsilon}\Bigg)\Bigg)\ .\end{aligned}$$

As a result of the evaluation of the Matsubara sums, the Fermi occupation functions $n_{n/p}(\vec{p})$ appear:

$$n(\vec{p}) = \frac{1}{e^{\beta(\omega_n(\vec{p})-\mu)}+1}$$

The abbreviations $\omega_{p,\pm}, \omega_{n,\pm}$ stem from the angular integration: $\omega_{N,\pm} = \sqrt{\vec{p}^2+\vec{k}^2+m_N^2\pm 2|\vec{p}||\vec{k}|}$

From Δ–hole we get

$$
\begin{aligned}
\Sigma_{\pi\Delta N}(\omega_k,\vec{k}) = {} & -4\,\vec{k}^2\,\frac{4}{3}\left(\frac{f_\Delta}{m_\pi}\right)^2\,\frac{1}{4\pi^2 k}\int_0^\infty dp\,p \\
& \Bigg[n_p(\vec{p})\,\Bigg(\frac{4}{3}\,(\,\Omega^+ - \Omega_-) \\
& +\ (\omega_p(\vec{p}) + k^0 + \mu_{\Delta^{++}} - \mu_p + \frac{i}{2}\,\Gamma_\Delta)\ln\frac{\Omega^+ - k^0 - \omega_p(\vec{p}) - \mu_{\Delta^{++}} + \mu_p - \frac{i}{2}\,\Gamma_\Delta}{\Omega^- - k^0 - \omega_p(\vec{p}) - \mu_{\Delta^{++}} + \mu_p - \frac{i}{2}\,\Gamma_\Delta} \\
& +\frac{1}{3}(\omega_p(\vec{p}) - k^0 + \mu_{\Delta^0} - \mu_p - \frac{i}{2}\,\Gamma_\Delta)\ln\frac{\Omega^+ + k^0 - \omega_p(\vec{p}) - \mu_{\Delta^0} + \mu_p + \frac{i}{2}\,\Gamma_\Delta}{\Omega^- + k^0 - \omega_p(\vec{p}) - \mu_{\Delta^0} + \mu_p + \frac{i}{2}\,\Gamma_\Delta}\Bigg) \\
& + n_n(\vec{p})\,\Bigg(\frac{4}{3}\,(\,\Omega^+ - \Omega_-) \\
& +\frac{1}{3}(\omega_n(\vec{p}) + k^0 + \mu_{\Delta^+} - \mu_n + \frac{i}{2}\,\Gamma_\Delta)\ln\frac{\Omega^+ - k^0 - \omega_n(\vec{p}) - \mu_{\Delta^+} + \mu_n - \frac{i}{2}\,\Gamma_\Delta}{\Omega^- - k^0 - \omega_n(\vec{p}) - \mu_{\Delta^+} + \mu_n - \frac{i}{2}\,\Gamma_\Delta} \\
& +\ (\omega_n(\vec{p}) - k^0 + \mu_{\Delta^-} - \mu_n - \frac{i}{2}\,\Gamma_\Delta)\ln\frac{\Omega^+ + k^0 - \omega_n(\vec{p}) - \mu_{\Delta^-} + \mu_n + \frac{i}{2}\,\Gamma_\Delta}{\Omega^- + k^0 - \omega_n(\vec{p}) - \mu_{\Delta^-} + \mu_n + \frac{i}{2}\,\Gamma_\Delta}\Bigg)\Bigg] \ .
\end{aligned}
$$

Again the angular integrations generate $\Omega_\pm = \sqrt{\vec{p}^2 + \vec{k}^2 + m_\Delta^2 \pm 2|\vec{p}||\vec{k}|}$.

Once all the Lindhard functions are calculated, the remaining procedure is the same as in the isospin symmetric case. In particular Migdal parameters and the πNN form factor are used to take into account the short–range repulsion and the finite–size effects.
To get the selfenergy of the π^- and also of the π^0 one has to go through the same procedure making the necessary changes of signs and labels.

Chemical potentials

The expressions given above contain the chemical potentials μ_i for the involved baryons. They can be derived in the following way:
We write

$$\mu = \mu_{isoscalar}\,B \ + \ \mu_{isovector}\,T_3\ ,$$

where B = baryon number and T_3 = 3. component of the isospin operator.

$$
\left.\begin{aligned}
\mu_{isoscalar} &= \frac{1}{2}\,(\mu_p + \mu_n) \\
\mu_{isovector} &= \mu_p - \mu_n
\end{aligned}\right\}
\qquad
\begin{aligned}
\mu_p &= \mu_{isoscalar} + \frac{1}{2}\,\mu_{isovector} \\
\mu_n &= \mu_{isoscalar} - \frac{1}{2}\,\mu_{isovector}
\end{aligned}
$$

$$\mu_{\pi^+} = \ \mu_{isovector} \qquad\qquad \mu_{\pi^-} = -\mu_{isovector} \qquad\qquad \mu_{\pi^0} = 0$$

$$\mu_{\Delta^{++}} = \mu_{isoscalar} + \frac{3}{2}\,\mu_{isovector} \qquad\qquad \mu_{\Delta^+} = \mu_{isoscalar} + \frac{1}{2}\,\mu_{isovector}$$

$$\mu_{\Delta^0} = \mu_{isoscalar} - \frac{1}{2}\,\mu_{isovector} \qquad\qquad \mu_{\Delta^-} = \mu_{isoscalar} - \frac{3}{2}\,\mu_{isovector}$$

Results

All of what follows has been calculated at normal nuclear matter density $\rho_0 = 0.16\,\mathrm{fm}^{-3}$. Only imaginary parts are shown. The pion has a 3–momentum of 100 MeV throughout.
First we inspect the effect of increasing asymmetry (proton:neutron ratios $50:50, 30:70, 10:90$) on the particle–hole Lindhard function Π_{NN}:

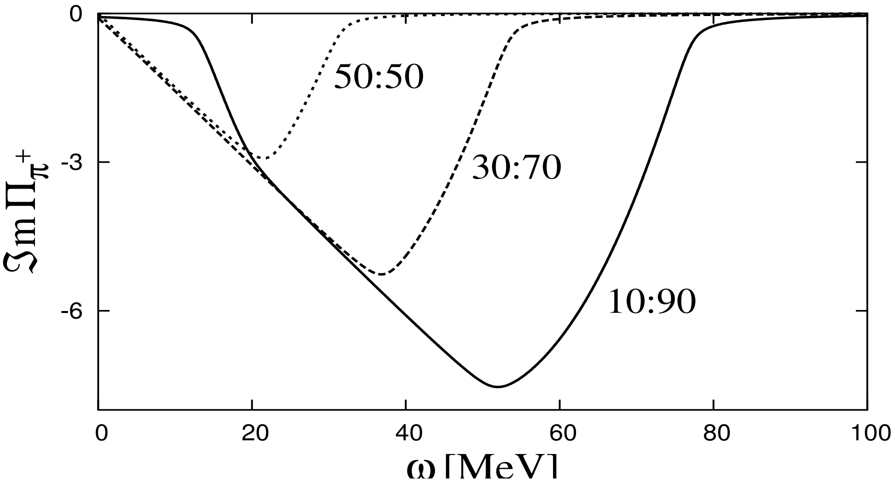

Figure 8.2: *Particle–hole Lindhard function at various proton : neutron asymmetries*

The particle–hole contribution to the π^+ propagation increases with increasing number of neutrons. This is understandable since in the case of the positive pion, particle–hole means a proton–particle, neutron–hole excitation. The π^+ has to meet a neutron for this process to happen, which will be more probable if there are more neutrons around.

The effect of increasing asymmetry on $\Pi_{\Delta N}$ is the other way around:

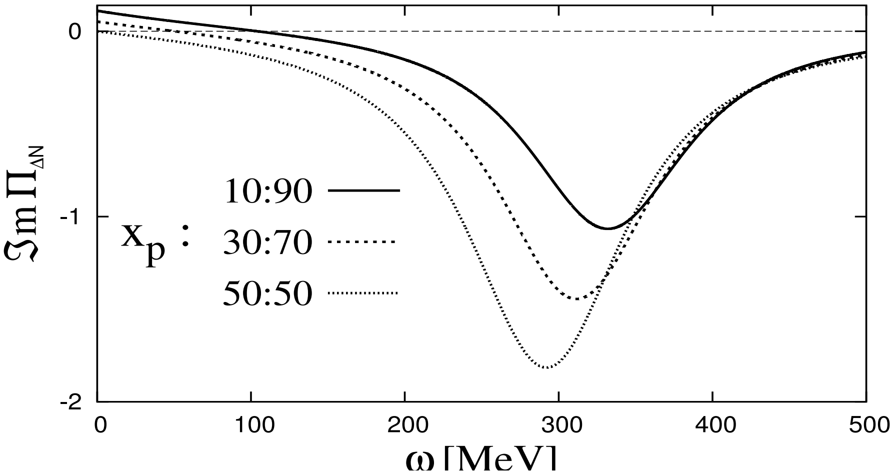

Figure 8.3: Δ*–hole selfenergy at various asymmetries*

This is now due to the different isospin transition factors at the $\pi N\Delta$ vertices (fig. D.1, appendix D.3). It is just the vertices with smaller amplitude that couple the π^+ to the neutron (and the respective Δ). Thus the π^+ does not gain in strength when the relative neutron density grows. Consequently, the ΔN contribution to the π^- grows with the increasing asymmetry.

There is yet another effect to be observed in fig. 8.3: The Δ–hole contribution becomes positive at small energies. This is an undesired but expected effect of the constant width built into the Δ propagator (eq.(5.5)). The effect gets stronger with increasing asymmetry.
To see the connection to the width, we inspect the low energy part of $\Pi_{\Delta N}$ for different values of Γ_Δ : 12 MeV, 60 MeV, 120 MeV:

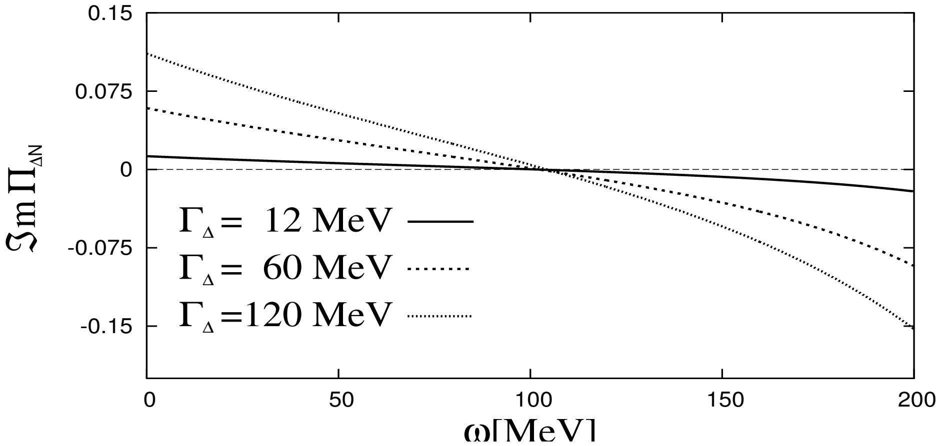

Figure 8.4: $\Pi_{\Delta N}$ *with different* Δ *widths*

An energy dependent width might have been a better choice. Urban et al. [58] chose the constant width because the resulting pion was to be used as input for the ρ meson selfenergy. Any other form of the Δ propagator caused considerable difficulties with gauge invariance, the latter being the building principle of their model.
In our case an improved Δ width is not really needed, because in the total polarization function Π (cf. eq. (5.8)) the unphysical effect is much smaller. This is due to the nucleon–hole contribution, which is strong and steep at low energies. Fig. 8.5 shows the function Π in the same sector as $\Pi_{\Delta N}$ above.

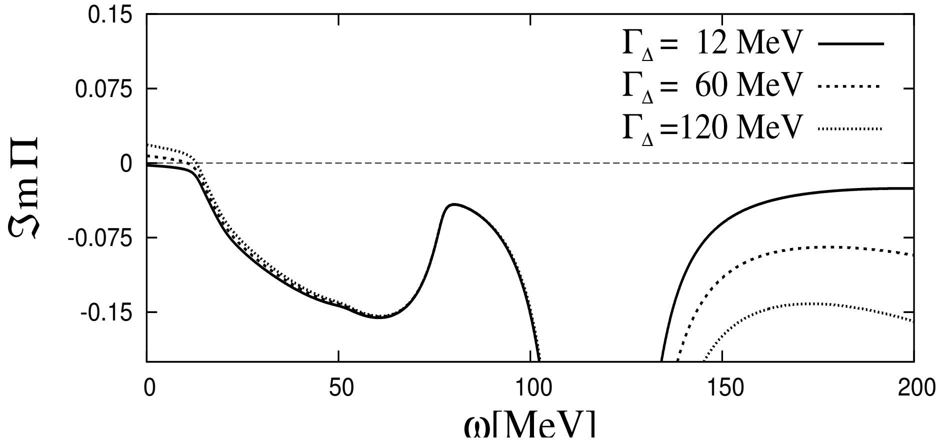

Figure 8.5: *Total* $\Pi_{\pi+}$ *with different* Δ *widths*

The pion propagator itself exhibits the same feature:

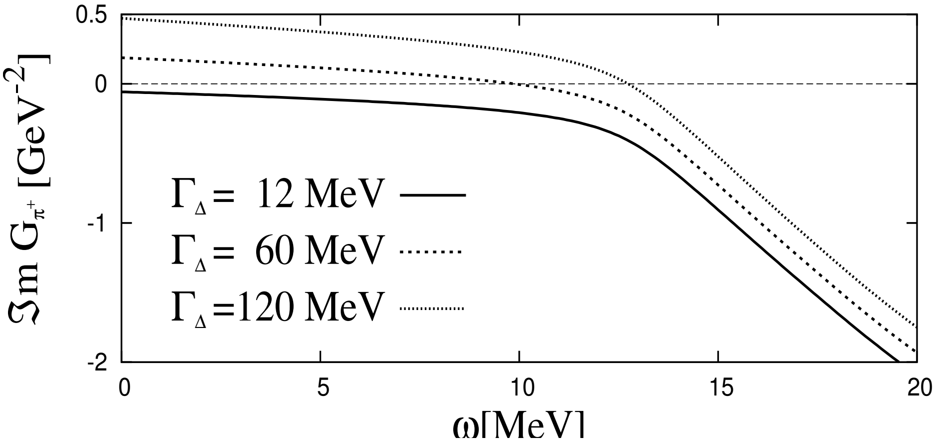

Figure 8.6: $\Im m G_{\pi^+}$ *for vanishing energy, for different widths of the* Δ

But this small deviation from zero at low energy proves to be irrelevant, because the peak value is approximately 1.4 10^3 GeV^{-2}:

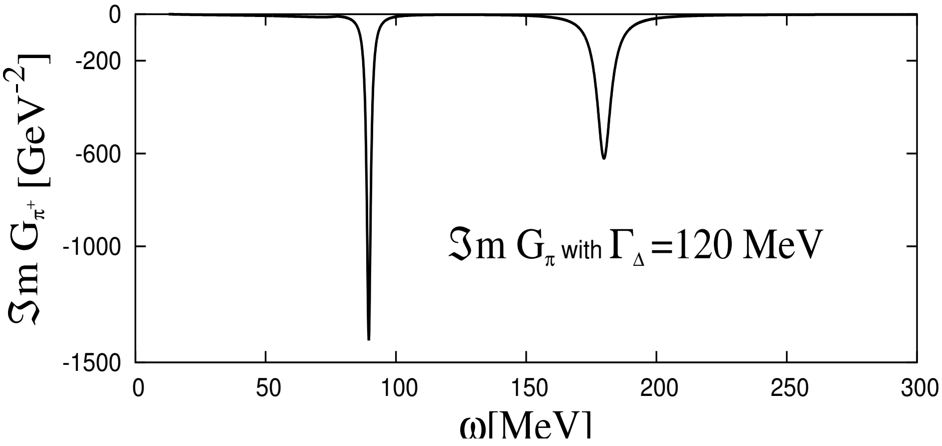

Figure 8.7: *Total* $\Im m G_{\pi^+}$

8.2.2 s–wave pion selfenergy

Following a suggestion by Oertel [72], we also check the influence of s–wave pion–nucleon interactions. The s–wave pion selfenergy is usually held responsible for the existence of deeply bound pionic states in heavy nuclei [73]. The complete expressions for asymmetric matter in two–loop chiral perturbation theory are given in a calculation by Kaiser and Weise [74]. In sec. (D.5) in appendix D their analytic expressions are listed. These terms depend mainly on the difference of neutron and proton Fermi momenta, which means that the s–wave selfenergy is especially important in isospin asymmetric matter. We take this result to include it into the program giving the total pion selfenergy.

The diagrams which are taken into account are displayed in fig. 8.8.

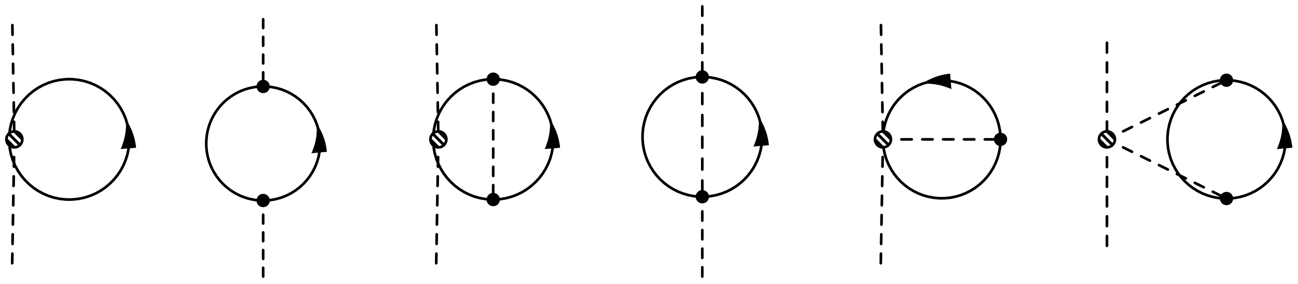

Figure 8.8: *s–wave in–medium pion selfenergy diagrams up to two loops. Solid and dashed lines represent nucleons and pions, respectively. From [74]*

In the approximation chosen by the authors of Ref. [74], the s–wave selfenergy remains purely real. Of the diagrams shown above, indeed only the second and fourth can develop an imaginary part. Thus the s–wave selfenergy is just a real constant. Nevertheless it has quite some influence on the pion propagator, as can be seen in fig. 8.9:

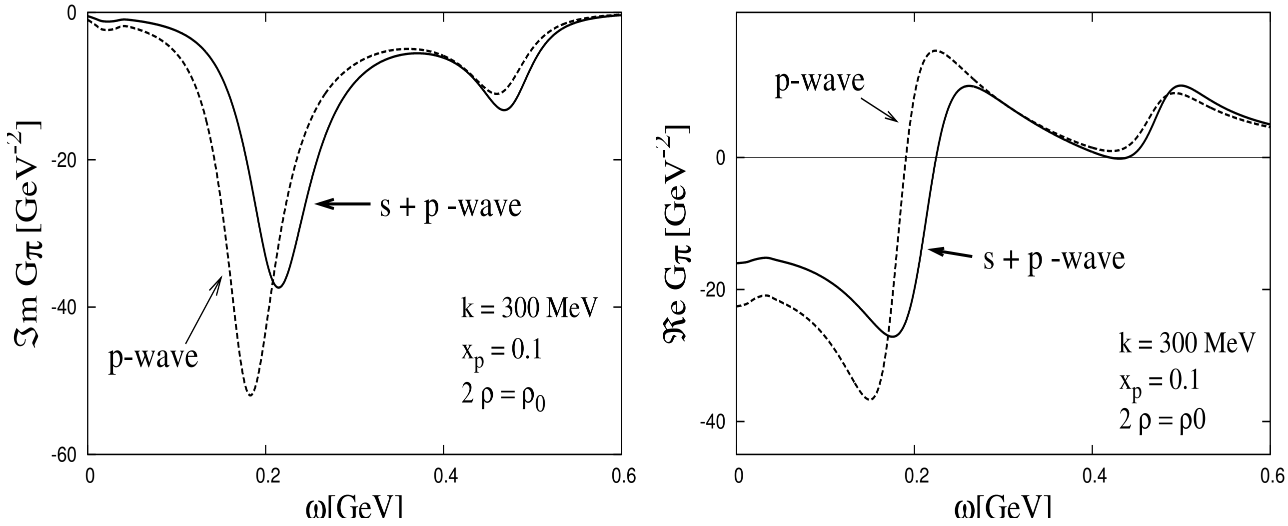

Figure 8.9: *Imaginary (left) and real part (right) of the π^- propagator including s–wave and p–wave contributions (solid line) and p–wave only (dashed line)*

The figure shows that the π^- is pushed upwards in energy, the *s*–wave selfenergy is here repulsive. In the case of the π^+ it is the other way around. Thus the π^+ mass is further lowered by the *s*–wave interactions. In this figure (8.9) as well as the following ones, the environment chosen has a density of $\rho = 2\,\rho_0$ and an asymmetry with 10% protons.

Here we are interested in the consequences the 'improved' pion has on the kaon properties. First the pions are incorporated in the loops with Λ and Σ. The left panel in fig. 8.10 shows the difference the *s*–wave pion selfenergy makes in the $\pi^0\Lambda$ loop.

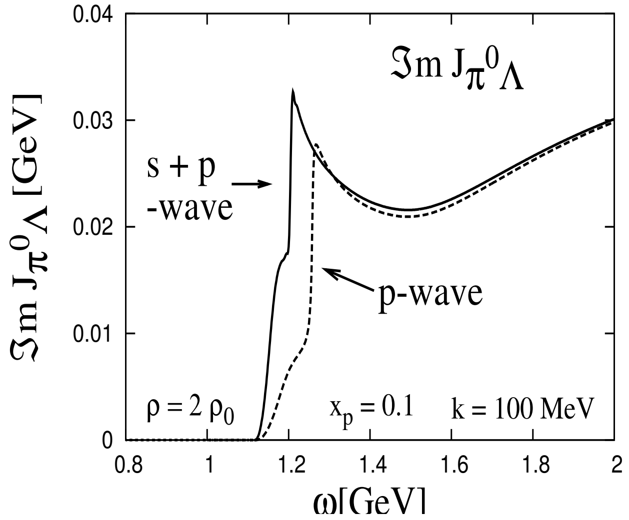

Figure 8.10: *Left: Imaginary part of $\pi^0\Lambda$ loop, π^0 including s–wave and p–wave selfenergies (solid line) and p–wave selfenergy only (dashed line) Right: Imaginary part of T–matrix element $n\bar{K}^0 \rightsquigarrow n\bar{K}^0$, pion loops including s–wave and p–wave selfenergies (solid line) and p–wave selfenergy only (dashed line)*

This difference is prominent but does not constitute a qualitative change (the same applies to all the other loops containing the pion). The significance of the s–wave selfenergy is further reduced in the following steps of our scheme. The right panel of fig. 8.10 exemplifies the impact that it has on the scattering amplitudes, here on the element $\mathcal{I}mT_{n\bar{K}^0\rightsquigarrow n\bar{K}^0}$.
Fig. 8.11 shows the K^- propagator after the first iteration when the pions in the underlying πY loops are modified by p –wave and $s+p$ –wave interactions.

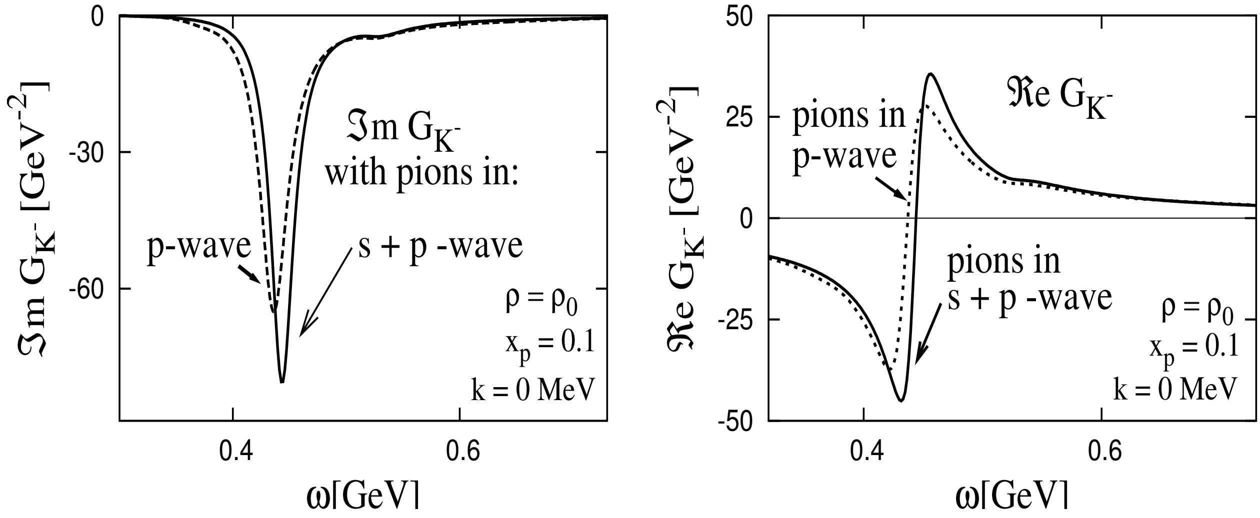

Figure 8.11: *Imaginary (left) and real part (right) of the K^- propagator after the first iteration containing pions with including s–wave and p–wave selfenergies (solid line) and p–wave selfenergy only (dashed line)*

Obviously, the influence of the s–wave selfenergies is still present but not very strong. The zero of the real part of G_{K^-} (the in–medium kaon mass) is shifted upwards by just a few MeV (right panel in fig. 8.11).

8.3 Kaons in asymmetric nuclear matter

The calculation of the $\bar{K}N$ scattering and the kaon selfenergy in the case of asymmetric nuclear matter follows the scheme developed in the previous chapters. The major difference to the symmetric case is the length of the relevant analytic expressions. All the meson–baryon pairs in eqs. (3.1)–(3.6) are now distinct channels and must be taken into account separately. The fully expanded T–matrix element comprises several thousand terms. Consequently, the expressions must be handled by computer algebra. Nevertheless, the procedure is quite straightforward. In the end, different selfenergies for the K^- and the $\bar{K}^0$ are obtained.

The densities and proton : neutron ratios investigated were:

$$\begin{aligned}
\rho &= \rho_0 = 0.16\mathrm{fm}^{-3}, && \text{proton fractions } x_p = 0.5, x_p = 0.3, x_p = 0.1\\
\rho &= 2\,\rho_0 = 0.32\mathrm{fm}^{-3}, && \text{proton fractions } x_p = 0.5, x_p = 0.3, x_p = 0.1, x_p = 0.01\\
\rho &= 5\,\rho_0 = 0.80\mathrm{fm}^{-3}, && \text{proton fractions } x_p = 0.5, x_p = 0.1
\end{aligned}$$

Once protons and neutrons contribute with different Fermi momenta to kaon–nucleon scattering, the scattering amplitudes for $pK^- \rightsquigarrow pK^-$ and $n\bar{K}^0 \rightsquigarrow n\bar{K}^0$ will be different. There is also a transition matrix element for $pK^- \rightsquigarrow n\bar{K}^0$. The imaginary parts of these T–matrix elements are shown in figs. 8.12 and 8.13. At a given density, only a proton fraction of 0.1 is considered. The differences between the amplitudes are quite sizeable.

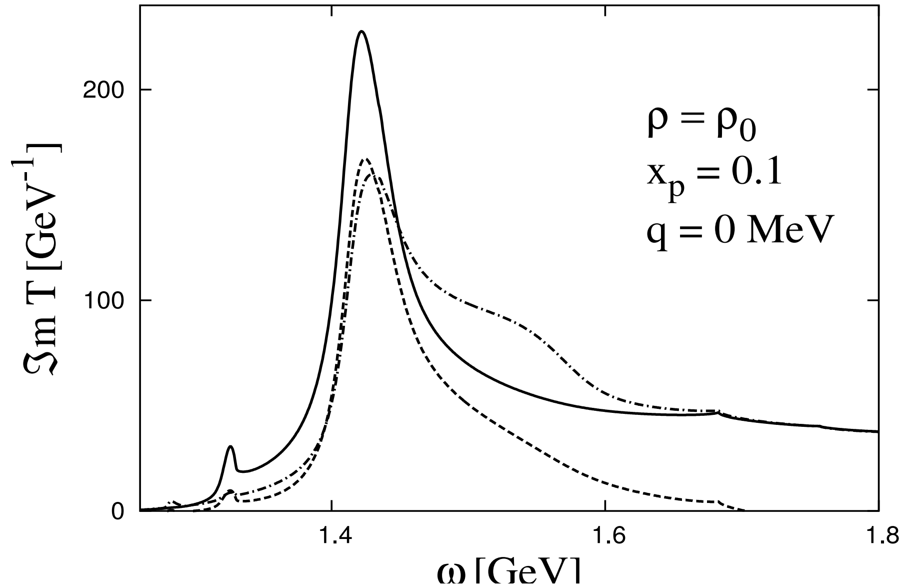

Figure 8.12: *$\bar{K}N$–T–matrix elements: $pK^- \rightsquigarrow pK^-$ (solid line), $n\bar{K}^0 \rightsquigarrow pK^-$ (dashed line), $n\bar{K}^0 \rightsquigarrow n\bar{K}^0$ (dashed–dotted line)*

At normal nuclear matter density, the amplitude for $n\bar{K}^0 \rightsquigarrow n\bar{K}^0$ is already much broader than the $pK^- \rightsquigarrow pK^-$ amplitude (fig. 8.12 above). At the given asymmetry, $x_p = 0.1$, there are many more neutrons around. The probability for an incoming kaon to interact is thus much higher for the $\bar{K}^0$.

The effect is basically the same also at higher densities. The pK^- amplitude is further broadened but remains recognizable. However, the strong coupling leads to a peculiar shaping of the $n\bar{K}^0$ amplitude (fig. 8.13 below):

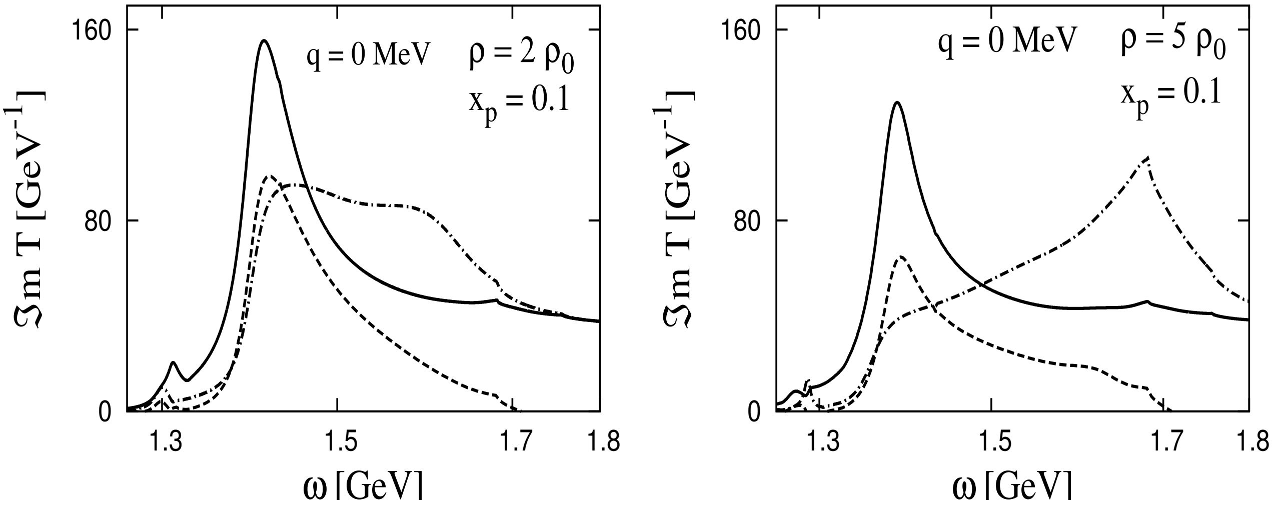

Figure 8.13: *$\bar{K}N$–T–matrix elements: $pK^- \rightsquigarrow pK^-$ (solid line), $n\bar{K}^0 \rightsquigarrow pK^-$ (dashed line), $n\bar{K}^0 \rightsquigarrow n\bar{K}^0$ (dashed–dotted line). Left panel: $\rho = 2\,\rho_0$, right panel: $\rho = 5\,\rho_0$*

The small peak that is always visible around 1.3 GeV can be attributed to the influence of the in–medium pion. The bump produced by the medium–modified pion (cf. fig. 5.3) sits at the $\pi\Sigma$ ($\pi\Lambda$) threshold. Although the main part of the amplitude gets flattened a lot due to the kaon broadening, that energy region is not ‘reached’ so the small peak does not merge entirely with the main amplitude. This is caused by the selfconsistency iteration: as we have seen in section (7.2), the selfconsistent amplitude is not shifted much from its vacuum position (in contrast to the ‘Pauli–blocking–only’ amplitude). Obviously the $\pi\Sigma$ threshold is too far below. If the pion were also to be included selfconsistently, this feature might vanish, yet this is mere speculation.

The $T_{n\bar{K}^0}$ amplitudes show another interesting feature: the peak around 1.7 GeV that builds up with increasing density. We can inspect this more closely by directly comparing the $T_{n\bar{K}^0}$ (and T_{pK^-}) amplitudes at different densities. Fig. 8.14 shows the evolution of the amplitudes going from ρ_0 to $5\,\rho_0$.

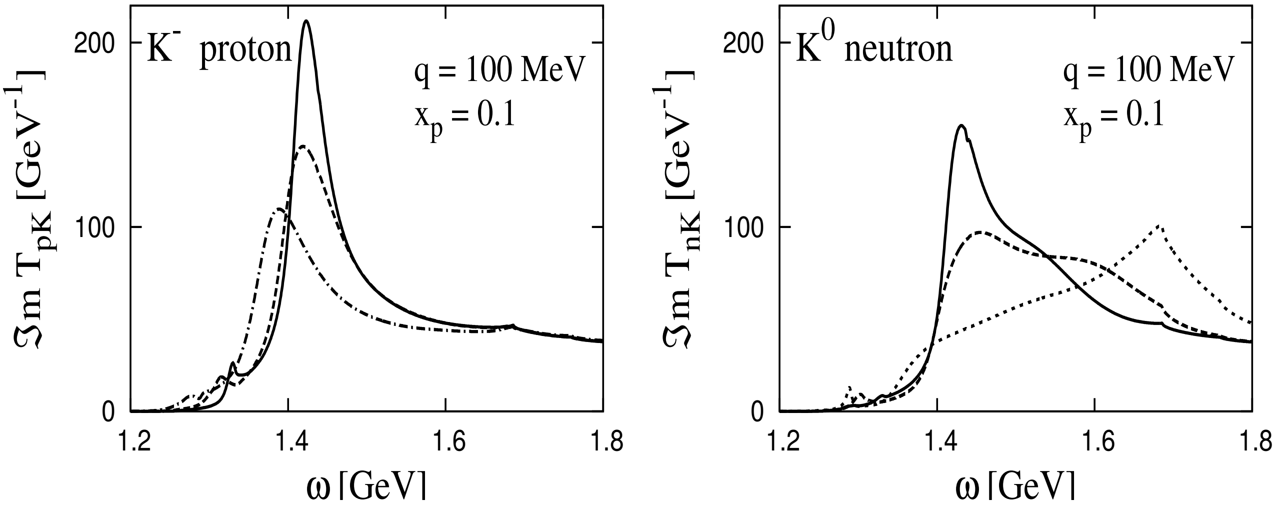

Figure 8.14: *Density dependence of* $\bar{K}N$*–*T*–matrix elements with* 10% *protons:* $\rho = \rho_0$ *(solid line),* $\rho = 2\,\rho_0$ *(dashed line),* $\rho = 5\,\rho_0$ *(dotted line). Left panel:* $pK^- \rightsquigarrow pK^-$*, right panel:* $n\bar{K}^0 \rightsquigarrow n\bar{K}^0$

Obviously, T_{pK^-} (on the left of fig. 8.14) is pushed to lower energies with increasing density. There is no such pronounced structure around 1.7 GeV as in $T_{n\bar{K}^0}$ (on the right). That amplitude gets pushed up in energy. This moved spectral strength seems to concentrate around 1.7 GeV – that is the region of the two channels involving the η. The fact that no in–medium modification of the η was included might have an influence on the shape of the resulting $T_{n\bar{K}^0}$ matrix element.

At a proton fraction of $x_p = 0.3$ no calculation was done at $\rho = 5\,\rho_0$. Still, an increase of the density from $\rho = \rho_0$ to $\rho = 2\,\rho_0$ broadens the T–matrix elements in a similar way, as is shown in fig. 8.15. However, the tendency of T_{pK^-} of getting shifted downwards in energy is now reversed:

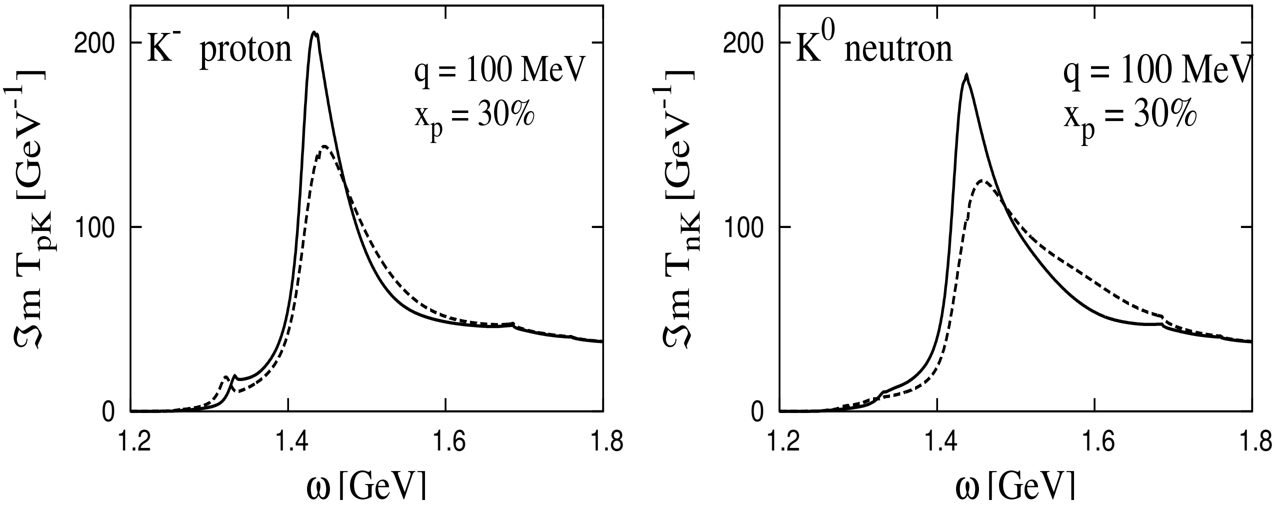

Figure 8.15: *Density dependence of* $\bar{K}N$*–*T*–matrix elements with* 30% *protons:* $\rho = \rho_0$ *(solid line),* $\rho = 2\,\rho_0$ *(dashed line). Left panel:* $pK^- \rightsquigarrow pK^-$*, right panel:* $n\bar{K}^0 \rightsquigarrow n\bar{K}^0$

For comparison fig. 8.16 again shows the density dependence of the T–matrix for all three densities in the symmetric case ($x_p = 0.5$).

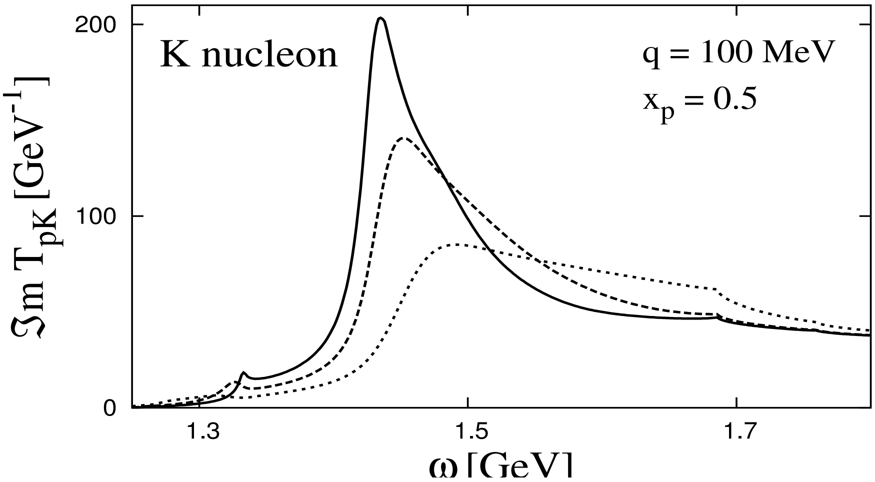

Figure 8.16: *Density dependence of $\bar{K}N$–T–matrix elements in symmetric matter ($x_p = 0.5$): ρ_0 (dotted line), $2\,\rho_0$ (dashed line), $5\,\rho_0$ (dotted line)*

Yet another comparison to demonstrate the effect of asymmetric proton : neutron ratios is given in fig. 8.17:

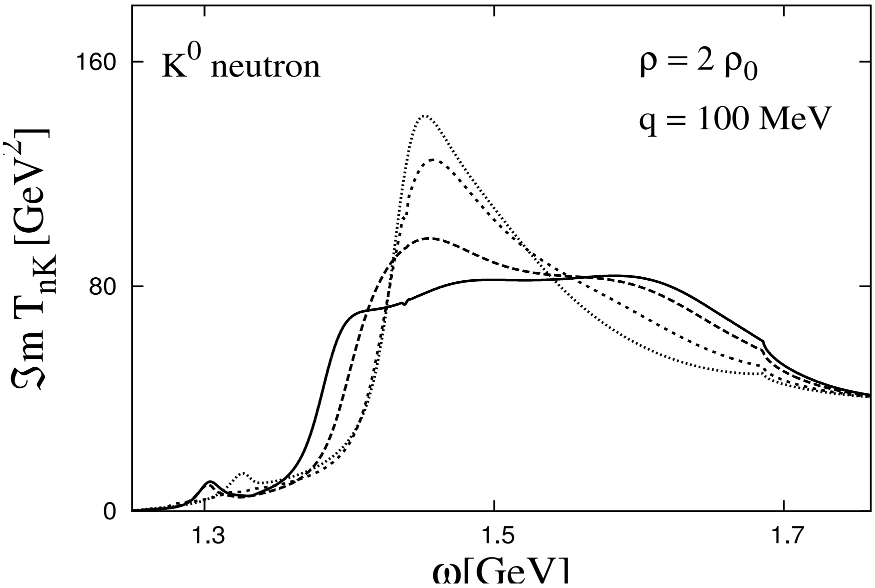

Figure 8.17: *Asymmetry dependence of $T_{n\bar{K}^0}$ at $\rho = 2\,\rho_0$: proton fractions $x_p = 0.5$ (solid line), $x_p = 0.3$ (dashed line), $x_p = 0.1$ (dotted line), $x_p = 0.01$ (small dots)*

The same effects that were described above for increasing the overall density $\rho_0 \rightarrow 5\,\rho_0$ are seen here for an increase in the relative density of neutrons.

However, one has to be careful drawing too simple conclusions. Increasing the relative density of neutrons is of course not the same as increasing the overall density. After all, the amplitudes are the result of a coupled–channels calculation. As an example one can compare the T_{pK^-} element at normal density and symmetric matter with the case of $\rho = 5\,\rho_0$ and just 10% protons: In both cases there will be 0.08 protons/fm^3 ! However, the corresponding amplitudes are quite different:

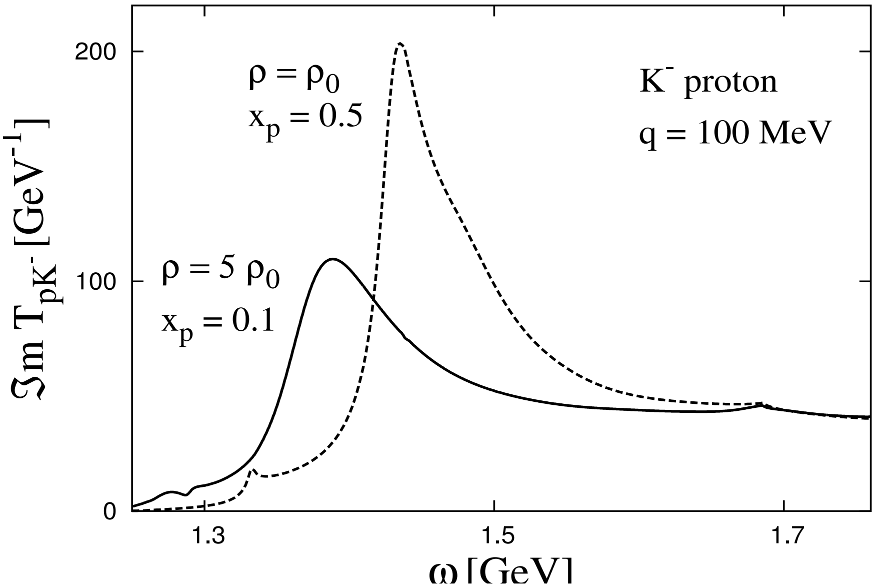

Figure 8.18: *Dependence on asymmetry and density of* T_{pK^-}*: Both at* $\rho = \rho_0, x_p = 0.5$ *(dashed line) and* $\rho = 5\,\rho_0, x_p = 0.5$ *(solid line) the number density of protons is* $0.08/fm^3$.

We have studied the behavior of the $\bar{K}N$–scattering amplitudes in dense matter. Now we are turning to the kaon selfenergy and propagator.
In analogy to the proton and neutron scattering amplitudes we ask how the K^- and $\bar{K}^0$ selfenergies differ in the asymmetric medium.

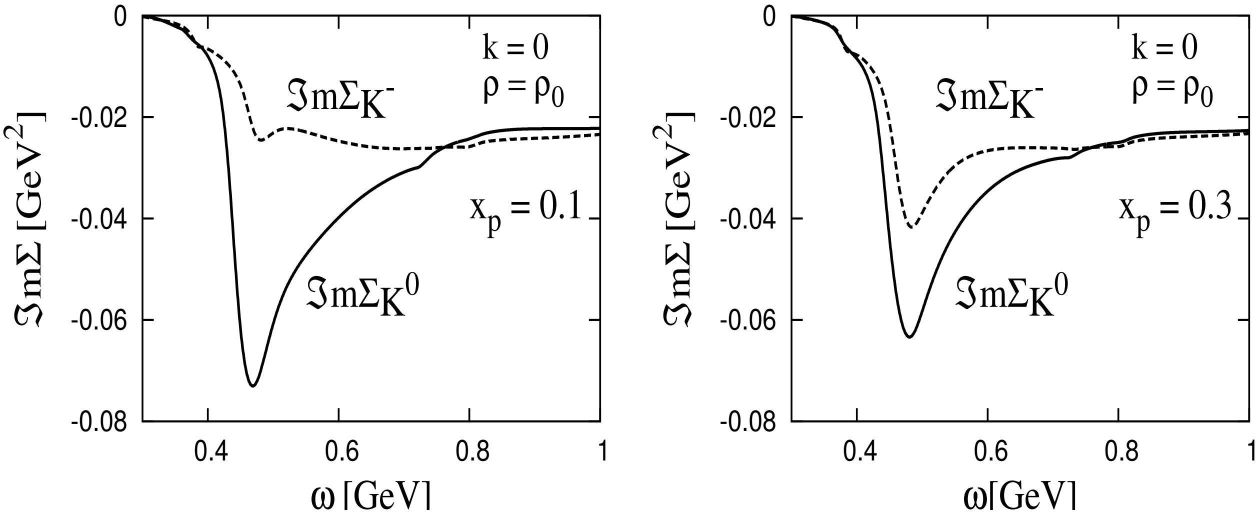

Figure 8.19: *K^- and $\bar{K^0}$ selfenergies at $\rho = \rho_0$ for proton fraction $x_p = 0.1$ (left panel) and $x_p = 0.3$ (right panel)*

The behavior is as expected: the difference is larger in the more asymmetric case, where the imaginary part of the $\bar{K^0}$ selfenergy is much stronger than the K^- selfenergy.

With increasing density this behavior does not change qualitatively. Figs. 8.20, 8.21 show the imaginary parts of the selfenergies at twice nuclear matter density.

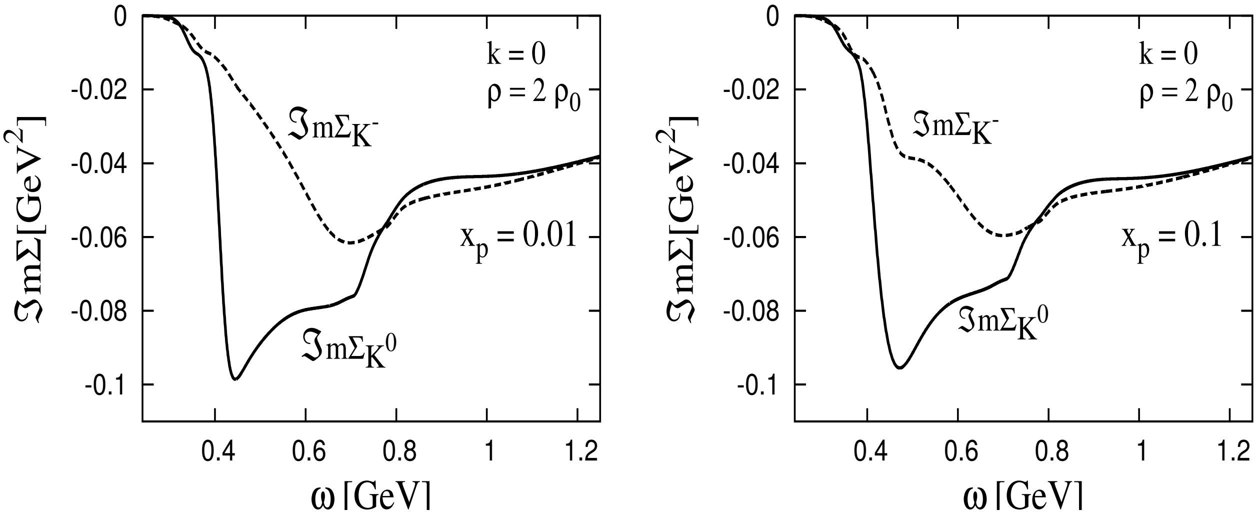

Figure 8.20: *K^- and $\bar{K^0}$ selfenergies at $\rho = \rho_0$ for proton fraction $x_p = 0.01$ (left), $x_p = 0.1$ (right)*

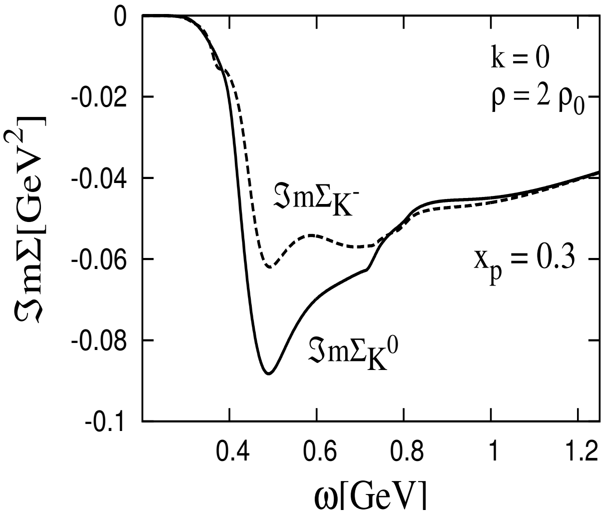

Figure 8.21: *K^- and $\bar{K^0}$ selfenergies at $\rho = \rho_0$ for proton fraction $x_p = 0.3$ (left) and symmetric matter ($x_p = 0.5$, right)*

Of course the total strength of the selfenergy does increase with growing density, as larger Fermi energies become available (cf. eq. 6.1). This is revealed by fig. 8.22:

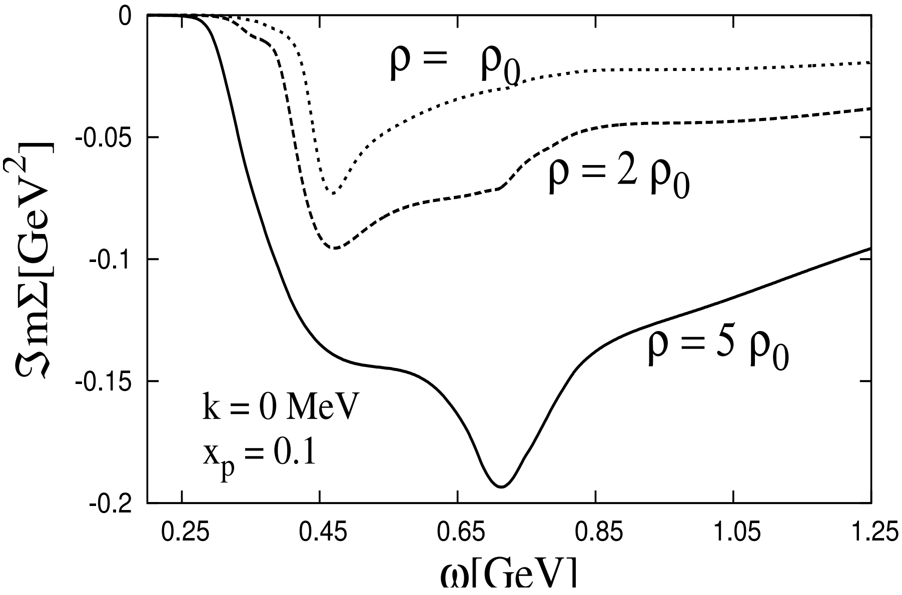

Figure 8.22: *$\bar{K^0}$ selfenergies at different densities (proton fraction $x_p = 0.1$, $|\vec{k}| = 0$)*

All these features are reflected in the kaon spectral functions which are shown in the following figures 8.23, 8.24:

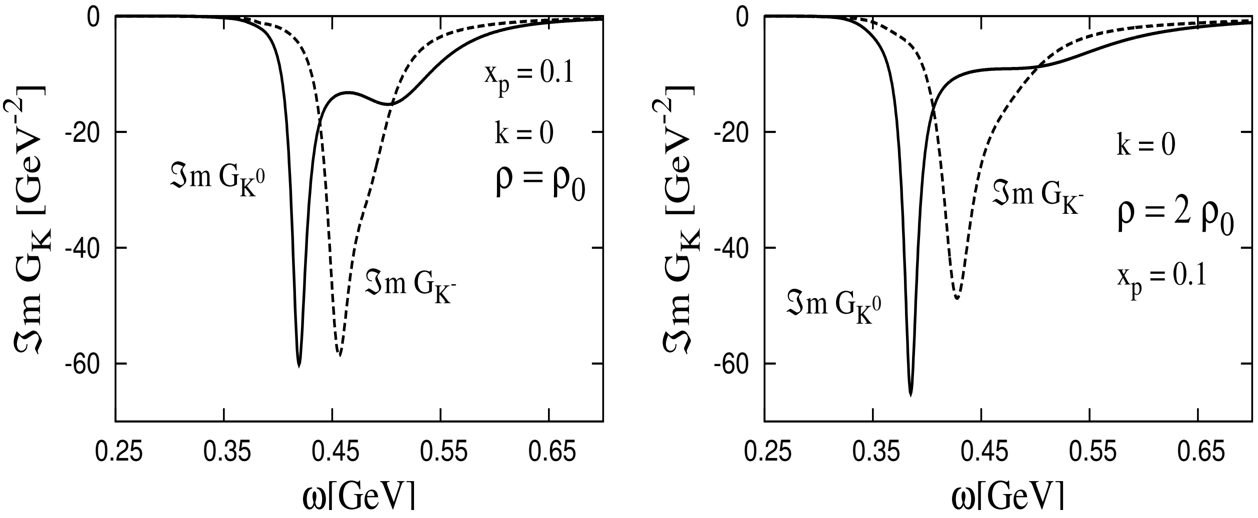

Figure 8.23: *K^- and $\bar{K}^0$ propagators at $\rho = \rho_0$ (left panel) and $\rho = 2\,\rho_0$ (right panel) at a proton fraction $x_p = 0.1$, $|\vec{k}| = 0$ MeV*

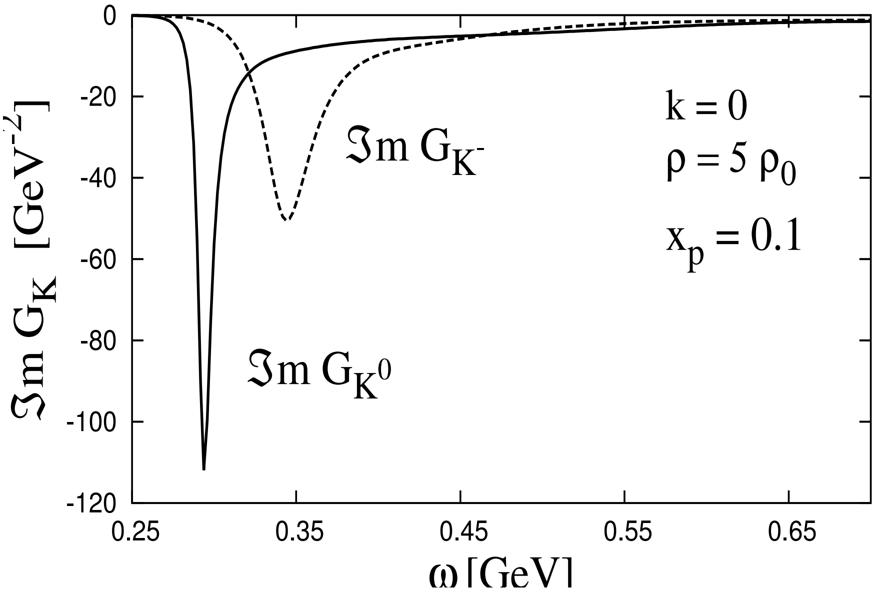

Figure 8.24: *K^- and $\bar{K}^0$ propagators at $\rho = 5\rho_0$, $x_p = 0.1$, $|\vec{k}| = 0$ MeV*

The momentum dependence of the kaon propagator is not changed in the asymmetric medium: Fig. 8.25 displays the imaginary parts of the K^- and $\bar{K}^0$ propagators at a density of $\rho = 2\,\rho_0$ and a proton fraction of 10%.

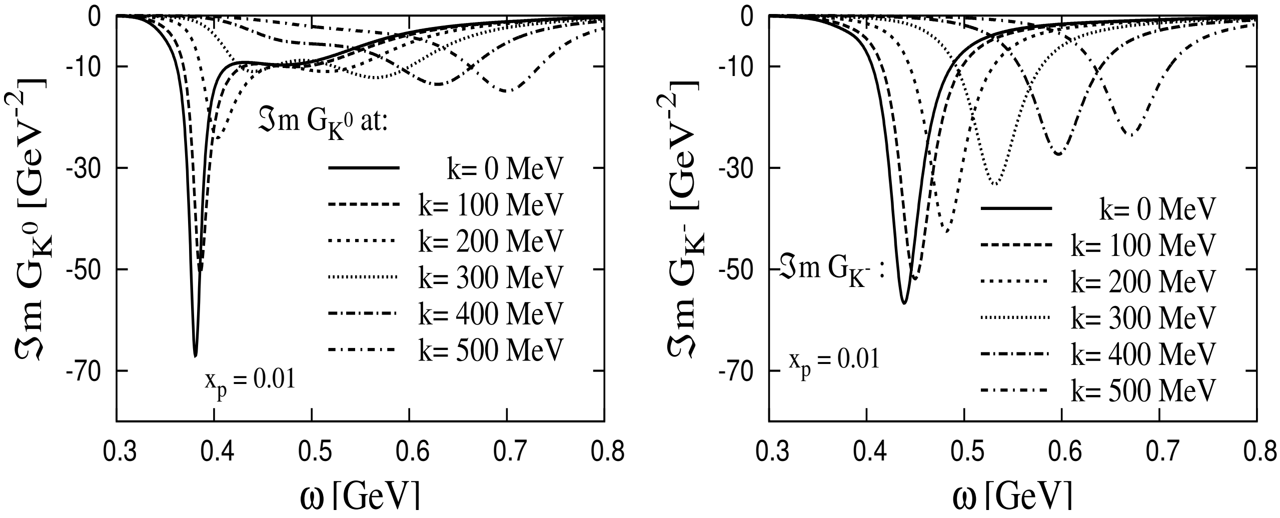

Figure 8.25: *$\bar{K^0}$ (left) and K^- propagators (right panel) at $\rho = 2\,\rho_0$, $x_p = 0.01$ for momenta $|\vec{k}| = 0 - 500$ MeV*

The K^- on the right of fig. 8.25 looks quite unspectacular. The relatively low density experienced by the K^- does not deform its spectral function. On the other hand, the $\bar{K^0}$ on the left shows the variation with momentum already familiar from the case of symmetric matter (chap. (7)).

The variation of $\Im m G_K$ with the proton–neutron asymmetry can be studied by comparing the curves in fig. 8.26 (normal matter density), fig. 8.27 (for $\rho = 2\,\rho_0$) and fig. 8.28 (for $\rho = 5\,\rho_0$).

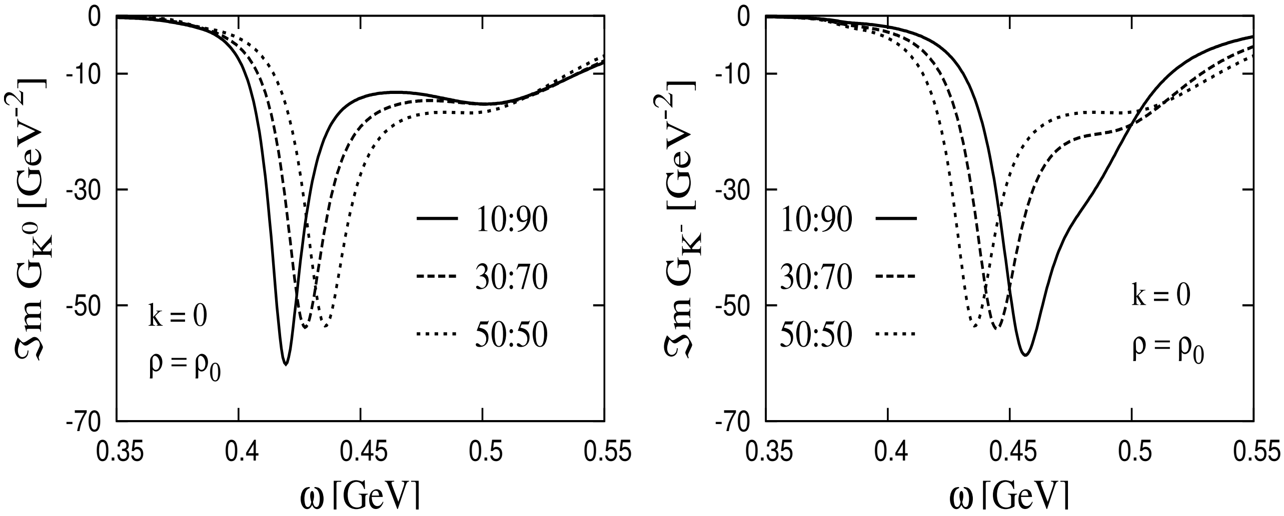

Figure 8.26: *Propagators of $\bar{K^0}$ (left) and K^- (right) at $\rho = \rho_0$ for different proton : neutron ratios*

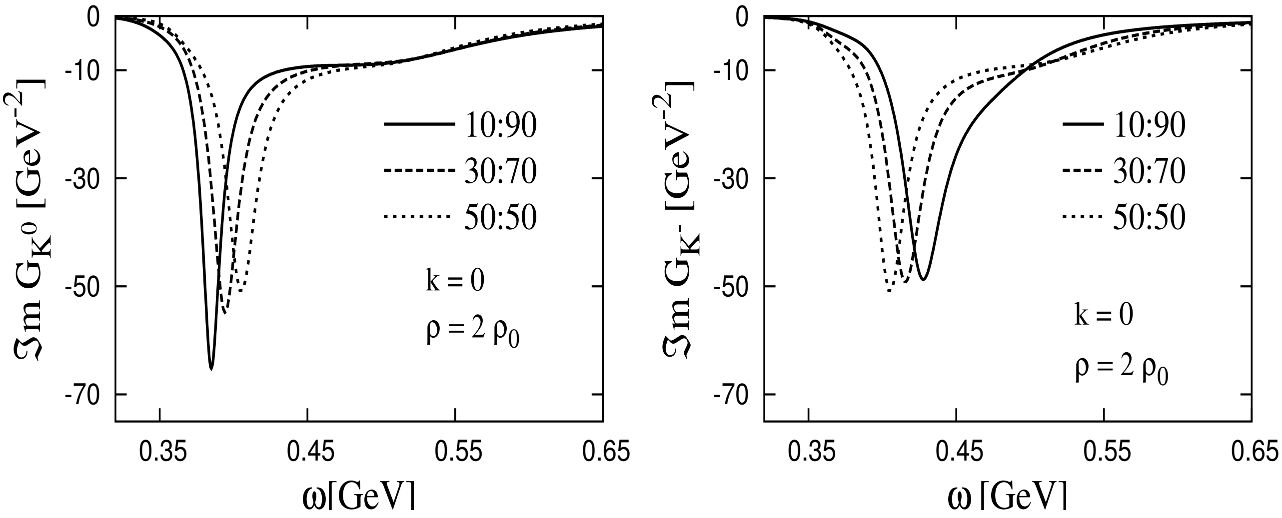

Figure 8.27: *Propagators of* $\bar{K^0}$ *(left) and* K^- *(right) at* $\rho = 2\,\rho_0$ *for different proton : neutron ratios*

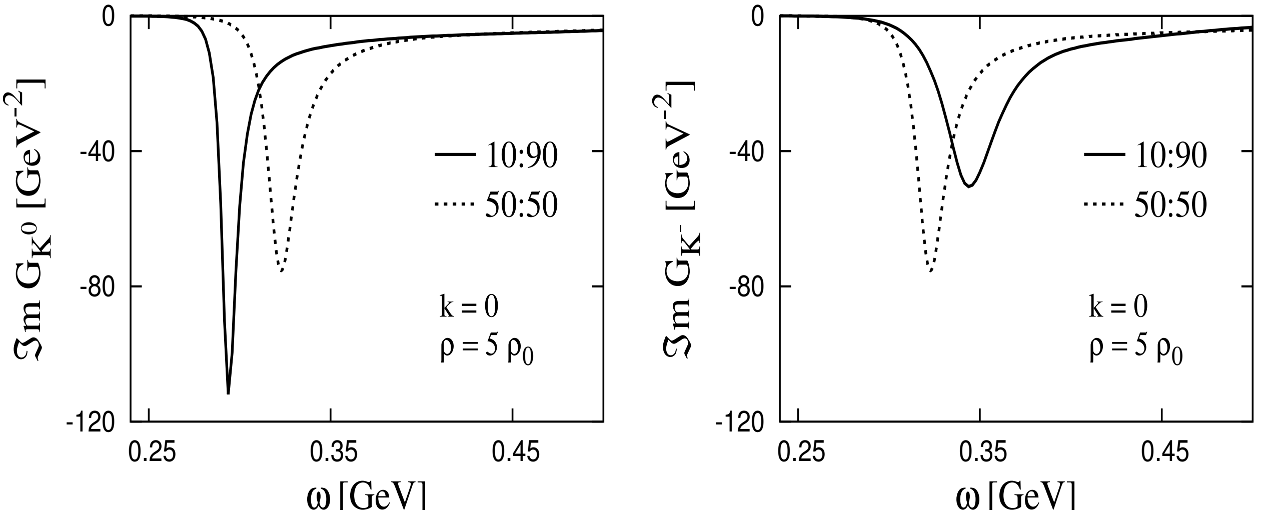

Figure 8.28: *Propagators of* $\bar{K^0}$ *(left) and* K^- *(right) at* $\rho = 5\,\rho_0$ *for different proton : neutron ratios*

There are no surprises in these figures. The properties of the kaon in the dense medium are obviously developing smoothly from the vacuum case to dense matter and from the symmetric to the asymmetric matter case.

As an overview at the end of this chapter fig. 8.29 shows the imaginary part of the kaon propagator, now comparing directly the different densities, at an asymmetry of $x_p = 0.1$.

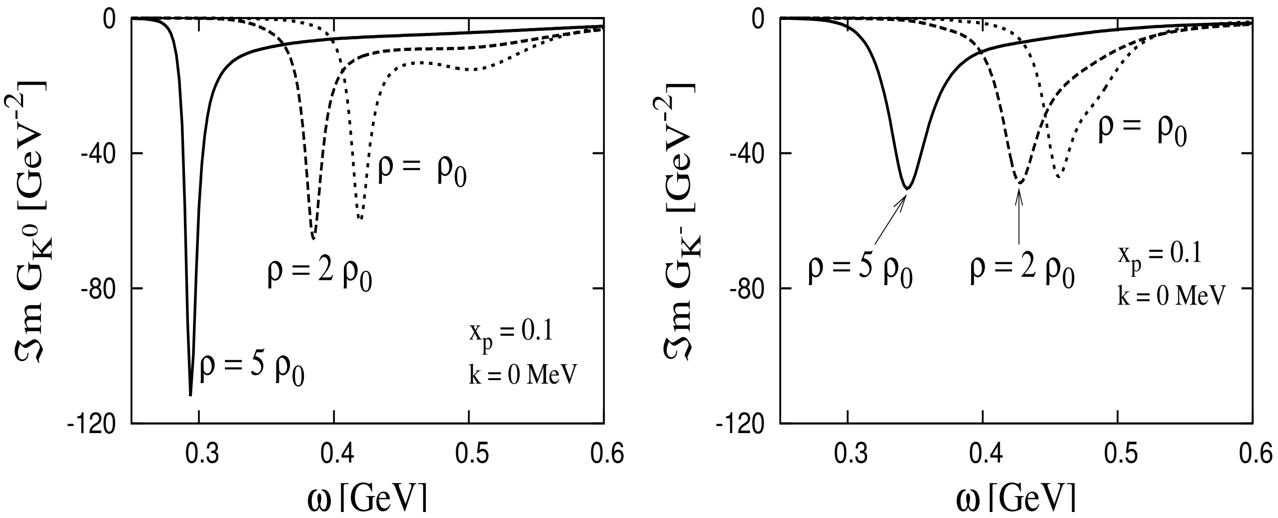

Figure 8.29: *Kaon propagator at* $x_p = 0.1, |\vec{k}| = 0$ *for different densities.* $\bar{K^0}$ *on the left,* K^- *on the right*

Chapter 9

Kaon condensation in neutron stars

The physics of neutron stars is intimately connected to nuclear and hadron physics. Neutron stars provide unique samples of nuclear matter. The equation of state of nuclear matter influences a number of astronomical observables such as the maximum mass and radius of the star or its cooling rate. In this way nuclear matter samples can actually be studied experimentally [75].

Sure enough a neutron star is not really a vast nucleus. For one thing, it is bound by gravity, not by nuclear forces. Actually, the density in the interior of neutron stars is so high that the nucleons mostly feel the repulsive part of the nucleon–nucleon interaction [75]. Thus neglecting any nuclear forces leads to a maximum mass for a stable neutron star of ~ 0.7 solar masses [76]. In model the compact star consists of an ideal Fermi gas of neutrons. It is only their degeneracy pressure that supports the star. The observed masses are scattered around 1.35 solar masses, however [77]. The pressure stabilizing these stars against gravitational collapse is indeed provided by the nuclear interactions [75].

There is another difference between nuclear matter and neutron star matter that provides the connection to kaon physics. The very high densities in neutron stars lead to very high Fermi energies for the involved particles. Then, various weak processes become energetically possible. Neutron star matter itself is produced because inverse beta decay ${}^{A}Z + e^{-} \rightarrow {}^{A}(Z-1) + \nu_e$ occurs once the electron Fermi energy is high enough. Otherwise matter would remain in a white–dwarf–like phase up to the collapse to a black hole.

In addition there are strangeness–changing reactions. Thus, nucleons from the top of their Fermi seas might convert into hyperons. Similarly, electrons might convert into kaons. This will occur if the electrochemical potential becomes equal to the kaon 'chemical potential' (which is just the kaon energy or in–medium mass): $\mu_e = \mu_K = m_K$ [69, 15, 16].

Then the processes

$$e^{-} \leftrightarrow K^{-} + \nu_e \qquad n \leftrightarrow p + K^{-} \tag{9.1}$$

become possible.

This will have an effect similar to the neutronization described above: Neutronization reduces the electron density and hence the electron pressure that stabilizes the (white dwarf) star. It is then the degeneracy pressure of the neutrons that prevents further collapse. In analog, conversion of electrons to kaons will also reduce the electron number and thus their pressure. On the other hand the kaons will form a condensate at zero momentum that just provides a background of negative charge but as a condensate of bosons does not exert a degeneracy pressure. Thus the formation of a condensate can considerably soften the nuclear equation of state [69, 78]. That is a welcome effect in neutron star models since usually the maximum neutron star mass comes out higher than the experimental 1.4 solar masses. In addition, the reaction eq. (9.1) increases the proton fraction in the system. Since the isospin–asymmetry part of the nuclear interaction is repulsive, a reduction of the asymmetry will further decrease the pressure or energy of the system.

The chemical potential of the boson K^- is given by its energy. Thus the kaon condensate will appear once the charge chemical potential μ_e reaches the in–medium energy of the kaon. This means that the inverse kaon propagator should vanish there [79, 78]:

$$G_K^{-1}(\omega = \mu_e, \vec{k} = 0) = \mu_e^2 - m_K^2 - \Sigma_K(\mu_e) = 0 \tag{9.2}$$

The task is now to determine the value of μ_e at a given density and to check whether it is large enough to fulfill condition (9.2). We have two physical constraints on the neutron star system that can be used here: beta equilibrium and charge neutrality.

First we count the degrees of freedom and realize that in addition to protons, neutrons and electrons also muons have to be taken into account in case the electron chemical potential is larger than the muon mass. Then the conversion

$$e^- \rightarrow \mu^- + \overline{\nu}_\mu + \nu_e$$

will lead to a finite density of muons. Thus there are four degrees of freedom, the four particle species involved respectively their chemical potentials.[1] The conversion of electrons to muons and the beta decay,

$$p + e^- \leftrightarrow n + \nu_e,$$

provide two beta–equilibrium conditions:

$$\begin{aligned} \mu_\mu &= \mu_e \\ \mu_e + \mu_p &= \mu_n \end{aligned} \tag{9.3}$$

A third condition is provided by charge neutrality: A neutron star must be perfectly neutral due to the large ratio of electrical to gravitational coupling. Hence, proton and lepton densities must be equal:

$$\rho_p = \rho_e + \rho_\mu \tag{9.4}$$

To connect density and chemical potential, we assume a noninteracting Fermi gas.

$$\rho = \int \frac{d^3p}{(2\pi)^3} \frac{g}{1 + e^{\beta(\varepsilon - \mu)}} \overset{T=0}{=} \frac{p_f^3}{3\pi^2} \qquad (g = 2 \text{ for spin } 1/2 \text{ fermions}, \varepsilon = \sqrt{p^2 + m_N^2})$$

Now we can solve for the charged chemical potential μ_{e^-} and find the relative densities of protons and neutrons.
Fig. 9.1 shows the result as fractions with respect to the total density for both protons and neutrons. The neutron fractions lie very close to one, the proton fractions are very small (note the logarithmic scale). The ground state of such a system of noninteracting but very densely packed nucleons would hence be almost pure neutron matter.

---

[1] No chemical potential is assigned to the neutrinos because we are interested in the later stages of neutron star development when the neutrinos can leave the star freely.

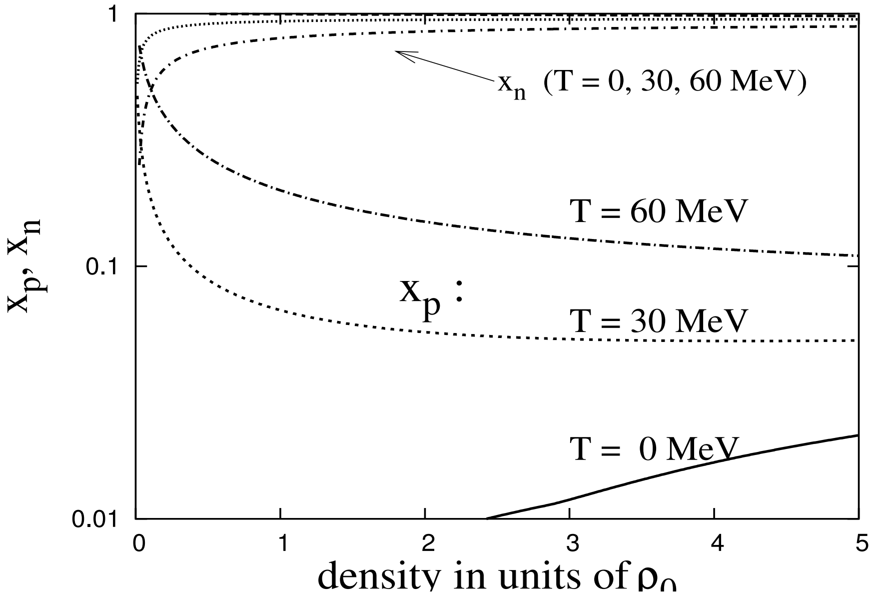

Figure 9.1: *Proton and neutron fractions of an ideal Fermi gas in beta equilibrium*

Consequently, the charge chemical potential also turns out to be rather small:

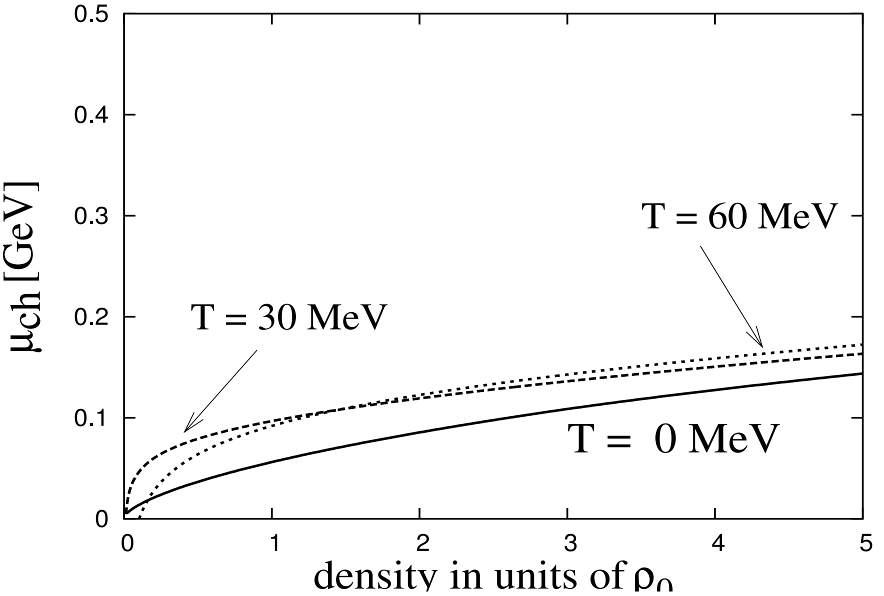

Figure 9.2: *Charge chemical potential*

The proton fraction has an ultrarelativistic limit we can compare with [75]. Starting with the beta equilibrium, we express everything in terms of the proton Fermi momentum p_{f_p}:

$$
\begin{aligned}
\mu_e + \mu_p &= \mu_n \\
(p_{f_e}^2 + m_e^2)^{1/2} + (p_{f_p}^2 + m_p^2)^{1/2} &= (p_{f_n}^2 + m_n^2)^{1/2} \\
\rho = \frac{1}{3\pi^2}(p_{f_n}^3 + p_{f_p}^3) \quad &\Rightarrow \quad (3\pi^2\rho - p_{f_p}^3)^{2/3} = p_{f_n}^2 \\
\Rightarrow (p_{f_e}^2 + m_e^2)^{1/2} + (p_{f_p}^2 + m_p^2)^{1/2} &= ((3\pi^2\rho - p_{f_p}^3)^{2/3} + m_n^2)^{1/2}
\end{aligned}
\tag{9.5}
$$

Setting all masses to zero in eq. (9.5) and expressing again in terms of $\rho_p = (p_{f_p}^3/(3\pi^2)$ gives

$$
\rho_p \to \frac{1}{9}\rho \tag{9.6}
$$

This ultrarelativistic limit will be reached if the Fermi momenta are all much larger than the masses of the particles: we see that it is not reached within a range of densities (1–$5\rho_0$) we can hope to apply our kaon calculation for.

On the other hand, the importance of nuclear interactions for the neutron star structure was already mentioned at the beginning of this chapter. If these forces are responsible for pushing the masses of observed neutron stars from the limit for non–interacting nucleons of $0.7M_\odot$ to $1.4M_\odot$, their influence on particle ratios and chemical potentials will be significant.

There is numerous work on the structure of neutron star, using all kinds of nuclear models. We pick out a collection of results by Pandharipande et al. [80]. The authors compare a variety of nuclear models such as the Bonn, Urbana and Argonne models as well as the Nijmegen results. Fig. 9.3 shows their results for the proton fraction in beta–stable matter. The curve labeled '$A18 + \delta_\nu + UIX^*$' is the authors' calculation, based on the Argonne NN interaction v_{18} and including boost corrections (δ_ν) and a parameterization of three nucleon forces (UIX^*).

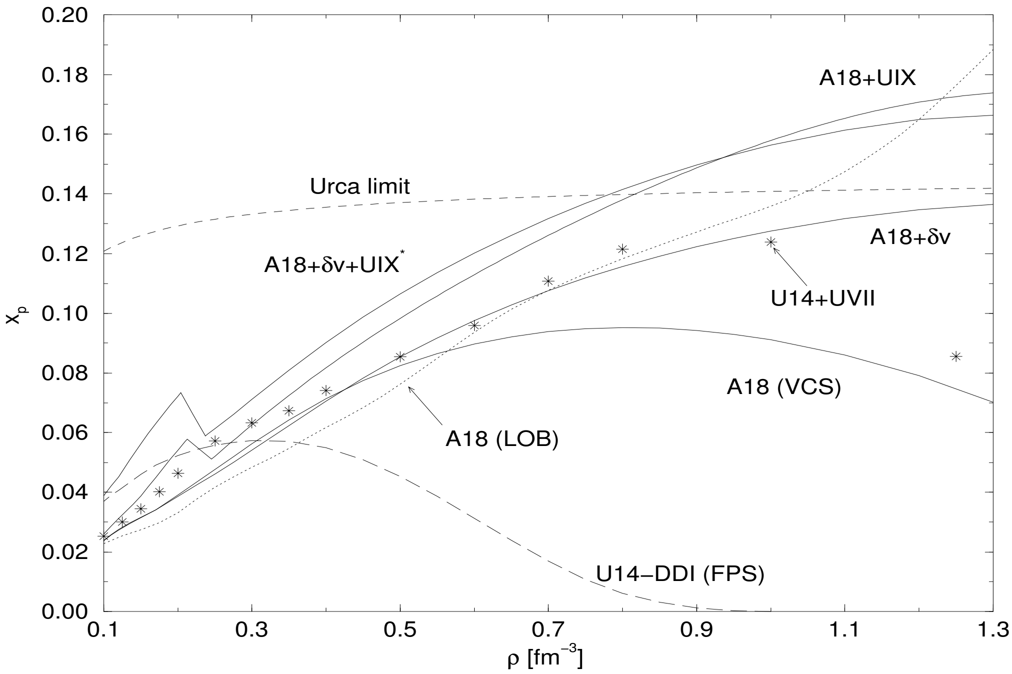

Figure 9.3: *Proton fraction x_p from [80]: Results for different nucleon–nucleon interactions.*

We can use this figure to obtain an estimate of the likely proton fraction at the densities treated in this work. Thus the potential $A18 + \delta\nu + UIX^*$ gives

$$\begin{aligned} \rho =& \rho_0 & \leadsto \quad & x_p = 0.06 \\ \rho =& 2\rho_0 & \leadsto \quad & x_p = 0.08 \\ \rho =& 5\rho_0 & \leadsto \quad & x_p = 0.14\ . \end{aligned}$$

Hence the proton fraction of $x_p = 0.1$ we used is a good choice.
In the cited publication by Pandharipande et.al. there is also a figure giving the density dependence of the charge chemical potential, fig. 9.4:

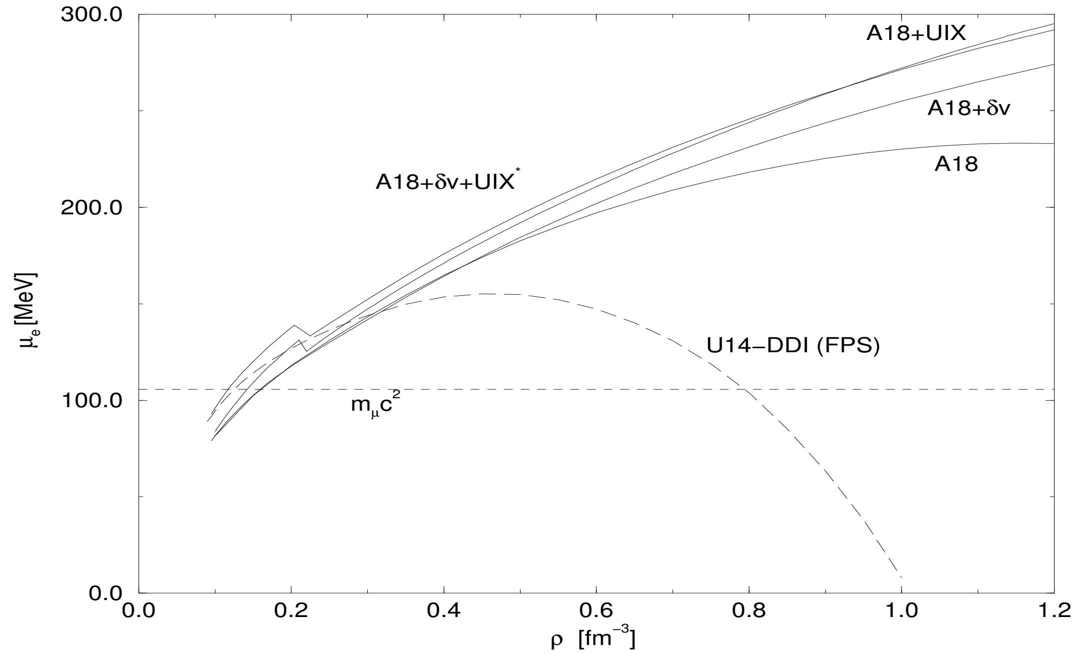

Figure 9.4: *Charge chemical potential μ_e from [80]: Results for different nucleon–nucleon interactions: Argonne model $A18$, with relativistic corrections δ_ν, Urbana IX three–body interaction UIX^* and older Urbana $U14$ density–dependent (DDI) interaction*

We can read off the values of interaction $A18 + \delta\nu + UIX^*$

$$\begin{aligned} \rho =& \rho_0 & \leadsto \quad & \mu_e = 124 \text{ MeV} \\ \rho =& 2\rho_0 & \leadsto \quad & \mu_e = 157 \text{ MeV} \\ \rho =& 5\rho_0 & \leadsto \quad & \mu_e = 245 \text{ MeV}\ . \end{aligned}$$

Now we can apply the criterion of eq.(9.2) to the kaon selfenergy calculated previously and see where that point lies in comparison to these chemical potentials.
Figs. 9.5, 9.6 show the real part of the inverse kaon propagator at vanishing momentum:

$$\tilde{G}_{\bar{K}}^{-1}(\omega, |\vec{k}| = 0) = \omega^2 - m_K^2 - \Re e(\Sigma_{\bar{K}}(\omega))$$

The imaginary part of the selfenergy is left out – this will have to be discussed later on.
The resulting curve $\tilde{G}_{\bar{K}}^{-1}$ will go through zero at the energy corresponding to the in–medium mass of the kaon. Of course there are different dispersion relations for the K^- and the $\bar{K^0}$. For comparison, also the free dispersion relation of the kaon is given.

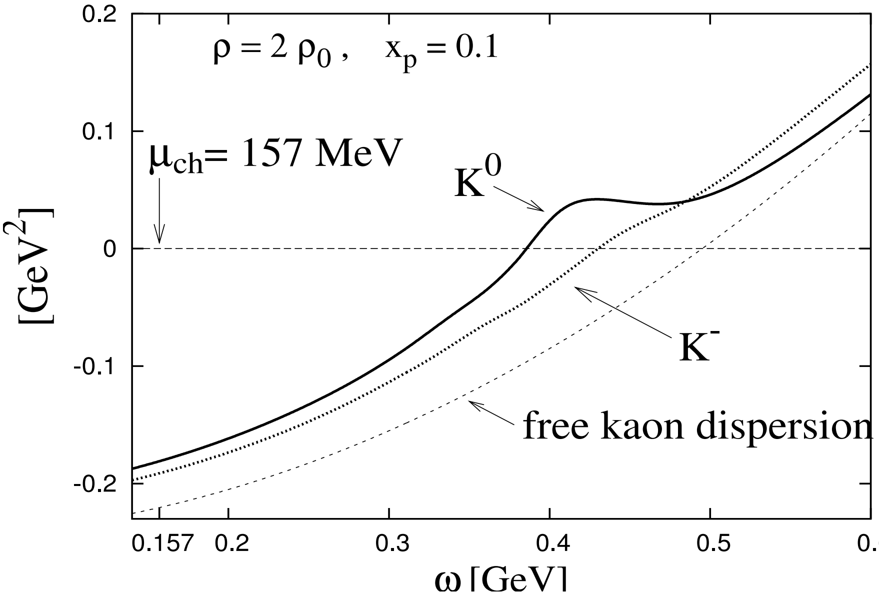

Figure 9.5: *In–medium kaon mass at $\rho = 2\rho_0$: as the solution of* $\omega^2 - m_K^2 - \Re e\Sigma_{\bar{K}}(\omega) = 0$

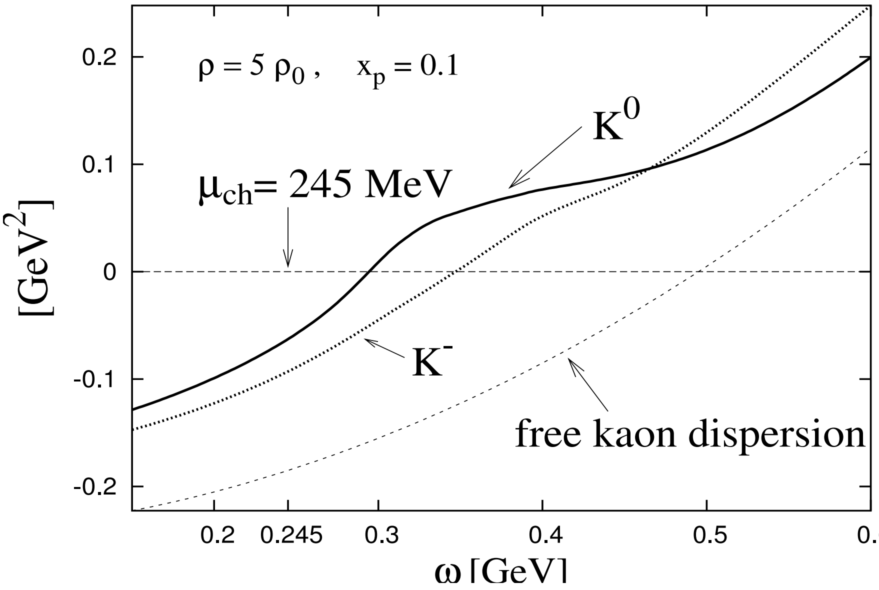

Figure 9.6: *In–medium kaon mass at $\rho = 5\rho_0$ as the solution of* $\omega^2 - m_K^2 - \Re e\Sigma_{\bar{K}}(\omega) = 0$

It is obvious that for both densities the chemical potentials from [80] lie far below the in–medium mass of the kaon.

One should realize that the curves for the $\bar{K}^0$ in the figs. 9.5, 9.6 are shown for mere illustrative purposes: The kaons that show up via the production mechanism eq. (9.1) will be the negative kaons K^-. Even if condensation of the $\bar{K}^0$ were to occur, it would play no role in the balance of leptons and nucleons in the neutron star. Yet the K^- is much less affected by the interactions in the dense medium, as we have seen in the previous chapters.

To summarize: The particle relevant for the neutron star structure is the K^-. At a density of $\rho = 5\rho_0$ the K^- has a mass of about $\tilde{m}_{K^-} = 347$ MeV. The charge chemical potential under these circumstances lies 100 MeV lower. From this point of view there is no chance for kaon condensation to occur.

Now fig. 9.3 seems to indicate that there is still some uncertainty concerning the correct form of the nuclear interaction for neutron star matter. The possible values for the proton fraction vary, but in no model does it rise to 0.20 or more. On the other hand, it was shown in chapter 8 that the variations of the selfenergies and spectral functions of the kaon that are due to variations in composition (different x_ps in e.g. figs. 8.26–8.28) are of the order of a few MeV only. Along similar lines we observe that the difference in masses from fig. 9.6 above is just $m_{K^-} - m_{\bar{K}^0} = 63$ MeV. So even if the prediction of having about 10 % protons in the interior of a neutron star were entirely wrong, the results for the kaon selfenergy would still not allow for condensation.
Similar reasoning applies to the uncertainties in the charge chemical potential as apparent in fig. 9.4: they are just as small. There is no indication that the real μ_{ch} would be a so much larger that the gap of 100 MeV might be closed.

The idea to take the calculation to even higher energies is also not promising. The density dependence of the kaon propagator as we observe it in fig. 8.23 indeed shows the kaon effective mass to move down in energy with increasing density. That looks quite impressive at first glance. On the other hand it becomes clear that even the extremely high density of $5\rho_0$ only has lead to a shift of about 150 MeV with respect to the vacuum. The conclusion is that even going to yet higher densities would not help much: the K^- would be pushed downwards further while the proton fraction and the electrochemical potential would increase, but not enough to induce a condensation process.

There is a caveat in the discussion above. The question was whether the in–medium mass of the K^- would sink below the charge chemical potential of the medium. However, the concept of an in–medium mass of the kaon is questionable in the first place.
A definition of mass exists only for free stable particles. For these their masses are given by the pole of their propagators. But what about instable, decaying particles? Mass is connected to inertia, and it is difficult to determine that for a particle that is never in an asymptotic state. Still, it is possible to determine the complex in–medium energy of such a particle as the solution of the dispersion relation [69]

$$\varepsilon^2(\vec{k}) = \vec{k}^2 + m^2 + \Sigma(\omega = \varepsilon(\vec{k}), \vec{k}). \tag{9.7}$$

For $|\vec{k}| = 0$ this gives the mass as the pole of the propagator in the complex plane. In general, this will be a complex number.
Another possible definition of the mass is via the extremum of the spectral function of the particle. In the limit of a small width Γ, i.e. a small imaginary part of the selfenergy, the particle's propagator will be of a Breit–Wigner form:

$$G \approx \frac{1}{\omega^2 - m^2 + \frac{i}{2}\Gamma}$$

The maximum of the spectral function $-\mathcal{I}mG$ will coincide with position of the pole on the real axis. Thus in the limit $\Gamma/m \ll 1$, the intuitive picture of the mass of a particle being where the strength of its spectral function is concentrated becomes exact. In fig. 9.7, the imaginary part of the K^- propagator is concentrated around 340 MeV, so one would talk about a K^- in–medium mass of roughly that value.

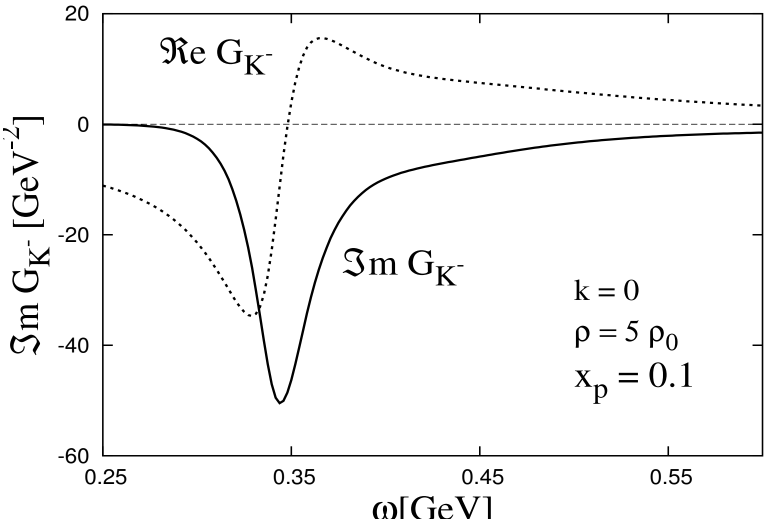

Figure 9.7: *K^- propagator at $\rho = 5\rho_0, x_p = 0.1$: real part (dotted) and imaginary part (solid line)*

One can solve eq. (9.7) and take the real part of $\varepsilon(0)$ or one can use the graphical method of figs. 9.5, 9.6 to obtain a value for the in–medium mass.
Of course it is already clear from fig. 9.7 that these numbers are very close: The width of the K^- is rather small: the FWHM from fig. 9.7 is just 37 MeV, so indeed $\Gamma/m \ll 1$. The maximum of the imaginary part and the zero of the real part of G_{K^-} are very close. In fact the values are 344 MeV and 348 MeV, respectively.

From this point of view, the in–medium kaon mass is defined quite well.

A counterexample could be the pion as in fig. 8.7. The in–medium pion is split into two or more branches which are well separated. A single dispersion relation for the pion would be entirely meaningless. However, each level of the pion has a quite well defined mass.
Another ficticious counterexample would be a particle with a spectral function as e.g. in fig. 7.12. There, it is the kaon at a finite 3–momentum of 300 MeV. However, there are particles such as the ρ meson that become as broad also at rest with respect to the surrounding matter. In such a case, the question of condensation cannot be discussed as above. The in–medium mass would be moved so far into the complex plane that the comparison with a real number μ_{ch} as in figs. 9.5, 9.6 would become meaningless.

Kaon condensation represents a possible phase transition of neutron star matter. To determine whether it really occurs, one should in principle construct the thermodynamic potential of the system

$$\Omega = U - TS - \mu N \;=\; U - \mu N \quad \text{at low or vanishing temperature}$$

and find its minimum respectively search for the phase of higher pressure.[2]
The grand partition function Z is given by

$$Z = e^{-\beta(H-\mu N)} \;=\; e^{-\beta\Omega}$$

where H represents the Hamiltonian of the system and makes the connection to (the nomenclature of) field theory or particle physics.

---

[2] μ and N are generic chemical potentials and particle numbers for all the particle species present.

An examination of the partition function as done in ref. [81] shows how it can be written in terms of diagrams. The contributing diagrams comprise all two–particle irreducible diagrams that can be constructed from the given interaction. Two–particle irreducible diagrams are those which cannot be split into parts by cutting two lines. All these contributions can be gathered in a functional commonly called Φ [82]. Deriving quantities from this functional gives rise to the method of Φ–derivable theory. The thermodynamic potential Ω can be expressed using the functional Φ:

$$\Omega = -i\mathcal{T}r(\ln i\mathcal{G}^{-1}) + \mathcal{T}r(\Sigma i\mathcal{G}) + \Phi(\mathcal{G}) \tag{9.8}$$

where $\mathcal{G}$ is the full Greens function, i.e. in our case the full two–particle propagator appearing in the Bethe–Salpeter equation. The traces $\mathcal{T}r$ are taken over internal degrees of freedom, including an integral over momentum space.

The selfenergies can now be obtained by varying the functional Φ with respect to the propagator:

$$\Sigma = -\frac{\delta\Phi}{\delta(i\mathcal{G})} \tag{9.9}$$

Amplitudes as e.g. the kaon–nucleon scattering are given by second derivatives, or variation of the selfenergy with respect to the propagator:

$$V = \frac{\delta\Sigma}{\delta(i\mathcal{G})} = -\frac{\delta^2\Phi}{\delta(i\mathcal{G})\delta(i\mathcal{G})} \tag{9.10}$$

These quantities that are derived from the functional Φ are then thermodynamically consistent, due to eq. (9.8). Such a description includes the reaction of the medium to the changes introduced by the onset of the kaon condensation. In contrast our calculation gives a kind of snapshot of the modifications of the antikaons at fixed environmental parameters, in particular at fixed proton fraction. On the other hand, we have seen how the condensation process will increase the proton fraction: $n \leftrightarrow p + K^-$. Consequently, one should re–enter the procedure of chap. 8 and repeat it until a selfconsistent result is achieved. This then would be thermodynamic selfconsistency. But that procedure is not feasible.[3]

Eqs. (9.9), (9.10) can be interpreted graphically. The diagrams found in literature that illustrate this point usually look nicer since they start with three–point vertices, nevertheless, starting from a Weinberg–Tomozawa type vertex, the simplest contributions to Φ are the ones displayed in fig. 9.8.

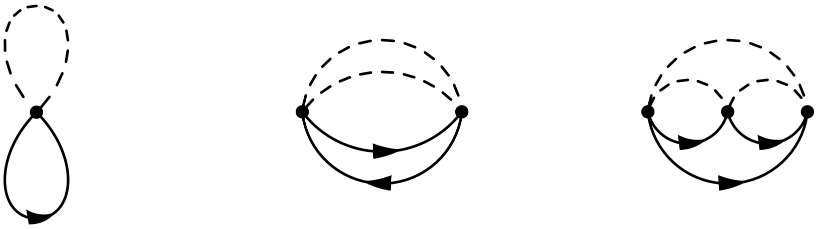

Figure 9.8: *Terms contributing to the functional* Φ

---

[3] One might also object that the kaon as described in chap. 8 does not even come near the condensation point, thus obliterating the need for such an involved calculation – if there is no conversion of neutrons to protons and kaons the medium does not have to react to it.

Variation with respect to a propagator can be done by cutting one line.
Thus if we cut the dashed line in the middle diagram of fig. 9.8, we get

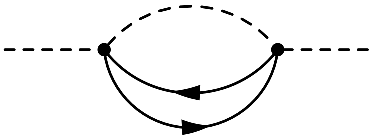

which is obviously one contribution to the kaon (dashed line) selfenergy.

Cutting a nucleon (solid) line in the diagram above means a second derivative and leads to

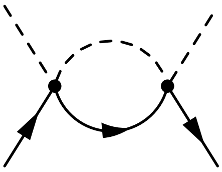

– a typical part of the scattering equation.

Since some elements of the calculations of the preceding chapters are recognizable here, one might think that the step towards the thermodynamical potential consists of just closing the remaining open line in

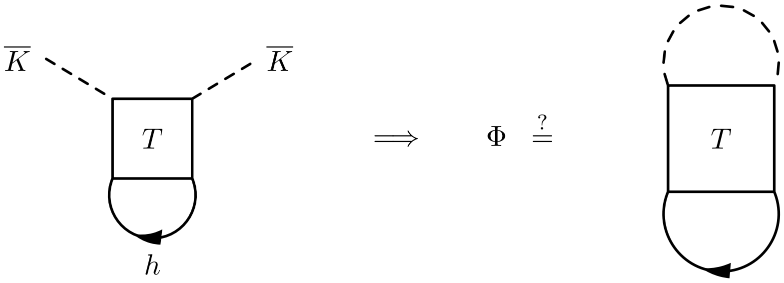

Figure 9.9: *(Incorrect) construction of* Φ *from the kaon selfenergy*

That approach would be inconsistent, however. The selfenergies that are contained in a functional Φ that gives the correct thermodynamic potential are obtained by cutting a line: if we do this for the diagrams in fig. 9.8, we immediately get a number of terms never considered in this work. Indeed, cutting the solid (nucleon) line in fig. 9.9 leads to the following graph that represents a selfenergy contribution to the nucleon:

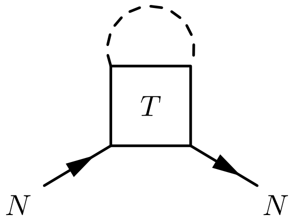

In addition the prescription to cut a line in Φ will lead to selfenergy diagrams for all other particles included. That is if the functional Φ was given, one could easily obtain rather exotic functions like the full in–medium selfenergy of the Σ^+ or the η, something that is at best done using a constant width, perhaps a Breit–Wigner form or a modified value for the mass but usually it is not accounted for at all. In reality, Φ is not given but has to be constructed from vertices upwards. The respective T–matrix elements would have to be constructed in a way similar to chapter 4 but including all the selfenergies. Obviously that calculation would be extremely involved.

Even if the technical difficulties did not prohibit such a calculation, it is not clear whether the resulting thermodynamic potential would give a more realistic description of neutron star matter. The interaction terms picked in chapter 3 are certainly not the interaction of choice for the calculation of nuclear matter. That is accomplished by interactions as e.g. in [80] which gives figs. 9.3,9.4. At the moment, there is just the beginning of successful descriptions of nuclear interactions derived from the more elementary chiral Lagrangian of chapter 3. A description of neutron star matter that is not just selfconsistent in the sense of section 7.1 and thermodynamically selfconsistent as discussed above but also consistent with the knowledge of nucleon interactions should include the non–strange sector of χPT, the pion–nucleon interaction, also in a selfconsistent way. This is certainly beyond the scope of this work but remains a task for future work.

Summary

In this work we have investigated the properties of antikaons in dense nuclear matter, focusing on the regime of zero temperature and high densities. We obtained a description of the in–medium kaon propagator that includes its full energy and momentum dependence over a large energy–momentum range. Applying the chiral $SU(3)$ Lagrangian to meson–baryon scattering, we have solved the Bethe–Salpeter scattering equation for coupled channels of mesons and baryons and calculated the antikaon selfenergy simultaneously, thus achieving a selfconsistent description of both, the scattering amplitudes and the kaon propagator.
The result was applied to neutron star matter in beta–equilibrium and the question of kaon condensation was investigated.

Observations of antikaon–nucleon scattering not only provide experimental constraints on the scattering amplitudes but indicate the most prominent feature in antikaon–nucleon scattering: the existence of a resonance named $\Lambda(1405)$. With a pole mass of 1.405 GeV it is located just below the kaon–nucleon threshold at 1.435 GeV. Scattering of antikaons on nucleons proceeds through this resonance and causes the K^-–proton scattering length to assume a negative, repulsive value at threshold. A perturbative treatment of the scattering process predicts a positive scattering length and thus an attractive potential. This apparent contradiction is remedied by treating the scattering by way of coupled channels of mesons and baryons instead of a perturbative calculation. The most important meson–baryon pairs are found to be $\bar{K}N$ and $\pi\Sigma$. The Bethe–Salpeter equation iterates the interaction of these channels to all orders. The $\Lambda(1405)$ resonance emerges immediately, and the repulsive behavior around threshold is recovered.
The interaction kernel which enters the scattering equation is taken from $SU(3)$ chiral perturbation theory. This theory rests on the observation that chiral symmetry is spontaneously broken in the vacuum. The values of a number of quantities such as the hadron masses can be attributed to this phenomenon. In chiral perturbation theory these quantities can be calculated in a manner that relies only on the underlying symmetry and is therefore model–independent. $SU(3)$ chiral perturbation theory is the form extended to the strange sector of hadronic flavors. It comprises the octet of pseudo–scalar mesons π, K, η and the octet of baryons N, Λ, Σ, Ξ.
The construction of our model was presented in chapter 3. After an inspection of the concept of chiral symmetry breaking and its implications for hadronic interactions we took the two most important elements of χPT as the basis for our model: the Weinberg–Tomozawa term and the explicit symmetry–breaking σ terms. With this choice the interactions are restricted to the s–wave sector. Several special problems were discussed that arise in chiral perturbation theory. One is the inclusion of baryons in the theory which, at first, seems to invalidate the convergence of the perturbative expansion. The solution given in [7] is the formalism of heavy baryon χPT. Another topic that has considerable impact on this work is the question of a proper counting scheme in χPT that is able to incorporate the result of higher loop calculations. A simple example of an application of χPT at lowest order (presented in chap. 3) is the derivation of meson masses and

relations among them, such as the Gell–Mann – Okubo mass formula. However, traditional χPT (using dimensional regularization) here lead to unacceptable large contributions from higher chiral orders [8]. Although our work does not use perturbative methods, these problems are of importance since they influence the values of the low energy constants (LECs) which fix the strength of the σ terms. The impact they have on our calculations were discussed in chapter 4.

Based on these interactions and the vertices derived from it, we have performed a calculation of the antikaon–nucleon scattering amplitude. To that end it is necessary to solve the Bethe–Salpeter T–matrix equation.

The details of this calculation were described in chapter 4. We have discussed an approximation that enabled us to to solve the scattering equation, treating it as a matrix equation where the matrices involved span the channels of meson–baryon pairs that were included.

After this formal solution of the Bethe–Salpeter equation, the basic technical problem was the regularization of the scattering amplitudes respectively the loop integral it contains. Several methods were tested. The application of a cut–off or of form factors as usually found in the literature proved to be unsuitable. Instead the regularization was accomplished by means of twice subtracted dispersion relations. At this stage parameters enter the model in the form of subtraction constants. The values of these parameters could be fixed by a fit to the experimental scattering lengths.

Having developed a satisfactory description of the scattering process in the vacuum, we extended the calculation to the medium. The medium was treated in the nucleon gas approximation, assuming a free Fermi gas of protons and neutrons. In this environment the antikaons scatter on nucleons that are Pauli–blocked. The implications of the thus modified KN–scattering for the scattering amplitude were investigated and found to be of considerable strength. The $\Lambda(1405)$ resonance seen in vacuum scattering is still existent but it is moved to higher energies and with increasing density it is also more and more broadened. Around threshold the sign of the amplitude is changed w.r.t. the vacuum. This is in accordance with experimental observations such as the level shifts in kaonic atoms or the antikaon yield in heavy–ion collisions which indicate an attractive in–medium kaon potential.

The in–medium interactions also change the properties of the kaon. It acquires a width and its mass is lowered. To incorporate the in–medium effects in the kaon propagator, the kaon selfenergy was evaluated using the scattering T–matrix elements as input. Selfconsistency is achieved once the in–medium T–matrix itself is evaluated in terms of the in–medium kaon propagator. This implies an iterative scheme where the result of one part of the calculation is inserted into the other until no more changes occur. Some four to five iterations were found to be sufficient. The actual implementation of this scheme proved to be of considerable difficulty, however. The values for the scattering amplitudes and the kaon propagator have to be determined for the entire energy–momentum plane and cannot be restricted to some smaller region of interest. A suitable method to implement this requirement was developed.

The final selfconsistent result shows the mass of the kaon lowered by about 100 MeV in comparison to the vacuum mass. The kaon spectral function is found to be strongly momentum dependent, emphasizing again the need for a calculation that correctly incorporates the finite 3–momentum of the scattering process and the in–medium kaon itself. The spectral function does not exhibit special structures at zero momentum. It is broad but the kaon mass seems to be still well defined. At finite but small momenta there are two branches that stem from the in–medium excitations at lower energies and the kaon pole at $\sqrt{s} \approx 500$ MeV. At higher momenta the kaon dispersion relation approaches its free form.

As an application the calculation has been also carried out for environments found in neutron stars. The motivation was the question of kaon condensation in neutron stars. If the in–medium mass of the kaon (or more precisely of the K^-) is shifted sufficiently to lower values, a Bose–Einstein condensate of K^- might form. This condensate provides a finite number of negatively charged particles that are not subject to the Pauli principle. Thus their presence would soften the equation of state of neutron stars considerably. The resulting stars would be more compact objects than ordinary neutron stars. In principle an observation of such objects could provide an experimental access to the nuclear high density phase. (The densities in the interior of neutron stars are estimated to range up to ten times nuclear matter density while the temperature is close to zero. That is well beyond the densities currently accessible in heavy–ion collisions.)

The results of our calculation however do not support the phenomenon of kaon condensation. The K^- mass is not nearly low enough compared with the relevant electrochemical potential, even at a density of $5\rho_0$. Furthermore, the effect of the medium modifications is stronger for the $\bar{K^0}$. The decisive fact is the interaction strength in the Weinberg–Tomozawa term. The $\bar{K^0}$ couples primarily to the neutron whereas the K^- has the strongest interaction with the proton, yet in neutron star matter the neutrons are much more abundant.

In the context of possible kaon condensation the question of thermodynamic selfconsistency arose. It would require the calculation of a functional that by functional derivatives gives the kaon selfenergy we calculated in this work. However it should also supply selfenergies for all other particles that were included in our calculation. The discussion in chapter 8 showed that a huge amount of subdiagrams would be required. The task seems not to be feasible using the techniques employed here but might be a general project for future work.

There are more prospects of extending the work on antikaons in dense matter. One step is to abandon the restriction to s–wave interactions and include higher partial waves. In that case, on–shell reduction of the T–matrix elements alone does not solve the Bethe–Salpeter equation. Instead a projection on partial waves has to be done first. Corresponding work was done by Lutz et al. [30].

Appendix A

Loop function in the medium

To carry out the in–medium loop integral, we proceed from eq. (4.29). The complex loop function $J_{\bar{K}N}$ reads

$$
\begin{aligned}
J_{\bar{K}N}(q) \;=\; & \int \frac{d^3l}{(2\pi)^3} (\frac{-i}{2\pi^3}) \int_0^\infty d\omega_1 \int_0^\infty d\omega_2 \int_{-\infty}^{\infty} dl^0 \left(\frac{ImG_{\bar{K}}(\omega_2, \vec{q}-\vec{l})}{q^0 - l^0 - \omega_2 + i\varepsilon} - \frac{ImG_{\bar{K}}(-\omega_2, \vec{q}-\vec{l})}{q^0 - l^0 + \omega_2 - i\varepsilon} \right) \\
& \left(\frac{ImG_N^{(p)}(\omega_1, \vec{l})}{l^0 - \omega_1 + i\varepsilon} - \frac{ImG_N^{(h)}(\omega_1, \vec{l})}{l^0 - \omega_1 - i\varepsilon} - \frac{ImG_N^{a}(-\omega_1, \vec{l})}{l^0 + \omega_1 - i\varepsilon} \right) .
\end{aligned}
$$

The l^0 integral is evaluated by closing the contour in the complex plane (cf. subsec. 4.2.1). This leads to

$$
\begin{aligned}
J_{\bar{K}N}(q) \;=\; & -\frac{1}{\pi^2} \int \frac{d^3l}{(2\pi)^3} \int_0^\infty d\omega_1 \int_0^\infty d\omega_2 \frac{ImG_N^{(p)}(\omega_1, \vec{l})\; ImG_{\bar{K}}(\omega_2, \vec{q}-\vec{l})}{q^0 - \omega_1 - \omega_2 + i\varepsilon} \\
& + \frac{1}{\pi^2} \int \frac{d^3l}{(2\pi)^3} \int_0^\infty d\omega_1 \int_0^\infty d\omega_2 \frac{ImG_N^{(h)}(\omega_1, \vec{l})\; ImG_{\bar{K}}(-\omega_2, \vec{q}-\vec{l})}{q^0 - \omega_1 + \omega_2 - i\varepsilon} \\
& + \frac{1}{\pi^2} \int \frac{d^3l}{(2\pi)^3} \int_0^\infty d\omega_1 \int_0^\infty d\omega_2 \frac{ImG_N^{a}(-\omega_1, \vec{l})\; ImG_{\bar{K}}(-\omega_2, \vec{q}-\vec{l})}{q^0 + \omega_1 + \omega_2 - i\varepsilon} .
\end{aligned}
$$

Taking the imaginary part gives:

$$
\begin{aligned}
ImJ_{\bar{K}N} \;=\; & \frac{1}{\pi} \int \frac{d^3l}{(2\pi)^3} \int_0^\infty d\omega_1 \int_0^\infty d\omega_2 \; ImG_N^{(p)}(\omega_1, \vec{l})\; ImG_{\bar{K}}(\omega_2, \vec{q}-\vec{l})\; \delta(q^0 - \omega_1 - \omega_2) \\
& + \frac{1}{\pi} \int \frac{d^3l}{(2\pi)^3} \int_0^\infty d\omega_1 \int_0^\infty d\omega_2 \; ImG_N^{(h)}(\omega_1, \vec{l})\; ImG_{\bar{K}}(-\omega_2, \vec{q}-\vec{l})\; \delta(q^0 - \omega_1 + \omega_2) \\
& + \frac{1}{\pi} \int \frac{d^3l}{(2\pi)^3} \int_0^\infty d\omega_1 \int_0^\infty d\omega_2 \; ImG_N^{a}(-\omega_1, \vec{l})\; ImG_{\bar{K}}(-\omega_2, \vec{q}-\vec{l})\; \delta(q^0 + \omega_1 + \omega_2)
\end{aligned}
$$

$$
\begin{aligned}
ImJ_{\bar{K}N} &= \frac{1}{\pi}\int\frac{d^3l}{(2\pi)^3}\int_0^{q^0} d\omega_1\; ImG_N^{(p)}(\omega_1,\vec{l})\; ImG_{\bar{K}}(q^0-\omega_1,\vec{q}-\vec{l}) \\
&+\frac{1}{\pi}\int\frac{d^3l}{(2\pi)^3}\int_{q^0}^{\infty} d\omega_1\; ImG_N^{(h)}(\omega_1,\vec{l})\; ImG_{\bar{K}}(-(\omega_1-q^0),\vec{q}-\vec{l}) \\
&+\frac{1}{\pi}\int\frac{d^3l}{(2\pi)^3}\int_0^{-q^0} d\omega_1\; ImG_N^{a}(-\omega_1,\vec{l})\; ImG_{\bar{K}}(-(-q^0-\omega_1),\vec{q}-\vec{l})
\end{aligned}
$$

The particle and hole propagators have the following imaginary parts:

$$
\begin{aligned}
ImG_N^{(p)}(\omega_1,\vec{l}) &= -\pi\,\frac{m_N}{\omega_N(\vec{l})}\,\delta(\omega_1-\omega_N(\vec{l}))\;\Theta(|\vec{l}|-p_f) \\
ImG_N^{(h)}(\omega_1,\vec{l}) &= \pi\,\frac{m_N}{\omega_N(\vec{l})}\,\delta(\omega_1-\omega_N(\vec{l}))\;\Theta(p_f-|\vec{l}|) \\
ImG_N^{a}(-\omega_1,\vec{l}) &= -\pi\,\frac{m_N}{-\omega_N(\vec{l})}\,\delta(-\omega_1+\omega_N(\vec{l}))
\end{aligned}
$$

Inserting these into the loop function leads to

$$
\begin{aligned}
ImJ_{\bar{K}N} &= -\int\frac{d^3l}{(2\pi)^3}\,\frac{m_N}{\omega_N(\vec{l})}\int_0^{q^0} d\omega_1\;\delta(\omega_1-\omega_N(\vec{l}))\;\Theta(|\vec{l}|-p_f)\; ImG_{\bar{K}}(q^0-\omega_1,\vec{q}-\vec{l}) \\
&+\int\frac{d^3l}{(2\pi)^3}\,\frac{m_N}{\omega_N(\vec{l})}\int_{q^0}^{\infty} d\omega_1\;\delta(\omega_1-\omega_N(\vec{l}))\;\Theta(p_f-|\vec{l}|)\; ImG_{\bar{K}}(q^0-\omega_1,\vec{q}-\vec{l}) \\
&-\int\frac{d^3l}{(2\pi)^3}\,\frac{m_N}{\omega_N(\vec{l})}\int_0^{-q^0} d\omega_1\;\;\delta(-\omega_1+\omega_N(\vec{l}))\; ImG_{\bar{K}}(q^0+\omega_1,\vec{q}-\vec{l}) \\
&= -\int\frac{d^3l}{(2\pi)^3}\,\frac{m_N}{\omega_N(\vec{l})}\; ImG_{\bar{K}}(q^0-\omega_N(\vec{l}),\vec{q}-\vec{l})\;\Theta(q^0-\omega_N(\vec{l}))\;\Theta(|\vec{l}|-p_f) \\
&+\int\frac{d^3l}{(2\pi)^3}\,\frac{m_N}{\omega_N(\vec{l})}\; ImG_{\bar{K}}(q^0-\omega_N(\vec{l}),\vec{q}-\vec{l})\;\Theta(\omega_N(\vec{l})-q^0)\;\Theta(p_f-|\vec{l}|) \\
&-\int\frac{d^3l}{(2\pi)^3}\,\frac{m_N}{\omega_N(\vec{l})}\; ImG_{\bar{K}}(q^0+\omega_N(\vec{l}),\vec{q}-\vec{l})\;\Theta(-q^0-\omega_N(\vec{l}))\;\Theta(\omega_N(\vec{l}))
\end{aligned}
$$

Now one has to examine the Θ–functions:

1. $\Theta(q^0-\omega_N(\vec{l}))\quad\Theta(|\vec{l}|-p_f)$:

$$
\begin{aligned}
& q^0 > \omega_N(\vec{l}), && |\vec{l}| > p_f \\
\Rightarrow\;\; & |\vec{l}| < \sqrt{{q^0}^2-m_N^2}, && |\vec{l}| > p_f \\
\Rightarrow\;\; & p_f < |\vec{l}| < \sqrt{{q^0}^2-m_N^2}
\end{aligned}
$$

   The condition $p_f < \sqrt{{q^0}^2-m_N^2}$ implies ${q^0}^2 > E_f$, so there is an additional Θ function: $\Theta(q^0-E_f)$.

2. $\Theta(\omega_N(\vec{l}) - q^0)\ \ \Theta(p_f - |\vec{l}|)$:

$$\begin{aligned} &\omega_N(\vec{l}) > q^0, && |\vec{l}| < p_f \\ &|\vec{l}| > \sqrt{q^{0\,2} - m_N^2}, && |\vec{l}| < p_f \end{aligned}$$

In any case, q^0 must lie below E_f: $\quad \Theta(E_f - q^0)$

If $q^0 \ < \ m_N$: $\qquad 0 \ < \ |\vec{l}| < p_f,$

if $q^0 \ > \ m_N$: $\qquad \sqrt{q^{0\,2} - m_N^2} < |\vec{l}| < p_f.$

3. $\Theta(-q^0 - \omega_N(\vec{l}))$:

$$\begin{aligned} &-q^0 > \omega_N(\vec{l}) && \Rightarrow\ \ q^0 < 0 \\ &|\vec{l}| < \sqrt{q^{0\,2} - m_N^2} && \Theta(-q^0)\ \ \Theta(|q^0| - m_N) \end{aligned}$$

In this way the Θ–functions provide bounds for the remaining integrations. After performing the trivial angular integration, the final expression in terms of $|\vec{l}|$ and $x_l = \cos\angle(\vec{q}, \vec{l})$ reads:

$$\begin{aligned} ImJ_{\bar{K}N} = &- \Theta(q^0 - E_f)\ \frac{m_N}{4\pi^2} \int_{p_f}^{\sqrt{q^{0\,2} - m_N^2}} d|\vec{l}|\ \frac{\vec{l}^2}{\omega_N(\vec{l})}\ \int_{-1}^{1} dx_l\ ImG_{\bar{K}}(q^0 - \omega_N(\vec{l}), \vec{q} - \vec{l}) \\ &+ \Theta(E_f - q^0)\ \Theta(q^0 - m_N)\ \frac{m_N}{4\pi^2} \int_{\sqrt{q^{0\,2} - m_N^2}}^{p_f} d|\vec{l}|\ \frac{\vec{l}^2}{\omega_N(\vec{l})}\ \int_{-1}^{1} dx_l\ ImG_{\bar{K}}(q^0 - \omega_N(\vec{l}), \vec{q} - \vec{l}) \\ &+ \Theta(m_N - q^0)\ \frac{m_N}{4\pi^2} \int_{0}^{p_f} d|\vec{l}|\ \frac{\vec{l}^2}{\omega_N(\vec{l})}\ \int_{-1}^{1} dx_l\ ImG_{\bar{K}}(q^0 - \omega_N(\vec{l}), \vec{q} - \vec{l}) \\ &- \Theta(|q^0| - m_N)\ \Theta(-q^0)\ \frac{m_N}{4\pi^2} \int_{0}^{\sqrt{q^{0\,2} - m_N^2}} d|\vec{l}|\ \frac{\vec{l}^2}{\omega_N(\vec{l})}\ \int_{-1}^{1} dx_l\ ImG_{\bar{K}}(q^0 + \omega_N(\vec{l}), \vec{q} - \vec{l}) \end{aligned}$$

Real part

The real part is calculated by a dispersion relation. No subtraction or other regularization scheme is necessary for the medium–part (all medium–quantities are finite).

Therefore we write

$$J(\omega) \ = \ \overset{(a)}{J^{vac}(\omega)} + \overset{(b)}{(J(\omega)} - \overset{(c)}{J^{vac}(\omega))}\ ,$$

and use the subtracted dispersion relations for **(a)** , but for **(b), (c)** we use non–subtracted dispersion relations. Thus only $ImJ^{vac}(\omega)$ will appear in **(a)** .

The full in–medium real part then reads

$$ReJ(\omega) = \overset{\boldsymbol{(a)}}{ReJ^{vac}(\omega)_{[subtracted]}} + \frac{1}{\pi}\int_0^\infty d\tilde{\omega}\ \left(\overset{\boldsymbol{(b)}}{\frac{ImJ(\tilde{\omega})}{\tilde{\omega}-\omega}} - \overset{\boldsymbol{(c)}}{\frac{ImJ^{vac}(\tilde{\omega})}{\tilde{\omega}-\omega}}\right)$$

As in chap. 4, we assume that there is an energy ω_{max} above which $ImJ(\omega > \omega_{max}) = const. = ImJ_\infty$. Then the expression becomes

$$\begin{aligned} ReJ(\omega) = ReJ^{vac}(\omega)_{[subtracted]} &+ \frac{1}{\pi}\int_0^{\omega_{max}} d\tilde{\omega}\ \left(\frac{ImJ(\tilde{\omega})}{\tilde{\omega}-\omega} - \frac{ImJ^{vac}(\tilde{\omega})}{\tilde{\omega}-\omega}\right) \\ &+ \frac{1}{\pi}(ImJ_\infty - ImJ^{vac}_\infty)\ \int_{\omega_{max}}^\infty \frac{d\tilde{\omega}}{\tilde{\omega}-\omega}\ . \end{aligned}$$

The constant asymptotic value of ImJ is identical in medium and vacuum, thus $ImJ_\infty = ImJ^{vac}_\infty$ and the remaining expression is quite simple:

$$ReJ(\omega) = ReJ^{vac}(\omega)_{[subtracted]} + \frac{1}{\pi}\int_0^{\omega_{max}} d\tilde{\omega}\ \left(\frac{ImJ(\tilde{\omega})}{\tilde{\omega}-\omega} - \frac{ImJ^{vac}(\tilde{\omega})}{\tilde{\omega}-\omega}\right)$$

Appendix B

Kaon selfenergy: Imaginary part

In this appendix we want to discuss the details of calculating the kaon selfenergy (cf. sec. 6.1). Starting point is the selfenergy diagram for the kaon (cf. fig. 6.1):

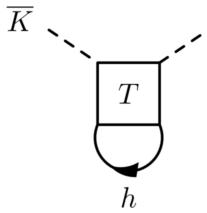

$$\Sigma(k) \;=\; -i \int \frac{d^4p}{(2\pi)^4}\, G_N(p)\, T(p+k)$$

As a fist step to handle this integral, we employ Lehmann representations for the nucleon propagator (cf. eq.(4.11)) and the T–matrix element:

$$\begin{aligned} G_N(p) &= \frac{m_N}{\omega_N(\vec{p})}\,\Big(\frac{\Theta(|\vec{p}|-p_f)}{p^0-\omega_N(\vec{p})+i\varepsilon} + \frac{\Theta(p_f-|\vec{p}|)}{p^0-\omega_N(\vec{p})-i\varepsilon} - \frac{1}{p^0+\omega_N(\vec{p})-i\varepsilon}\Big) \\ &= -\frac{1}{\pi}\int_0^\infty d\omega\, \frac{ImG_N^{(p)}(\omega,\vec{p})}{p^0-\omega+i\varepsilon} + \frac{1}{\pi}\int_0^\infty d\omega\, \frac{ImG_N^{(h)}(\omega,\vec{p})}{p^0-\omega-i\varepsilon} + \frac{1}{\pi}\int_0^\infty d\omega\, \frac{ImG_N^{a}(-\omega,\vec{p})}{p^0+\omega-i\varepsilon} \end{aligned} \tag{B.1}$$

$$T(p+k) = -\frac{1}{\pi}\int_0^\infty d\omega\, \frac{ImT(\omega,\vec{p}+\vec{k})}{p^0+k^0-\omega+i\varepsilon} \;+\; \frac{1}{\pi}\int_0^\infty d\omega\, \frac{ImT(-\omega,\vec{p}+\vec{k})}{p^0+k^0+\omega-i\varepsilon}$$

Then the selfenergy integral reads

$$\begin{aligned} \Sigma(k) = -i \int \frac{d^3p}{(2\pi)^3}\,\frac{1}{\pi^2}\int_0^\infty d\omega_1 \int_0^\infty d\omega_2 \int_{-\infty}^\infty dp^0 \left(\frac{ImT(\omega_2,\vec{p}+\vec{k})}{p^0+k^0-\omega_2+i\varepsilon} - \frac{ImT(-\omega_2,\vec{p}+\vec{k})}{p^0+k^0+\omega_2-i\varepsilon}\right) \\ \left(\frac{ImG_N^{(p)}(\omega_1,\vec{p})}{p^0-\omega_1+i\varepsilon} - \frac{ImG_N^{(h)}(\omega_1,\vec{p})}{p^0-\omega_1-i\varepsilon} - \frac{ImG_N^{a}(-\omega_1,\vec{p})}{p^0+\omega_1-i\varepsilon}\right)\,. \end{aligned}$$

Evaluating the p^0 integration in the complex plane gives

$$\begin{aligned}
\frac{-i}{2\pi}\int dp^0\,\frac{1}{p^0-\omega_1+i\varepsilon}\,\frac{1}{p^0+k^0-\omega_2+i\varepsilon} &= 0\\
\frac{i}{2\pi}\int dp^0\,\frac{1}{p^0-\omega_1+i\varepsilon}\,\frac{1}{p^0+k^0+\omega_2-i\varepsilon} &= \frac{1}{k^0+\omega_1+\omega_2-i\varepsilon}\\
\frac{i}{2\pi}\int dp^0\,\frac{1}{p^0-\omega_1-i\varepsilon}\,\frac{1}{p^0+k^0-\omega_2+i\varepsilon} &= -\frac{1}{k^0+\omega_1-\omega_2+i\varepsilon}\\
\frac{i}{2\pi}\int dp^0\,\frac{1}{p^0+\omega_1-i\varepsilon}\,\frac{1}{p^0+k^0-\omega_2+i\varepsilon} &= -\frac{1}{k^0-\omega_1-\omega_2+i\varepsilon}\,.
\end{aligned}$$

Thus

$$\begin{aligned}
\Sigma(k) &= \frac{1}{\pi^2}\int\frac{d^3p}{(2\pi)^3}\int_0^\infty d\omega_1\int_0^\infty d\omega_2\left(\frac{ImG_N^{(p)}(\omega_1,\vec{p})\,ImT(-\omega_2,\vec{p}+\vec{k})}{k^0+\omega_1+\omega_2-i\varepsilon}\right.\\
&\left.-\frac{ImG_N^{(h)}(\omega_1,\vec{p})\,ImT(\omega_2,\vec{p}+\vec{k})}{k^0+\omega_1-\omega_2+i\varepsilon}-\frac{ImG_N^{a}(-\omega_1,\vec{p})\,ImT(\omega_2,\vec{p}+\vec{k})}{k^0-\omega_1-\omega_2+i\varepsilon}\right)\,.
\end{aligned}$$

Now we take the imaginary part (and get the real part via a dispersion relation later):

$$\begin{aligned}
Im\Sigma(k) &= \frac{1}{\pi}\int\frac{d^3p}{(2\pi)^3}\int_0^\infty d\omega_1\int_0^\infty d\omega_2\,\Big(ImG_N^{(p)}(\omega_1,\vec{p})\,ImT(-\omega_2,\vec{p}+\vec{k})\;\;\delta(k^0+\omega_1+\omega_2)\\
&+ImG_N^{(h)}(\omega_1,\vec{p})\,ImT(\omega_2,\vec{p}+\vec{k})\;\;\delta(k^0+\omega_1-\omega_2)\\
&+ImG_N^{a}(-\omega_1,\vec{p})\,ImT(\omega_2,\vec{p}+\vec{k})\;\;\delta(k^0-\omega_1-\omega_2)\Big)
\end{aligned}$$

$$\begin{aligned}
Im\Sigma(k) &= \frac{1}{\pi}\int\frac{d^3p}{(2\pi)^3}\int_0^\infty d\omega_1 ImG_N^{(p)}(\omega_1,\vec{p})\,ImT(k^0+\omega_1,\vec{p}+\vec{k})\;\;\Theta(-k^0-\omega_1)\\
&+\frac{1}{\pi}\int\frac{d^3p}{(2\pi)^3}\int_0^\infty d\omega_1 ImG_N^{(h)}(\omega_1,\vec{p})\,ImT(k^0+\omega_1,\vec{p}+\vec{k})\;\;\Theta(k^0+\omega_1)\\
&+\frac{1}{\pi}\int\frac{d^3p}{(2\pi)^3}\int_0^\infty d\omega_1 ImG_N^{a}(-\omega_1,\vec{p})\,ImT(k^0-\omega_1,\vec{p}+\vec{k})\;\;\Theta(k^0-\omega_1)
\end{aligned}$$

$$\begin{aligned}
Im\Sigma(k) &= -\int\frac{d^3p}{(2\pi)^3}\;\frac{m_N}{\omega_N(\vec{p})}\;\;\Theta(|\vec{p}|-p_f)\;\int_0^\infty d\omega_1\;\;\delta(\omega_1-\omega_N(\vec{p}))\;\;ImT(k^0+\omega_1,\vec{p}+\vec{k})\;\;\Theta(-k^0-\omega_1)\\
&+\int\frac{d^3p}{(2\pi)^3}\;\frac{m_N}{\omega_N(\vec{p})}\;\;\Theta(p_f-|\vec{p}|)\;\int_0^\infty d\omega_1\;\;\delta(\omega_1-\omega_N(\vec{p}))\;\;ImT(k^0+\omega_1,\vec{p}+\vec{k})\;\;\Theta(k^0+\omega_1)\\
&-\int\frac{d^3p}{(2\pi)^3}\;\frac{m_N}{\omega_N(\vec{p})}\;\;\int_0^\infty d\omega_1\;\;\delta(-\omega_1+\omega_N(\vec{p}))\;\;ImT(k^0-\omega_1,\vec{p}+\vec{k})\;\;\Theta(k^0-\omega_1)
\end{aligned}$$

$$\begin{aligned}
Im\Sigma(k) &= -\int\frac{d^3p}{(2\pi)^3}\;\frac{m_N}{\omega_N(\vec{p})}\;\;\Theta(|\vec{p}|-p_f)\;\;ImT(k^0+\omega_N(\vec{p}),\vec{p}+\vec{k})\;\;\Theta(-k^0-\omega_N(\vec{p}))\\
&+\int\frac{d^3p}{(2\pi)^3}\;\frac{m_N}{\omega_N(\vec{p})}\;\;\Theta(p_f-|\vec{p}|)\;\;ImT(k^0+\omega_N(\vec{p}),\vec{p}+\vec{k})\;\;\Theta(k^0+\omega_N(\vec{p}))\\
&-\int\frac{d^3p}{(2\pi)^3}\;\frac{m_N}{\omega_N(\vec{p})}\;\;ImT(k^0-\omega_N(\vec{p}),\vec{p}+\vec{k})\;\;\Theta(k^0-\omega_N(\vec{p}))
\end{aligned}$$

The Θ–functions put constraints on the ranges of integration:

- 1. Θ–function $\Theta(-k^0 - \omega_N(\vec{p}))$:

$$\begin{aligned} k^0 + \omega_N(\vec{p}) &< 0 \qquad \Rightarrow \qquad k^0 < 0 \\ \omega_N(\vec{p}) &< -k^0 \quad (= |k^0|) \\ p_f < |\vec{p}| &< \sqrt{|k^0|^2 - m_N^2} \end{aligned}$$

- 2. Θ–function $\Theta(k^0 + \omega_N(\vec{p}))$:

$$k^0 + \omega_N(\vec{p}) > 0$$

  - [i] $k^0 > 0$: no restraint
  - [ii] $k^0 < 0: \; -|k^0| + \omega_N(\vec{p}) > 0$
    - (a) If $|k^0| > m_N: \; \sqrt{|k^0|^2 - m_N^2} < |\vec{p}| < p_f, \quad -E_f < k^0 < m_N$.
    - (b) If $-m_N < k^0 < 0$, no restraint for $|\vec{p}|: \; 0 \leq |\vec{p}| \leq p_f$.

- 3. Θ–function $\Theta(k^0 - \omega_N(\vec{p}))$:

$$\begin{aligned} k^0 - \omega_N(\vec{p}) &> 0 \\ k^0 &> \omega_N(\vec{p}) \qquad \Rightarrow \qquad k^0 > 0 \\ |\vec{p}| &< \sqrt{|k^0|^2 - m_N^2} \end{aligned}$$

Thus the imaginary part of the kaon selfenergy reads:

$$\begin{aligned} Im\Sigma(k) = &- \; \Theta(-k^0)\,\Theta(|k^0| - E_f)\; \frac{m_N}{4\pi^2} \int_{p_f}^{\sqrt{|k^0|^2 - m_N^2}} d|\vec{p}|\; \frac{\vec{p}^2}{\omega_N(\vec{p})} \int_{-1}^{1} dx_l\; ImT(k^0 + \omega_N(\vec{p}), \vec{p} + \vec{k}) \\ &+ \; \Theta(-k^0)\,\Theta(|k^0| - m_N)\,\Theta(E_f - |k^0|)\; \frac{m_N}{4\pi^2} \int_{\sqrt{|k^0|^2 - m_N^2}}^{p_f} d|\vec{p}|\; \frac{\vec{p}^2}{\omega_N(\vec{p})} \int_{-1}^{1} dx_l\; ImT(k^0 + \omega_N(\vec{p})) \\ &+ \; \Theta(k^0 + m_N)\; \frac{m_N}{4\pi^2} \int_{0}^{p_f} d|\vec{p}|\; \frac{\vec{p}^2}{\omega_N(\vec{p})} \int_{-1}^{1} dx_l\; ImT(k^0 + \omega_N(\vec{p}), \vec{p} + \vec{k}) \\ &- \; \Theta(k^0)\,\Theta(|k^0| - m_N)\; \frac{m_N}{4\pi^2} \int_{0}^{\sqrt{|k^0|^2 - m_N^2}} d|\vec{p}|\; \frac{\vec{p}^2}{\omega_N(\vec{p})} \int_{-1}^{1} dx_l\; ImT(k^0 - \omega_N(\vec{p}), \vec{p} + \vec{k}) \end{aligned} \tag{B.2}$$

Note that this expression still allows for all energies k^0. Interestingly, the full expression contains a part that does not vanish for $p_f = 0$.

$$
\begin{aligned}
Im\Sigma(k)\Bigg|_{p_f=0} =& -\frac{m_N}{4\pi^2}\int_0^{\sqrt{|k^0|^2-m_N^2}} d|\vec{p}|\ \frac{\vec{p}^2}{\omega_N(\vec{p})}\ \int_{-1}^{1} dx_l\ ImT(k^0+\omega_N(\vec{p}),\vec{p}+\vec{k})\ \ \Theta(-k^0)\ \ \Theta(|k^0|-m_N) \\
& -\frac{m_N}{4\pi^2}\int_0^{\sqrt{|k^0|^2-m_N^2}} d|\vec{p}|\ \frac{\vec{p}^2}{\omega_N(\vec{p})}\ \int_{-1}^{1} dx_l\ ImT(k^0-\omega_N(\vec{p}),\vec{p}+\vec{k})\ \ \Theta(k^0)\ \ \Theta(|k^0|-m_N) \\
=& -\frac{m_N}{4\pi^2}\int_0^{\sqrt{|k^0|^2-m_N^2}} d|\vec{p}|\ \frac{\vec{p}^2}{\omega_N(\vec{p})}\ \int_{-1}^{1} dx_l \Theta(|k^0|-m_N) \\
& \qquad \Big[\ \Theta(-k^0)\ ImT(k^0+\omega_N(\vec{p}),\vec{p}+\vec{k})\ +\ \Theta(k^0)\ ImT(k^0-\omega_N(\vec{p}),\vec{p}+\vec{k})\ \Big]\ .
\end{aligned}
$$

The argument of ImT in the $(k^0 < 0)$ - term is negative, $k^0 + \omega_N < 0$, in the $(k^0 > 0)$ - term it is positive, $k^0 - \omega_N > 0$.
Terms remaining in the limit of vanishing Fermi momentum constitute a part of the vacuum selfenergy of the kaon. These terms stem from contributions of antinucleons or antihyperons. Since we are rather interested in the in–medium modifications of the kaons, these terms have to be dropped.

For the in–medium selfenergy of the $\bar{K}$ we only need the $k^0 > 0$ component of the expression (B.2), without the antinucleon part. The remaining integral reads

$$
Im\Sigma(k) = \frac{m_N}{4\pi^2}\int_0^{p_f} d|\vec{p}|\ \frac{\vec{p}^2}{\omega_N(\vec{p})}\ \int_{-1}^{1} dx_l\ ImT(k^0+\omega_N(\vec{p}),\vec{p}+\vec{k})\ .
$$

Appendix C

Dispersion relation for asymmetric functions

Let $f(\omega)$ be a function with the following properties:

1.) f has cuts along the real axis (✕), but elsewhere it is analytic.

2.) The real part $\Re ef$ is continuous on the real axis (for real ω : $\Re ef(\omega + i\varepsilon) = \Re ef(\omega - i\varepsilon)$), the imaginary part changes its sign discontinuously: $\Im mf(\omega + i\varepsilon) = -\Im mf(\omega - i\varepsilon)$.

3.) The function behaves at least like $|f(\omega)| \propto \frac{1}{|\omega|}$ for large $|\omega|$.

(For symmetric functions we would additionally have $f(\omega) = f(-\omega)$.)

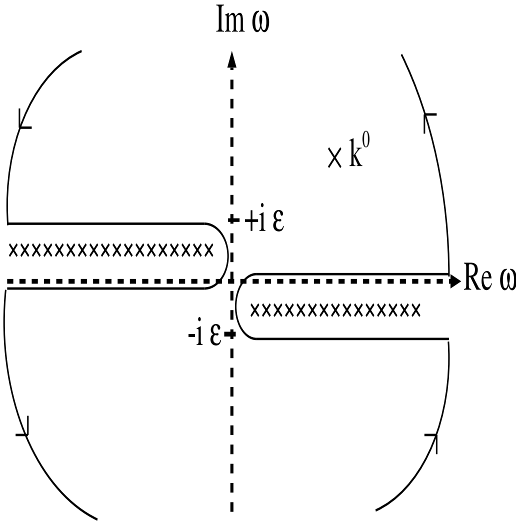

Figure C.1: Complex ω–plane: The real axis is approached from below for $\Re e\omega > 0$ and from above for $\Re e\omega < 0$. The path of integration as indicated is already shifted by $i\varepsilon$.

Now the function $\frac{f(\omega)}{\omega - k^0}$ is integrated along the closed path in fig. C.1

$$2\pi i f(k^0) = \oint d\omega \frac{f(\omega)}{\omega - k^0}$$

Due to condition 3.) the arcs do not contribute:

$$2\pi i f(k^0) = \int\limits_0^\infty d\omega \frac{f(\omega)}{\omega - k^0} + \int\limits_{-\infty + i\varepsilon}^{i\varepsilon} d\omega \frac{f(\omega)}{\omega - k^0} + \int\limits_{i\varepsilon}^{0} d\omega \frac{f(\omega)}{\omega - k^0} + \int\limits_{0}^{-\infty} d\omega \frac{f(\omega)}{\omega - k^0} + \int\limits_{-i\varepsilon}^{0} d\omega \frac{f(\omega)}{\omega - k^0} + \int\limits_{\infty - i\varepsilon}^{-i\varepsilon} d\omega \frac{f(\omega)}{\omega - k^0}$$

The integrals from $+i\varepsilon \to 0$ and $-i\varepsilon \to 0$ will vanish in the limit $\varepsilon \to 0$.
Substitution of $\omega \to -\omega$ in the fourth term yields

$$2\pi i f(k^0) \ = \int\limits_0^\infty d\omega \frac{f(\omega)}{\omega - k^0} \ + \int\limits_{-\infty+i\varepsilon}^{i\varepsilon} d\omega \ \frac{f(\omega)}{\omega - k^0} \ + \int\limits_0^\infty d\omega \ \frac{f(-\omega)}{\omega + k^0} \ + \int\limits_{\infty-i\varepsilon}^{-i\varepsilon} d\omega \ \frac{f(\omega)}{\omega - k^0} \ .$$

Due to condition 2.), in the first and third term we can replace $f(\omega) = f(\omega + i\varepsilon)$ and $f(-\omega) = f(-\omega - i\varepsilon)$. In the other two terms one has to be careful with these shifts because of the cuts below the real axis (for $\Re e\omega > 0$) and above (for $\Re e\omega < 0$). Thus we get

$$2\pi i f(k^0) \ = \int\limits_0^\infty d\omega \ \frac{f(\omega + i\varepsilon)}{\omega - k^0} + \int\limits_{-\infty}^0 d\omega \ \frac{f(\omega + i\varepsilon)}{\omega - k^0} + \int\limits_0^\infty d\omega \ \frac{f(-\omega - i\varepsilon)}{\omega + k^0} + \int\limits_\infty^0 d\omega \ \frac{f(\omega - i\varepsilon)}{\omega - k^0} \ .$$

After another substitution of $\omega \to -\omega$ in the second term,

$$2\pi i f(k^0) \ = \int\limits_0^\infty d\omega \ \frac{f(\omega + i\varepsilon)}{\omega - k^0} + \int\limits_\infty^0 d\omega \ \frac{f(-\omega + i\varepsilon)}{\omega + k^0} + \int\limits_0^\infty d\omega \ \frac{f(-\omega - i\varepsilon)}{\omega + k^0} + \int\limits_\infty^0 d\omega \ \frac{f(\omega - i\varepsilon)}{\omega - k^0} \ ,$$

the expressions can be combined as

$$2\pi i f(k^0) \ = \int\limits_0^\infty d\omega \ \frac{f(\omega + i\varepsilon) - f(\omega - i\varepsilon)}{\omega - k^0} \ + \ \int\limits_0^\infty d\omega \ \frac{f(-\omega - i\varepsilon) - f(-\omega + i\varepsilon)}{\omega + k^0}$$

According to condition 2.),

$$\begin{aligned} f(\omega + i\varepsilon) - f(\omega - i\varepsilon) &= 2iImf(\omega + i\varepsilon) \\ f(-\omega - i\varepsilon) - f(-\omega + i\varepsilon) &= 2iImf(-\omega - i\varepsilon) \ . \end{aligned}$$

Hence

$$f(k^0) \ = \ -\frac{1}{\pi} \int\limits_0^\infty d\omega \ \frac{Imf(\omega + i\varepsilon))}{k^0 - \omega} + \frac{1}{\pi} \int\limits_0^\infty d\omega \ \frac{Imf(-\omega - i\varepsilon))}{k^0 + \omega}$$

For real k^0 this reads

$$f(k^0) \ = \ -\frac{1}{\pi} \int\limits_0^\infty d\omega \ \frac{Imf(\omega)}{k^0 - \omega + i\varepsilon} \quad + \quad \frac{1}{\pi} \int\limits_0^\infty d\omega \ \frac{Imf(-\omega)}{k^0 + \omega - i\varepsilon} \ .$$

Appendix D

Pions in asymmetric matter

In this appendix we take up the issues that were skipped in the sections on pions in matter, chap. 5 and sec. 8.2.

D.1 Retarded versus time-ordered propagators

First we note that the finite–temperature formalism that is used to calculate the pion selfenergy in nuclear matter makes use of retarded Green functions (or propagators) [67], while our expressions for the loop integrals have involved time–ordered functions (cf. eqs.(4.12), (4.13)). The reason for the different conventions in the Matsubara formalism is outlined in the following. The calculations for finite temperature $\mathcal{T}$ are formulated in terms of imaginary–time propagators $\mathcal{G}(\tau, \vec{r})$, where τ is understood as an imaginary time. $\mathcal{G}$ is periodic in τ with period $1/\mathcal{T}$, so it can be expanded into a Fourier series with frequencies $\omega_n = 2n\pi\mathcal{T}$ for bosons and $\omega_n = (2n-1)\,\pi\mathcal{T}$, which are called Matsubara frequencies. After evaluating the Matsubara sums that will arise in a particular problem (an example will be studied in sec. D.3 below, cf. eq. (D.3)–(D.5)), the calculation has to be analytically continued from imaginary time to real time (cf. eq. (D.7)). This step is substantially facilitated by the use of the retarded instead of the time–ordered propagators.
To accomplish this analytic continuation, $\mathcal{G}(\omega_n, \vec{k})$ is written as a function of a complex variable ω_n. It has the Lehmann representation

$$\mathcal{G}(\omega_n, \vec{k}) = \int_{-\infty}^{\infty} \frac{d\omega'}{2\pi} \frac{\rho(\omega', \vec{k})}{i\omega_n - \omega'} \,. \tag{D.1}$$

Now the Fourier transform of the retarded propagators $G(t, \vec{r})$ has the Lehmann representation

$$G(\omega, \vec{k}) = \int_{-\infty}^{\infty} \frac{d\omega'}{2\pi} \frac{\rho(\omega', \vec{k})}{\omega - \omega' + i\varepsilon} \,,$$

with the same spectral function $\rho(\omega', \vec{k})$ as in eq. (D.1). Thus the retarded propagator constitutes the analytic continuation of $\mathcal{G}(\omega_n, \vec{k})$.

To inspect the difference to time–ordered functions, we examine the retarded pion propagator which has the following form:

$$G_\pi(k) = \frac{1}{2\omega(\vec{k})} \left(\frac{1}{k^0 - \omega(\vec{k}) + i\varepsilon} - \frac{1}{k^0 + \omega(\vec{k}) + i\varepsilon} \right)$$

Its imaginary part reads

$$\Im m G_\pi(k) = -\frac{\pi}{2\omega(\vec{k})}\,\delta(k^0-\omega(\vec{k})) + \frac{\pi}{2\omega(\vec{k})}\,\delta(k^0+\omega(\vec{k}))$$

which means that around the pole at positive energies ($k^0 = \omega_\pi(\vec{k})$) $\Im m G_\pi$ has a negative value, while around the one at negative energies ($k^0 = -\,\omega_\pi(\vec{k})$) it is positive: this is the correct behavior of a retarded function.

The dispersion relation given in appendix C has to be modified before it can be applied to the retarded propagator: The imaginary part does not change its sign discontinuously on the real axis (condition 2. in appendix C). Thus we have to write

$$G_\pi(k) = -\frac{1}{\pi}\int_0^\infty d\omega \frac{\Im m G_\pi(\omega)}{k^0-\omega+i\varepsilon} \quad -\frac{1}{\pi}\int_0^\infty d\omega \frac{\Im m G_\pi(-\omega)}{k^0+\omega+i\varepsilon}\ ,$$

which can also be put into the form of eq. (3.29) of ref. [67]:

$$G_\pi(k) = -\frac{1}{\pi}\int_0^\infty d\omega \frac{\Im m G_\pi(\omega)}{k^0-\omega+i\varepsilon} \quad +\frac{1}{\pi}\int_0^{-\infty} d\omega \frac{\Im m G_\pi(\omega)}{k^0-\omega+i\varepsilon} = -\frac{1}{\pi}\int_{-\infty}^\infty d\omega \frac{\Im m G_\pi(\omega)}{k^0-\omega+i\varepsilon}\ .$$

D.2 $\pi\,\Sigma$ loop retarded

To find out how the use of retarded propagators influences our calculation, we use the dispersion relation derived above for a loop function involving the pion, e.g. $J_{\pi\Sigma}$:

$$J_{\pi\Sigma}(q) = -i\int\frac{d^4l}{(2\pi)^4}\,G_\pi(q-l)\,G_\Sigma(l)$$

If G_π and G_Σ are retarded functions, the expression becomes

$$\begin{aligned}
J_{\pi\Sigma}(q) &= -\frac{i}{\pi^2}\int\frac{d^4l}{(2\pi)^4}\int_{-\infty}^\infty d\omega_1\int_{-\infty}^\infty d\omega_2\left(\frac{\Im m G_\pi(\omega_2)}{q^0-l^0-\omega_2+i\varepsilon} - \frac{\Im m G_\Sigma(\omega_1)}{l^0-\omega_1+i\varepsilon}\right)\\
&= -\frac{1}{\pi^2}\int\frac{d^3l}{(2\pi)^3}\int_{-\infty}^\infty d\omega_1\int_{-\infty}^\infty d\omega_2\frac{\Im m G_\pi(\omega_2)\,\Im m G_\Sigma(\omega_1)}{q^0-\omega_1-\omega_2+i\varepsilon}
\end{aligned}$$

$$\begin{aligned}
\Im m J_{\pi\Sigma}(q) &= \frac{1}{\pi}\int\frac{d^3l}{(2\pi)^3}\int_{-\infty}^\infty d\omega_1\int_{-\infty}^\infty d\omega_2\ \Im m G_\pi(\omega_2)\,\Im m G_\Sigma(\omega_1)\,\delta(q^0-\omega_1-\omega_2)\\
&= \frac{1}{\pi}\int\frac{d^3l}{(2\pi)^3}\int_{-\infty}^\infty d\omega_1\ \Im m G_\pi(q^0-\omega_1)\,\Im m G_\Sigma(\omega_1)
\end{aligned}$$

The imaginary part of the (retarded !) Σ–propagator reads

$$\begin{aligned}\Im m G_\Sigma(\omega_1,\vec{l}) &= \Im m\left(\frac{m_\Sigma}{\omega_\Sigma(\vec{l})}\,(\frac{1}{\omega_1-\omega_\Sigma(\vec{l})+i\varepsilon}-\frac{1}{\omega_1+\omega_\Sigma(\vec{l})+i\varepsilon})\right)\\ &= -\pi\frac{m_\Sigma}{\omega_\Sigma(\vec{l})}\,\Big(\delta(\omega_1-\omega_\Sigma(\vec{l}))-\delta(\omega_1+\omega_\Sigma(\vec{l}))\Big)\end{aligned}$$

$$\begin{aligned}\Rightarrow \Im m J_{\pi\Sigma}(q) &= \int\frac{d^3l}{(2\pi)^3}\,\frac{m_\Sigma}{\omega_\Sigma(\vec{l})}\int\limits_{-\infty}^{\infty}d\omega_1\;\Im m G_\pi(q^0-\omega_1)\;((\delta(\omega_1+\omega_\Sigma(\vec{l}))-\delta(\omega_1-\omega_\Sigma(\vec{l})))\\ &= -\int\frac{d^3l}{(2\pi)^3}\,\frac{m_\Sigma}{\omega_\Sigma(\vec{l})}\,(\,\Im m G_\pi(q^0-\omega_\Sigma(\vec{l}))\;-\;\Im m G_\pi(q^0+\omega_\Sigma(\vec{l}))\,)\end{aligned}$$

This result differs from the expression obtained for $\Im m J_{\pi\Sigma}$ if we start with time–ordered functions (cf. appendix A):

$$\Im m J^{t.o.}_{\pi\Sigma} = -\int\frac{d^3l}{(2\pi)^3}\,\frac{m_\Sigma}{\omega_\Sigma(\vec{l})}\,\Big(\Im m G^{t.o.}_\pi(q^0-\omega_\Sigma(\vec{l}))\;\Theta(q^0-\omega_\Sigma(\vec{l}))+\Im m G^{t.o.}_\pi(q^0+\omega_\Sigma(\vec{l}))\;\Theta(-q^0-\omega_\Sigma(\vec{l}))\Big)$$

Tracing back the root of this difference, it turns out to be due to the sign of the $i\varepsilon$ terms in the negative energy part of the propagators respectively in the dispersion relation.

Thus the loop function behaves as the propagators that constituted its input – just as expected: the retarded function is point–symmetric relative to energy $q^0 = 0$, the time–ordered function is axially symmetric. Therefore, the difference does not pose a problem for our calculation: the imaginary parts of time ordered and retarded G_π are identical in the energy range of interest – there is nothing to worry about using the retarded pion propagator calculating the time–ordered loop function.

D.3 Pions in asymmetric matter: interaction vertices

Here the details of the calculation of the π^+ selfenergy of subsec. 8.2.1 will be worked out.
The πN Lagrangian reads

$$\mathcal{L}_{\pi N} \;=\; \frac{f_N}{m_\pi}\,\bar{\psi}\,\gamma^5\,\gamma^\mu\;\vec{\tau}\,\psi\;\cdot\;\partial_\mu\,\vec{\phi}\;.$$

Inserting the Pauli matrices and the isospin vectors of eq. (5.4) gives the following relativistic and non–relativistic ('n.r.') vertices:

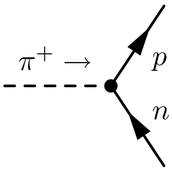

$$= \;-\sqrt{2}\,\frac{f_N}{m_\pi}\,\gamma_5\gamma^\mu\,k_\mu \overset{\text{n.r.}}{=} -\sqrt{2}\,\frac{f_N}{m_\pi}\,\vec{k}\cdot\vec{\sigma}$$

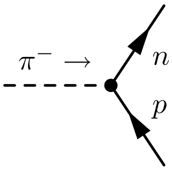

$$= \;\sqrt{2}\,\frac{f_N}{m_\pi}\,\gamma_5\gamma^\mu\,k_\mu \overset{\text{n.r.}}{=} \sqrt{2}\,\frac{f_N}{m_\pi}\,\vec{k}\cdot\vec{\sigma}$$

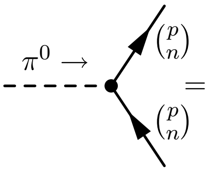

$$= \;\pm\,\frac{f_N}{m_\pi}\,\gamma_5\gamma^\mu\,k_\mu \overset{\text{n.r.}}{=} \pm\,\frac{f_N}{m_\pi}\,\vec{k}\cdot\vec{\sigma}\;.$$

For the Δ, the procedure leads to a larger number of vertices.
The Lagrangian reads

$$\mathcal{L}_{\pi N\Delta} = -\frac{f_\Delta}{m_\pi}\,\overline{\Psi}\,\vec{T}^\dagger\,\Psi^\mu\cdot\partial_\mu\vec{\Phi} - \frac{f_\Delta}{m_\pi}\,\overline{\Psi}^\mu\,\vec{T}\,\Psi\cdot\partial_\mu\vec{\Phi}\;.$$

The isospin transition operators are given in eq. (C.9) of [58]:

$$T_1 = \begin{pmatrix} -\sqrt{\frac{1}{2}} & 0 \\ 0 & -\sqrt{\frac{1}{6}} \\ \sqrt{\frac{1}{6}} & 0 \\ 0 & \sqrt{\frac{1}{2}} \end{pmatrix}\,,\quad T_2 = \begin{pmatrix} i\sqrt{\frac{1}{2}} & 0 \\ 0 & i\sqrt{\frac{1}{6}} \\ i\sqrt{\frac{1}{6}} & 0 \\ 0 & i\sqrt{\frac{1}{2}} \end{pmatrix}\,,\quad T_3 = \begin{pmatrix} 0 & 0 \\ \sqrt{\frac{2}{3}} & 0 \\ 0 & \sqrt{\frac{2}{3}} \\ 0 & 0 \\ 0 & \end{pmatrix}$$

The isospin vectors eq.(5.4) for the π^+ and π^- lead to combinations

$$T_1 + iT_2 = \begin{pmatrix} -\sqrt{2} & 0 \\ 0 & -\frac{2}{\sqrt{6}} \\ 0 & 0 \\ 0 & 0 \end{pmatrix} \qquad \text{and} \qquad T_1 - iT_2 = \begin{pmatrix} 0 & 0 \\ 0 & 0 \\ +\frac{2}{\sqrt{6}} & 0 \\ 0 & +\sqrt{2} \end{pmatrix}$$

$$T_1^\dagger + iT_2^\dagger = \begin{pmatrix} 0 & 0 & \frac{2}{\sqrt{6}} & 0 \\ 0 & 0 & 0 & \sqrt{2} \end{pmatrix} \qquad \text{and} \qquad T_1^\dagger - iT_2^\dagger = \begin{pmatrix} -\sqrt{2} & 0 & 0 & 0 \\ 0 & -\frac{2}{\sqrt{6}} & 0 & 0 \end{pmatrix} \,,$$

which are to be sandwiched between the nucleon and Δ fields.
The result are the following eight vertices for the charged pions with nucleon and Δ:

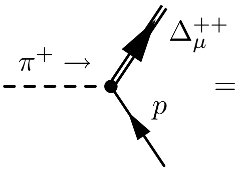

$$= -\frac{f_\Delta}{m_\pi}\, k^\mu \overset{\text{n.r.}}{\rightarrow} \frac{f_\Delta}{m_\pi}\, \vec{k}\cdot\vec{S}$$

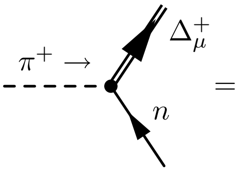

$$= -\frac{1}{\sqrt{3}}\frac{f_\Delta}{m_\pi}\, k^\mu \overset{\text{n.r.}}{\rightarrow} \frac{1}{\sqrt{3}}\frac{f_\Delta}{m_\pi}\, \vec{k}\cdot\vec{S}$$

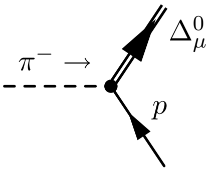

$$= -\frac{1}{\sqrt{3}}\frac{f_\Delta}{m_\pi}\, k^\mu \overset{\text{n.r.}}{\rightarrow} \frac{1}{\sqrt{3}}\frac{f_\Delta}{m_\pi}\, \vec{k}\cdot\vec{S}$$

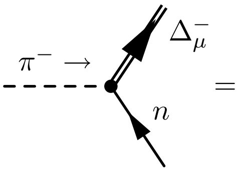

$$= -\frac{f_\Delta}{m_\pi}\, k^\mu \overset{\text{n.r.}}{\rightarrow} \frac{f_\Delta}{m_\pi}\, \vec{k}\cdot\vec{S}$$

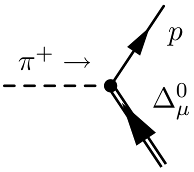

$$= \frac{1}{\sqrt{3}}\frac{f_\Delta}{m_\pi}\, k^\mu \overset{\text{n.r.}}{\rightarrow} -\frac{1}{\sqrt{3}}\frac{f_\Delta}{m_\pi}\, \vec{k}\cdot\vec{S}^\dagger\, \vec{k}\vec{S}^\dagger$$

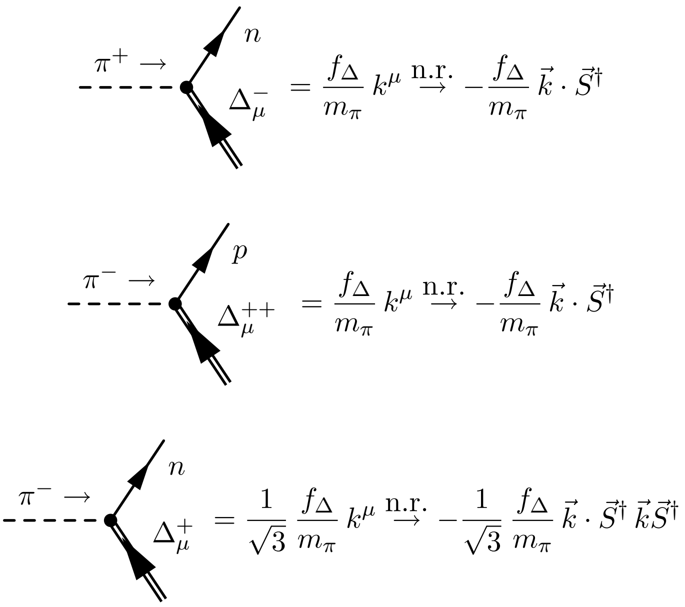

$$= \frac{f_\Delta}{m_\pi}\, k^\mu \overset{\text{n.r.}}{\rightarrow} -\frac{f_\Delta}{m_\pi}\, \vec{k}\cdot\vec{S}^\dagger$$

$$= \frac{f_\Delta}{m_\pi}\, k^\mu \overset{\text{n.r.}}{\rightarrow} -\frac{f_\Delta}{m_\pi}\, \vec{k}\cdot\vec{S}^\dagger$$

$$= \frac{1}{\sqrt{3}}\frac{f_\Delta}{m_\pi}\, k^\mu \overset{\text{n.r.}}{\rightarrow} -\frac{1}{\sqrt{3}}\frac{f_\Delta}{m_\pi}\, \vec{k}\cdot\vec{S}^\dagger\, \vec{k}\vec{S}^\dagger$$

Figure D.1: $\pi N\Delta$ *vertices*

In addition there are the vertices with the π^0.

D.4 Example: π^+ selfenergy

The vertices of the preceeding section are now applied to calculate the π^+ selfenergy. In subsec. 8.2.1 we found the following particle–hole diagram (fig. 8.1):

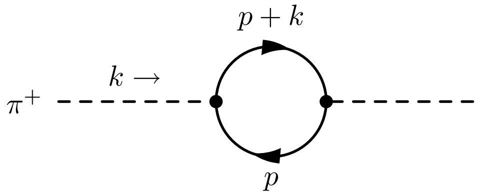

$$= -\Sigma$$

The diagram is evaluated to:

$$
\begin{aligned}
-\Sigma &= -T\sum_l \int \frac{d^3p}{(2\pi)^3}\, tr[(-i\sqrt{2}\,\frac{f_N}{m_\pi}\,\vec{k}\vec{\sigma})(-G_p(i(\omega_l+\omega_k),\vec{k}+\vec{p}))\,(i\sqrt{2}\,\frac{f_N}{m_\pi}\,\vec{k}\vec{\sigma})(-G_{nh}(i\omega_l,\vec{p}))] \\
\Rightarrow\ \Sigma &= 4\,\vec{k}^2\left(\frac{f_N}{m_\pi}\right)^2 T\sum_l \int \frac{d^3p}{(2\pi)^3}\, G_p(i(\omega_l+\omega_k),\vec{k}+\vec{p})\, G_{nh}(i\omega_l,\vec{p}) \\
&=: 4\,\vec{k}^2\,\Pi(\omega_k,\vec{k})
\end{aligned}
$$

The polarization function Π thus reads

$$\Pi(\omega_k,\vec{k}) = \left(\frac{f_N}{m_\pi}\right)^2 T\sum_l e^{i\omega_l\eta} \int \frac{d^3p}{(2\pi)^3}\, G_p(i(\omega_l+\omega_k),\vec{k}+\vec{p})\, G_{nh}(i\omega_l,\vec{p}) \tag{D.2}$$

where we have introduced a factor $e^{i\omega_l\eta}$ to facilitate convergence (cf. [71], p.247).

The imaginary–time propagators for the nucleons read

$$\begin{aligned} G_p &= \frac{1}{i(\omega_l + \omega_k) + \mu_p - \omega_p(\vec{p} + \vec{k})} \\ G_{nh} &= \frac{1}{i(\omega_l) + \mu_n - \omega_n(\vec{p})} \ . \end{aligned}$$

What does G_{nh} mean? At $T = 0$, the nucleon propagator as given in eq. (4.10) contains one term with $+i\varepsilon$ and a Theta function $\Theta(|\vec{p}| - p_f)$ for the particles and one term with $-i\varepsilon$ and $\Theta(p_f - |\vec{p}|)$ for the holes. Here such a distinction is not obvious. However, the Fermi occupation functions that are going to develop will take over from the Theta functions and help disentangle the various terms.

$$\begin{aligned} \Pi(\omega_k, \vec{k}) = \left(\frac{f_N}{m_\pi}\right)^2 \int \frac{d^3p}{(2\pi)^3} \frac{1}{i\omega_k - \omega_p(\vec{p} + \vec{k}) + \omega_n(\vec{p}) + \mu_p - \mu_n} \\ T \sum_l e^{i\omega_l \eta} \left(\frac{1}{i\omega_l + \mu_n - \omega_n(\vec{p})} - \frac{1}{i(\omega_l + \omega_k) + \mu_p - \omega_p(\vec{p} + \vec{k})} \right) \end{aligned} \tag{D.3}$$

In the second term the following shift can be carried out:

$$\begin{aligned} & T \sum_{l\, odd} e^{i\omega_l \eta} \frac{1}{i(\omega_l + \omega_k) + \mu_p - \omega_p(\vec{p} + \vec{k})} \\ =& T \sum_{l\, odd} e^{i\omega_l \eta} \frac{1}{i(\omega_{l+k}) + \mu_p - \omega_p(\vec{p} + \vec{k})} \\ =& T \sum_{l\, odd} e^{i\omega_l \eta} \frac{1}{i(\omega_l) + \mu_p - \omega_p(\vec{p} + \vec{k})} \end{aligned} \tag{D.4}$$

That is possible since the outer frequency ω_k is a bosonic one, and adding an even number to l in the sum makes no difference.

We can proceed with the Matsubara sums by extending the variable $i\omega_l$ to the general complex variable z. The Matsubara sum can then be understood as the result of a complex integration over the function $1/(e^{\beta z} + 1)$ that has poles at $i\omega_l$ (l odd), and residue -1:

$$T \sum_l \frac{e^{i\omega_l \eta}}{i\omega_l + \kappa} = -\frac{1}{2\pi i} \oint dz \, \frac{e^{\eta z}}{e^{\beta z} + 1} \, \frac{1}{z - \kappa}$$

The path of integration encloses the imaginary axis. As the parts at $\pm i\,\infty$ do not contribute, this path can be deformed such that it encircles the poles $\pm\kappa$ on the real axis. This is indicated in fig. D.2:

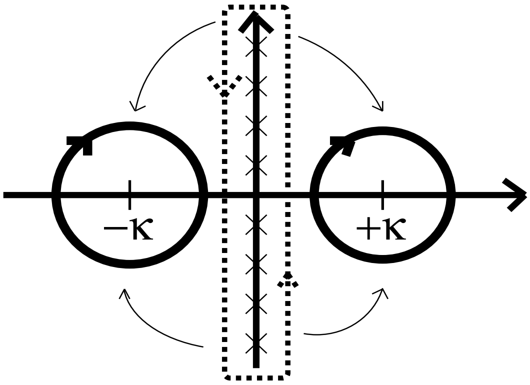

Then the complex integral evaluates to

$$= -2\pi i \; Res(integrand(\pm\kappa))$$
$$= \frac{e^{\eta\kappa}}{e^{\pm\beta\kappa}+1}$$

Figure D.2: Path of integration in complex plane

$$\Rightarrow \lim_{\eta\to 0} \; T \sum_l e^{i\omega_l \eta} \, G_p(i(\omega_l+\omega_k),\vec{k}+\vec{p}) \, G_{nh}(i\omega_l,\vec{p})$$
$$= \frac{1}{i\omega_k - \omega_p(\vec{p}+\vec{k}) + \omega_n(\vec{p}) + \mu_p - \mu_n}\left(\frac{1}{e^{\beta(\omega_n(\vec{p})-\mu_n)}+1} - \frac{1}{e^{\beta(\omega_p(\vec{p}+\vec{k})-\mu_p)}+1}\right) \quad \text{(D.5)}$$

The second Fermi distribution in eq. (D.5) above depends on the angle between $\vec{p}$ and $\vec{k}$. This can be remedied by a substitution $\vec{p} \leftrightarrow -\vec{p}-\vec{k}$.

Then

$$\begin{aligned}\Pi(\omega_k,\vec{k}) = \; & \left(\frac{f_N}{m_\pi}\right)^2 \int \frac{d^3p}{(2\pi)^3}\, n_n(\vec{p}) \frac{1}{i\omega_k - \omega_p(\vec{p}+\vec{k}) + \omega_n(\vec{p}) + \mu_p - \mu_n} \\ & - \left(\frac{f_N}{m_\pi}\right)^2 \int \frac{d^3p}{(2\pi)^3}\, n_p(\vec{p}) \frac{1}{i\omega_k - \omega_p(\vec{p}) + \omega_n(\vec{p}+\vec{k}) + \mu_p - \mu_n} \, .\end{aligned}$$

Now analytic continuation of Π onto the real axis can be performed: $i\,\omega_k \to k^0 + i\varepsilon$.

$$\Rightarrow \quad \text{(D.6)}$$

$$\begin{aligned}\Sigma(\omega_k,\vec{k}) = \; & 4\,\vec{k}^2 \left(\frac{f_N}{m_\pi}\right)^2 \int \frac{d^3p}{(2\pi)^3}\, n_n(\vec{p}) \frac{1}{k^0 - \omega_p(\vec{p}+\vec{k}) + \omega_n(\vec{p}) + \mu_p - \mu_n + i\varepsilon} \\ & - 4\,\vec{k}^2 \left(\frac{f_N}{m_\pi}\right)^2 \int \frac{d^3p}{(2\pi)^3}\, n_p(\vec{p}) \frac{1}{k^0 + \omega_n(\vec{p}+\vec{k}) - \omega_p(\vec{p}) + \mu_p - \mu_n + i\varepsilon} \quad \text{(D.7)}\end{aligned}$$

After performing the angular integration which gives rise to the abbreviations

$$\omega_{p,n,\pm} = \sqrt{\vec{p}^2 + \vec{k}^2 + m_{p,n}^2 \, \pm \, 2|\vec{p}||\vec{k}|},$$

we obtain the final expression of the particle–hole selfenergy:

$$\begin{aligned}\Sigma(\omega_k,\vec{k}) = -4\,\vec{k}^2\left(\frac{f_N}{m_\pi}\right)^2\frac{1}{4\pi^2 k}\,\Bigg(&\int_0^\infty dp\,p\,n_n(\vec{p})\;(\omega_{p,+}-\omega_{p,-}\\ &+(\omega_n(\vec{p})+k^0+\mu_p-\mu_n+i\varepsilon)\ln\frac{\omega_{p,+}-\omega_n(\vec{p})-k^0-\mu_p+\mu_n-i\varepsilon}{\omega_{p,-}-\omega_n(\vec{p})-k^0-\mu_p+\mu_n-i\varepsilon}\Bigg)\\ &+\int_0^\infty dp\,p\,n_p(\vec{p})\;(\omega_{n,+}-\omega_{n,-}\\ &+(\omega_p(\vec{p})-k^0-\mu_p+\mu_n-i\varepsilon)\ln\frac{\omega_{n,+}-\omega_p(\vec{p})+k^0+\mu_p-\mu_n+i\varepsilon}{\omega_{n,-}-\omega_p(\vec{p})+k^0+\mu_p-\mu_n+i\varepsilon}\Bigg)\Bigg)\end{aligned}$$

Deltas

The other four selfenergy diagrams for the π^+ consist of Δ-hole excitations:

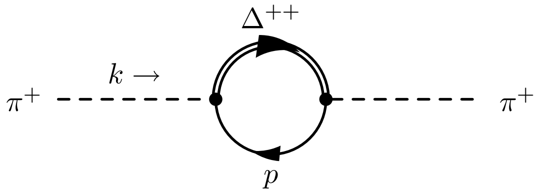

$= -\Sigma_1$

$$-\Sigma_1 = -T\sum_l\int\frac{d^3p}{(2\pi)^3}\,tr[(i\frac{f_\Delta}{m_\pi}\,\vec{k}\cdot\vec{S}^\dagger)\,(-G_{\Delta^{++}}(i(\omega_l+\omega_k),\vec{k}+\vec{p}))\,(-i\frac{f_\Delta}{m_\pi}\,\vec{k}\cdot\vec{S})\,(-G_{ph}(i\omega_l,\vec{p}))]$$

$$\Rightarrow\ \Sigma_1 = \left(\frac{f_\Delta}{m_\pi}\right)^2\frac{4}{3}\,\vec{k}^2\,T\sum_l\int\frac{d^3p}{(2\pi)^3}\,G_{\Delta^{++}}(i(\omega_l+\omega_k),\vec{k}+\vec{p})\,G_{ph}(i\omega_l,\vec{p})$$

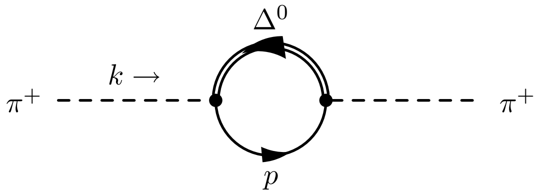

$= -\Sigma_2$

$$-\Sigma_2 = -T\sum_l\int\frac{d^3p}{(2\pi)^3}\,tr[(\frac{i}{\sqrt{3}}\frac{f_\Delta}{m_\pi}\,\vec{k}\cdot\vec{S}^\dagger)\,(-G_{\Delta^0}(i(\omega_l-\omega_k),\vec{p}-\vec{k}))\,(\frac{-i}{\sqrt{3}}\frac{f_\Delta}{m_\pi}\,\vec{k}\cdot\vec{S})\,(-G_{ph}(i\omega_l,\vec{p}))]$$

$$\Rightarrow\ \Sigma_2 = \left(\frac{f_\Delta}{m_\pi}\right)^2\frac{4}{3}\,\vec{k}^2\,T\sum_l\int\frac{d^3p}{(2\pi)^3}\,\frac{1}{3}\,G_{\Delta^0}(i(\omega_l-\omega_k),\vec{p}-\vec{k})\,G_{ph}(i\omega_l,\vec{p})$$

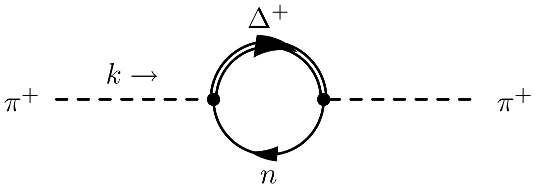

$= -\Sigma_3$

$$-\Sigma_3 = -T\sum_l \int \frac{d^3p}{(2\pi)^3}\, tr[(\frac{i}{\sqrt{3}}\frac{f_\Delta}{m_\pi}\,\vec{k}\vec{S}^\dagger)\,(-G_{\Delta^+}(i(\omega_l+\omega_k),\vec{k}+\vec{p}))\,(\frac{-i}{\sqrt{3}}\frac{f_\Delta}{m_\pi}\,\vec{k}\vec{S})\,(-G_{nh}(i\omega_l,\vec{p}))]$$

$$\Rightarrow\ \Sigma_3 = \left(\frac{f_\Delta}{m_\pi}\right)^2 \frac{4}{3}\vec{k}^2\, T\sum_l \int \frac{d^3p}{(2\pi)^3}\,\frac{1}{3}\, G_{\Delta^+}(i(\omega_l+\omega_k),\vec{k}+\vec{p})\, G_{nh}(i\omega_l,\vec{p})$$

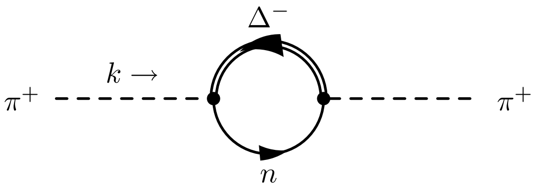

$= -\Sigma_4$

$$-\Sigma_4 = -T\sum_l \int \frac{d^3p}{(2\pi)^3}\, tr[(-i\frac{f_\Delta}{m_\pi}\,\vec{k}\cdot\vec{S}^\dagger)\,(-G_{\Delta^-}(i(\omega_l-\omega_k),\vec{p}-\vec{k}))\,(i\frac{f_\Delta}{m_\pi}\,\vec{k}\cdot\vec{S})\,(-G_{nh}(i\omega_l,\vec{p}))]$$

$$\Rightarrow\ \Sigma_4 = \left(\frac{f_\Delta}{m_\pi}\right)^2 \frac{4}{3}\vec{k}^2\, T\sum_l \int \frac{d^3p}{(2\pi)^3}\, G_{\Delta^-}(i(\omega_l-\omega_k),\vec{p}-\vec{k})\, G_{nh}(i\omega_l,\vec{p})$$

The expressions for $\Sigma_1 - \Sigma_4$ are quite similar. For the evaluation of the Matsubara sums we only have to heed the difference in the Δ–propagators (depending on $\omega_l + \omega_k$ or $\omega_l - \omega_k$).

a) $\omega_l + \omega_k$:

$$\begin{aligned}
& T\sum_l e^{i\omega_l\eta}\, G_\Delta(i(\omega_l+\omega_k),\vec{k}+\vec{p})\, G_N(i\omega_l,\vec{p}) \\
&= T\sum_l e^{i\omega_l\eta}\,\frac{1}{i(\omega_l+\omega_k)+\mu_\Delta-\omega_\Delta(\vec{k}+\vec{p})}\,\frac{1}{i\omega_l+\mu_N-\omega_N(\vec{p})} \\
&= T\sum_l e^{i\omega_l\eta}\,\frac{1}{i\omega_k+\mu_\Delta-\mu_N-\omega_\Delta(\vec{k}+\vec{p})+\omega_N(\vec{p})} \\
&\qquad \left(\frac{1}{i\omega_l+\mu_N-\omega_N(\vec{p})} - \frac{1}{i(\omega_l+\omega_k)+\mu_\Delta-\omega_\Delta(\vec{k}+\vec{p})}\right) \\
&= \frac{1}{i\omega_k+\mu_\Delta-\mu_N-\omega_\Delta(\vec{k}+\vec{p})+\omega_N(\vec{p})}\left(\frac{1}{e^{\beta(\omega_N(\vec{p})-\mu_N)}+1} - \frac{1}{e^{\beta(\omega_\Delta(\vec{k}+\vec{p})-\mu_\Delta)}+1}\right)
\end{aligned}$$

Shift in the 2. term: $\vec{p} \;\rightarrow\; -\vec{p}-\vec{k}$

$$\begin{aligned}
\Rightarrow \qquad & \int \frac{d^3p}{(2\pi)^3}\, \frac{1}{i\omega_k + \mu_\Delta - \mu_N - \omega_\Delta(\vec{k}+\vec{p}) + \omega_N(\vec{p})}\; \frac{1}{e^{\beta(\omega_\Delta(\vec{k}+\vec{p})-\mu_\Delta)}+1} \\
\rightarrow \qquad & \int \frac{d^3p}{(2\pi)^3}\, \frac{1}{i\omega_k + \mu_\Delta - \mu_N - \omega_\Delta(\vec{p}) + \omega_N(\vec{p}+\vec{p})}\; \frac{1}{e^{\beta(\omega_\Delta(\vec{p})-\mu_\Delta)}+1}
\end{aligned}$$

$$\begin{aligned}
\Pi_{a)} = \frac{4}{3}\left(\frac{f_\Delta}{m_\pi}\right)^2 \int \frac{d^3p}{(2\pi)^3} \Bigg[& n_N(\vec{p})\, \frac{1}{i\omega_k - \omega_\Delta(\vec{k}+\vec{p}) + \omega_N(\vec{p}) + \mu_\Delta - \mu_N} \\
& - n_\Delta(\vec{p})\, \frac{1}{i\omega_k - \omega_\Delta(\vec{p}) + \omega_N(\vec{p}+\vec{k}) + \mu_\Delta - \mu_N} \Bigg]
\end{aligned}$$

The width of the Δ is introduced only at this stage, in connection with the analytic continuation: $i\omega_k \;\rightarrow\; k^0 \,+\, \frac{i}{2}\,\Gamma_\Delta$.

$$\begin{aligned}
\Pi_{a)} = \frac{4}{3}\left(\frac{f_\Delta}{m_\pi}\right)^2 \int \frac{d^3p}{(2\pi)^3} \Bigg[& n_N(\vec{p})\, \frac{1}{k^0 - \omega_\Delta(\vec{k}+\vec{p}) + \omega_N(\vec{p}) + \mu_\Delta - \mu_N + \frac{i}{2}\,\Gamma_\Delta} \\
& - n_\Delta(\vec{p})\, \frac{1}{k^0 - \omega_\Delta(\vec{p}) + \omega_N(\vec{p}+\vec{k}) + \mu_\Delta - \mu_N + \frac{i}{2}\,\Gamma_\Delta} \Bigg]
\end{aligned}$$

b) $\omega_l - \omega_k$:

$$\begin{aligned}
& T \sum_l e^{i\omega_l \eta}\, G_\Delta(i(\omega_l - \omega_k), \vec{p}-\vec{k})\, G_N(i\omega_l, \vec{p}) \\
&= T \sum_l e^{i\omega_l \eta}\, \frac{1}{i(\omega_l - \omega_k) + \mu_\Delta - \omega_\Delta(\vec{p}-\vec{k})}\; \frac{1}{i\omega_l + \mu_N - \omega_N(\vec{p})} \\
&= T \sum_l e^{i\omega_l \eta}\, \frac{1}{-i\omega_k + \mu_\Delta - \mu_N - \omega_\Delta(\vec{p}-\vec{k}) + \omega_N(\vec{p})} \\
&\qquad \left(\frac{1}{i\omega_l + \mu_N - \omega_N(\vec{p})} \;-\; \frac{1}{i(\omega_l - \omega_k) + \mu_\Delta - \omega_\Delta(\vec{p}-\vec{k})} \right) \\
&= \frac{1}{-i\omega_k + \mu_\Delta - \mu_N - \omega_\Delta(\vec{p}-\vec{k}) + \omega_N(\vec{p})} \left(\frac{1}{e^{\beta(\omega_N(\vec{p})-\mu_N)}+1} - \frac{1}{e^{\beta(\omega_\Delta(\vec{p}-\vec{k})-\mu_\Delta)}+1} \right)
\end{aligned}$$

Shift in the 2. term: $\vec{p} \;\rightarrow\; -\vec{p}-\vec{k}$

$$\begin{aligned}
\Pi_{b)} = \frac{4}{3}\left(\frac{f_\Delta}{m_\pi}\right)^2 \int \frac{d^3p}{(2\pi)^3} \Bigg[& n_N(\vec{p})\, \frac{1}{-i\omega_k - \omega_\Delta(\vec{p}-\vec{k}) + \omega_N(\vec{p}) + \mu_\Delta - \mu_N} \\
& - n_\Delta(\vec{p})\, \frac{1}{-i\omega_k - \omega_\Delta(\vec{p}) + \omega_N(\vec{p}-\vec{k}) + \mu_\Delta - \mu_N} \Bigg]
\end{aligned}$$

Analytic continuation: $i\omega_k \;\to\; k^0 + \frac{i}{2}\Gamma_\Delta$

$$
\begin{aligned}
\Pi_{b)} = \frac{4}{3}\left(\frac{f_\Delta}{m_\pi}\right)^2 \int\frac{d^3p}{(2\pi)^3} \Bigg[& n_N(\vec{p})\,\frac{1}{-k^0-\omega_\Delta(\vec{p}-\vec{k})+\omega_N(\vec{p})+\mu_\Delta-\mu_N-\frac{i}{2}\Gamma_\Delta} \\
& -n_\Delta(\vec{p})\,\frac{1}{-k^0-\omega_\Delta(\vec{p})+\omega_N(\vec{p}-\vec{k})+\mu_\Delta-\mu_N-\frac{i}{2}\Gamma_\Delta}\Bigg]
\end{aligned}
$$

Now we insert the proper particle indices back into $\Pi_{a)}, \Pi_{b)}$ and collect all terms containing Fermi factors n_p and n_n. Those containing n_Δ can be neglected, since the density of Deltas vanishes at low temperatures $T \to 0$.

$$
\begin{aligned}
\Pi_{\Delta N} = {} & \frac{4}{3}\left(\frac{f_\Delta}{m_\pi}\right)^2 \int\frac{d^3p}{(2\pi)^3}\, n_p(\vec{p}) \left(\frac{1}{k^0-\omega_\Delta(\vec{k}+\vec{p})+\omega_p(\vec{p})+\mu_{\Delta^{++}}-\mu_p+\frac{i}{2}\Gamma_\Delta}\right. \\
& \left. -\frac{1}{3}\,\frac{1}{k^0+\omega_\Delta(\vec{p}-\vec{k})-\omega_p(\vec{p})-\mu_{\Delta^0}+\mu_p+\frac{i}{2}\Gamma_\Delta}\right) \\
& +\frac{4}{3}\left(\frac{f_\Delta}{m_\pi}\right)^2 \int\frac{d^3p}{(2\pi)^3}\, n_n(\vec{p}) \left(\frac{1}{3}\,\frac{1}{k^0-\omega_\Delta(\vec{k}+\vec{p})+\omega_n(\vec{p})+\mu_{\Delta^{+}}-\mu_n+\frac{i}{2}\Gamma_\Delta}\right. \\
& \left. -\frac{1}{k^0+\omega_\Delta(\vec{p}-\vec{k})-\omega_n(\vec{p})-\mu_{\Delta^-}+\mu_n+\frac{i}{2}\Gamma_\Delta}\right)
\end{aligned}
$$

Angular integration gives rise to the energy bounds $\Omega_\pm$ which for the Δ read

$$
\Omega_\pm = \sqrt{\vec{p}^2+\vec{k}^2+m_\Delta^2 +\, 2\,|\vec{p}||\vec{k}|}\ .
$$

The final expression for the Δ – nucleon contribution then reads:

$$
\begin{aligned}
\Sigma_{\Delta N} = {} & -4\vec{k}^2\,\frac{4}{3}\left(\frac{f_\Delta}{m_\pi}\right)^2 \frac{1}{4\pi^2 k}\int_0^\infty dp\,p \\
& \Bigg[n_p(\vec{p}) \left(\frac{4}{3}\,(\Omega^+-\Omega_-)\right. \\
& +\ (\omega_p(\vec{p})+k^0+\mu_{\Delta^{++}}-\mu_p+\frac{i}{2}\Gamma_\Delta)\ln\frac{\Omega^+-k^0-\omega_p(\vec{p})-\mu_{\Delta^{++}}+\mu_p-\frac{i}{2}\Gamma_\Delta}{\Omega^--k^0-\omega_p(\vec{p})-\mu_{\Delta^{++}}+\mu_p-\frac{i}{2}\Gamma_\Delta} \\
& \left.+\frac{1}{3}(\omega_p(\vec{p})-k^0+\mu_{\Delta^0}-\mu_p-\frac{i}{2}\Gamma_\Delta)\ln\frac{\Omega^++k^0-\omega_p(\vec{p})-\mu_{\Delta^0}+\mu_p+\frac{i}{2}\Gamma_\Delta}{\Omega^-+k^0-\omega_p(\vec{p})-\mu_{\Delta^0}+\mu_p+\frac{i}{2}\Gamma_\Delta}\right) \\
& +n_n(\vec{p}) \left(\frac{4}{3}\,(\Omega^+-\Omega_-)\right. \\
& +\frac{1}{3}(\omega_n(\vec{p})+k^0+\mu_{\Delta^+}-\mu_n+\frac{i}{2}\Gamma_\Delta)\ln\frac{\Omega^+-k^0-\omega_n(\vec{p})-\mu_{\Delta^+}+\mu_n-\frac{i}{2}\Gamma_\Delta}{\Omega^--k^0-\omega_n(\vec{p})-\mu_{\Delta^+}+\mu_n-\frac{i}{2}\Gamma_\Delta} \\
& \left.+\ (\omega_n(\vec{p})-k^0+\mu_{\Delta^-}-\mu_n-\frac{i}{2}\Gamma_\Delta)\ln\frac{\Omega^++k^0-\omega_n(\vec{p})-\mu_{\Delta^-}+\mu_n+\frac{i}{2}\Gamma_\Delta}{\Omega^-+k^0-\omega_n(\vec{p})-\mu_{\Delta^-}+\mu_n+\frac{i}{2}\Gamma_\Delta}\right)\Bigg]
\end{aligned}
$$

D.5 s-wave pion selfenergy

The s–wave contributions to the pion selfenergy are taken from [74]. There the calculation is based on χPT and comprises all diagrams up to two loop order. It is restricted to on–shell pions with zero three-momentum. The result for the π^- then reads:

$$\Sigma_{\pi^-} = \frac{p_{f_n}^3}{3\pi^2}\,(T^-_{\pi N} - T^+_{\pi N}) - \frac{p_{f_p}^3}{3\pi^2}\,(T^-_{\pi N} + T^+_{\pi N}) + \Sigma^-_{rel} + \Sigma^-_{cor}$$

For the first two terms, the linear density approximation for the two (isospin–odd and isospin–even) T–matrix elements is used, putting in the experimental results

$$T^-_{\pi N} = (1.847 \pm 0.086)\mathrm{fm}, \qquad\qquad T^+_{\pi N} = (-0.045 \mp 0.088)\mathrm{fm}\ .$$

The terms going beyond the linear density approximation are a relativistic correction from the second diagram in fig. 8.8

$$\Sigma^-_{rel} = \frac{g_A^2 m_\pi^2}{10(\pi f_\pi m_N)^2}\,(p_{f_p}^5 - p_{f_n}^5),$$

and the contributions from the last three terms in fig. 8.8

$$\begin{aligned}
\Sigma^-_{cor} =& \frac{4m_\pi^2}{(4\pi f_\pi)^4}\Bigg(2(p_{f_p}^2 + p_{f_n}^2)^2 + 2p_{f_p}p_{f_n}(p_{f_p} - p_{f_n})^2 + (p_{f_p}^2 - p_{f_n}^2)^2 \ln\frac{|p_{f_p} - p_{f_n}|}{p_{f_p} + p_{f_n}}\Bigg)\\
&+ \frac{g_A^2 m_\pi^2}{(4\pi f_\pi)^4}\Bigg(2p_{f_p}^2(m_\pi^2 - 2p_{f_p}^2) + 2p_{f_n}^2(m_\pi^2 - 2p_{f_n}^2)\\
&+8p_{f_p}^3 m_\pi \arctan\frac{2p_{f_p}}{m_\pi} + 8p_{f_n}^3 m_\pi \arctan\frac{2p_{f_n}}{m_\pi})\\
&-m_\pi^2(\frac{m_\pi^2}{2} + 4p_{f_p}^2)\ln(1 + \frac{4p_{f_p}^2}{m_\pi^2}) - m_\pi^2(\frac{m_\pi^2}{2} + 4p_{f_n}^2)\ln(1 + \frac{4p_{f_n}^2}{m_\pi^2})\Bigg)\ .
\end{aligned}$$

The π^+ selfenergy can be obtained by an isospin transformation

$$\Sigma^+(p_{f_p}, p_{f_n}) = \Sigma^-(p_{f_n}, p_{f_p})\ .$$

Similar expressions for the π^0 can be found in [74].

Bibliography

[1] Z. Fodor, *Lattice QCD Results at Finite Temperature and Density*, Nucl. Phys. **A 715**, 319 (2003), hep-lat/0209101.

[2] A. Wirzba, *The pion propagator in isospin-asymmetric isotropic homogeneous nuclear matter to second order in the momentum expansion*, private communication.

[3] J. Gasser and H. Leutwyler, *Chiral perturbation theory: Expansions in the mass of the strange quark*, Nucl. Phys. **B 250**, 465 (1985).

[4] S. Weinberg, *Pion scattering lengths*, Phys. Rev. Lett. **17**, 616 (1966).

[5] Y. Tomozawa, *Axial-vector coupling constant renormalization and the meson-baryon scattering lengths*, Nuov. Cim. **XLVI**, 707 (1966), Serie X.

[6] J. Gasser and H. Leutwyler, *Spontaneously broken symmetries: Effective Lagrangians at finite volume*, Nucl. Phys. **B 307**, 763 (1988).

[7] E. Jenkins and A. V. Manohar, *Baryon chiral perturbation theory using a heavy fermion lagrangian*, Phys. Lett. **B 255**, 558 (1991).

[8] J. F. Donoghue, B. R. Holstein and B. Borasoy, *SU(3) baryon chiral perturbation theory and long distance regularization*, Phys. Rev. **D 59**, 036002 (1999), hep-ph/9804281.

[9] U.-G. Meißner, J. A. Oller and A. Wirzba, *In-medium chiral perturbation theory beyond the mean-field approximation*, Ann. Phys. (N. Y.) **297**, 27 (2002), nucl-th/0109026.

[10] E. Epelbaum, W. Glöckle and U.-G. Meißner, *Improving the convergence of the chiral expansion for nuclear forces I: Peripheral phases*, Eur. Phys. J. **A 19**, 125 (2004), nucl-th/0304037.

[11] D. B. Kaplan and A. E. Nelson, *Strange goings on in dense nucleonic matter*, Phys. Lett. **B 175**, 57 (1986).

[12] D. B. Kaplan and A. E. Nelson, *Strange condensate realignment in relativistic heavy ion collisions*, Phys. Lett. **B 192**, 193 (1987).

[13] B. Borasoy, *Sigma-terms in heavy baryon chiral perturbation theory revisited*, Eur. Phys. J. **C 8**, 121 (1999), hep-ph/9807453.

[14] X. S. Fang, C. M. Ko, G. E. Brown and V. Koch, *Medium effects on kaon and antikaon spectra in heavy-ion collisions*, Phys. Rev. **C 47**, 1678 (1993).

[15] G. E. Brown, C.-H. Lee, M. Rho and V. Thorsson, *From kaon-nuclear interactions to kaon condensation*, Nucl. Phys. **A 567**, 937 (1994), hep-ph/9304204.

[16] C.-H. Lee, G. E. Brown, D.-P. Min and M. Rho, *An Effective Chiral Lagrangian Approach to Kaon-Nuclear Interactions: Kaonic atom an kaon condensation*, Nucl. Phys. **A 585**, 401 (1995), hep-ph/9406311.

[17] G. E. Brown, V. Koch and M. Rho, *The pion at finite temperature and density*, Nucl. Phys. **A 535**, 701 (1991).

[18] E. Friedman, A. Gal and C. J. Batty, *Density-dependent K^- nuclear optical potentials from kaonic atoms*, Nucl. Phys. **A 579**, 518 (1994).

[19] N. Kaiser, T. Waas and W. Weise, *SU(3) chiral dynamics with coupled channels Eta and kaon photoproduction*, Nucl. Phys. **A 612**, 297 (1997), hep-ph/9607459.

[20] T. Waas, N. Kaiser and W. Weise, *Effective kaon masses in dense nuclear and neutron matter*, Phys. Lett. **B 379**, 34 (1996).

[21] J. Schaffner-Bielich, V. Koch and M. Effenberger, *Medium Modified Cross Sections, Temperature and Finite Momentum Effects for Antikaon Production in Heavy-Ion Collisions*, Nucl. Phys. **A 669**, 153 (2000), nucl-th/9907095.

[22] T. Nakano et al., (LEPS Collaboration), *Evidence for Narrow S=+1 Baryon Resonance in Photo-production from Neutron*, Phys. Rev. Lett. **91**, 012002 (2003), hep-ex/0301020.

[23] N. Herrmann, (FOPI Collaboration), *Particle production and flow at SIS energies*, Nucl. Phys. **A 610**, 49c (1996), nucl-ex/9610007.

[24] F. Laue et al., (KaoS Collaboration), *Medium Effects in Kaon and Antikaon Production in Nuclear Collisions at Subthreshold Beam Energies*, Phys. Rev. Lett. **82**, 1640 (1999), nucl-ex/9901005.

[25] P. Senger, (KaoS Collaboration), *Strange mesons in dense matter*, in *Hadrons in dense matter*, page 96, Proceedings of the Intl. Workshop XXVIII on Gross Porperties of Nuclei and Nuclear Excitations, Hirschegg, Austria, 2000.

[26] A. Devismes, (FOPI Collaboration), *Results from FOPI on strangeness production and propagation in hot and dense nuclear matter*, in *Hadrons in dense matter*, page 104, Proceedings of the Intl. Workshop XXVIII on Gross Porperties of Nuclei and Nuclear Excitations, Hirschegg, Austria, 2000.

[27] P. Senger, (KaoS Collaboration), *Strangeness and charm production in nucleus-nucleus collisions at beam energies near the thresholds*, in *Structure of hadrons*, page 259, Proceedings of the Intl. Workshop XXIX on Gross Porperties of Nuclei and Nuclear Excitations, Hirschegg, Austria, 2001.

[28] V. Koch, *K^--proton scattering and the $\Lambda(1405)$ in dense matter*, Phys. Lett. **B 337**, 7 (1994), nucl-th/9406030.

[29] M. Lutz, *Nuclear kaon dynamics*, Phys. Lett. **B 426**, 12 (1998), nucl-th/9709073.

[30] M. F. M. Lutz and E. E. Kolomeitsev, *Relativistic chiral SU(3) symmetry, large N_c sum rules and meson-baryon scattering*, GSI Preprint (2001), nucl-th/0105042.

[31] E. Oset and A. Ramos, *The properties of $\bar{K}$ in the nuclear medium*, Nucl. Phys. **A 671**, 481 (2000), nucl-th/9906016.

[32] B. Borasoy and U.-G. Meißner, *Chiral Expansion of Baryon Masses and σ-Terms*, Ann. Phys. (N. Y.) **254**, 192 (1997), hep-ph/9607432.

[33] E. Oset and A. Ramos, *Non-perturbative chiral approach to s-wave $\bar{K}N$ interactions*, Nucl. Phys. **A 635**, 99 (1998), nucl-th/9711022.

[34] J. A. Oller, E. Oset and A. Ramos, *Chiral Unitary approach to meson-meson and meson-baryon interactions and nuclear applications*, Progr. Part. Nucl. Phys. **45**, 157 (2000), hep-ph/0002193.

[35] V. Bernard, N. Kaiser and U.-G. Meißner, *Chiral dynamics in nucleons and nuclei*, Int. J. Mod. Phys. **E 4**, 193 (1995), hep-ph/9501384.

[36] E. E. Salpeter and H. A. Bethe, *A Relativistic Equation for Bound-State Problems*, Phys. Rev. **84**, 1232 (1951).

[37] R. Hemingway, *Production of* $\Lambda(1405)$ *in* K^-p *reactions at* 4.2 *GeV/c*, Nucl. Phys. **B 253**, 742 (1985).

[38] C. B. Dover and G. E. Walker, *The interaction of kaons with nucleons and nuclei*, Phys. Rep. **89**, 44 (1982).

[39] R. J. Iwasaki et al., *Production of* $\Lambda(1405)$ *in* K^-p *reactions at* 4.2 *GeV/c*, Phys. Rev. Lett. **78** (1997).

[40] A. D. Martin, *A Relativistic Equation for Bound-State Problems*, Nucl. Phys. **B 179**, 33 (1981).

[41] B. R. Holstein, *A brief introduction to Chiral Perturbation Theory*, hep-ph/9911449.

[42] B. R. Holstein, *Chiral Perturbation Theory: a Primer*, hep-ph/9510344.

[43] B. R. Holstein, *Effective interactions are effective interactions*, hep-ph/0010033.

[44] U.-G. Meißner, *Chiral dynamics with strange quarks: Mysteries and opportunities*, Phys. Scripta **T 99**, 68 (2002), hep-ph/0201078.

[45] U.-G. Meißner, *Chiral QCD: Baryon Dynamics*, hep-ph/0007092.

[46] J. Gasser and H. Leutwyler, *Chiral perturbation theory to one loop*, Ann. Phys. (N. Y.) **158**, 142 (1984).

[47] J. F. Donghoe, E. Golowich and B.R.Holstein, *Dynamics of the Standard Model*, Cambridge Monographs on Particle Physics, Nuclear Physics and Cosmology, Cambridge University Press, 1992.

[48] J. Gasser, M. E. Sainio and A. Svarc, *Nucleons with chiral loops*, Nucl. Phys. **B 307**, 779 (1988).

[49] V. Bernard, N. Kaiser, J. Kambor and U.-G. Meißer, *Chiral structure of the nucleon*, Nucl. Phys. **B 388**, 315 (1992).

[50] N. Fettes, U.-G. Meißner and S. Steininger, *Pion-nucleon scattering in chiral perturbation theory I: Isospin-symmetric case*, Nucl. Phys. **A 640**, 199 (1998), hep-ph/9803266.

[51] V. Bernard, N. Kaiser and U.-G. Meißner, *Critical analysis of baryon masses and sigma-terms in heavy baryon chiral perturbation theory*, Z. Phys. **C 60**, 111 (1993), hep-ph/9303311.

[52] H. W. Fearing, *The Off-shell Nucleon-Nucleon Amplitude: Why it is unmeasurable in Nucleon-Nucleon Bremsstrahlung*, nucl-th/0006040.

[53] S. Scherer and H. W. Fearing, *A simple model illustrating the impossibility of measuring off-shell effects*, Nucl. Phys. **A 684**, 499 (2001), nucl-th/0006076.

[54] V. Thorsson and A. Wirzba, *S-wave Meson-Nucleon Interactions and the Meson Mass in Nuclear Matter from Chiral Effective Lagrangians*, Nucl. Phys. **A 589**, 633 (1995), nucl-th/9502003.

[55] J. A. Oller and E. Oset, *Chiral symmetry amplitudes in the s-wave isoscalar and isovector channels and the* $\sigma, f_0(980), a_0(980)$ *scalar mesons*, nucl-th/9601031.

[56] J. A. Oller, E. Oset and J. R. Pelaez, *Non-perturbative Approach to effective chiral Lagrangians and Meson Interactions*, Phys. Rev. Lett. **80**, 3452 (1998).

[57] C. Sauermann, *Photoproduktion von* η*-Mesonen an Protonen und Deuteronen*, doctoral thesis, TH Darmstadt, 1996.

[58] M. Urban, *Impulsabhängigkeit des* ρ*-Meson-Propagators in kalter Kernmaterie*, diploma thesis, TH Darmstadt, 1997.

[59] S. M. Flatté, *Coupled-channel analysis of the* $\pi\eta$ *and* $K\bar{K}$ *threshold*, Phys. Lett. **B 63**, 224 (1976).

[60] M. Lutz, *KN amplitudes*, private communication, 2002.

[61] P. J. Fink, G. He, R. H. Landau and J. W. Schnick, *Bound states, resonances and poles in low-energy* $\bar{K}N$ *interaction models*, Phys. Rev. **C 41**, 2720 (1990).

[62] M. Baldo et al., *Neutron stars and the transition to color-superconducting quark matter*, Phys. Lett. **B 562**, 153 (2003), nucl-th/0212096.

[63] M. Cubero, *Relativistische Landau-Vlasov-Gleichungen für hadronische Materie und Mediumeffekte bei der Pionenproduktion in Schwerionenreaktionen mittlerer Energie*, doctoral thesis, GSI - TH Darmstadt, 1990.

[64] A. B. Migdal, *Pion fields in nuclear matter*, Rev. Mod. Phys. **50**, 107 (1978).

[65] G. Chanfray, R. Rapp and J. Wambach, *Medium modifications of the Rho meson at CERN Super Proton Synchroton Energies (200 GeV/nucleon)*, Phys. Rev. Lett. **76**, 368 (1996), hep-ph/950835.

[66] M. Herrmann, B. Friman and W. Nörenberg, *Properties of Rho mesons in nuclear matter*, Nucl. Phys. **A 560**, 411 (1993).

[67] M. Urban, *Vektormesonen in dichter und heisser Materie*, doctoral thesis, TU Darmstadt, 2001.

[68] M. Lutz, A. Steiner and W. Weise, *Kaons in baryonic matter*, Nucl. Phys. **A 574**, 755 (1994).

[69] A. Ramos, J. Schaffner-Bielich and J. Wambach, *Kaon condensation in Neutron Stars*, nucl-th/0011003.

[70] V. R. Pandharipande, A. Akmal and D. G. Ravenhall, *Many-body theory of nuclear and neutron star matter*, in *Nuclear Astrophysics*, Proceedings of the Intl. Workshop XXVI on Gross Porperties of Nuclei and Nuclear Excitations, Hirschegg, Austria, 1998, nucl-th/9802048.

[71] Fetter and Walecka, *Quantum theory of many particle systems*, McGraw-Hill, 1971.

[72] M. Oertel and M. Urban, Calculations in the context hot and dense hadronic matter, private communication, 1999-2003.

[73] H. Gilg et al., *Deeply bound* π^- *states in* ^{207}*Pb formed in the* ^{208}*Pb(d,*^{3}*He) reaction*, Phys. Rev. **C 62**, 025201 (2000).

[74] N. Kaiser and W. Weise, *Systematic calculation of s-wave pion and kaon self-energies in asymmetric nuclear matter*, Phys. Lett. **B 512**, 283 (2001), nucl-th/0102062.

[75] N. K. Glendenning, *Compact stars*, Astronomy and astrophysics library, Springer, 1996.

[76] J. R. Oppenheimer and G.M.Volkoff, *On massive neutron cores*, Phys. Rev. **55**, 374 (1939).

[77] S. E. Thorsett and D. Chakrabarty, *Neutron Star Mass Measurements. I. Radio Pulsars*, Astrophys. J. **512**, 288 (1999), astro-ph/9803260.

[78] G. Q. Li, C.-H. Lee and G. E. Brown, *Kaons in dense matter, kaon production in heavy-ion collisions, and kaon condensation in neutron stars*, Nucl. Phys. **A 625**, 372 (1997), nucl-th/9706057.

[79] V. Thorsson, M. Prakash and J. M. Lattimer, *Composition, structure and evolution of neutron stars with kaon condensates*, Nucl. Phys. **A 572**, 693 (1994).

[80] A. Akmal, V. R. Pandharipande and D. G. Ravenhall, *The equation of state in nucleon matter and neutron star structure*, Phys. Rev. **C 58**, 1804 (1998), nucl-th/9804027.

[81] J. M. Luttinger and J. C. Ward, *Ground-State Energy of a Meny-Fermion System II*, Phys. Rev. **118**, 1417 (1960).

[82] M. Oertel, *Investigation of meson loop effects in the Nambu-Jona-Lasinio model*, doctoral thesis, TU Darmstadt, 2000.

[83] A. Sibirtsev and W. Cassing, *Antikaon Production in Proton-Nucleus Reactions and the* K^- *properties in nuclear matter*, Nucl. Phys. **A 641**, 476 (1998), nucl-th/9805021.

[84] A. Ramos et al., *Antikaons in nuclei and dense nuclear matter*, Nucl. Phys. **A 691**, 258 (2001), nucl-th/0101031.

[85] G. E. Brown, C.-H. Lee and R. Rapp, *Strange particles in dense matter and kaon condensates*, Nucl. Phys. **A 639**, 455 (1998), hep-ph/9712017.

[86] J. Gasser, H. Leutwyler and M. E. Sainio, *Sigma-term update*, Phys. Lett. **B 253**, 252 (1991).

Erklärung

Hiermit bestätige ich, daß ich die vorliegende Arbeit selbständig angefertigt und keine anderen als die angegebenen Hilfsmittel verwendet habe.

Darmstadt, 24.5.2004

Danksagung

Herrn Prof. J. Wambach danke ich für die Gelegenheit zur Anfertigung dieser Arbeit sowie für viele Anregungen und hilfreiche Gespräche.

Bei Herrn Prof. Dr. R. Roth möchte ich mich für dir Übernahme des Korreferats und die Bereitstellung von viel Rechenpower bedanken.

Besonderen Dank schulde ich meinem Betreuer Dr. M. Buballa, der mir mit unendlicher Geduld und Hilfsbereitschaft zur Seite gestanden ist und diese Arbeit damit ermöglicht hat.

Bei Herrn Dr. M. Lutz bedanke ich mich für etliche Anregungen und Erläuterungen während dieser Arbeit.

Herrn Dr. M. Urban danke ich für wertvolle Erläuterungen und Hilfestellungen in der Physik wie auch im Programmieren.

Allen Mitarbeitern der NHQ–Gruppe danke ich für ihre stete Hilfsbereitschaft.
Die angenehme Arbeitsatmosphäre in der NHQ–Gruppe hat dazu geführt, daßdiese Arbeit auch mit viel Spaßverbunden war.

Mein herzliches Dankeschön den Korrekturlesern dieser Arbeit, Dr. M. Buballa, Stephanie Roth und Sissel Preuss.

Schließlich gilt mein Dank meinen Eltern für ihre Unterstützung, ihre Geduld und ihr Verständnis, die mir mein Studium ermöglicht haben.

Lebenslauf

Name	Thomas Roth
Geburtsdatum	28. 2. 1970
Geburtsort	Hanau
Staatsangehörigkeit	deutsch
Familienstand	ledig

September 1976 - Juni 1980	Besuch der Grundschule Birstein
September 1980 - Juni 1989	Besuch des Wolfgang–Ernst–Gymnasiums in Büdingen
Juni 1989	Abitur
Dezember 1989 - März 1991	Zivildienst beim Roten Kreuz Büdingen
April 1991 - Sommer 1999	Studium der Physik an der TU Darmstadt
September 1993	Vordiplom in Physik
November 1997 - August 1999	Diplomarbeit bei Prof. Dr. Wambach über *“Die Reaktion $\pi N \rightarrow \rho N$ und der πN–Formfaktor”*
seit Oktober 1999	Wissenschaftlicher Mitarbeiter am Institut für Kernphysik der TU Darmstadt, Doktorarbeit über *“Medium modifications of antikaons in dense matter”* bei Prof. Dr. Wambach

Darmstadt, 24.5.2004